Architecture design for highly efficient perovskite solar cells

Contents

Abstract

Hybrid organic/inorganic metal halide perovskite solar cells (PSCs) have emerged widespread attentions and interesting because of the unprecedented progress of power conversion efficiency (PCE), which has been regarded as a most-promising for next-generation photovoltaics. Although the rapid development on PCE, the stability of PSCs is still far behind the industrial application requirement and the single-time utilization of metal electrode also increase the fabrication cost of perovskite-photovoltaics, induce environmental pollution and resource waste.

The stability and photovoltaic performance of PSCs are mainly determined by the quality of perovskite light harvester layer and its coverage. The polymer layers have been introduced into the PSCs for passivation of perovskite. The PCE of PSCs has been promoted to 20.5 and 19.1% under reverse scanning after poly(methyl 2-methylpropenoate) and polycarbonate passivation, respectively. The photovoltaic stability has also been enhanced, however, it is not so enough due to the ultraviolet sensitive TiO_2 electron transport materials (ETM). Moreover, the polymer deteriorates the hysteresis of PSCs because of its insulating nature and carrier accumulation during solar cells working.

Hence, the SnO_2 and Cs-perovskite have been employed into planar PSCs as ETM and light harvester to replace TiO_2 and $MAPbI_3$ perovskite. The stability and PCE have been significantly enhanced on SnO_2 based PSCs compared with that of the TiO_2 based PSCs. The low temperature fabrication process of SnO_2 has been also introduced into flexible PSCs (fPSCs). The fPSCs using SnO_2 as ETM could achieve a high PCE of 17.1% with an ignorable hysteresis, sustaining an excellent bending durability of ca. 76.5% even after 2000 bending cycles at bending radius of 4 mm. The improvement of bending durability should mainly come from superior bending resistance of nanoparticle component of SnO_2 ETM film, because the SnO_2 nanoparticle can release the bending stress.

The excessive PbI_2 of Cs-perovskite precursor has severely limited the PCE and stability of PSCs, even though the excessive PbI_2 contribute to form large crystal size perovskite. Thus, the second solution growth process (SSGP) has been employed into the perovskite crystal growth to eliminate the excessive PbI_2 and maintain the large crystal size. The PCE of SSGP PSCs has promoted to 21.6% with a negligible hysteresis, and kept a much better stability at continuous light soaking and thermal treatment conditions.

The SSGP PSCs have also realized a high PCE of 20.1% on large active area of 1.0 cm^2 with comparable high fill factor of records.

The single-time utilization of metal electrode fabricated by complicated deposition process of high vacuum thermal evaporation, which increases the fabrication cost of PSCs and wastes resource, and also causes ecological environmental pollution and hinders commercial application at the same time. Thus, the nanoporous Au film fabricated by simple and directly transfer process has been introduced into the PSCs. The nanoporous Au-PSCs achieve a high PCE of 19.0% with a negligible hysteresis. Moreover, the nanoporous Au film can realize more than 12 times reusing for the PSCs with a little reduction of PCE. The nanoporous Au film has also employed into fPSCs and obtained a high PCE of 17.3% with an excellent bending durability of ca. 98.5% even after 1000 bending cycles at a bending radius of 5 mm.

Improving the photovoltaic performance of PSCs by an approach of architecture design by varying the stacking configuration, passivation, and material innovation paves a potential way toward its commercial application.

Chapter 1. Introduction

1.1 Research background

Human civilization is usually accompanied with the utilization of energy. The unprecedented rapid growth of world's economy and population is accelerating the consumption and demand of energy, especially the fossil fuels, in which the society has witnessed the deteriorating environment and resource wasting. Therefore, the clean and renewable energy source has become a more preferable choice, especially the solar energy. The solar energy is a kind inexhaustible and clean source, which can solve the growing energy demand and environment. Photovoltaic device is a main path way to realize the conversion of solar energy to electricity[1,2]. Some photoactive materials, such as silicon[3–5], dyes[6,7], organic molecules[8,9], and perovskite[10–14], have been explored for high efficiency photovoltaic devices. Currently, the mainstream of photovoltaic device is silicon solar cells, which can realize a power conversion efficiency (PCE) of 26.6% in single crystal and large scale industrial application due to its high stability[15,16]. However, the energy payback time of silicon solar cells is still every long (ca. 25 years) because of the high cost of fabrication and high quality silicon crystals. Therefore, it is necessary to explore more affordable and cheaper photovoltaic devices.

Recently, the organic/inorganic hybrid perovskite has become the most promising materials as light harvesting semiconductor for solar cells and promoted the perovskite solar cells (PSCs) become a most promising next-generation photovoltaics. The organic/inorganic hybrid perovskites consist with ABX_3 structure, where A is organic-inorganic component with single valence state (methyl ammonium (MA^+), formamidinium (FA^+) and caesium (Cs^+)), B is Pb^{2+} and Sn^{2+}, X is a halide element of I^-, Cl^- and Br^-, respectively. The superior properties of organic/inorganic hybrid perovskites have promoted PCE of their devices from 3.8 to 24.2% only within a decade and partly taken away the shine from silicon solar cells[10,16–19], including the large light absorption coefficient[12], tunable band gap[13,20,21], low exciton binding energy[22], high carrier mobility[23], long distance of carrier diffusion[22], and low-temperature fabrication process[24]. The solution and low temperature fabrication approaches of perovskites can also be applied to flexible photovoltaics, light weight, wearable equipment, portable systems and bending displays[25–32].

The stability of PSCs becomes a critical limitation to replace the silicon solar cells due to the quality of perovskites film, organic component of perovskites and organic carrier transport materials, even though the PSCs has achieved an unprecedented development. Recently, the stability of PSCs has been remarkably enhanced by designing devices architecture, replacing organic component using Cs^+ and applying inorganic carriers transport materials such as CuSCN[33,34]. However, the latest results of stability of PSCs is still far behind the requirements of industrial application. Therefore, stability of PSCs should be promoted at the same pace as the photovoltaic performance to realize final commercial utilization.

1.2 Basic principle and type of solar cells

Basic principle of semiconductor photovoltaic

I will start to explain the basic principle of power conversion process and efficiency of solar cells[1]. Solar cell is a kind of photovoltaic device to realize the incident light energy conversion into the electrochemical potential and electricity by light harvester materials and external circuit. The light harvesting materials capture the photons of light. The solar light excites the electron from conduction band to valance band in the light harvesting materials, in other words, the electron has promoted from ground state to excited states as shown in **Figure 1**. The electron-hole pairs are generated by light, and separated electron and hole as carriers are delivered to external circuit and converted into electricity. The electrons and holes quickly decay to the lower available energy level inside the conduction and valance band in semiconductors, in which this process is much faster than the radiative and non-radiative recombination process of electron and hole corresponding to relaxation of excited to ground state. The population of generated excited electrons is usually dependent on the energy of incident light (E) and bandgap of semiconductor (E_g). Here, we assume the $E \gg E_g$ to obtain a perfectly light absorbing.

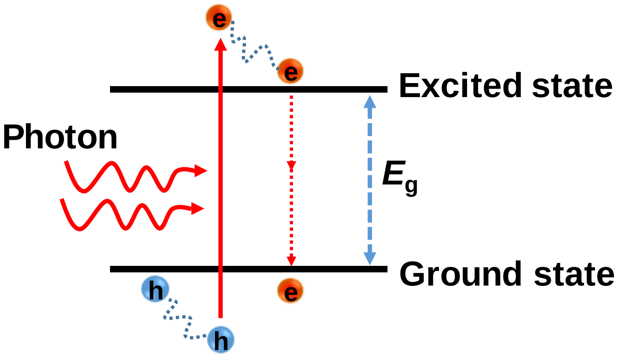

Figure 1. Schematic diagram of an electron excitation from ground state to excited state by the solar light energy.

The generated electrons and holes in light harvester of photovoltaics should be separated, extracted and delivered to external circuit to complete the light-electric conversion process. In an ideal condition, we assume that the carriers are delivered to external circuit without any loss and generated into electric current. The short-circuit current density (J_{SC}) is usually described as following,

$$J_{SC}=q\int_0^\infty \eta_c(E)\big(1-R(E)\big)a(E)b_s(E)dE, \tag{1.1}$$

where the $\eta_c(E)$ is the collected efficiency to external circuit, $R(E)$ is the reflectivity, $a(E)$ is an absorbed photon energy, $b_s(E)$ is the incident photon flux density, and q is an elementary charge of electron.

The maximum current density should be considered at an ideal condition, where all incident photons energy E is higher than E_g. The absorbed energy promotes the electron to excited state and carrier separations without any loss. The short-circuit current density can be described as following,

$$J_{SC}=q\int_{E_g}^\infty b_s(E)dE. \tag{1.2}$$

The incident and extracted power from the photons fluxes has been used in the calculation of power conversion efficiency. The incident power density (P_i) is calculated by integrating the incident irradiance over photon energy of photovoltaics and described as following,

$$P_s=\int_0^\infty Eb_s(E_s)dE. \tag{1.3}$$

Then, in the ideal condition, the conversion process is assumed without any loss during carrier deliver to external circuit for output power. The extracted power density can be described as $P_{\mathrm{output}}=VJ(V)$, where V and J are voltage and current density, respectively. To calculate the power conversion efficiency η. The formula is described as following,

$$\eta=\frac{VJ(V)}{P_s} \tag{1.4}$$

The maximum power conversion efficiency is achieved at the following condition,

$$\frac{d}{dV}(J(V)V)=0 \tag{1.5}$$

Therefore, the maximum of power conversion efficiency of single junction solar cell is ca. 33.0% at the bandgap of 1.35 eV according to the Shockley-Queisser limit[35].

Characterization of solar cells performance

The power output of solar cells is evaluated by using a simulated irradiation sunlight (one Sun, AM 1.5) with an incident light power (P_{in}) of about 100 mW/cm^2. The sun spectrum and simulated equivalent circuit of ideal solar cells are shown in **Figures 2a** and b. The current-voltage (J–V) curves measured by using various driving voltage are exhibited in Figure 2c. The open-circuit voltage (V_{OC}) means the voltage at the current density of zero, and the J_{SC} means the current density at the voltage of zero. The power density of solar cells is given by $P=JV$. When the P increases to a maximum value at the cell's operating point or maximum power point, the V and J also reaches to the maximum

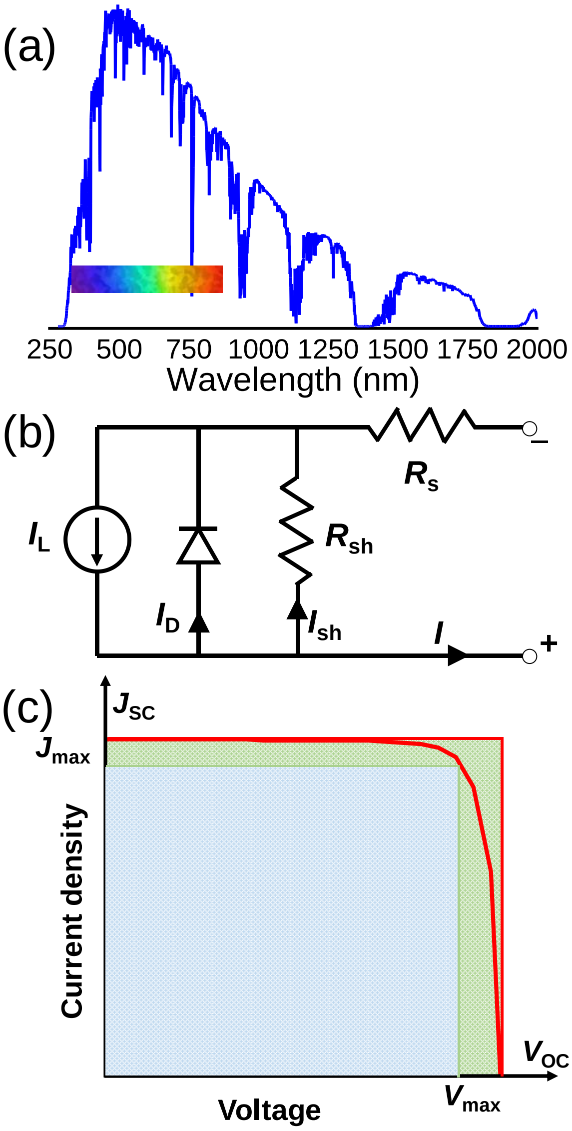

Figure 2. (a) Standard one sun spectrum (Air Mass 1.5), (b) Simulated equivalent circuit of a solar cell, (c) J–V curves of a solar cell.

values of V_{m} and J_{m}. The sheet resistance and fill factor (FF) can be calculated as $V_{\mathrm{m}}/J_{\mathrm{m}}$ and $J_{\mathrm{m}}V_{\mathrm{m}}/J_{\mathrm{SC}}V_{\mathrm{OC}}$. The efficiency of solar cells is also calculated because the power density delivered at maximum power point as some fraction of incident light power, P_{in}, as $\eta= J_{\mathrm{m}}V_{\mathrm{m}}/P_{\mathrm{in}}$. Efficiency is also related to J_{SC} and V_{OC} using FF, as $\eta= \mathrm{FF}J_{\mathrm{SC}}V_{\mathrm{OC}}/P_{\mathrm{in}}$. The J_{SC}, V_{OC}, FF and η are the key parameters to characterize the performance of a solar cell.

Categories of solar cells

The photovoltaic devices are divided into three types: crystalline, thin film and emerging solar cells. Silicon solar cell is a kind and high efficiency photovoltaics, achieving 26.6% without concentrator[15] and 27.6% with concentrator[36] in a single junction cell. The solar cell of un-doped gallium arsenide (GaAs) with a small bandgap of 1.42 eV achieved 27.8%[37]. In the typical thin film solar cells of copper indium diselenide ($CuInSe_2$, or CIS), the efficiency of arsenide doped CIS solar cells has increased to 22.9% on the rigid and 18.7% on flexible substrate[38,39]. The cadmium telluride (CdTe) thin film solar cells also obtained the efficiency of 22.1%[16]. The emerged dye-sensitized solar cells (DSSCs) showed slowly development and its efficiency increased to 11.9%[40]. The most promising system among emerging solar cells is organic/inorganic hybrid perovskite solar cells (PSCs) developed in 2009. The first demonstrated PSCs achieved the efficiency of 3.8%[10]. After that, the PSCs achieved an unprecedented development and their efficiency have rapidly increased up to 24.2% on single junction cell only within a decade[16]. Moreover, the perovskite/silicon tandem structure solar cells showed the efficiency of 28.0% in 2018[16]. Thus, the PSCs have regarded as the most promising next-generation photovoltaics. Even though the PSCs achieved rapid progress, the stability of photovoltaic performance still limits the industrial application.

1.3 Brief history of perovskite solar cells

The hybrid halide compound with perovskite structure[41,42] was first reported in 1978 based on the previous studies of inorganic lead halides[43] since 19th century and organic-inorganic halides[44] since 20th century. The unique chemical and physical properties of organic/inorganic hybrid perovskites have been studied. The firstly application of hybrid halide in solar cells was in 2009[10].

The name of “perovskite” comes from the typical mineral structure of $CaTiO_3$. The crystal consists with corner-sharing TiO_6 octahedra in three dimensions, and the Ca atom

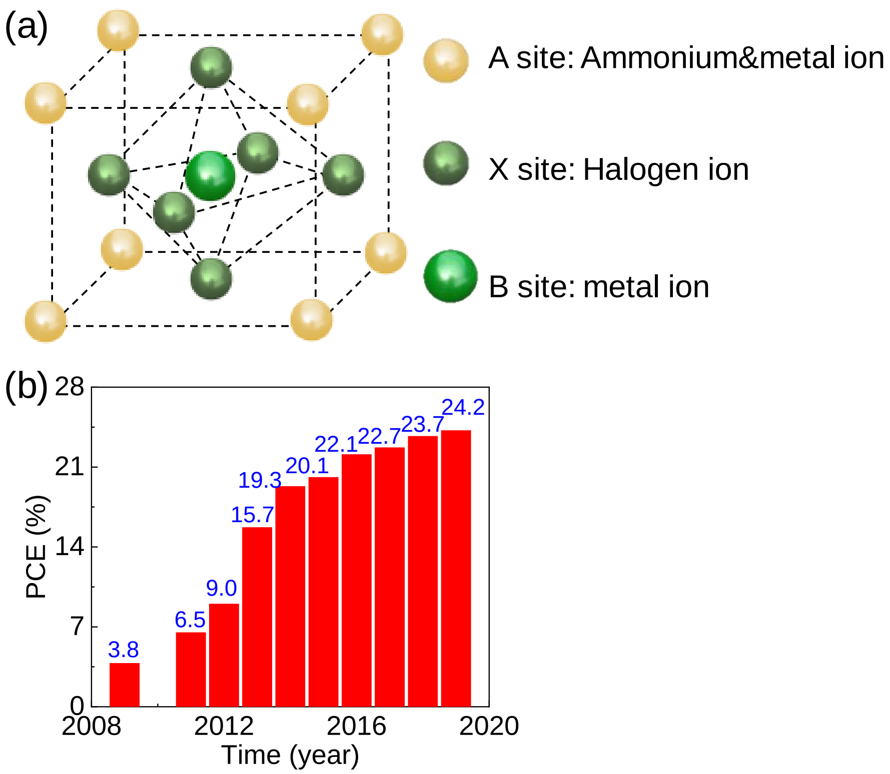

Figure 3. (a) Crystal structure of ABX_3 perovskite, (b) Progress of perovskite solar cells.

locates the cuboctahedral cavity in each unit cell. Therefore, the ABX_3 stoichiometry has been used to definite the same crystal of a wide range of materials. The organic/inorganic hybrid perovskites have a same structure of $CaTiO_3$ and is defined as ABX_3, where A site is component of organic and inorganic cations (methyl ammonium (MA^+), formamidinium (FA^+) and caesium (Cs^+)), B site is component of metal atoms of Pb^{2+} and Sn^{2+}, X site is component of halide atoms of I^-, Cl^- and Br^-, respectively, as shown in **Figure 3a.** The organic/inorganic hybrid perovskites have multifunctions as light harvester and carriers transport, resulting in the photo-electric conversion without electron and hole transport materials. The bandgap of organic/inorganic hybrid perovskites can be tuned from 1.58 eV (pure I) to 2.20 eV (pure Br) only by changing the halide atoms[45]. The organic/inorganic hybrid perovskites were first applied in solar cells and achieved a PCE of 3.8% in 2009 by Prof. Miyasaka, where he used $MAPbBr_3$ perovskite in dye-sensitized solar cells (DSSCs) as a dye[10]. The PCE increased up to 10.9% in PSCs reported by Prof. Henry, in which the solution spin coating technique was used to fabricate the perovskite films[11]. To prevent the nonuniform properties of perovskites film, the sequential deposition process has been utilized in PSCs with a high efficiency of 15.0% in 2013 by Prof. Gratzel[12]. In the same year, Prof. Henry also reported a vapour deposition approach to achieve very uniform perovskite film on the planar structure substrate and obtained the efficiency of 15.4%[46]. In 2015, Prof. Seok reported the method of intramolecular exchange between dimethylsulphoxide (DMSO) and formamidinium iodide (FAI) intercalated in PbI_2 to fabricate perovskite on mesoporous architecture. The PSCs achieved a high PCE of 20.1% with a negligible hysteresis, which is the first time of PCE over 20%[47]. Then, the PSCs achieved much higher PCE of 22.1, 23.3 and reached to 24.2% in 2019[14,16,18], as shown in Figure 3b.

Even though the PSCs has already achieved an explosive and faster development within a decade, which is much different from the situation of others photovoltaics, the photovoltaic stability still limits to realize the industrial application and replace the marketplace leader of silicon solar cells. The quality of perovskite has become a key to overcome the stability problems. Prof. Nazeeruddin developed two-dimensional (2D)/three-dimensional (3D) interface engineering technique to realize one-year stability, but the PCE of PSCs is still too low[33]. In the same year, Prof. Gratzel reported the inorganic hole transport materials of CuSCN and replacement of organic A site of FA and MA partially by Cs cation. The PSCs have realized a high PCE of 20.8% and kept over 95% of initial efficiency even after 1000 hours continuous light soaking at 60 °C by inserting buffer layer of reduced graphene oxide between hole transport layer (HTL) and Au electrode[34]. Recently, a high PCE of 20.8% at 1 cm^2 has been demonstrated using compositional engineering approach and 92% of initial efficiency was kept at condition of 85 °C and 85% humidity[48]. Although the stability of PSCs has been improved, the stability cannot be met on the industrial application. Thus, the stability of PSCs is a tough challenge in near future.

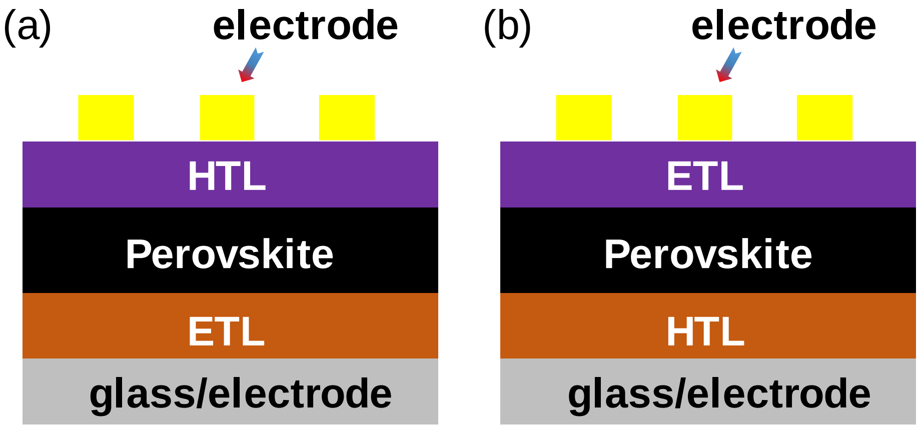

Figure 4. Typical architecture of perovskite solar cells. (a) n-i-p structure, (b) p-i-n structure. ETL: electron transport layer, HTL: hole transport layer.

1.4 Architectures and working mechanism of perovskite solar cells

Architectures category of PSCs

The architecture of PSCs consists of transparent electrode/carrier extraction material/perovskite/carrier extraction material/contact electrode. According to the stacking sequence of layers, the PSCs can be divided into two groups as shown in **Figure 4**. As for the first category, the structure is defined as n-i-p architecture (normal architecture), in which the electron transport layer (ETL) is underneath the perovskite, hole transport layer (HTL) is on the top of perovskite and the perovskite film is sandwiched between ETL and HTL. The p-i-n architecture (inverted architecture) is inverse of n-i-p in the layers' configuration.

According to the morphology of substrate, the PSCs can be classified into mesoporous and planar structure. The mesoporous structure consists of mesoporous TiO_2 or Al_2O_3 as a scaffold of ETL[11,49,50], as shown in **Figure 5.** The mesoporous TiO_2 is most frequently adapted by researchers and PSCs using TiO_2 achieved a high efficiency of 22.7%[18]. However, the stability of TiO_2 based PSCs is still misgivings, because the TiO_2 shows quite sensitive photocatalytic reaction under the light continuous soaking (with UV light component)[51,52]. Therefore, the other electron extraction materials are explored as ETL for improving the stability of PSCs, such as ZnO[53], SnO_2[54–59] and phenyl-C61-butyric acid methyl ester ($PC_{61}BM$)[60] in normal planner architecture, and PEDOT:PSS[61–63] in inverted planar architecture. The stability of planar architecture PSCs become much better because of improved light soaking stability of carrier extraction materials. The PCE of PSCs has increased up to 23.3% using surface passivation approach by an organic halide salt phenethylammo-nium iodide (PEAI)[14].

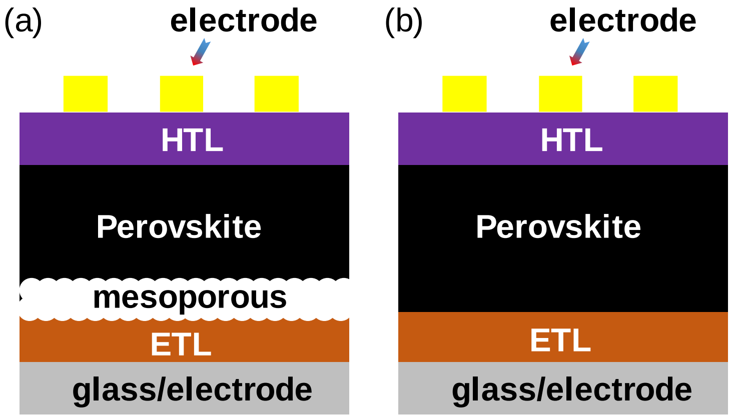

Figure 5. General architecture of perovskite solar cells of mesoporous (a) and planar (b) structure, respectively.

Working mechanism of PSCs

Figure 6a shows an example structure of normal architecture PSCs. The PSCs architecture contains a glass substrate, transparent conductive oxide (TCO) electrode (fluorine-doped tin oxide: FTO, indium tin oxide: ITO), ETL, perovskite, HTL and metallic electrode of Au or Ag. The carriers (electrons and holes) are generated in perovskite layer with irradiated of solar light, then the electrons and holes as carriers are separated on perovskite and extracted by ETL and HTL, respectively. The electrons and holes as carriers are delivered to external circuit and photocurrent is detected by a source meter. The carrier generation and transport can be understood more deeply on the energy diagrams, as shown in Figure 6b. The carriers are generated in the perovskite photoactive layer by solar light, then, the generated electrons transferred to bottom of conduction band (CB) of perovskite, are extracted by ETL, and finally reached to TCO layer; at the same time, the generated holes transferred to top of valance band (VB) of perovskite, are extracted by HTL and reached to metallic electrode of Au or Ag. In order to achieve high performance of PSCs, the CB bottom of perovskite must be higher than the lowest occupied molecular orbital (LOMO) of ETL, and VB top of perovskite must be lower than the highest occupied molecular orbital (HOMO) of HTL. Therefore, the energy alignment of each component of PSCs is quite important, which seriously determine the carriers' extraction, transport and recombination processes.

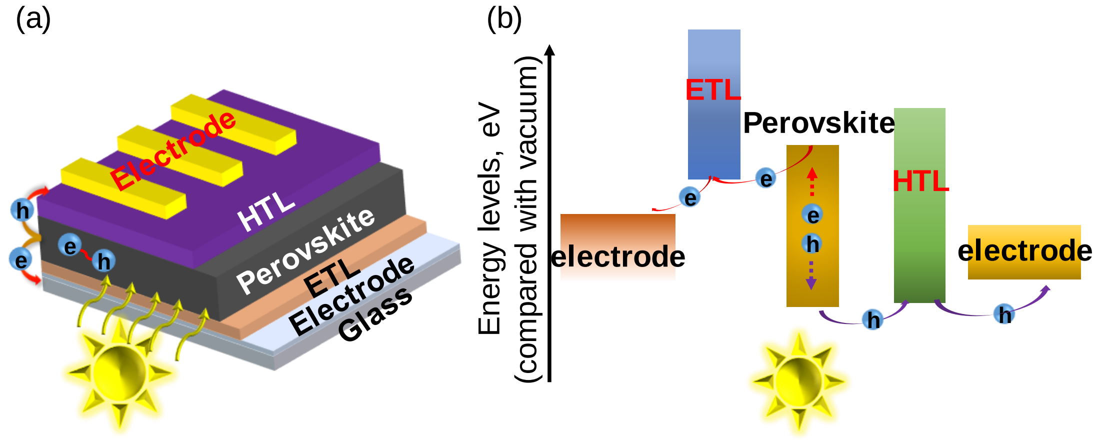

Figure 6. Working mechanism of perovskite solar cells. (a) Working principle of n-i-p structure of perovskite solar cells in real space. (b) Dynamics of carriers in perovskite solar cells on energy diagram.

1.5 Perovskite materials as light harvester

Metal-halide perovskites have been widely applied for solar cells due to their ideal properties as semiconductors. The perovskite usually consists of organic or inorganic cations based on amine and metallic salt (*e.g.* $CH_3NH_3^+$, $CH_5N_2^+$, Cs^+) at A sites, metal cations (*e.g.* Pb^{2+}, Sn^{2+}) at B sites, and halide anions (*e.g.* Cl^-, Br^-, I^-) at X site to form ABX_3 crystal structure. The structure of organic/inorganic perovskites can be easy modulated by incorporated atoms into crystal. The stability of perovskite structure can be calculated from tolerance factor[64] as,

$$t = \frac{R_A + R_B}{\sqrt{2}\,(R_B + R_X)}, \tag{1.6}$$

and octahedral factor

$$\mu = R_B / R_X, \tag{1.7}$$

where R_A, R_B and R_X are the effective ionic radii of A, B, X, respectively. The perovskite structure can stable at $0.813 \leq t \leq 1.107$, and $0.442 \leq \mu \leq 0.895$[65].

The organic/inorganic perovskites have incomparable characteristics to other semiconductors, including large light absorption coefficient throughout visible light region[12,45], high carrier mobility in both of electron and hole[23], long distance of carrier diffusion[22], low exciton binding energy[22] and low-temperature fabrication process[24]. Moreover, the band gap (E_g) of perovskite can be tuned by changing the component of ABX_3. The E_g can be tuned from 1.48 eV in $FAPbI_3$[66,67], 1.58 eV in $MAPbI_3$[68–70] and 2.28 eV in $MAPbBr_3$[71] on organic/inorganic hybrid perovskites, 1.73 eV in $CsPbI_3$[72,73], 2.3 eV[74] in $CsPbBr_3$ on inorganic perovskite, and 1.17 eV (50% of Pb and 50% of Sn) to 1.58 eV (pure Pb) on Pb-Sn mixed perovskite[45,75–77]. Moreover, the organic/inorganic perovskites can be easy applied in the hybrid structure, such as perovskite-silicon, perovskite-CIGS and perovskite-perovskite, altering the component of perovskite to realize ideal tandem solar cells. The hybrid structure is a main path-way to overcome the Shockly-Queisser limit in single junction cell.

1.6 Electron transport materials

Various electron transport materials (ETMs) can be utilized in PSCs due to the tunable band gap of perovskites. The metal oxides based ETMs are usually used because of stability, easy fabrication and deposition on the transparent conductive oxide (TCO) substrate. The typical ETMs are shown with their schematic energy-level diagram[78] in **Figure 7**. The ETMs are usually deposited on TCO substrate by approaches of spin coating[79], spray[80], chemical bath deposition[81], atomic layer deposition[21,25], and so on. The TiO_2 is a most typical ETM, firstly used in dye-sensitized solar cells[6] of perovskites in 2009[10]. The PCE of PSCs using TiO_2 ETM has rapidly increased from 3.8 to 22.7%[18]

until now. However, the stability of TiO_2 ETM based PSCs is still criticism subject, because the TiO_2 causes photo-catalytic reaction under continuous light soaking[51].

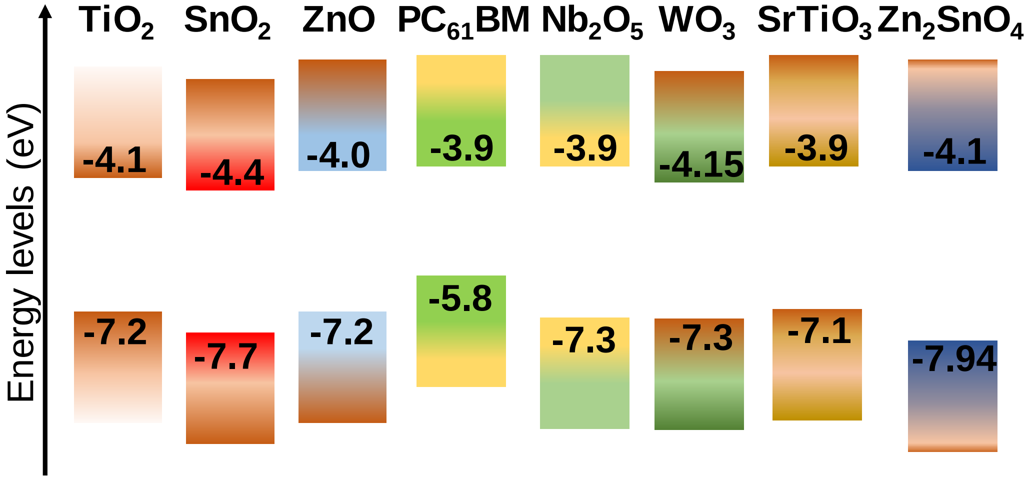

Figure 7. Schematic energy-level diagrams of typical electron transport materials (ETM), including TiO_2, SnO_2, $PC_{61}BM$, ZnO, Nb_2O_5, WO_3, $SrTiO_3$, and Zn_2SnO_4, respectively.

SnO_2 is an another typical ETM frequently used in planar architecture PSCs due the high carrier mobility up to 240 $cm^2/(V{\cdot}s)$ (100 times larger than that of TiO_2) and more deep bottom conduction band (CB) compared with TiO_2[82]. The PCE of SnO_2 base PSCs has increased from 16 to 23.3% by optimizing the quality of SnO_2 film and perovskites[14,21,54,56,58,59,83]. Interesting, the SnO_2 based PSCs could achieve a very high open-circuit voltage of 1.19 V[21,83]. The relative lower deposition temperature of SnO_2 could be also used in flexible PSCs (fPSCs). The PCE of fPSCs has enhanced to 18.4%[58] with very excellent bending durability of ca. 76.5% after 2000 bending cycles testing at bending radius of 4 mm much better than those of TiO_2 and Zn_2SnO_4 based flexible devices[32].

ZnO is frequently applied as ETM with high carrier mobility of 0.1 $cm^2/(V{\cdot}s)$ and a similar energy structure to TiO_2[84,85]. The PCE of ZnO based PSCs has also been obtained great development from 15.7[53] to 21.1% by inserting thin film of MgO and protonated ethanolamine[86–88]. However, the poor chemical compatibility between perovskite and ZnO easily causes the degradation of perovskite even at low annealing temperature[89–91] and decrease of stability of PSCs.

Some other organic materials are also used as ETM in PSCs, especially in fPSCs, such as phenyl-C_{61}-butyric acid methyl ester ($PC_{61}BM$)[92] and C_{60} pyrrolidine tris-acid (CPTA)[93]. The PCE of PSCs has increased to 18.0% on glass substrate and 17.0% on flexible substrate with an excellent bending duruability[93], exhibiting a potential application.

1.7 Hole transport materials

Hole transport materials (HTMs) play a crucial role in the PSCs to realize the holes' extraction and transport from perovskite to metal electrode. HTMs are divided into organic molecule, polymeric and inorganic categories. The compatible valance band energy (VBE) of HTMs facilitates the holes transfer in PSCs. Some inorganic HTMs possess excellent thermal and photochemical stability with reasonable carrier mobility. **Figure 8** shows the energy diagram of some HTMs that have been used in PSCs[94,95].

The 2,2′,7,7′-Tetrakis(*N*,*N*-di-*p*-methoxyphenylamino)-9,9′-spirobifluorene (spiro-OMeTAD) and Poly[bis(4-phenyl)(2,4,6-trimethylphenyl)amine] (PTAA) are frequently used HTMs in PSCs with high PCE. The conductivity and hole mobility of pristine spiro-OMeTAD and PTAA are relative low, such as ca.10^{-5} Scm^{-2} and ca.10^{-4} $cm^2V^{-1}s^{-1}$, which are too low and unsatisfied as the carrier transport layer. The PCE of spiro-OMeTAD

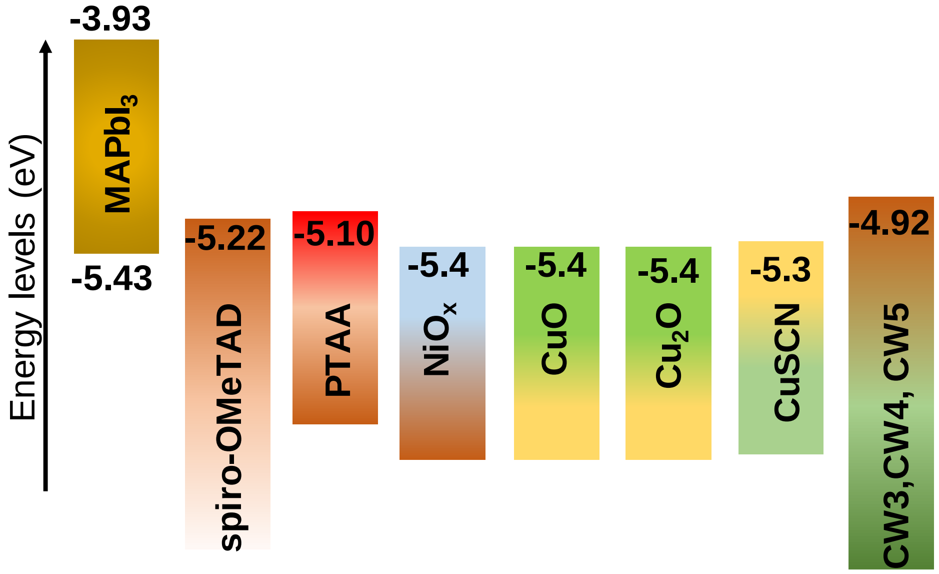

Figure 8. Schematic energy-level diagram of hole transport materials, including $MAPbI_3$, spiro-OMeTAD, PTAA, NiO_x, CuO, Cu_2O, CuSCN, CW_3, CW_4 and CW_5, respectively.

based solid-state DSSCs are relatively lower than that using other HTMs[96–98]. Therefore, the dopants of lithium bis(trifluoromethylsulfonyl)-imide (Li-TFSi), tert-butylpyridine (tBP) and cobalt bis(trifluoromethylsulfonyl)-imide (Co-TFSi) are used to enhance the conductivity and hole mobility of spiro-OMeTAD and PTAA. The PCE of spiro-OMeTAD based PSCs has achieved a great development and increased to 23.3% by optimizing the architecture and enhancing the quality of perovskites[11,14,16,18,46,47]. However, the stability of doped spiro-OMeTAD become much weaker and deteriorate lifetime of PSCs[34,51,56,99]. Therefore, the stability of doped spiro-OMeTAD limits the industrial application.

Compared with classical HTMs of spiro-OMeTAD, the PTAA has more shallow top VB according to the energy-level diagrams of Figure 8, which realizes optimized energy alignment between perovskite and HTMs, and the PSCs using PTAA holds the highest record PCE of PSCs. The PTAA was partially infiltrated into mesoporous PSCs and delivered to high PCE of 12.0% in 2013[100,101]. After optimization and enhancement of the quality of perovskite using mixed perovskite, the PCE of PSCs has increased to over 20.0% with a negligible hysteresis using PTAA HTMs[47].

Even though the doped organic molecule HTMs can deliver very high PCE of PSCs, the organic materials seriously affect the thermal and continuous light soaking stability, and hampers the industrial application of PSCs. Thus, the inorganic HTMs are a more preferable selection, such as NiO, CuO_x and CuSCN, and so on.

NiO is a kind of wide-band p-type material and has been successfully applied in DSSCs and organic photovoltaics (OPV) devices as a HTM. A layer of NiO is deposited using electrodeposition in the inverted architecture and PSCs using NiO could achieve a PCE of 7.3%[102]. The PCE has increased up to about 17% using Cu doping[103], nanoparticles type[104] and room temperature sputtering technique[105]. In order to enhance the PCE of PSCs, the CuO_x has been selected as a HTM and PSCs could achieve a high efficiency of 19.0% by optimizing the perovskite quality using Cl doping approach[106]. To pursue more high PCE of PSCs, the HTM of CuSCN has been employed in PSCs due to the effective carrier extraction from perovskite as well as the efficient transportation to the Au electrode. An impressive PCE of 16.6 and 18.8% has been achieved on inverted architecture PSCs using electrodeposition and spin coating techniques to deposit the CuSCN and mixed CuI/CuSCN as HTMs, respectively[107,108]. In normal architecture, PSCs have also achieved a high PCE of 17 and 20.8% using a facile spray deposition and spin coating techniques to deposit CuSCN[34,109]. The stability of PSCs has been significantly enhanced after inserting a reduced graphene oxide (RGO) between the CuSCN and Au electrode, realizing an excellent stability over 95% compared with that of initial efficiency after 1000 hours continuous light soaking at 60 °C in nitrogen condition[34]. Even though the improvement of stability in PSCs by using various HTMs, these results are still unsatisfied for the industrial application compared with typical silicon solar cells.

1.8 Contact electrode materials

The high efficient PSCs are usually consist with a typical architecture of glass substrate/TCO electrode/carrier transport layer/perovskite harvesters/carrier transport layer/contact electrode for the n-i-p and p-i-n structure. The contact electrode materials including the energy level of each material have been summarized in **Figure 9**. The metallic materials are typical applied as the contact electrode, for instance, Au[110–112], Cu[113,114], Ag[11,45,53,115,116] and Al[92,117–119], for high PCE of PSCs, in which the fabrication cost obviously increases and the higher cost hampers the PSCs industrial application. The metallic electrodes are usually deposited using a complicated process of high vacuum and long-term thermal evaporation.

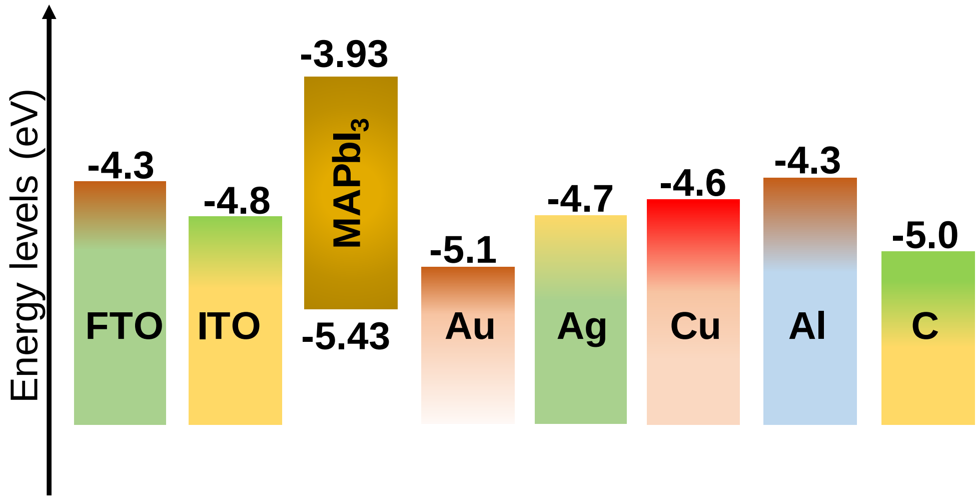

Figure 9. Schematic energy-level diagrams of typical contact electrode materials, including FTO, ITO, $MAPbI_3$, Au, Ag, Cu, Al and C, respectively.

More simplified deposition and cheaper material has been selected as contact electrodes, i.e. carbon based materials. The carbon based materials can hold the excellent electrochemical stability, such as the chemical corrosion of Au electrode from thiocyanate anions of CuSCN HTMs[34]. A variety types of carbon materials have been used as electrodes with a relative high efficiency via various simple approach, such as doctor blade[120,121], printing[68,122–124], directly transfer[125,126] and embedment approach[127]. The PCE of carbon based PSCs has increased up to 19.2% by using the adhesive macroporous carbon electrode and maintained a relative high stability on the rigid substrate[126]. Moreover, the carbon materials have also been used as TCO electrode to replace the ITO, especially for fPSCs[28,31,128]. The graphene electrode fPSCs achieved high efficiency of 16.8% and sustained ca. 85% bending durability at a bending radius of 2 mm by additionally depositing thin film of molybdenum trioxide (MoO_3) to improve conductivity of graphene[28]. Even though the performance of carbon based PSCs has achieved remarkable development, the PCEs are still far behind compared with that using noble metal electrodes, and also still can single-time utilization in PSCs.

1.9 Current stage of development and issues of perovskite solar cells

Since the first application of perovskites in photovoltaic device with a PCE of 3.8% in 2009[10], the PSCs have achieved an unprecedented development and PCE has increased up to 24.2%[16]. Even though the PSCs have achieved an impressive development, the stability has become a controversial issue to replace the long-term energy payback photovoltaics of silicon for industrial application. The critical problems of PSCs can be divided into three main subjects: quality of perovskite quality, properties of carrier transport materials, and electrode materials for low and economic-friendly fabrication.

Organic/inorganic hybrid perovskite is a kind specially and ideal semiconductor compared with those of mainstream inorganic semiconductors of silicon, CIGS, CdTe and organic molecules. The high carrier mobility of electrons and holes, long length of carrier diffusion, high absorption coefficient in visible range of light, tunable band gap, low exciton binding energy and low fabrication temperature of organic/inorganic hybrid perovskites, make them become the most promising photovoltaics material for next-generation. The organic/inorganic hybrid perovskite sandwiched between electron and hole transport layer in the PSCs devices. Thus, the quality of organic/inorganic hybrid perovskite seriously determines the photovoltaic performance of PSCs, including PCE and stability. The uniform and fully coverage of organic/inorganic hybrid perovskite film with large crystal size is the first critical requirement of perovskite quality. Moreover, the low density trap states are other aspects for perovskite quality. The high quality perovskite can reduce the trap states, and contribute to improve the stability in the PSCs.

Certainly, the PCE and stability of PCS are not determined only by the quality of organic/inorganic hybrid perovskite. The properties of electron and hole transport materials also determine them. The *n*-type TiO_2 is typically used as electron transport materials and PSCs using TiO_2 could achieve very a high PCE of 22.7%. However, the stability of TiO_2 based PSCs is still a criticized topic, because the TiO_2 causes easily photocatalytic reaction under continuous light soaking even at low humidity condition. Moreover, the relatively high bottom CB and low carrier mobility of TiO_2 also limit the efficiency of carriers' extraction and transportation. Thus, the exploring and applying more excellent electron materials have become a key pathway to enhance the performance and stability of PSCs.

The stability of PSCs is also affected by quality of interface between the hole transport materials and metal electrode. The degradation of perovskite at the initial stage usually happens by attacking of moisture at heated condition from the interfacial deterioration related to the metal electrodes. Moreover, the metallic electrode is fabricated by a complicated process of high vacuum and long-term thermal deposition, which will increase the fabrication cost of PSCs and seriously hinder industrial application. Moreover, the noble metal electrodes are usually used as only a single-time after degradation of perovskite, which will increase the limited resource waste and environmental pollution. Thus, the bearing capacity for environment should be seriously considered when we pursue the ultimate performance of PSCs.

1.10 Overview of this thesis

In this thesis, I mainly focus on the architecture design approach to significantly promote the photovoltaic performance and the stability of the PSCs, including the polymer materials interface passivation and second solution growth process (SSGP) of perovskite, excellent electron transport materials, and new structure of Au electrode.

To enhance perovskite film quality, especially the coverage surface trap states, I used the polymethyl methacrylate (PMMA) and polycarbonate (PC) as the interface modifiers to passivate the $MAPbI_3$-perovskite surface. The coverage and the surface roughness of perovskite films have become much better and flatter after PMMA and PC modification, and remarkably reduced surface trap states of perovskites, in which the photovoltaic performance of perovskite solar cells (PSCs) has been significantly enhanced. Moreover, the PMMA and PC based PSCs achieved a high power conversion efficiency (PCE) of 20.5 and 19.1%, respectively, and much better stability compared with those of standard devices without polymer passivation layer.

However, the periodical enhancement of PSCs stability is still not enough even using passivation of PMMA and PC, especially the continuous light soaking, because the UV light sensitive ETL of TiO_2 severely deteriorates the stability of PSCs. Therefore, I replaced the TiO_2 by SnO_2 as ETL. The much better stability of PSCs employed by SnO_2 ETL and $Cs_{0.05}(MA_{0.17}FA_{0.83})_{0.95}Pb(I_{0.83}Br_{0.17})_3$-perovskite light harvester has been realized. The SnO_2 ETL has also been employed into flexible PSCs (fPSCs) taking the advantage of low fabrication temperature of SnO_2. As a result, the fPSCs achieved a high PCE of 17.1% with a negligible hysteresis and excellent bending durability of ca. 76.5% compared with the initial efficiency even after 2000 bending cycles testing at the bending radius of 4 mm. The severe cracks on flexible substrate and noble Au electrode limits the bending durability of fPSCs, therefore, it is necessary to explore new materials or new structure to further promoting the bending durability of fPSCs.

The excessive PbI_2 on perovskite film surface still limit the further enhancement of the photovoltaic performance of PSCs on SnO_2 ETL, therefore, the SSGP has been introduced to enhance the quality of perovskite film. The crystal size of perovskite has dramatically increased on excessive PbI_2 condition after quickly annealing at 150 °C. The SSGP has been employed into reacting the excessive PbI_2 with sustaining large crystal size, and significantly reducing the trap states of perovskite. The SSGP PSCs obtained a very high PCE of 21.6% with a negligible hysteresis, and obtained the highest FF of 83.4% on planar PSCs as our knowledge. The SSGP PSCs also showed much better stability under long-term continuous light soaking and thermal treatment compared with those of standard PSCs.

To realize simplify the fabrication process and reduce the cost of PSCs for industrial application, the nanoporous Au film has been introduced into PSCs as the electrode to replace the typical Au electrode fabricated by high vacuum and temperature thermal deposition process. The nanoporous Au based PSCs achieved a high PCE of 19.0% with a very small hysteresis using direct transfer process. The application of nanoporous Au film enables several times recycled utilization in PSCs. The PCEs in the metal electrode reused PSCs only decreased from 16.5 to 14.7% after 12 times recycling. Moreover, the nanoporous Au fPSCs also obtained a high PCE of 17.3% and sustained a very high bending durability of ca. 98.5% even after 1000 bending cycles at bending radius of 5 mm.

This thesis consists of 6 chapters, including introduction of chapter 1, polymer passivated perovskite solar cells of chapter 2, SnO_2 based flexible perovskite solar cells of chapter 3, SnO_2 based perovskite solar cells by second solution growth process of chapter 4, recycled utilization of nanoporous Au film in perovskite solar cells of chapter 5, conclusion of chapter 6, lists of publications and conferences, and acknowledgements.

Reference

1. Jenny Nelson. The physics of solar cells. *Imperial College Press* **50**, 5356 (1979).
2. Baxter, J. Physics of solar cells: from basic principles to advanced concepts. *Wiley*, (2005).
3. Carlson, D. E. & Wronski, C. R. Amorphous silicon solar cells. *Appl. Phys. Lett.* **11**, 671–673 (1976).
4. M. A. Green. Solar cells: operating principles, technology and system applications. *Semiconductor Devices: Physics and Technology* (1992).
5. Tian, B. *et al.* Coaxial silicon nanowires as solar cells and nanoelectronic power sources. *Nature* **449**, 885–889 (2007).
6. Hagfeldt, A. *et al.* Dye-sensitized solar cells. *Chem. Rev.* **110**, 6595–6663 (2010).
7. Grätzel, M. Dye-sensitized solar cells. *J. Photochem. Photobiol. C Photochem. Rev.* **4**, 145–153 (2003).
8. Yu, G. *et al.* Polymer photovoltaic cells: enhanced efficiencies via a network of internal donor-acceptor heterojunctions. *Science* **270**, 1789–1791 (1995).
9. Park, S. H. *et al.* Bulk heterojunction solar cells with internal quantum efficiency approaching 100%. *Nat. Photon.* **3**, 297–303 (2009).
10. Kojima, A. *et al.* Organometal halide perovskites as visible-light sensitizers for photovoltaic cells. *J. Am. Chem. Soc.* **131**, 6050–6051 (2009).
11. Lee, M. M. *et al.* Efficient hybrid solar cells based on meso-superstructured organometal halide perovskites. *Science* **338**, 643–647 (2012).
12. Burschka, J. *et al.* Sequential deposition as a route to high-performance perovskite-sensitized solar cells. *Nature* **499**, 316–319 (2013).
13. Jeon, N. J. *et al.* Compositional engineering of perovskite materials for high-performance solar cells. *Nature* **517**, 476–480 (2015).
14. Jiang, Q. *et al.* Surface passivation of perovskite film for efficient solar cells. *Nat. Photon.* **10**, 1038 (2019).
15. Yoshikawa, K. *et al.* Silicon heterojunction solar cell with interdigitated back

contacts for a photoconversion efficiency over 26%. *Nat. Energy* **2**, 17032 (2017).

16. Best Research-Cell Efficiencies Chart. National Renewable Energy Laboratory (NREL), https://www.nrel.gov/pv/assets/pdfs/best-research-cell-efficiencies-190416 (2019).
17. Wang, S. *et al.* Accelerated degradation of methylammonium lead iodide perovskites induced by exposure to iodine vapour. *Nat. Energy* **2**, 16195 (2017).
18. Yang, W. S. *et al.* Iodide management in formamidinium-lead-halide-based perovskite layers for efficient solar cells. *Science* **356**, 1376–1379 (2017).
19. Peng, J. *et al.* A universal double-side passivation for high open-circuit voltage in perovskite solar cells : role of carbonyl groups in poly (methyl methacrylate). *Adv. Energy Mater.* **8**, 1801208 (2018).
20. Eperon, G. E. *et al.* Perovskite-perovskite tandem photovoltaics with optimized band gaps. *Science* **354**, 861–865 (2016).
21. Saliba, M. *et al.* Cesium-containing triple cation perovskite solar cells: improved stability, reproducibility and high efficiency. *Energy Environ. Sci.* **9**, 1989–1997 (2016).
22. Stranks, S. D. *et al.* Electron-hole diffusion lengths exceeding 1 micrometer in an organometal trihalide perovskite absorber. *Science* **342**, 341–344 (2013).
23. Herz, L. M. Charge-carrier mobilities in metal halide perovskites: fundamental mechanisms and limits. *ACS Energy Lett.* **2**, 1539–1548 (2017).
24. Ball, J. M. *et al.* Low-temperature processed meso-superstructured to thin-film perovskite solar cells. *Energy Environ. Sci.* **6**, 1739–1743 (2013).
25. Kim, B. J. *et al.* Highly efficient and bending durable perovskite solar cells: Toward a wearable power source. *Energy Environ. Sci.* **8**, 916–921 (2015).
26. Kaltenbrunner, M. *et al.* Flexible high power-per-weight perovskite solar cells with chromium oxide-metal contacts for improved stability in air. *Nat. Mater.* **14**, 1032–1039 (2015).
27. Yang, D. *et al.* High efficiency flexible perovskite solar cells using superior low temperature TiO_2. *Energy Environ. Sci.* **8**, 3208–3214 (2015).
28. Yoon, J. *et al.* Superflexible, high-efficiency perovskite solar cells utilizing graphene electrodes: Towards future foldable power sources. *Energy Environ. Sci.* **10**, 337–345 (2017).
29. Yang, D. *et al.* Hysteresis-suppressed high-efficiency flexible perovskite solar cells using solid-state ionic-liquids for effective electron transport. *Adv. Mater.* **28**, 5206–5213 (2016).
30. Bi, C. *et al.* Efficient flexible solar cell based on composition-tailored hybrid

perovskite. *Adv. Mater.* **29**, 1605900 (2017).

31. Heo, J. H. *et al.* Highly flexible, high-performance perovskite solar cells with adhesion promoted $AuCl_3$-doped graphene electrodes. *J. Mater. Chem. A* **5**, 21146–21152 (2017).
32. Yang, F. *et al.* High bending durability of efficient flexible perovskite solar cells using metal oxide electron transport layer. *J. Phys. Chem. C* **122**, 17088–17095 (2018).
33. Grancini, G. *et al.* One-year stable perovskite solar cells by 2D/3D interface engineering. *Nat. Commun.* **8**, 15864 (2017).
34. Arora, N. *et al.* Perovskite solar cells with CuSCN hole extraction layers yield stabilized efficiencies greater than 20%. *Science* **358**, 768–771 (2017).
35. Shockley, W. & Queisser, H. J. Detailed balance limit of efficiency of p-n junction solar cells. *J. Appl. Phys.* **32**, 510–519 (1961).
36. Kayes, B. M. *et al.* 27.6% Conversion efficiency, a new record for single-junction solar cells under 1 sun illumination. *Conf. Rec. IEEE Photovolt. Spec. Conf.* (2011).
37. Steiner, M. A. *et al.* Optical enhancement of the open-circuit voltage in high quality GaAs solar cells. *J. Appl. Phys.* **113**, 123109 (2013).
38. Green, M. A. *et al.* Solar cell efficiency tables (Version 52). *Prog. Photovoltaics Res. Appl.* **27**, 3–12 (2019).
39. Bloesch, A. *et al.* $Cu(In,Ga)Se_2$ solar cell grown on flexible polymer substrate with efficiency exceeding 17%. *Prog. Photovoltaics* **19**, 560–564 (2011).
40. Lee, W. J. *et al.* Improvement of the conversion efficiency of a monolithic type dye-sensitized solar cell module. *Tech. Dig. 21st Int. Photovolt. Sci. Eng. Conf.* **194**, 27–30 (2011).
41. Weber, D. $CH_3NH_3SnBr_xI_{3-x}$ (x = 0–3), a Sn(II)-system with the cubic perovskite structure. *Zeitschrift für Naturforsch* **33**, 862–865 (1978).
42. Weber, D. $CH_3NH_3PbX_3$, a Pb(II)-system with cubic perovskite structure. *Zeitschrift für Naturforsch* **33**, 1443–1445 (1978).
43. Wells, H. L. Uber die caesium- und kalium-bleihalogenide. *Zeitschrift fur Anorg. Chemie* **3**, 195–210 (1893).
44. Wyckoff, R. W. G. The crystal structures of monomethyl ammonium chlorostannate and chloroplatinate. *Am. J. Sci.* **5**, 349–359 (1928).
45. McMeekin, D. P. *et al.* A mixed-cation lead mixed-halide perovskite absorber for tandem solar cells. *Science* **351**, 151–155 (2016).
46. Liu, M. *et al.* Efficient planar heterojunction perovskite solar cells by vapour deposition. *Nature* **501**, 395–398 (2013).

47. Yang, W. S. *et al.* High-performance photovoltaic perovskite layers fabricated through intramolecular exchange. *Science* **348**, 1234–1237 (2015).
48. Matsui, T. *et al.* Compositional engineering for thermally stable, highly efficient perovskite solar cells exceeding 20% power conversion efficiency with 85C/85% 1000 h stability. *Adv. Mater.* 1806823 (2019).
49. Crossland, E. J. W. *et al.* Mesoporous TiO_2 single crystals delivering enhanced mobility and optoelectronic device performance. *Nature* **495**, 215–219 (2013).
50. Guarnera, S. *et al.* Improving the long-term stability of perovskite solar cells with a porous Al_2O_3 buffer layer. *J. Phys. Chem. Lett.* **6**, 432–437 (2015).
51. Leijtens, T. *et al.* Overcoming ultraviolet light instability of sensitized TiO_2 with meso-superstructured organometal tri-halide perovskite solar cells. *Nat. Commun.* **4**, 2885 (2013).
52. Li, X. *et al.* Improved performance and stability of perovskite solar cells by crystal crosslinking with alkylphosphonic acid ω-ammonium chlorides. *Nat. Chem.* **7**, 703–711 (2015).
53. Liu, D. & Kelly, T. L. Perovskite solar cells with a planar heterojunction structure prepared using room-temperature solution processing techniques. *Nat. Photon.* **8**, 133–138 (2014).
54. Ke, W. *et al.* Low-temperature solution-processed tin oxide as an alternative electron transporting layer for efficient perovskite solar cells. *J. Am. Chem. Soc.* **137**, 6730–6733 (2015).
55. Wang, C. *et al.* Understanding and eliminating hysteresis for highly efficient planar perovskite solar cells. *Adv. Energy Mater.* **7**, 1700414 (2017).
56. Jiang, Q. *et al.* Enhanced electron extraction using SnO_2 for high-efficiency planar-structure $HC(NH_2)_2PbI_3$-based perovskite solar cells. *Nat. Energy* **2**, 16177 (2016).
57. Yu, H. *et al.* Superfast room-temperature activation of SnO_2 thin films via atmospheric plasma oxidation and their spplication in planar perovskite photovoltaics. *Adv. Mater.* **30**, 1704825 (2018).
58. Wang, C. *et al.* Water vapor treatment of low-temperature deposited SnO_2 electron selective layers for efficient flexible perovskite solar cells. *ACS Energy Lett.* **2**, 2118–2124 (2017).
59. Jiang, Q. *et al.* Planar-structure perovskite solar cells with efficiency beyond 21%. *Adv. Mater.* **29**, 1703852 (2017).
60. Ryu, S. *et al.* Fabrication of metal-oxide-free $CH_3NH_3PbI_3$ perovskite solar cells processed at low temperature. *J. Mater. Chem. A* **3**, 3271–3275 (2015).
61. Liang, P. W. *et al.* Additive enhanced crystallization of solution-processed

perovskite for highly efficient planar-heterojunction solar cells. *Adv. Mater.* **26**, 3748–3754 (2014).

62. Xiao, Z. *et al.* Efficient, high yield perovskite photovoltaic devices grown by interdiffusion of solution-processed precursor stacking layers. *Energy Environ. Sci.* **7**, 2619–2623 (2014).
63. Zhang, H. *et al.* Pinhole-free and surface-nanostructured niox film by room-Temperature solution process for high-performance flexible perovskite solar cells with good stability and reproducibility. *ACS Nano* **10**, 1503–1511 (2016).
64. Goldschmidt, V. M. Die gesetze der krystallochemie. *Naturwissenschaften* **14**, 477–485 (1926).
65. Li, C. *et al.* Formability of ABX_3 (X = F, Cl, Br, I) halide perovskites. *Acta Crystallogr. Sect. B Struct. Sci.* **64**, 702–707 (2008).
66. Eperon, G. E. *et al.* Formamidinium lead trihalide: a broadly tunable perovskite for efficient planar heterojunction solar cells. *Energy Environ. Sci.* **7**, 982–988 (2014).
67. Niu, T. *et al.* High performance ambient-air-stable $FAPbI_3$ perovskite solar cells with molecule-passivated Ruddlesden–Popper 3D heterostructured film. *Energy Environ. Sci.* **11**, 3358–3366 (2018).
68. Mei, A. *et al.* A hole-conductor-free, fully printable mesoscopic perovskite solar cell with high stability. *Science* **345**, 295–298 (2014).
69. Jeon, N. J. Solvent engineering for high-performance inorganic–organic hybrid perovskite solar cells. *Nat. Mater.* **13**, 897–903 (2014).
70. Azpiroz, J. M. *et al.* Defect migration in methylammonium lead iodide and its role in perovskite solar cell operation. *Energy Environ. Sci.* **8**, 2118–2127 (2015).
71. Ryu, S. *et al.* Voltage output of efficient perovskite solar cells with high open-circuit voltage and fill factor. *Energy Environ. Sci.* **7**, 2614–2618 (2014).
72. Xiang, S. *et al.* Highly air-stable carbon-based α-$CsPbI_3$ perovskite solar cells with a broadened optical spectrum. *ACS Energy Lett.* **3**, 1824–1831 (2018).
73. Wang, Y. *et al.* Bifunctional stabilization of all-inorganic α-$CsPbI_3$ perovskite for 17% efficiency photovoltaics. *J. Am. Chem. Soc.* **140**, 12345–12348 (2018).
74. Yuan, H. *et al.* All-inorganic $CsPbBr_3$ perovskite solar cell with 10.26% efficiency by spectra engineering. *J. Mater. Chem. A* **6**, 24324–24329 (2018).
75. Hao, F. *et al.* Anomalous band gap behavior in mixed Sn and Pb perovskites enables broadening of absorption spectrum in solar cells. *J. Am. Chem. Soc.* **136**, 8094–8099 (2014).
76. Liao, W. *et al.* Fabrication of efficient low-bandgap perovskite solar cells by

combining formamidinium tin iodide with methylammonium lead iodide. *J. Am. Chem. Soc.* **138**, 12360–12363 (2016).

77. Zhao, D. *et al.* Low-bandgap mixed tin-lead iodide perovskite absorbers with long carrier lifetimes for all-perovskite tandem solar cells. *Nat. Energy* **2**, 17018 (2017).
78. Haque, M. A. *et al.* Metal oxides as efficient charge transporters in perovskite solar cells. *Adv. Energy Mater.* **7**, 1602803 (2017).
79. Sheikh, A. D. *et al.* Atmospheric effects on the photovoltaic performance of hybrid perovskite solar cells. *Sol. Energy Mater. Sol. Cells* **137**, 6–14 (2015).
80. Kim, M. C. *et al.* Electro-spray deposition of a mesoporous TiO_2 charge collection layer: Toward large scale and continuous production of high efficiency perovskite solar cells. *Nanoscale* **7**, 20725–20733 (2015).
81. Kumar, M. H. *et al.* Flexible, low-temperature, solution processed ZnO-based perovskite solid state solar cells. *Chem. Commun.* **49**, 11089–11091 (2013).
82. Dong, Q. *et al.* Insight into perovskite solar cells based on SnO_2 compact electron-selective layer. *J. Phys. Chem. C* **119**, 10212–10217 (2015).
83. Yang, F. *et al.* Planar perovskite solar cells with high efficiency and fill factor obtained using two-step growth process. *ACS Appl. Mater. Interfaces* **11**, 15680–15687 (2019).
84. Li, F. M. *et al.* Zinc oxide nanostructures and high electron mobility nanocomposite thin film transistor. *IEEE Trans. Electron Devices* **56**, 3001–3011 (2008).
85. Han, B. S. *et al.* Room temperature deposition of crystalline nanoporous ZnO nanostructures for direct use as flexible DSSC photoanode. *Nanoscale Res. Lett.* **11**, 221 (2016).
86. Zheng, Y. Z. *et al.* Iodine-doped ZnO nanopillar arrays for perovskite solar cells with high efficiency up to 18.24%. *J. Mater. Chem. A* **5**, 12416–12425 (2017).
87. Azmi, R. *et al.* High-efficiency low-temperature ZnO based perovskite solar cells based on highly polar, nonwetting self-assembled molecular layers. *Adv. Energy Mater.* **8**, 1701683 (2017).
88. Cao, J. *et al.* Efficient, hysteresis-free, and stable perovskite solar cells with ZnO as electron-transport layer: effect of surface passivation. *Adv. Mater.* **30**, 1705596 (2018).
89. Yang, J. *et al.* Origin of the thermal instability in $CH_3NH_3PbI_3$ thin films deposited on ZnO. *Chem. Mater.* **27**, 4229–4236 (2015).
90. Cheng, Y. *et al.* Decomposition of organometal halide perovskite films on zinc oxide nanoparticles. *ACS Appl. Mater. Interfaces* **7**, 19986–19993 (2015).

91. Kumar, S. & Dhar, A. Accelerated thermal-aging-induced degradation of organometal triiodide perovskite on ZnO nanostructures and its effect on hybrid photovoltaic devices. *ACS Appl. Mater. Interfaces* **8**, 18309–18320 (2016).
92. Kuang, C. *et al.* Highly efficient electron transport obtained by doping PCBM with graphdiyne in planar-heterojunction perovskite solar cells. *Nano Lett.* **15**, 2756–2762 (2015).
93. Wang, Y.-C. *et al.* Efficient and hysteresis-free perovskite solar cells based on a solution processable polar fullerene electron transport layer. *Adv. Energy Mater.* **7**, 1701144 (2017).
94. Liu, T. *et al.* Inverted perovskite solar cells: progresses and perspectives. *Adv. Energy Mater.* **6**, 1600457 (2016).
95. Calió, L. *et al.* Hole-transport materials for perovskite solar cells. *Angew. Chemie - Int. Ed.* **55**, 14522–14545 (2016).
96. Burschka, J. *et al.* Tris(2-(1 H -pyrazol-1-yl)pyridine)cobalt(III) as p-type dopant for organic semiconductors and its application in highly efficient solid-state dye-sensitized solar cells. *J. Am. Chem. Soc.* **133**, 18042–18045 (2011).
97. Leijtens, T. *et al.* Hole transport materials with low glass transition temperatures and high solubility for application in solid-state dye-sensitized solar cells. *ACS Nano* **6**, 1455–1462 (2012).
98. Leijtens, T. *et al.* Charge density dependent mobility of organic hole-transporters and mesoporous TiO_2 determined by transient mobility spectroscopy: Implications to dye-sensitized and organic solar cells. *Adv. Mater.* **25**, 3227–3233 (2013).
99. Bryant, D. *et al.* Light and oxygen induced degradation limits the operational stability of methylammonium lead triiodide perovskite solar cells. *Energy Environ. Sci.* **9**, 1655–1660 (2016).
100. Heo, J. H. *et al.* Efficient inorganic-organic hybrid heterojunction solar cells containing perovskite compound and polymeric hole conductors. *Nat. Photon.* **7**, 486–491 (2013).
101. Im, S. H. *et al.* Chemical management for colorful, efficient, and stable inorganic–organic hybrid nanostructured solar cells. *Nano Lett.* **13**, 1764–1769 (2013).
102. Subbiah, A. S. *et al.* Inorganic hole conducting layers for perovskite-based solar cells. *J. Phys. Chem. Lett.* **5**, 1748–1753 (2014).
103. Kim, J. H. *et al.* High-performance and environmentally stable planar heterojunction perovskite solar cells based on a solution-processed copper-doped nickel oxide hole-transporting layer. *Adv. Mater.* **27**, 695–701 (2015).
104. Liu, Z. *et al.* Nickel oxide nanoparticles for efficient hole transport in p-i-n and n-

i-p perovskite solar cells. *J. Mater. Chem. A* **5**, 6597–6605 (2017).

105. Aydin, E. *et al.* Room-temperature-sputtered nanocrystalline nickel oxide as hole transport layer for p-i-n perovskite solar cells. *ACS Appl. Energy Mater.* **1**, 6227–6233 (2018).
106. Rao, H. *et al.* A 19.0% efficiency achieved in CuO_x-based inverted $CH_3NH_3PbI_{3-x}Cl_x$ solar cells by an effective Cl doping method. *Nano Energy* **27**, 51–57 (2016).
107. Ye, S. *et al.* CuSCN-based inverted planar perovskite solar cell with an average PCE of 15.6%. *Nano Lett.* **15**, 3723–3728 (2015).
108. Wang, H. *et al.* One plus one greater than two: high-performance inverted planar perovskite solar cells based on a composite CuI/CuSCN hole-transporting layer. *J. Mater. Chem. A* **6**, 21435–21444 (2018).
109. Yang, I. S. *et al.* Formation of pristine CuSCN layer by spray deposition method for efficient perovskite solar cell with extended stability. *Nano Energy* **32**, 414–421 (2017).
110. Hao, F. *et al.* Lead-free solid-state organic-inorganic halide perovskite solar cells. *Nat. Photon.* **8**, 489–494 (2014).
111. Heo, J. H. *et al.* Efficient inorganic–organic hybrid heterojunction solar cells containing perovskite compound and polymeric hole conductors. *Nat. Photon.* **7**, 486–491 (2013).
112. Wang, Z. *et al.* Efficient ambient-air-stable solar cells with 2D–3D heterostructured butylammonium-caesium-formamidinium lead halide perovskites. *Nat. Energy* **2**, 17135 (2017).
113. Deng, Y. *et al.* Air-stable , efficient mixed-cation perovskite solar cells with Cu electrode by scalable fabrication of active layer. *Adv. Energy Mater.* **6**, 1600372 (2016).
114. Zheng, X. *et al.* Defect passivation in hybrid perovskite solar cells using quaternary ammonium halide anions and cations. *Nat. Energy* **2**, 17102 (2017).
115. Liu, J. *et al.* Crystal growth lead-free solar cells based on tin halide perovskite films with high coverage and improved aggregation angewandte. *Angew. Chemie - Int. Ed.* **57**, 13221–13225 (2018).
116. Yang, M. *et al.* Facile fabrication of large-grain $CH_3NH_3PbI_{3-x}Brx$ films for high-efficiency solar cells via CH_3NH_3Br-selective Ostwald ripening. *Nat. Commun.* **7**, 12305 (2016).
117. You, J. *et al.* Improved air stability of perovskite solar cells via solution-processed metal oxide transport layers. *Nat. Nanotechnol.* **11**, 75–81 (2016).

118. Nie, W. *et al.* High-efficiency solution-processed perovskite solar cells with millimeter-scale grains. *Science* **347**, 522–525 (2015).
119. Li, Y. *et al.* High-efficiency robust perovskite solar cells on ultrathin flexible substrates. *Nat. Commun.* **7**, 10214 (2016).
120. Liu, Z. *et al.* Using a low-temperature carbon electrode for preparing hole-conductor-free perovskite heterojunction solar cells under high relative humidity. *Nanoscale* **8**, 7017–7023 (2016).
121. Liang, J. *et al.* $CsPb_{0.9}Sn_{0.1}IBr_2$ based all-inorganic perovskite solar cells with exceptional efficiency and stability. *J. Am. Chem. Soc.* **139**, 14009–14012 (2017).
122. Chen, H. *et al.* Solvent engineering boosts the efficiency of paintable carbon-based perovskite solar cells to beyond 14%. *Adv. Energy Mater.* **6**, 1502087 (2016).
123. Zhu, W. *et al.* Intermolecular exchange boosts efficiency of air-stable, carbon-based all-inorganic planar $CsPbIBr_2$ perovskite solar cells to over 9%. *Adv. Energy Mater.* **8**, 1802080 (2018).
124. Duan, M. *et al.* Efficient hole-conductor-free, fully printable mesoscopic perovskite solar cells with carbon electrode based on ultrathin graphite. *Carbon* **120**, 71–76 (2017).
125. Luo, Q. *et al.* All-carbon-electrode-based endurable flexible perovskite solar cells. *Adv. Funct. Mater.* **28**, 1706777 (2018).
126. Zhang, H. *et al.* Self-adhesive macroporous carbon electrodes for efficient and stable perovskite solar cells. *Adv. Funct. Mater.* **28**, 1802985 (2018).
127. Wei, Z. *et al.* Cost-efficient clamping solar cells using candle soot for hole extraction from ambipolar. *Energy Environ. Sci.* **7**, 3326–3333 (2014).
128. Jeon, I. *et al.* Single-walled carbon nanotube film as electrode in indium-free planar heterojunction perovskite solar cells: investigation of electron-blocking layers and dopants. *Nano Lett.* **15**, 6665–6671 (2015).

Chapter 2. Polymer materials passivated perovskite solar cells

2.1 Abstract

Organic/inorganic metal hybrid perovskites have regarded as the most promising photo-electric materials and next-generation photovoltaics. The quality of organic/inorganic metal hybrid perovskites seriously determine the performance of perovskite solar cells (PSCs) due to the role of solar energy harvester. Interface engineering of organic/inorganic metal hybrid perovskites has regarded as an effective way to enhancing the power conversion efficiency (PCE) of PSCs by improving perovskite film's coverage and minimizing the charge recombination loss. Therefore, the polymethyl methacrylate (PMMA) and polycarbonate (PC) were applied to modified interface between the perovskite photoactive layer and the hole transport layer, and achieved a high PCE of 20.5 and 19.1%, respectively. The morphology modification, surface passivation, and protection of the perovskite layer by the insulating PMMA and PC layer substantially contribute to the enhancement of photovoltaic performance and its stability despite a slight reduction of the charge extraction efficiency. And, the working mechanism of polymers passivation was studied by electrochemical analysis.

Keywords: perovskite solar cells, power conversion efficiency, surface passivation, polymethyl methacrylate, polycarbonate

2.2 Introduction

Organic/inorganic metal hybrid perovskite materials have been regarded as a most promising photo-electric semiconductor for photovoltaics and drawn an enormous attention due to the rapid development of power conversion efficiency (PCE) of perovskite solar cells (PSCs) from 3.8% to the latest value of 24.2% within a decade[1]. The unprecedented development in PCE of PSCs mainly determines by the superior properties of organic/inorganic metal hybrid perovskite photoactive materials, including small exciton bending energy[2–4], micrometer-scale carrier diffusion legnths[2,5], high carrier collection ability[6], tunable band gap energy[7–9], strong light absorption from the visible to the infrared region[10], high carrier mobility[11] and low temperature fabrication process[12]. The PCE of PSCs based on the methylammonium lead halide ($CH_3NH_3PbX_3$, $MAPbX_3$) perovskite as a light harvester layer have realized ca. 20% both in normal (n-i-p) and inverted (p-i-n) architectures[13,14]. The quality of perovskite has been substantially enhanced after several endeavors, such as DMF used as a fumed source of perovskite and CH_3NH_3I vapor, and CH_3NH_3I employed in mixed solvents[15,16], however, some of tough challenges still need to be solved for more higher PCE of $MAPbX_3$ based PSCs. For example, a) the dense, fully coverage and void-free perovskite films should be fabricated to prevent the leakage of photocurrent and enhance the open-circuit voltage of PSCs, b) an approach of perovskite films with a flat surface morphology is required to enhance adhesiveness to the hole transport layer and c) a resistance against of humidity, oxygen, and ambient temperature of perovskite phase should be improved. Therefore, it is necessary to develop an effective method to engineer the interface of perovskite layer, which is urgently required for high PCE and stability of PSCs.

Enormous approaches, such as controlled formation[17], solvent treatment[18], inserting a buffer layer material[19–21], incorporation of chloride[22], interface engineering[23–25], and interface passivation[26,27], have developed to improve carrier mobility and promote the photovoltaic performance of PSCs. Even though countless endeavors have been invested, more superior materials that could improve surface quality and function as excellent passivation properties of the underneath perovskite light harvester layer are still pursued. An insulating organic polymer material has been introduced because it can form a dense buffer layer on perovskite light harvester layer surface to meet the above requirements. The enhancement of performance of PSCs using an insulating polymer material as a passivated interface of perovskite have been published[21,28–30]. However, the PCEs of polymer material passivated $MAPbX_3$ PSCs are still unsatisfied. Moreover, the detailed working mechanism of this inserted polymer layer for the photovoltaic performance in

PSCs is still unclear.

In this chapter, an effective strategy of interface engineering between the perovskite light harvester layer and hole transport layer is adopted to further improving the photovoltaic performance of PSCs via enhancing perovskite light harvester layer quality and reducing interface's carrier recombination loss. I successfully demonstrated that the enhanced photovoltaic performance of PSCs by incorporating a thin film of poly(methyl methacrylate) (PMMA) and polycarbonate (PC), and achieved a high PCE of 20.4 and 19.1% on PMMA and PC based PSCs under revise scanning, which are much higher than the standard PSCs without any treatment. The highest stabilized power output (SPO) of 19.9 and 19.1% are obtained on PMMA and PC based PSCs under maximum power point (MPP) tracking, respectively, which are much higher than the standard device (14.9%). Moreover, the detailed working mechanism and carrier recombination process of PSCs has been analyzed by photoluminescence spectroscopy and impedance spectroscopy without and with polymer passivation.

2.3 Experimental section

Materials: Chemicals are used as obtained without any further purification. Fluorine-doped tin oxide substrate (FTO, 10 Ω) is ordered from Asahi Glass Co., Ltd., Japan. Lead iodide (PbI_2, L0279), methylammonium iodide (CH_3NH_3I, MAI, M2556), mesoporous titanium oxide (PST-18NR, ca. 20 nm), and titanium diisopropoxide bis(acetylacetonate) are ordered from Tokyo Chemical Industry Co., Ltd. poly(methyl methacrylate) (PMMA, Mw ≈ 15,000, powder), polycarbonate (PC, Mw ≈ 43,200, particle), 4-tert-butylpyridine (tBP) and Co(4-tert-butylpyridyl-2-1H-pyrazole)3·3TFSI (TFSI = bis(trifluoromethanesulfonyl) imide), titanium chloride ($TiCl_4$, 99.0%) and zinc power (99.995%, Aldrich) are ordered from Sigma-Aldrich Co., Ltd. Dehydrated N,N-dimethylformamide (DMF), dimethyl sulfoxide (DMSO), and chlorobenzene are dried before utilization. 2,2′,7,7′-Tetrakis(N,N-di-p-methoxyphenylamino)-9,9′-spirobifluorene (spiro-OMeTAD) was purchased from Merck Co., Ltd. Lithium bis(trifluoromethanesulfonyl)imide (Li-TFSI), dehydrated ethanol, acetone, isopropyl alcohol (IPA), and other solvents were purchased from Wako Chemical Co., Ltd. and are used as received unless noted otherwise.

TiO_2 electron transport layer fabrication: The FTO glass substrates are etched using zinc powder and 6 M HCl solution. The etched FTO glass substrates are washed in concentration of about 1 wt% aqueous detergent solution, acetone, IPA and distilled water under sonication for 10 min in each step, respectively. The cleaned FTO glass substrates are dried using an air gun and stored at a relative dry condition. An about 25 nm thick of TiO_2 compact layer is deposited using spraying titanium diisopropoxide bis(acetylacetonate) with 0.05 M dehydrated ethanol solvent at 450 °C hotplate with a 0.5 MPa pressure and repeated three times. The sprayed FTO glass substrates are immersed into a cooled solution of mixed with $TiCl_4$ and distilled water for 30 min at temperature of 70 °C and then substrates are washed and dried using distilled water and an air gun, respectively. Then, the substrates are sintered at 500 °C for 20 min. The cooled substrates are cut into 25×25 mm^2 and treated by Ozone killer about 27 min for mesoporous TiO_2 deposition. The dehydrated ethanol mesoporous TiO_2 suspension with concentration of 1:8 of TiO_2 paste and ethanol is spin coated at 5000 rpm for 30 s and annealed at 125 °C for 30 min. The substrates are sintered again at 500 °C for 30 min and then stored at a dried box for following experiment.

PSCs devices fabrication: All the procedures of PSCs devices fabrication are finished in a nitrogen-filled glovebox.

Perovskite light harvester layer deposition: The FTO substrates are treated at Ozone killer and then transferred into glovebox. The 1.5 M concentration of perovskite precursor solution consist of MAI (717 mg) and PbI_2 (2076 mg) at a molar ratio of 1:1 in a mixed solvent of DMSO (750 μL) and DMF (2250 μL) with a volume ratio of 1:3 and dissolve at 40 °C until fully dissolving. The 200 μL perovskite precursor solution is deposited on substrates at spin coating program of 5000 rpm for 5 s, and the anti-solvent of 500 μL of toluene is dropped on at 2 s before finishing spin coating; the coated substrates are treated at 100 °C for 30 min on a hotplate.

Polymer layer deposition: The polymer materials of PMMA and PC are dissolved in chlorobenzene solvent with various concentration at a temperature of 50 °C for 30 min. The 200 μL of PMMA or PC solution spin-coats on above perovskite photoactive layer surface at program of 4000 rpm for 30 s after 10 s of dropping solution, and then the substrates are post-treated at 70 °C for 30 min on a hotplate.

Hole transport layer deposition and electrode evaporation: The hole transport layer (HTL) material consists of 8.6 mg mmol Li-TFSI, 27 μL tBP, 13.5 mg Co(4-*tert*-butylpyridyl-2-1*H*-pyrazole)3·3TFSI and 73.5 mg spiro-OMeTAD dissolves in 1 mL chlorobenzene solvent. The HTL solution is spin coated on perovskite surface before and after polymer passivation at a program of 4000 rpm for 30 s and post-treated at 70 °C for 30 min on a hotplate. Finally, the Au electrode film about 80 nm is thermal deposited on above substrates surface.

Characterization: All characterizations of PSCs and perovskite light harvester layer are conducted at ambient condition. A thin thickness of perovskite light harvester layer is used to check the optical properties of photoluminescence (PL) and absorption spectra using the same fabrication of PSCs in micro-Raman setup (Nnaophoton, Ramantouch) with an excitation wavelength of 532 nm and a power of 75 μW and UV/Vis spectrophotometer (Shimadzu, UV-1800). The time resolved PL is conducted by a time-correlated single-photon counting setup using a power of 2.7 nW, a pulse width of 6.9 ns and 516 nm wavelength laser source.

The photovoltaic performance of PSCs is measured using a solar simulator (San-Ei Electric, XES-40S1) under AM 1.5 conditions (100 mW/cm^2). Before start measurement, a standard cell (Bunkoukeiki, BS-500BK) is used to calibrate power of light source. The current-density (*J*–*V*) curves of PSCs are measured at scanning speed of 50 mV/s from (−0.1 to 1.2 V) and reverse (1.2 to −0.1 V) scanning directions without any pretreatment such as light soaking or applied bias voltage for a prolonged period before stating measurement. The stabilized power output (SPO) is recorded with a bias voltage at the maximum power point (MPP). This bias voltage is closed to the maximum PCE of *J*–*V* curves from the forward reverse scanning. The incident-to-power conversion efficiency is evaluated at a monochromatic Xe arc light system (Bunkoukeiki, SMO-250III) in the dark condition. The surface and cross-sectional morphology of perovskite photoactive layer and PSCs devices are characterized by a SEM (JEOL, JEM-6500F). The atomic force microscopy (AFM) (SII, Nanocute) setup is used to characterize the surface roughness of perovskite photoactive layer. The electrochemical properties of PSCs are measured by an electrochemical analyzer (ALS/HCH, 660 EAW) at a low light density (0.1 sun) with various bias voltages, a perturbative voltage of 5 mV (rms), and a sweeping frequency from 0.1 Hz to 1 MHz. The data are analyzed using an equivalent circuit diagram. The residual thickness of PMMA on the perovskite light harvester layer surface is characterized by SEM. The samples are cut into two pieces with equal size, where one piece is used to confirm the thickness of PMMA before chlorobenzene wash and other one is used to confirm the thickness after chlorobenzene wash.

2.4 Results and discussion

2.4.1 Perovskite light harvester layer characterization after PMMA passivation

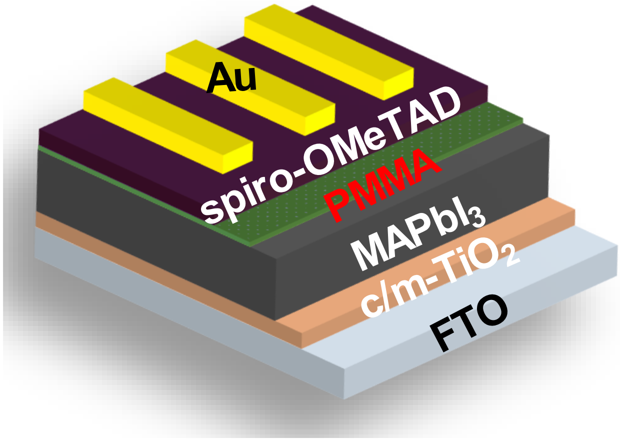

Figure 1. Architecture of PMMA passivated $MAPbI_3$-PSCs, including of glass FTO, c/m-TiO_2, $MAPbI_3$-perovskite, spiro-OMeTAD, and Au. Reprinted with permission from ref. 31.

Architecture of PSCs

Figure 1 shows the schematic structure of methylammonium lead iodide ($CH_3NH_3PbI_3$) PSCs with a PMMA polymer material between the perovskite light harvester layer and hole transport layer (HTL) of 2,2′,7,7′-tetrakis(*N*,*N*-di-*p*-methoxyphenylamino)-9,9′-spirobifluorene (spiro-OMeTAD)[31]. The perovskite harvester layer is sandwiched between the fluorine-doped tin oxide (FTO) substrate/contact TiO_2/mesoporous TiO_2 (electron transport layer) and HTL using one-step spin coating approach. The PMMA passivation, the PMMA chlorobenzene precursor solution is spin coated on perovskite light harvester layer surface after 10 s dropping solution, where the PMMA can be spread on the perovskite surface and form a homogenous dense protected layer. Then, the HTL is fabricated within 2 s after splashing spiro-OMeTAD chlorobenzene solution to prevent washing out of PMMA by chlorobenzene.

Surface and cross-sectional morphology of perovskite light harvester layer

Figure 2 shows the surface and cross-sectional morphology characterizations of perovskite light harvester films and PSCs with and without PMMA modifications using SEM. The perovskite light harvester layer is fully and homogeneously deposited on the TiO_2 layer surface with well crystallized, as shown in Figures 2a and b. The PMMA formed a dense and uniformly layer on the top of perovskite, and surface morphology seems become much clear after PMMA deposition according to Figure 2b. A typical crystal size of about 300 nm of perovskite polycrystalline layer is observed with voids free. The quality of perovskite light harvester films is much better than that of previous reports via two-step method of perovskite fabrication[30], reducing the density of macroscale voids on perovskite film according to Figure 2a. Moreover, the perovskite light harvester layer surface become much denser and flatter after PMMA modification compared with that of perovskite layer without PMMA, as shown in Figures 2c and d. The contact of perovskite light harvester layer and HTL of spiro-OMeTAD become much better and macroscale holes have been covered after PMMA passivation.

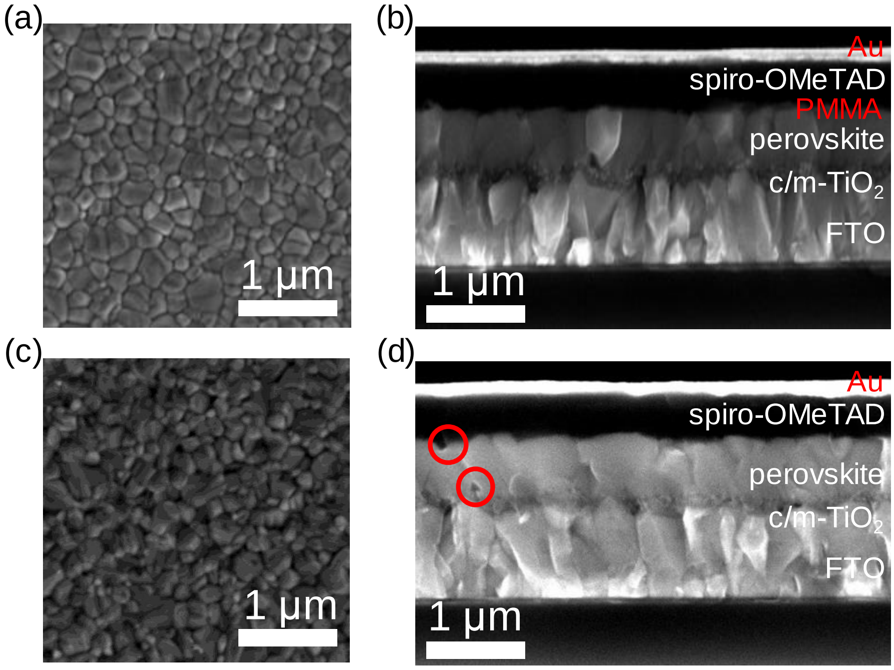

Figure 2. SEM characterization of surface and cross-sectional morphology of perovskite and PSCs with and without PMMA passivation. (a, b) SEM images of perovskite and PSCs with PMMA passivation, (c, d) SEM images of perovskite and PSCs without PMMA passivation. The scale bar is 1 μm.

Figure 3 shows the surface roughness evaluations of perovskite light harvester layers without and with PMMA passivation. Figure 3a shows the AFM image of perovskite film without PMMA treatment, where the surface contains some dark points of deep grain boundaries with large roughness compared with those of perovskite light harvester layers with PMMA passivation. The surface roughness of perovskite light harvester layers become smaller as the concentration of PMMA increment, as shown in the AFM images and summarized results of average value of surface roughness in Figures 3b-g. The average value of surface roughness of perovskite light harvester layer decreases as the concentration increase of PMMA, which means that the PMMA solution fills the grain boundaries and fine pinholes of perovskite films. This function contributes to form a monolithic flat and dense surface of perovskite&PMMA layer, thereby enhancing a much better contact of HTL and perovskite films. The enhanced quality of surface and cross section of perovskite light harvester films can significantly improve the photovoltaic performance and stability of PSCs[22,30,32].

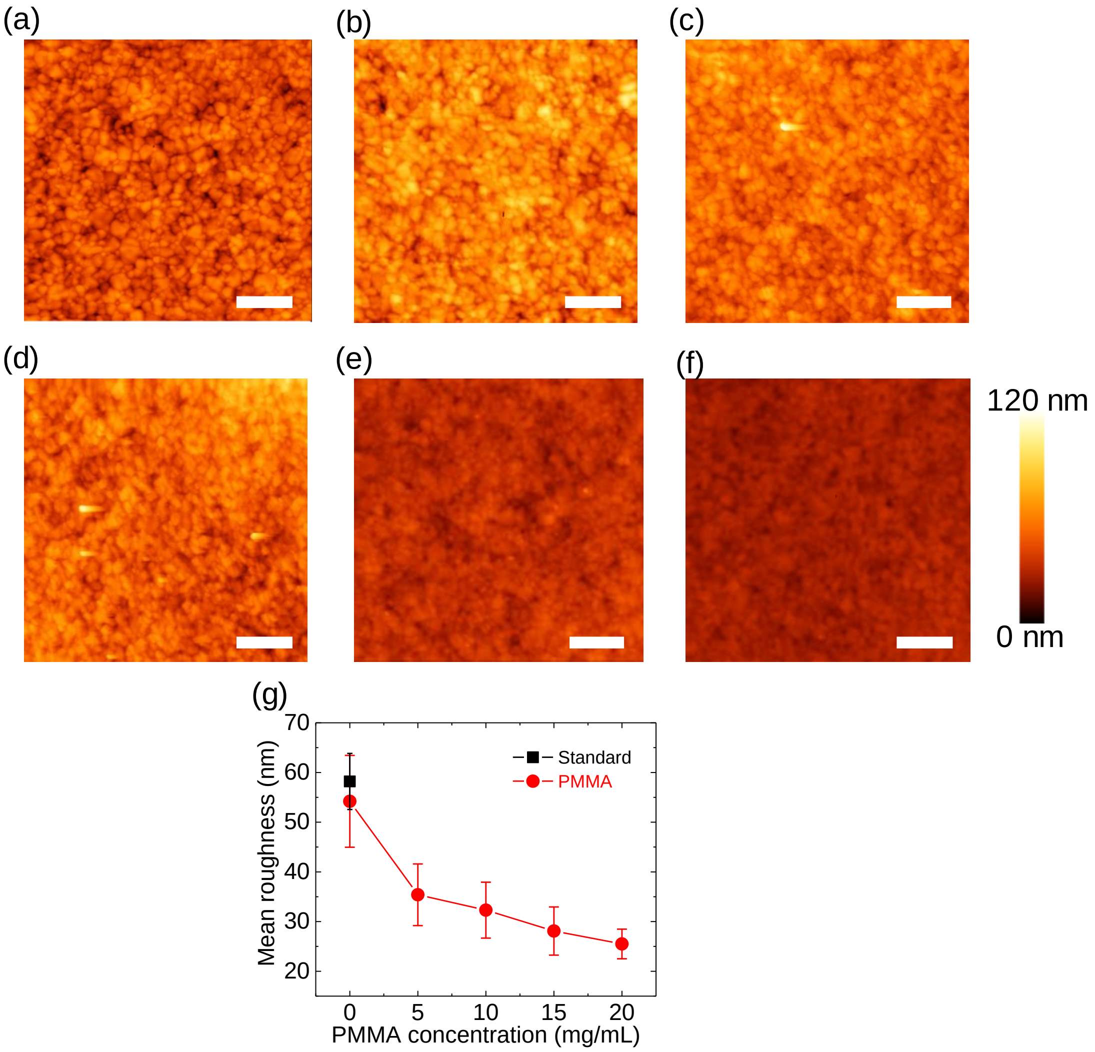

Figure 2. AFM characterization of surface roughness of perovskites with and without PMMA passivation. (a) AFM image of perovskite without PMMA passivation, (b-f) AFM images of perovskites with PMMA passivation under various concentration of 5, 10, 15 and 20 mg/mL. The scale bar is 1 μm. (g) Summary of surface roughness of perovskites without and with PMMA passivation.

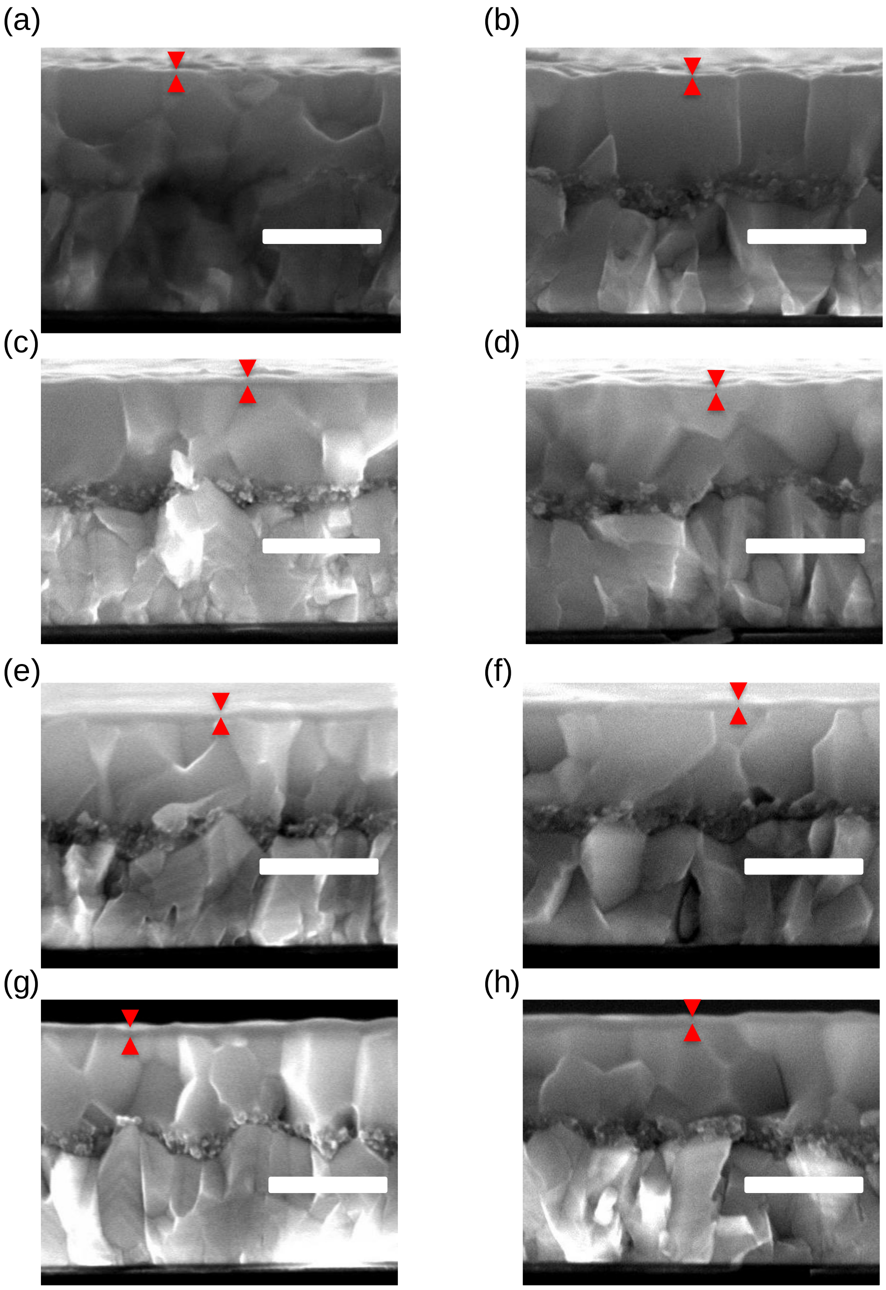

Figure 4. SEM characterization of cross-sectional morphology of perovskites with PMMA passivation and residual PMMA on perovskites' surface using simulated process of chlorobenzene splashing. (a, c, e, g) SEM images of perovskites with PMMA passivation under concentration of 5, 10, 15 and 20 mg/mL. (b, d, f, h) SEM images of perovskites with PMMA washing by chlorobenzene with 100 μL. The scale bar is 1 μm.

Figure 4 and **Table 1** show the cross-sectional images of perovskite light harvester layers without and with PMMA to check the thickness of PMMA. The chlorobenzene is used to simulate the HTL solution deposition process to confirm the optimized the thickness of PMMA. As shown in Figures and table, the PMMA can form a dense and uniformly layer on perovskite surface even after chlorobenzene splashing, and the thickness of PMMA can remain ca. 50% at low concentration and increase to ca. 91% at 20 mg/mL.

Table 1. Summary of the PMMA thickness on perovskites surface before and after chlorobenzene splashing.

Concentration (mg/mL)	Before (nm)	After (nm)
5	17.6 ± 0.5	9 ± 0.4
10	30.4 ± 1.9	21.6 ± 0.9
15	42.2 ± 1.4	35.2 ± 1.0
20	46.4 ± 0.7	42.4 ± 1.1

Optical properties of perovskite light harvester layer

The optical absorption, steady-state photoluminescence (PL), and time-resolved PL are used to study the charge carrier dynamics of perovskite light harvester layers and demonstrated the functions of PMMA. **Figure 5a** shows the optical absorption spectra of perovskite light harvester layers without and with PMMA passivation. The main features of absorption profile are almost same without and with PMMA deposition, including

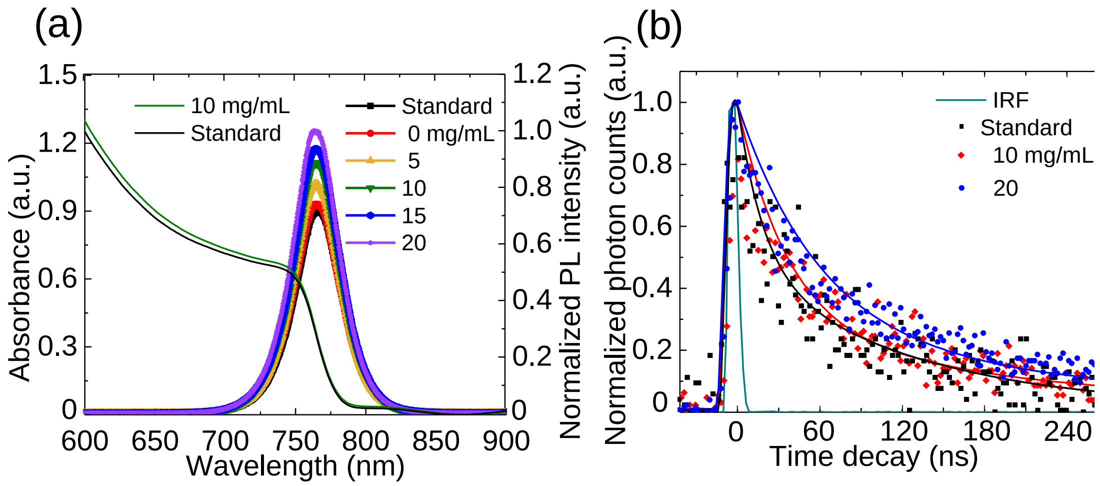

Figure 5. Optical characterization of perovskites without and with PMMA passivation. (a) Absorption and PL spectra, (b) TRPL decay profiles of perovskites without and with PMMA passivation under various concentrations.

shoulder peak position and intensity, because the PMMA is a kind of polymer with extremely high transparency from near-infrared and visible regions[30].

Figure 5a also shows the PL spectra of perovskite light harvester layers with PMMA deposition under various concentrations. The PL profile of perovskite light harvester layer without PMMA deposition is similar to the previous results[30]. The position and shape of PL spectra of perovskite light harvester layer have no obviously changes as the PMMA concentration extension, however, the intensity of PL has substantially increased as the increment of PMMA and reached to the highest value at the concentration of 20 mg/mL. These phenomena should come from the quality enhancement of perovskite light harvester layers attributing to the reduction of perovskite light harvester layer, the voids and grain boundaries filling by PMMA. Therefore, the trap states of perovskite light harvester layer surface have been passivated, reduced the carrier trapping loss and enhanced the PL intensity by PMMA modification layer[33].

The time-resolved PL (TRPL) spectroscopy has been used to characterize the photoexcited carrier dynamics in the perovskite layers. Figure 5b shows the TRPL profiles of perovskite light harvester layers passivated by various PMMA concentrations. TRPL spectra are reproduced by bi-exponential functions with amplitudes and life-time parameters. The life-time of perovskite light harvester layers have been summarized and shown in **Table 2**. The fast and slow decay components in the bi-exponential functions are understood by the result of surface recombination and bulk radiative recombination

Table 2. Summary of time-resolved PL spectroscopy of perovskites without and with PMMA passivation under various concentrations, where *a* is a amplitude ratio of fast (τ_1) and slow decay (τ_2) component.

Concentration (mg/mL)	a	τ_1 (ns)	τ_2 (ns)	τ_{PL} (ns)
Standard	0.50±0.0	16.7±2.2	80.0±10.0	51.3±1.3
PhCl	0.47±0.0	19.0±0.7	80.0±3.3	51.1±2.2
5	0.50±0.0	30.0±3.3	105.0±6.7	69.3±6.2
10	0.47±0.0	38.3±2.2	104.3±7.1	73.0±3.0
15	0.47±0.0	45.7±0.4	108.3±2.2	78.4±0.7
20	0.47±0.0	49.0±2.0	115.0±13.3	84.1±7.4

processes of electron-hole pairs[34,35]. The values of lifetimes of perovskite light harvester layers increased as the concentration increment of PMMA. The increased lifetime of perovskite light harvester layers is well consistent with the integrated PL intensity, as shown in Figure 5a, because the time-integrated PL intensity is proportional to the average PL lifetime. The lifetime of perovskite photoactive layer increases from 51.3 ± 1.2 to 84.0 ± 7.4 ns as the PMMA thickness increments, as shown in Figure 5c. The carrier relaxation dynamics seriously affects the PL lifetime values in the electron-hole radiative recombination and surface carrier trapping (electron or hole) processes. The longer lifetime of perovskite light harvester layers with high PMMA concentrations (thickness) means that the surface trap states and non-radiative recombination centers are passivated and alleviated in perovskites protected by PMMA because the surface trap states and non-radiative recombination centers in perovskite light harvester layer reduce the PL lifetime by increasing the carrier trapping possibility.

2.4.2 *J–V* characterization of perovskite solar cells passivated by PMMA

After above analysis of the perovskite light harvester layers' properties, the PSCs have been fabricated and evaluated the photovoltaic (PV) performance. **Figure 6a** shows the current density–voltage (*J–V*) curves of a PSC without PMMA passivated layer (Standard PSC) and a PMMA-incorporated PSC (PMMA-PSC) fabricated using a PMMA layer with concentration of 10 mg/mL. The *J–V* curves of PSCs are recorded under various scanning directions: forward scans from the short-circuit current (J_{SC}) to the open-circuit voltage (V_{OC}) with a forward bias voltage with a rate of 50 mV/s, reverse scans from V_{OC} to the J_{SC} with same rate, and the all measurements are finished in ambient condition without any pre-treatments. The standard PSC without PMMA layer exhibits a V_{OC} of 1.09 V, a J_{SC} of 22.0 mA/cm^2, a fill factor (FF) of 65.9%, and a PCE of 15.8% under forward scanning conditions and a V_{OC} of 1.11 V, a J_{SC} of 20.9 mA/cm^2, a FF of 73.1%, and a PCE of 16.8% under reverse scanning conditions. In comparison, the PV performance has been much enhanced in PMMA-PSC, with a V_{OC} of 1.12 V, a J_{SC} of 23.4 mA/cm^2, and a FF of 71.2%, resulting in a PCE of 18.7% under forward scanning conditions. Moreover, a V_{OC} of 1.14 V, a J_{SC} of 23.4 mA/cm^2, and a FF of 76.6% resulted in a substantially high PCE of 20.4% under reverse scanning conditions with a concentration of 10 mg/mL PMMA. All PV parameters of PMMA-PSC are much higher than those of the standard PSC, resulting from the quality enhancement of perovskite light harvester layer by PMMA. The enhancements of PMMA-PSC in all parameters are substantially higher than the modification PSCs[22]. However, the hysteresis of PMMA-PSCs become slightly larger than the standard PSC, which will be discussed later.

Figure 6b shows the external quantum efficiency (EQE) of standard and PMMA PSCs. The EQE exhibits a response from about 300 to 800 nm in both devices. The highest value of EQE in PMMA-PSC is 92.8%, which is much higher than that of 87.5% on the standard PSCs. Moreover, the integrated photocurrent density of 22.9 mA/cm^2 obtained from the PMMA-PSC is much higher than that of 20.5 mA/cm^2 of standard device and recently reported result[22], which are consistent with the *J–V* values.

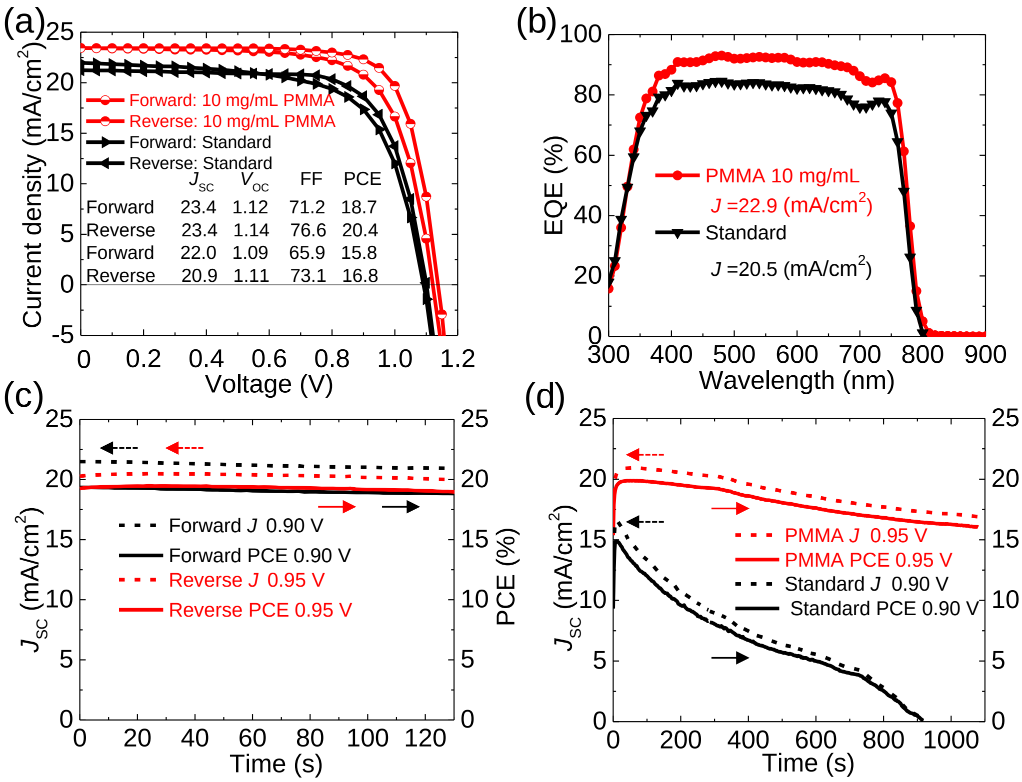

	J_{SC}	V_{OC}	FF	PCE
Forward	23.4	1.12	71.2	18.7
Reverse	23.4	1.14	76.6	20.4
Forward	22.0	1.09	65.9	15.8
Reverse	20.9	1.11	73.1	16.8

Figure 6. Photovoltaic performance characterization of PSCs without and with PMMA passivation. (a) Current density–voltage (*J–V*) curves of PSCs without (standard) and with PMMA passivation at concentration of 10 mg/mL. (b) EQE spectra and integrated current-density of PSCs. (c) SPO at MPP of PMMA passivated PSCs under forward and reverse scanning condition. (d) SPO at MPP of PSCs under reverse scanning with a bias voltage of 0.9 and 0.95 V of standard and PMMA PSCs.

The stabilized power output (SPO) value is also a parameter for evaluation of the PV performance of PSCs. The SPO usually is determined at a fixed bias voltage close to the maximum power point (MPP) on forward and reverse *J–V* curves under continuous light soaking. Figure 6c shows the SPO of the PMMA-PSC under forward and reverse scanning conditions at time evolution, respectively, indicating that the SPO values of forward and reverse are almost same independent on the scanning directions. Figure 6d exhibits the highest SPO in PMMA-PSC under reverse scanning with a bias voltage of 0.95 V, which is much higher than those of the chloride modification and crosslinking protected layer incorporation[22]. This SPO value is also higher than that of the standard PSC and consistent with the J–V curves value, as shown in Figure 6a. The stability of

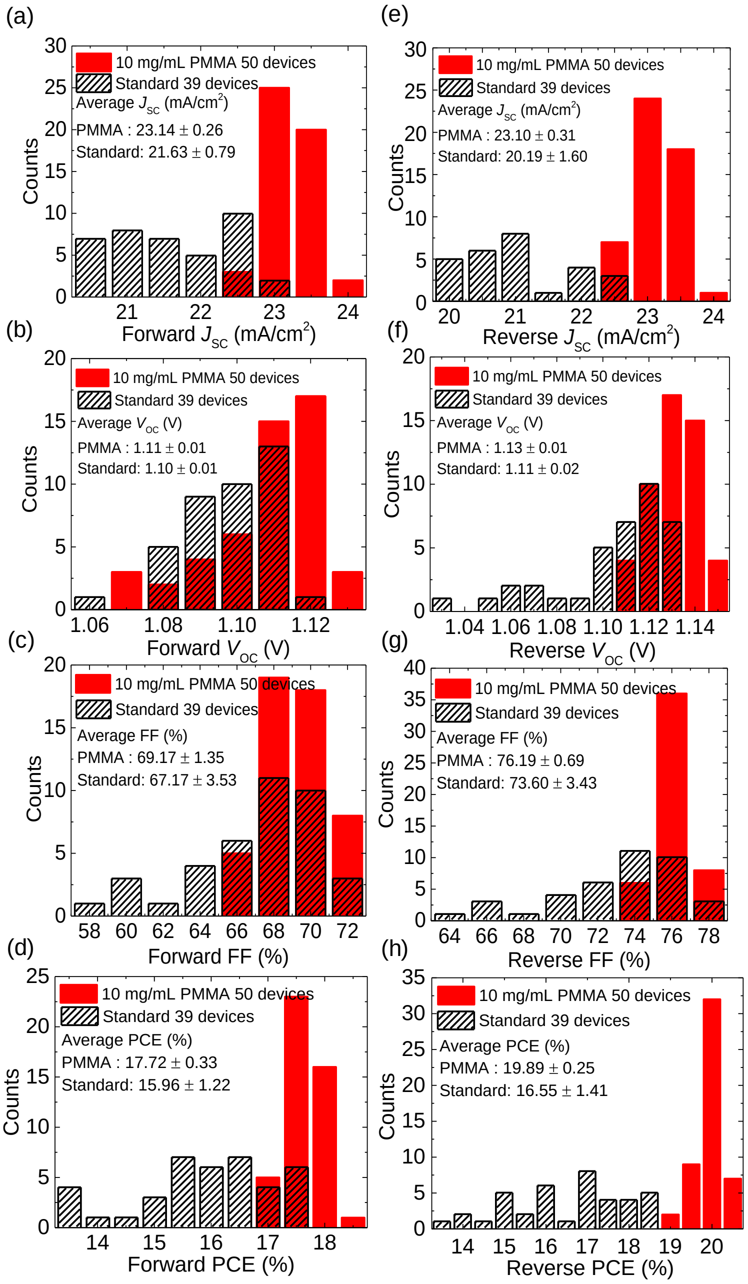

Figure 7. Repeatability characterization of PSCs without and with PMMA passivation. (a-d) and (e-h) statistic calculations of PSCs without and with PMMA passivation under forward and reverse scanning (red: 50 PMMA-incorporated devices; black: 39 standard devices).

SPO value in PMMA-PSC is much better than that of standard PSC, indicating that the decrease of PV performance under ambient and continuous light soaking has been significantly suppressed in PMMA-PSC using PMMA protected layer on perovskite light harvester layer surface.

The repeatability is another factor to characterize the PV performance for PSCs and potentially industrial applications. A large number of PSCs devices have been fabricated using the same approach and condition—39 standard and 50 PMMA-PSC devices—to evaluate the reproducibility of their PV performances. **Figure 7** shows the histograms of all PV parameters of PSCs with and without PMMA passivation under forward and reverse scanning conditions. The standard PSC exhibits a relative lower average value with a broader distribution of 16.0 ± 1.2% from 13.5 to 17.5% under forward scanning, 16.6 ± 1.4% from 13.7 to 18.5% under reverse scanning. By comparison, the PMMA-PSCs shows the much higher values and narrow distribution of 17.7 ± 0.3% from 16.9 to 18.9% and 19.9 ± 0.3% from 18.9 to 20.5% under forward and reverse scanning conditions, respectively, as shown in Figures 7a and b. The values of J_{SC}, V_{OC}, and FF in PMMA-PSCs are also much higher than those of the standard PSCs. These results strongly suggest that PMMA-PSCs can achieve much high repeatability compared with that of standard PSCs.

In order to investigate the optimize condition of PMMA on perovskite light harvester layer passivation and the PV performance of PSC, the PMMA concentration dependence of PSCs have been investigated and the results are shown in **Figure 8**. Figure 8a shows the *J–V* curves of PMMA-PSCs under reverse scanning with various concentration of PMMA from 0 to 20 mg/mL. Noted that the concentration of 0 mg/mL means the PSC that has been only spin coated chlorobenzene solution. The PV parameters of J_{SC}, V_{OC},

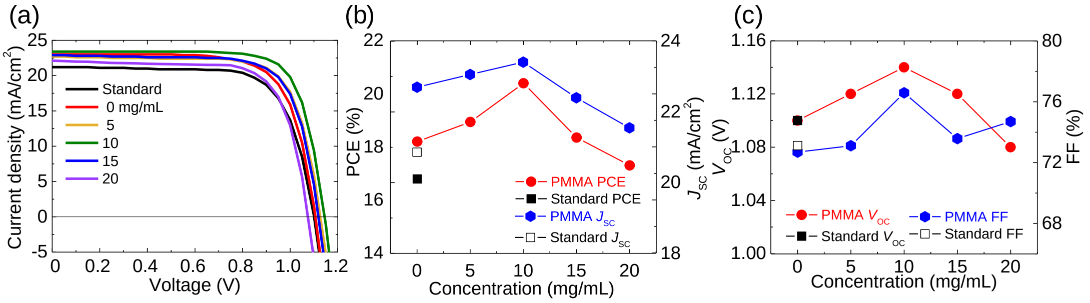

Figure 8. *J–V* curves of PSCs under various concentration of PMMA passivation. (a) *J–V* curves of PSCs under reverse scanning. (b, c) Summary the PMMA concentration dependent of PCE, J_{SC}, V_{OC} and FF of PSCs.

FF, and PCEs in PMMA-PSCs are much higher than those of the standard device, and the results have been summarized in **Table 3**. Figures 8b and c shows the J_{SC}, V_{OC}, FF, and PCEs of PSCs as a function of concentration of PMMA, where the parameters of PMMA-PSCs reach to the maximum at the concentration of 10 mg/mL of PMMA and become worse after exceeding this condition. The PMMA can promote the quality and reduce surface trap-states' recombination loss of perovskite light harvester layer, and promoting the PV performance of PSCs as shown in Figures 5 and 8. But the carrier extraction process on PMMA insulating layer is not the same as the improvement of optical properties. Because the low concentration of PMMA can fill out the voids and grain boundaries of perovskite light harvester layer, which can eliminate the possibilities of shunt-current leakage in PSCs[34,36]. But, the insulating nature of PMMA also functions as a potential barrier to hinder the carrier transport at the interface between the perovskite light harvester layer and HTL of spiro-OMeTAD, in which the carrier recombination loss possibilities will be increased and hysteresis become deteriorated when the thickness of PMMA after exceeds the optimized value. Therefore, the PV performance of PSCs reach to maximum at the concentration of 10 mg/mL of PMMA.

Table 3. Summary of the photovoltaic performance of PSCs without and with PMMA passivation under various concentrations.

Concentration (mg/mL)	Scan directions	J_{SC} (mA/cm^2)	V_{OC} (V)	FF (%)	PCE (%)
Standard	Forward	21.6 ± 0.8	1.10 ± 0.01	67.2 ± 3.5	16.0 ± 1.2
	Reverse	20.2 ± 1.6	1.11 ± 0.02	73.6 ± 3.4	16.6 ± 1.4
PhCl	Forward	22.6 ± 0.3	1.08 ± 0.02	64.9 ± 1.1	15.9 ± 0.2
	Reverse	22.5 ± 0.5	1.12 ± 0.01	73.3 ± 1.1	18.4 ± 0.2
5	Forward	22.9 ± 0.2	1.10 ± 0.01	66.1 ± 1.4	16.6 ± 0.3
	Reverse	22.7 ± 0.4	1.12 ± 0.01	74.1 ± 1.3	18.9 ± 0.3
10	Forward	23.1 ± 0.3	1.11 ± 0.01	69.2 ± 1.4	17.7 ± 0.3
	Reverse	23.1 ± 0.3	1.13 ± 0.01	76.2 ± 0.7	19.9 ± 0.3
15	Forward	22.7 ± 0.2	1.11 ± 0.01	67.0 ± 2.0	16.8 ± 0.6
	Reverse	22.4 ± 0.2	1.12 ± 0.01	75.2 ± 0.8	18.9 ± 0.3
20	Forward	22.7 ± 0.1	1.06 ± 0.01	64.6 ± 4.8	16.1 ± 0.3
	Reverse	22.1 ± 0.3	1.08 ± 0.01	75.5 ± 0.5	18.0 ± 0.4

2.4.3 Impedance spectroscopy analysis of perovskite solar cells passivated by PMMA

To further confirm the roles of PMMA layer on perovskite light harvester layer, the impedance spectroscopy has been used to characterize the electrochemical properties of PSC. **Figure 9a** shows the Nyquist plots from impedance spectra of PSCs with various

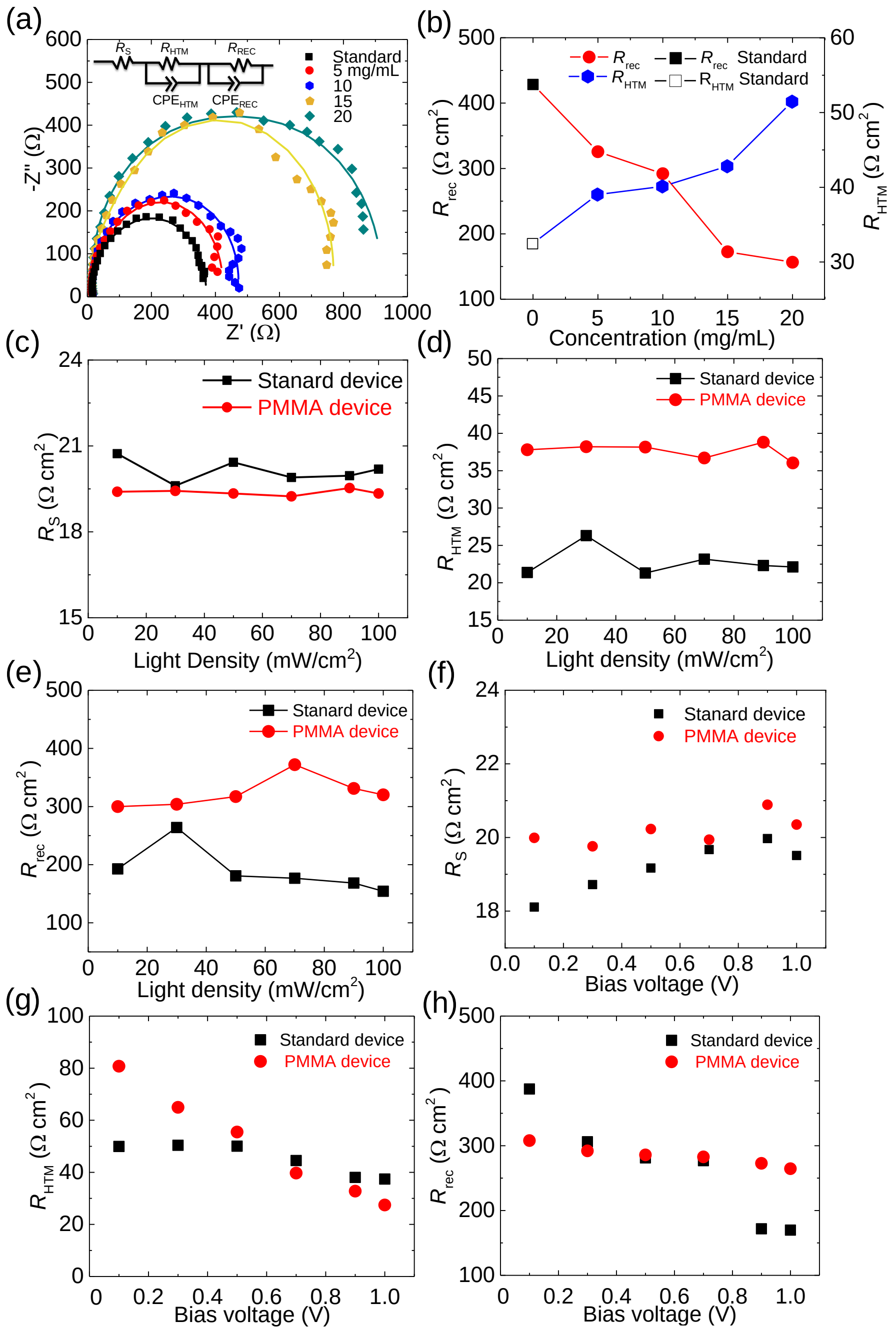

Figure 9. Electrochemical properties of PSCs without and with PMMA passivation. (a) Nyquist profile of impedance of PSCs without and with PMMA passivation, as recorded at a bias voltage of 0.3 V under 0.1 sun illumination conditions. Simulated equivalent circuit is shown inset. The fitting curves of Nyquist plots are also shown according to the equivalent circuit. (b) R_{HTM} and R_{rec} as a function of concentration of PMMA. (c-e) R_{S}, R_{HTM} and R_{rec} extracted from fitting of the impedance spectra collected at various illumination densities under an applied bias of 0.3 V. (f-h) Bias-voltage dependence of the R_{S}, R_{HTM} and R_{rec}.

PMMA concentrations. Impedance spectra show the similar behavior in all PMMA-PSCs with different PMMA concentration showing the different radius of curves. The impedance plots are divided into two components of high and low frequency regions, in which the high and low-frequency come from the contributions of hole transport from perovskite light harvester layer to the HTL of spiro-OMeTAD layer and carrier recombination process[35,37,38], respectively. All the measured spectra are well reproduced using an equivalent circuit model with the fitting parameters of recombination resistance (R_{rec})[38] and hole transport resistance (R_{HTM}), as shown in the inset of Figure 9a.

Figure 9b shows the PMMA concentration function of the calculated values of R_{rec} and R_{HTM}. The value of R_{rec} decreases as the concentration increment of PMMA, indicating that the carrier recombination loss deteriorates with the thickness of PMMA layer. Whereas, the R_{HTM} slightly increases as the concentration increase of PMMA, attributing to the insulating nature of PMMA. The series resistance (R_{S}) is determined by carrier transport from perovskite light harvester layer to electron transport layer, keeping almost constant as a function of the PMMA concentration, which strongly supports the validity of this analysis. The R_{rec} and R_{HTM} reach an optimized point when the concentration of PMMA is 10 mg/mL. The R_{S}, R_{rec} and R_{HTM} of standard PSCs and PMMA-PSCs are also measured under various simulated light illumination density from 10 to 100 mW/cm^2 at a 0.3 V bias voltage, as shown in Figures 9c-e. Confirming that the values of R_{S}, R_{rec} and R_{HTM} of PMMA-PSCs are higher than those of standard device and keep almost constant under all experimental conditions.

Figures 9 f-h exhibit the R_{S}, R_{rec} and R_{HTM} of standard and PMMA-PSCs under various bias voltages conditions. The bias voltage from 0.1 to 1.0 V are changed.[37,39] The R_{S} slightly increase in both PSCs, while the R_{HTM} continuously decreases as the bias voltage increment in PMMA-PSCs, the R_{HTM} keeps almost constant value in standard devices. The value of R_{HTM} decreases from 80 to 20 Ω in PMMA-PSCs and lower than that of standard device after bias voltage higher than 0.7 V, indicating that the carrier extraction ability become much better than that of standard device after PMMA passivation. Moreover, the R_{rec} of standard device decreases from 400 to lower than 200 Ω, however, the R_{rec} of PMMA-PSCs exhibits an almost constant value and litter higher than that of standard device after bias voltage exceeding 0.7 V, indicating that the carrier recombination loss becomes larger at high value of bias voltage due to the high trap states density of standard device.

The slight reduction of R_{rec} and increase of R_{HTM} come from the thicker insulating PMMA protected layer, which deteriorates the carrier recombination possibility on the bottom side of PMMA, adversely impacting on the PV performance of PSCs. The adverse properties of PMMA functions reducing the efficiency of carrier extraction from the perovskite light harvester layer to the HTL by crossing the PMMA layer and a relative lower R_{rec} (relative higher carrier accumulation possibility) of higher possibility of hysteresis. As a result, the hysteresis in PMMA-PSCs is much higher than that of standard device. However, the functions of surface passivation and morphology modification using PMMA induce a more major effects that enhance the PV performance of PSCs. Hence, the balance both positive of surface passivation and negative of increasing the R_{HTM} and reducing the R_{rec} determines the optimization condition of PMMA with 10 mg/mL for the highest performance of PSCs.

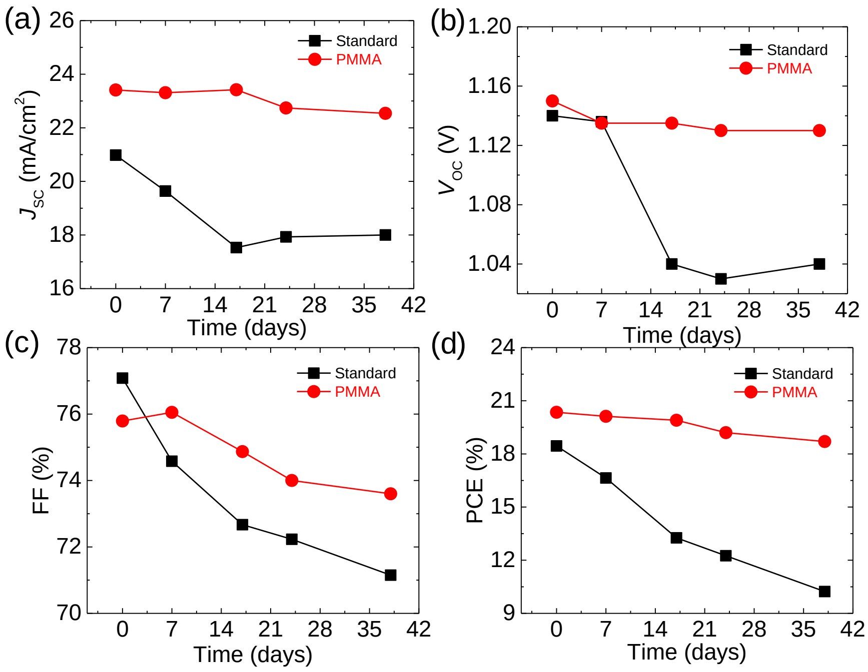

Figure 10. Stability of PSCs without and with PMMA passivation under room temperature with a humidity of ca. 40%. Time evolution of (a) J_{SC}, (b) V_{OC}, (c) FF, and (d) PCE of PSCs.

2.4.4 Stability evaluation of perovskite solar cells passivated by PMMA

The stability of PSCs will become much better with PMMA passivation perovskite light harvester layer, because the PMMA passivated layer can protect the perovskite from the invasion of moisture and oxygen, which prevent the $CH_3NH_3PbI_3$ perovskite light harvester layer degrading into CH_3NH_2I and PbI_2[28,30,40]. The PSCs were stored in the dark ambient condition with about 40% humidity. The PCE of PMMA-PSCs slightly reduces from 20.5 to 18.5% even after 40 days. In comparison, the standard devices quickly decrease from 18.5 to 10.0%. The all parameters of J_{SC}, V_{OC}, FF, and PCE of PSCs with and without PMMA passivation are shown in Figures **10a-d**. **Figures 11a** and b show the cross-sectional SEM images of the standard and PMMA-PSCs after storing 7 days in ambient conditions. The voids have been labeled by red circles. Interesting, the density of voids in standard device is much higher than that of PMMA-PSCs, indicating that the stability of PSCs has been significantly enhanced by protecting the perovskite light harvester layer from the oxygen and humidity.

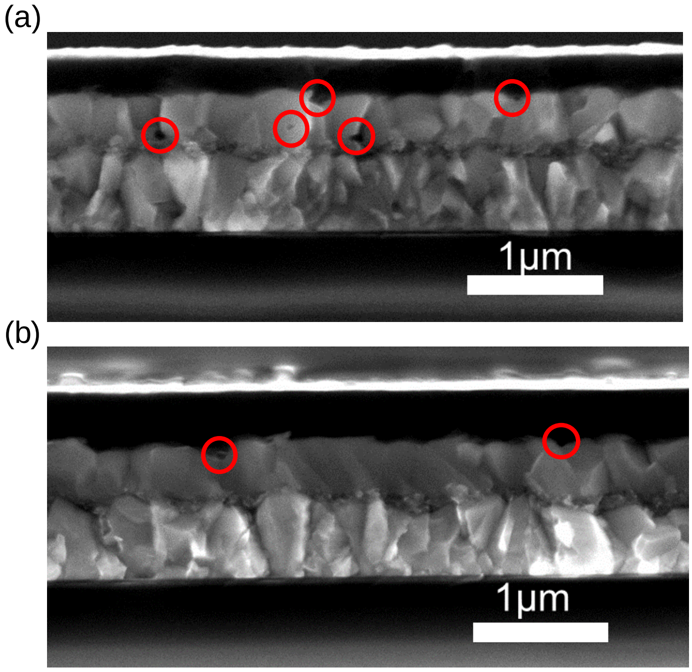

Figure 11. Typical cross-sectional SEM images of (a) PSC without PMMA and (b) PSC with PMMA passivation stored for 7 days under room temperature with a humidity of ca. 40%.

2.4.5 Perovskite light harvester layer characterization after PC passivation

Surface morphology, optical properties characterizations of perovskite light harvester layer

To demonstrate other polymer materials can be also used to passivate perovskite light harvester layer. The polycarbonate (PC) is employed to improve the perovskite layer and enhance the PV performance of PSCs. **Figure 12** shows the surface and cross-

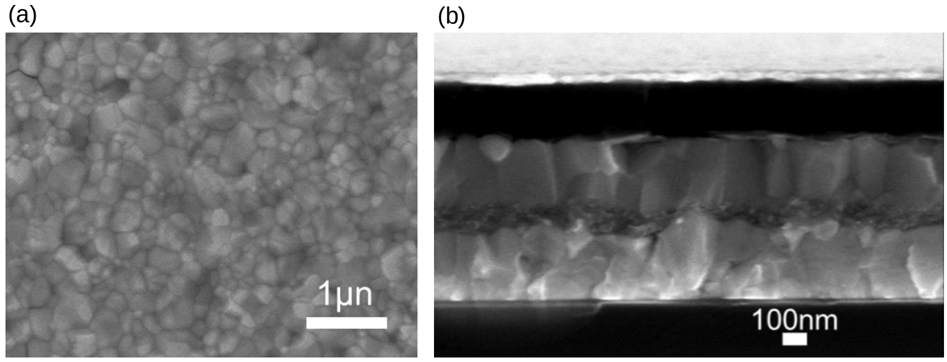

Figure 12. Surface (a) and cross-sectional (b) morphology characterization of perovskite and PSCs passivated by 7 mg/mL of PC.

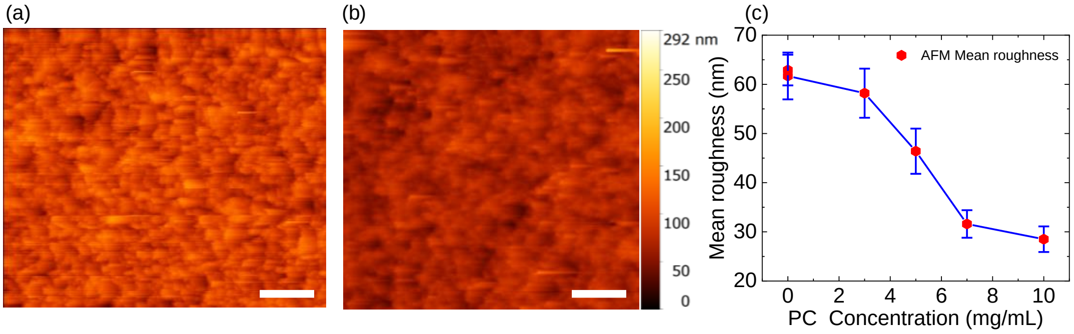

Figure 13. AFM topographical images and surface mean roughness of perovskite layer with different concentrations of PC. (a, b) AFM images of perovskite without and with PC layer (7 mg/mL). (c) Surficial mean roughness of perovskite with different concentration of PC.

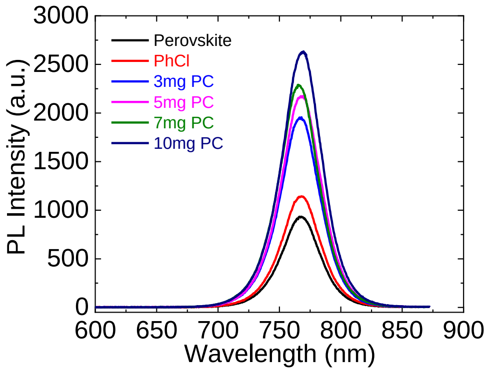

Figure 14. PL spectra of perovskites passivated under various concentrations of PC.

sectional SEM images of PC passivated perovskite light harvester layer. The PC-perovskite light harvester layer exhibits a similar surface morphology of PMMA-perovskite as dense, compact and voids-free film. However, the PC-perovskite shows relative low transparency compared with that of PMMA, as shown in Figure 12a. The PC seems to form an independent thin film on the perovskite surface according to the cross-sectional SEM images, as shown in Figure 12b. These properties will affect the carrier transport from perovskite light harvester layer.

Figure 13 shows the surface roughness of perovskite light harvester layer after PC passivation measured by AFM. According to Figures 13a and b, the surface of perovskite light harvester layers become flatter after passivation of PC with 7 mg/mL compared with that of standard one. The average surface roughness of perovskite light harvester layer decreases as the concentration of PC increment, which exhibits a similar result as those in perovskite-PMMA. As the concentration of PC increase as shown in **Figure 14**, the PL intensity of perovskite light harvester layer is also enhanced, which is the same as the PMMA, indicating that the perovskite quality has been improved, and the surface trap states and carrier recombination loss has been reduced.

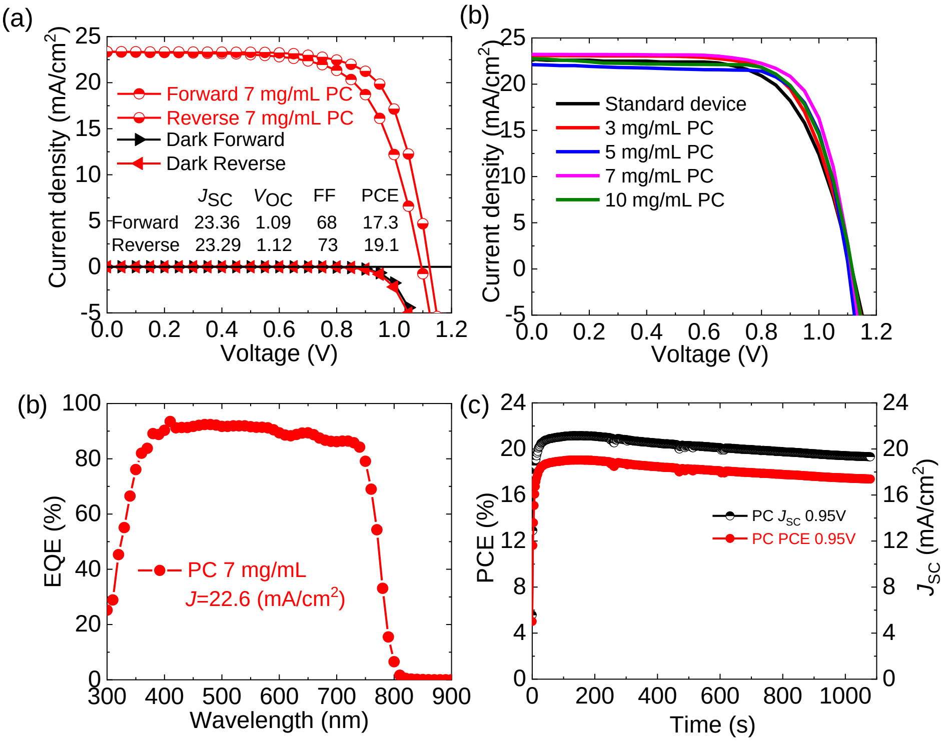

Figure 15. Photovoltaic performance of PSCs with PC passivation of 7 mg/mL. (a) *J*–*V* curves of the best PSCs, (b) *J*–*V* curves of PSCs with various concentrations of PC under reverse scanning, (c) EQE spectrum and (d) SPO of PSCs with PC passivation.

2.4.6 *J–V* characterization of perovskite solar cells passivated by PC

Figure 15a shows the *J–V* curves of the highest PV performance of PC passivated PSCs at concentration of 7 mg/mL. The PC-PSCs achieves a high PCE of 17.3%, a J_{SC} of 23.4 mA/cm^2, a V_{OC} of 1.09 V and a FF of 68.0% on the forward scanning, and a PCE of 19.1 %, a J_{SC} of 23.3 mA/cm^2, a V_{OC} of 1.12 V and a FF of 73.0% on the reverse scanning, which are relative lower than the PMMA-PSCs. The PV performance of PC-PSCs with various concentration of PC has been summarized and shown in Figure 15b and **Table 4**. As the concentration increase of PC, the PV performance of PSCs has been enhanced especially the J_{SC}, but the performance decreases after exceeding 7 mg/mL of PC concentration. Moreover, the hysteresis of PSCs also increases after PC passivation compared with the standard device.

Table 4. Summary of photovoltaic performance of PSCs with PC passivation under various concentrations.

Samples	Scan directions	J_{SC} (mA/cm^2)	V_{OC} (V)	FF (%)	PCE (%)
Standard	Forward	22.0	1.09	65.9	15.8
	Reverse	20.9	1.10	73.1	16.8
3 mg/mL PC	Forward	22.9	1.08	58.4	14.4
	Reverse	23.1	1.11	69.5	17.8
5 mg/mL PC	Forward	23.2	1.09	70.0	17.8
	Reverse	21.6	1.1	75.0	17.8
7 mg/mL PC	Forward	23.4	1.09	69.0	17.6
	Reverse	23.2	1.11	73.0	18.8
10 mg/mL PC	Forward	22.9	1.09	60.0	15.1
	Reverse	22.2	1.12	73.0	17.9

Figure 15c shows the EQE spectra of PC-PSC. The EQE exhibits a response from about 300 to 800 nm and the highest value of EQE in PC-PSC is 91.8%, which is much higher than that of standard PSCs. Moreover, the integrated photocurrent-density of 22.6 mA/cm^2 obtained from the PC-PSCs is much higher than that of 20.5 mA/cm^2 of standard device and recently reported result[34], which is well consistent with the *J–V* values.

To evaluate the SPO and short time stability of PC-PSCs under continuous light soaking condition, the solar cell device has continuously characterized at ambient condition without encapsulation. The PC-PSCs can obtain about 19.1% of SPO and slowly decrease to 18.7% even after 1100 s continuously measurement under MPP with a bias voltage of 0.95 V, which can keep almost same short time SPO stability compared with the PMMA device, as shown in Figure 15d.

The repeatability of PC-PSCs also has been evaluated using 21 devices and shows the summarized results in **Figure 16**. The PC-PSCs can achieve an average PCE of 18.5 ± 0.6%, a 22.5 ± 0.7 mA/cm^2 of J_{SC}, a 1.12 ± 0.0 V of V_{OC}, a 74.6 ± 0.9% of FF on the reverse scanning as shown in Figures 16a-d, which are higher than those of standard

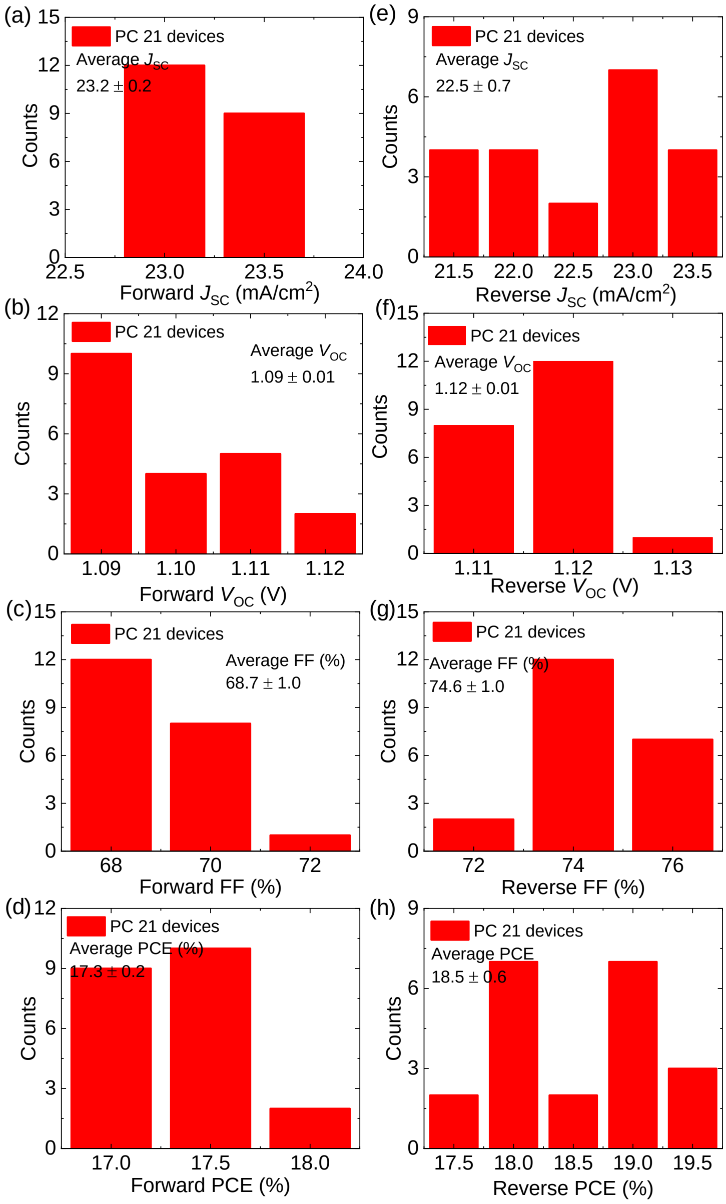

Figure 16. Repeatability evaluations of PSCs with PC passivation. (a-d) and (e-h) Statistic calculations of PSCs with PC passivation under forward and reverse scanning.

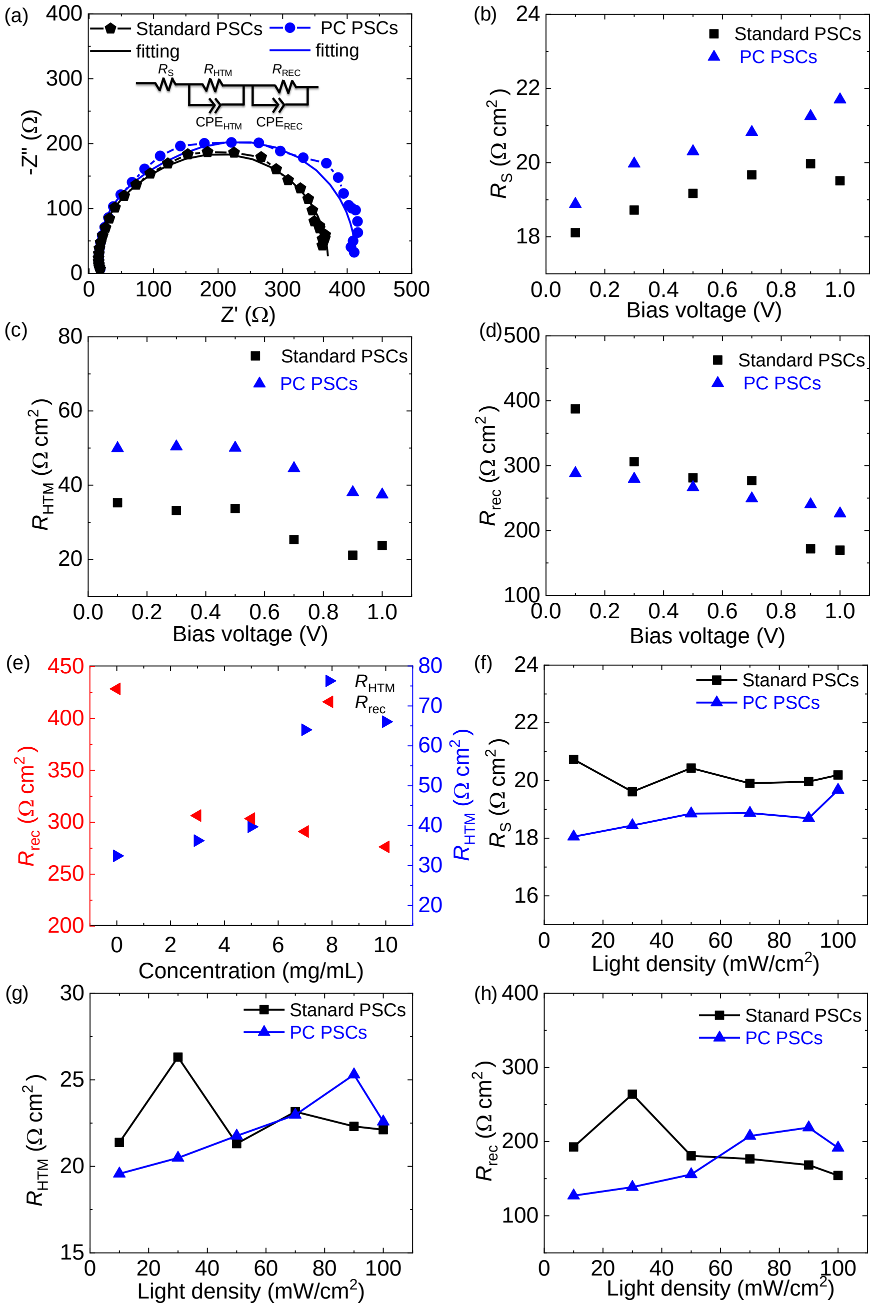

Figure 17. Electrochemical properties of PSCs without and with PC passivation. (a) Nyquist profile of impedance of PSCs without and with PC passivation, as recorded at a 0.3 V bias voltage under 0.1 sun illumination conditions. Simulated equivalent circuit is shown inset. The fitting curves of Nyquist plots are also shown according to the equivalent circuit. (b-d) Bias-voltage dependence of the R_S, R_{HTM} and R_{rec}. (e) R_{HTM} and R_{rec} function as the concentration of PC. (f-h) R_S, R_{HTM} and R_{rec} extracted from fitting of the impedance spectra collected at various illumination densities under an applied bias of 0.3 V.

devices. However, the PV performance of PC-PSCs is slightly lower than that of PMMA-PSCs, which should be come from the independent layer of PC on perovskite light harvester layer and its relative higher viscosity, because the PC cannot be fully dissolved in chlorobenzene solvent after the same dissolving time and temperature compared with that of PMMA. Therefore, the high viscosity of PC reduces the ability of film-forming and affects the PV performance of PC-PSCs.

2.4.7 Impedance spectroscopy analysis of perovskite solar cells passivated by PC

The impedance spectroscopy has been applied to investigate the carrier recombination process of PC-PSCs. **Figure 17a** shows the Nyquist plot of standard and PC-PSC with 7 mg/mL concentration. The simulated equivalent circuit model has been shown in inset. The measurement results can be reproduced using the equivalent circuit and the profile consist with two of component of high and low frequency. Figures 17b-d show the analyzed results of R_S, R_{HTM} and R_{rec} of standard and PC-PSCs under various bias voltages at 0.1 sun conditions. The R_S slightly increase as the bias voltage increment, however, the R_{HTM} and R_{rec} continuous decrease as the increase of bias voltage in both PSCs, which is similar with those in the PMMA-PSCs. Therefore, the carrier recombination possibility becomes worse as the bias voltage increment. Figure 17e shows the R_{HTM} and R_{rec} as a function of the PC concentration. The R_{HTM} and R_{rec} reach to an optimized balance, as

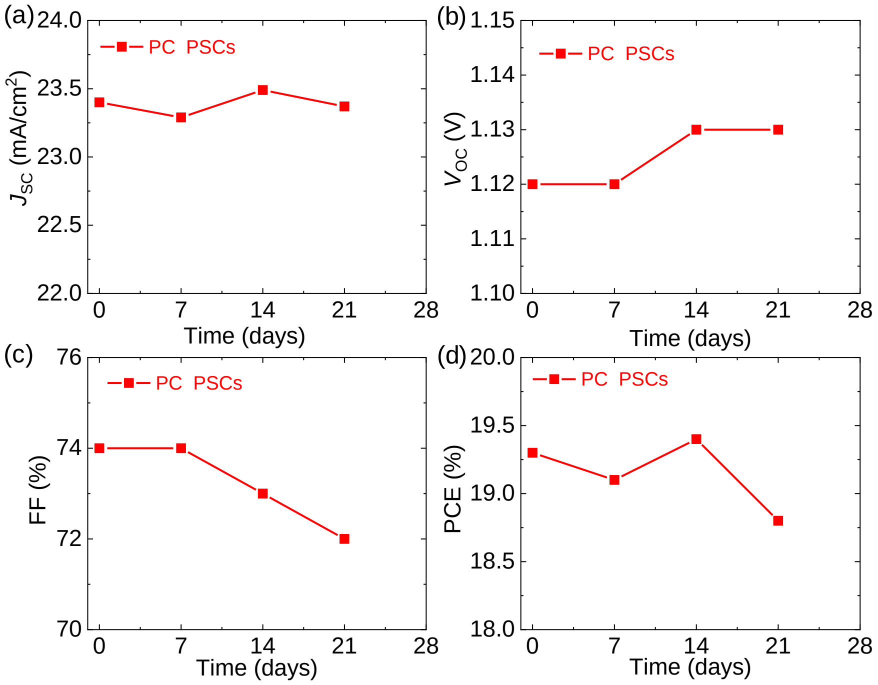

Figure 18. Stability of PSCs with PC passivation under room temperature with a humidity of ca. 40%. Time evolution of (a) J_{SC}, (b) V_{OC}, (c) FF, and (d) PCE of PSCs.

similar to that in PMMA-PSCs, indicating that the performance of the PC-PSCs reaches to a best condition. Figures 17 f-h show the R_s, R_{HTM} and R_{rec} of PC-PSCs under various density of illumination light. The PC-PSCs sustain relative lower R_s, but the R_{HTM} and R_{rec} increase as the illumination light density increment, indicating that the photovoltaic performance and carrier recombination loss of the PC-PSCs become better, which are similar to the PMMA passivated PSCs.

2.4.8 Stability evaluation of perovskite solar cells passivated by PC

Figure 18 shows the storage stability of PC-PSCs without encapsulation in ambient condition with humidity of about 40%. The PV performance of PC-PSCs slowly decreases as the keeping time extension and sustained about 18.7% even after 21 days later. The reduction of FF is the main reason for decrease of PV performance as shown in Figure 18c, which should come from the PC form of a non-monolithic film with the perovskite photoactive layer and increase the series resistance of devices.

2.5 Chapter summary

An effective strategy for interface engineering to further enhancing the PV performance of $CH_3NH_3PbI_3$ PSCs by reducing the interface carrier recombination loss and improving perovskite light harvester layer quality has been proposed. Based on this strategy, the PMMA- and PC-PSCs have achieved a high PCE of 20.4 and 19.1% from reverse *J–V* curves and a high SPO of 19.9 and 19.1%. These values are much higher than the standard device without PMMA and PC passivation. The PL and impedance spectroscopy have been applied to demonstrate the surface morphology modification, passivation and protection of perovskite light harvester layer after using insulating polymer layer. These results suggest that the quality of passivated film seriously affects the PV performance of PSCs. The high PV performance, repeatability and stability of PSCs are evidenced that the PMMA passivation is an effective way to realize the industrial application of PSCs. The periodical enhancement of the photovoltaic performance and stability of PSCs using polymers passivation is still not enough for the industrial application, which the typical and common used TiO_2 materials severely limits the PCE and stability of PSCs because of the UV light sensitive and energy mismatch. Therefore, it is necessary to further enhance the perovskite film quality on more excellent electron transport materials.

Reference

1. Best Research-Cell Efficiencies Chart. National Renewable Energy Laboratory (NREL), https://www.nrel.gov/pv/assets/pdfs/best-research-cell-efficiencies-190416 (2019).
2. Stranks, S. D. *et al.* Electron-hole diffusion lengths exceeding 1 micrometer in an organometal trihalide perovskite absorber. *Science* **342**, 341–344 (2013).
3. Miyata, A. *et al.* Direct measurement of the exciton binding energy and effective masses for charge carriers in an organic-inorganic tri-halide perovskite. *Nat. Phys.* **11**, 582–587 (2015).
4. Yamada, Y. *et al.* Photoelectronic responses in solution-processed perovskite $CH_3NH_3PbI_3$ solar cells studied by photoluminescence and photoabsorption spectroscopy. *IEEE J. Photovoltaics* **5**, 401–405 (2014).
5. Dong, Q. *et al.* Electron-hole diffusion lengths >175 μm in solution-grown $CH_3NH_3PbI_3$ single crystals. *Science* **347**, 967–970 (2015).
6. Wehrenfennig, C. *et al.* High charge carrier mobilities and lifetimes in organolead trihalide perovskites. *Adv. Mater.* **26**, 1584–1589 (2014).
7. Jeon, N. J. *et al.* Compositional engineering of perovskite materials for high-performance solar cells. *Nature* **517**, 476–480 (2015).
8. Eperon, G. E. *et al.* Perovskite-perovskite tandem photovoltaics with optimized band gaps. *Science* **354**, 861–865 (2016).
9. Saliba, M. *et al.* Cesium-containing triple cation perovskite solar cells: improved stability, reproducibility and high efficiency. *Energy Environ. Sci.* **9**, 1989–1997 (2016).
10. Burschka, J. *et al.* Sequential deposition as a route to high-performance perovskite-sensitized solar cells. *Nature* **499**, 316–319 (2013).
11. Herz, L. M. Charge-carrier mobilities in metal halide perovskites: fundamental mechanisms and limits. *ACS Energy Lett.* **2**, 1539–1548 (2017).
12. Ball, J. M. *et al.* Low-temperature processed meso-superstructured to thin-film perovskite solar cells. *Energy Environ. Sci.* **6**, 1739–1743 (2013).
13. Chiang, C. H. *et al.* The synergistic effect of H_2O and DMF towards stable and 20% efficiency inverted perovskite solar cells. *Energy Environ. Sci.* **10**, 808–817 (2017).
14. Wu, Y. *et al.* Thermally stable $MAPbI_3$ perovskite solar cells with efficiency of 19.19% and area over 1 cm^2 achieved by additive engineering. *Adv. Mater.* **29**, 1701073 (2017).

15. Zhu, W. *et al.* A facile, solvent vapor–fumigation-induced, self-repair recrystallization of $CH_3NH_3PbI_3$ films for high-performance perovskite solar cells. *Nanoscale* **5**, 5427–5434 (2015).
16. Chen, Q. *et al.* Planar heterojunction perovskite solar cells via vapor-assisted solution process. *J. Am. Chem. Soc.* **136**, 622–625 (2014).
17. Liu, M. *et al.* Efficient planar heterojunction perovskite solar cells by vapour deposition. *Nature* **501**, 395–398 (2013).
18. Cao, J. *et al.* Thiols as interfacial modifiers to enhance the performance and stability of perovskite solar cells. *Nanoscale* **7**, 9443–9447 (2015).
19. Hu, Q. *et al.* Efficient and low-temperature processed perovskite solar cells based on a cross-linkable hybrid interlayer. *J. Mater. Chem. A* **3**, 18483–18491 (2015).
20. Capasso, A. *et al.* Few-layer MoS_2 flakes as active buffer layer for stable perovskite solar cells. *Adv. Energy Mater.* **6**, 1600920 (2016).
21. Lee, J. *et al.* A protective layer approach to solvatochromic sensors. *Nat. Commun.* **4**, 2461 (2013).
22. Liao, H. C. *et al.* Enhanced efficiency of hot-cast large-area planar perovskite solar cells/modules having controlled chloride incorporation. *Adv. Energy Mater.* **7**, 1601660 (2017).
23. Zhou, H. *et al.* Interface engineering of highly efficient perovskite solar cells. *Science* **345**, 542 (2014).
24. Li, Y. *et al.* Multifunctional fullerene derivative for interface engineering in perovskite solar cells. *J. Am. Chem. Soc.* **137**, 15540–15547 (2015).
25. Zuo, L. *et al.* Enhanced photovoltaic performance of $CH_3NH_3PbI_3$ perovskite solar cells through interfacial engineering using self-assembling monolayer. *J. Am. Chem. Soc.* **137**, 2674–2679 (2015).
26. Chen, Q. *et al.* Controllable self-induced passivation of hybrid lead iodide perovskites toward high performance solar cells. *Nano Lett.* **14**, 4158–4163 (2014).
27. Yang, X. *et al.* High-performance TiO_2-based electron-selective contacts for crystalline silicon solar cells. *Adv. Mater.* **28**, 5891–5897 (2016).
28. Wang, Q. *et al.* Thin insulating tunneling contacts for efficient and water-resistant perovskite solar cells. *Adv. Mater.* **28**, 6734–6739 (2016).
29. Wang, F. *et al.* Highly stable perovskite solar cells with an all-carbon hole transport layer. *Nanoscale* **8**, 11882–11888 (2016).
30. Wang, F. *et al.* Highly efficient and stable perovskite solar cells by interfacial engineering using solution-processed polymer layer. *J. Phys. Chem. C* **121**, 1562–1568 (2017).

31. Yang, F. *et al.* Roles of polymer layer in enhanced photovoltaic performance of perovskite solar cells via interface engineering. *Adv. Mater. Interfaces* **5**, 1701256 (2018).
32. Guo, Q. *et al.* The growth of a $CH_3NH_3PbI_3$ thin film using simplified close space sublimation for efficient and large dimensional perovskite solar cells. *Energy Environ. Sci.* **9**, 1486–1494 (2016).
33. Shao, Y. *et al.* Origin and elimination of photocurrent hysteresis by fullerene passivation in $CH_3NH_3PbI_3$ planar heterojunction solar cells. *Nat. Commun.* **5**, 5784 (2014).
34. Correa Baena, J. P. *et al.* Highly efficient planar perovskite solar cells through band alignment engineering. *Energy Environ. Sci.* **8**, 2928–2934 (2015).
35. Cells, D. S. *et al.* Temperature dependence of transport properties of spiro-MeOTAD as a hole transport material in solid-state. *ACS Nano* **7**, 2292–2301 (2013).
36. Kim, W. *et al.* Hysteresis caused by water molecules in carbon nanotube field-effect transistors. *Nano Lett.* **3**, 193–198 (2003).
37. Li, Z. *et al.* Laminated carbon nanotube networks for metal electrode-free efficient perovskite solar cells. *ACS Nano* **8**, 6797–6804 (2014).
38. Ke, W. *et al.* Low-temperature solution-processed tin oxide as an alternative electron transporting layer for efficient perovskite solar cells. *J. Am. Chem. Soc.* **137**, 6730–6733 (2015).
39. Juarez-perez, E. J. *et al.* Role of the selective contacts in the performance of lead halide perovskite solar cells. *J. Phys. Chem. Lett.* **5**, 680–685 (2014).
40. Yun, J. H. *et al.* Synergistic enhancement and mechanism study of mechanical and moisture stability of perovskite solar cells introducing polyethylene-imine into the $CH_3NH_3PbI_3$/HTM interface. *J. Mater. Chem. A* **3**, 22176–22182 (2015).

Chapter 3. SnO_2 based flexible perovskite solar cells

3.1 Abstract

An unprecedented development of the photovoltaic (PV) performance of organic/inorganic perovskite solar cells (PSCs) within few years, the perovskite photovoltaics have been regarded as the most promising candidate for new generation solar-electric conversion devices. The low temperature of fabrication of perovskites promote they can apply in flexible PVs equipment, wearable electronics, portable system and bendable displays. But the main evaluation factor of bending durability of flexible PSCs (fPSCs) is still far behind the realistic application, especially the dissatisfied properties of metal oxide electron transport materials (ETM) for fPSCs. Here, the SnO_2 nanoparticle has been used for ETM for fPSCs (SnO_2-fPSCs), realizing excellent PV performance and bending durability. The 17.1% of power conversion efficiency (PCE) with a negligible hysteresis and a 17.0% stabilized power output (SPO) of SnO_2-fPSCs on 0.1 cm^2 active area. Moreover, this SnO_2-fPSCs can sustain an extremely high bending durability of 76.5% compared with its initial PCE even after 2000 bending cycles at a small of bending radius 4 mm, which comes from the excellent mechanic resistance of nanoparticle of SnO_2 film. The large active area of 1 cm^2 of SnO_2-fPSCs has also realized and achieved a 16.2% PCE and 15.9% SPO, respectively. Interesting finding of application of SnO_2 as ETM in fPSCs for high PV performance and mechanical properties pave a new way for PSCs industrial application.

Keywords: flexible perovskite solar cells, SnO_2, electron transport materials, bending durability, large active area

3.2 Introduction

Hybrid organic/inorganic perovskite solar cells (PSCs) have drawn a numerous attention because the power conversion efficiency (PCE) has rapidly developed up to 24.2% within a decade[1–5]. One of an interesting research topic of PSCs is the low temperature fabrication of flexible PSCs (fPSCs), which has been regarded as a promising candidate for the new photovoltaic (PV) devices in the wearable and lightweight PV assembles, portable system and bendable displays[6–23].

However, the PV performance of fPSCs still cannot compare with the conventional PSCs on rigid substrates of ITO or FTO. The fPSCs can be realized on the normal (n-i-p)[6,8,9,11,13–15,22–25] and inverted (p-i-n) structures[7,10,12,18,21,26]. The fPSCs has achieved remarkable development and the PCE increased up to 18.4% on the metal oxide electron transport materials (ETM) in the normal architecture[27], however, the bending durability of normal architecture fPSCs is still lower than that of the inverted structure devices[17,18], because the low mechanical resistance of metallic oxide ETM[14,27]. In order to achieve high mechanical resistance of fPSCs, the preparation process of inverted architecture always is complicated than that of normal structure and the active area is still extremely small, which will severely limit the industrial application[18]. Moreover, the large amount of organic materials introduced into the inverted architectures fPSCs, such as hydrophilic property of poly(3,4-ethylenedioxythiophene) polystyrene sulfonate (PEDOT:PPS), which seriously affect the stability of PV performance due to the hydrophily in the ambient condition.

The PV performance of normal architecture fPSCs has obtained substantial progress due to the new ETM exploration, and the stability also has been dramatically enhanced due to the metal oxide ETM application. Various materials have be applied as the ETMs in normal fPSCs, such as TiO_2[6,16,28,29], ZnO[24,30–33], $ZnSnO_2$[25], SnO_2[13,14,27] and fullerene derivatives[34,35], where the highest PCE reported to date is over 18.0%. Even though the PV performance has been enhanced after several years' endeavors on using metal oxide ETM, the notorious hysteresis still happens[14,24,27,28]. Moreover, the mechanical resistance of n-i-p fPSCs is still unsatisfied and much lower than that of p-i-n devices[6,14,21,27,28]. Therefore, it is necessary to explore new ETM or structure to enhance the bending durability of n-i-p fPSCs and promote it to realize industrial application. Moreover, the active area is an another important factor for application and enhance the competence of fPSCs.

Metal oxide material of SnO_2 has been widely applied in the PV devices as the ETM because of high conductivity and carrier mobility, such as dye-sensitized solar cells[36,37], glass substrate PSCs[4,38–43] and fPSCs[13,14,27,44–46]. The properties of high carrier mobility and perfect energy alignment with a deep conduction band for efficient electron extraction of SnO_2 has been demonstrated, resulting a high PV performance and negligible hysteresis in solar cells[4,38,42]. The low temperature fabrication of SnO_2 films promote it possibility for application in fPSCs as ETM[4,38,39,41,42]. However, the bending durability of SnO_2-fPSCs still locates at an unsatisfied state and much lower than that of the p-i-n structure devices and small active area[27,44,45], which seriously limits the commercial utilization.

Here, I successfully realized an application of SnO_2 as the ETM in normal architecture fPSCs (SnO_2-fPSCs) with a perovskite light harvester layer of $Cs_{0.05}(MA_{0.17}FA_{0.83})_{0.95}Pb(I_{0.83}Br_{0.17})_3$. A high PCE of 17.0% and a stabilized power output (SPO) of 17.0% have been achieved with a negligible hysteresis on small active area of 0.1 cm^2 SnO_2-fPSCs. The SnO_2-fPSCs can maintain a high bending durability of ca. 76.5% compared with the initial efficiency even after 2000 bending cycles testing at a small bending radius of 4 mm. A high PV performance of 16.2% PCE and 15.9% SPO have been obtained on the large active area of 1 cm^2. The outstanding PV performance and mechanical resistance of SnO_2-fPSCs promote the future commercial application of fPSCs.

3.3 Experimental section

Materials: All chemicals were used as received, without further purification. Tin oxide substrate (ITO, 10 Ω) and flexible PEN/ITO (10 Ω) were obtained from GEOMATEC and Oike & Co., Ltd. SnO_2 nanoparticles (15 wt%) with a particle size of 10–15 nm in H_2O colloidal dispersion were acquired from Alfa Aesar. Lead (II) iodide (PbI_2, 99.99%), lead (II) bromide ($PbBr_2$, 99%), methylammonium bromide (MABr, > 98.0%) formamidinium iodide (FAI, > 98.0%), cesium iodide (CsI, 99.9%) and titanium diisopropoxide bis(acetylacetonate) (TiAcac) were purchased from Tokyo Chemical Industry Co., Ltd. Benzyl alcohol (99.8%) and $TiCl_4$ (99.0%) were acquired from Sigma-Aldrich Co., Ltd. The solvent chemicals *N*,*N*-dimethylformamide (DMF), dimethyl sulfoxide (DMSO), and chlorobenzene were dried before use. 2,2′,7,7′-Tetrakis(*N*,*N*-di-*p*-methoxyphenylamino)-9,9′-spirobifluorene (spiro-OMeTAD) was purchased from Merck Co., Ltd. Lithium bis(trifluoromethanesulfonyl)imide (Li-TFSI) salt powder, dehydrated ethanol, acetone, 2-propanol, other solvents were purchased from Wako

Chemical Co., Ltd. and used as received without no special treatment unless otherwise noted.

ITO substrate preparation: The glass/ITO and PEN/ITO substrate are etched using zinc powder and 6 M HCl solution. The etched ITO glass substrates are washed in concentration of about 1 wt% aqueous detergent solution, acetone, IPA and distilled water with a sonication each step for 10 min, respectively. The cleaned ITO glass substrates are dried by an air gun and cut into 25×25 mm^2 size. As for the PEN/ITO substrates are washed by distilled water after etching and dried by bibulous papers to remove the residual water on surface. The all substrates are stored in a dry box for following experiment.

SnO_2 ETM deposition: The SnO_2 nanoparticle is directly spin coated on the glass ITO substrate at program of 3000 rpm for 30 s and post-treated at temperature of 150 °C for 30 min in ambient condition with a concentration of 5 wt%. As for the PEN/ITO/SnO_2 substrates, the same deposition process of SnO_2 has been employed after pasting the flexible substrate on glass substrate. As for the TiO_2 sample, the TiO_2 crystal is fabricated using the non-hydrolytic sol-gel approach as according to previous reported[47]. The TiO_2 crystals are deposited on glass ITO substrate using the same process as that of SnO_2 and then post-treated at 150 °C for 30 min.

Fabrication of PSCs: The perovskite precursor solution consists of excess PbI_2[48,49] with component of FAI (1 M), PbI_2 (1.1 M), MABr (0.2 M) and $PbBr_2$ (0.2 M) in anhydrous DMF:DMSO 4:1 (v:v), a pre-dissolved 1.5 M solution of CsI in DMSO is mixed into the precursor solution. The mixed precursor solution dissolves at 40 °C for 40 min to guarantee all chemicals fully dissolving.

The prepared perovskite precursor solution is spin coated on ITO/SnO_2 and TiO_2 glass substrates at 1000 and 6000 rpm for 10 and 20 s of two steps, respectively, after treating the substrates with Ozone killer to enhance the affinity between the perovskite and substrates. The anti-solvent of toluene with 400 μL is quickly splashed within 2 s at 6 s before finishing the spin coating program. The sample's color quickly changes from transparency to the light brown after splashing the toluene. Then, the sample is directly transferred to the hotplate for post-treatment at 150 °C and 10 min to realize high quality perovskite light harvester with a large crystal size. The spin coating and post-treatment processes of flexible PEN/ITO are same as the glass substrate. The HTL solution is prepared with 0.06 mmol spiro-OMeTAD, 0.009 mmol Co(4-*tert*-butylpyridyl-2-1*H*-pyrazole)3·3TFSI, 0.03 mmol Li-TFSI and 0.1 mmol tBP in 1 mL chlorobenzene. The fully dissolved HTL solution is spin coated at 4000 rpm for 30 s and post-treated at 70 °C for 30 min. Finally, the ca. 80 nm of Au electrode film is thermal deposited on vacuum condition.

Characterizations: All evaluations of perovskite light harvester layers and PSCs are finished at ambient condition. The perovskite light harvester layer with about 500 nm thickness is used to the photoluminescence (PL) and absorption measurements at an excitation wavelength of 532 nm (a power of 75 μW) and UV/Vis spectrophotometer (Shimadzu, UV-1800) apparatuses. The time resolved PL of perovskite photoactive layer is recorded by a single-photon counting setup with a 516 nm wavelength and 6.9 ns width pulsed laser using 2.7 nW power.

Photovoltaic performance of PSCs is conducted at a solar simulator (San-Ei Electric, XES-40S1) under AM 1.5 conditions (100 mW/cm^2) with a calibration cells (Bunkoukeiki, BS-500BK). The current density–voltage (*J*–*V*) curves are measured using a source meter (Keithley, 2400) and a 0.1 cm^2 metal mask at ambient condition. *J*–*V* curves of PSCs are recorded from forward (−0.1 to 1.2 V) and reverse (1.2 to −0.1 V) scanning directions without any preconditioning (light soaking or the application of a forward bias voltage for a prolonged period before starting the measurement) at a 50 mV/s voltage sweep rate. The stabilized power output (SPO) is evaluated under maximum power point (MPP) tracking with a bias voltage from the *J*–*V* scanning. The external quantum efficiency (EQE) is analyzed at a monochromatic Xe arc light system (Bunkoukeiki, SMO-250III) by measuring incident-to-power conversion efficiency. Atomic force microscopy (AFM) (SII, Nanocute) and SEM (JEOL, JEM-6500F) are applied to characterize the surface roughness, surface and cross-sectional morphology of perovskite light harvester layer and PSCs, respectively. An electrochemical analyzer (ALS/HCH, 660 EAW) is used to record the impedance spectroscopy of PSCs with a 5 mV AC amplitude and frequency ranging from 100 kHz to 0.1 Hz. The continuous light soaking stability of PSCs is conducted at the heat and weather resistibility test system (Bunkoukeihi, BIR-50P1). The bending durability testing is conducted by a home-made system with various bending radius.

3.4 Results and discussion

3.4.1 Films characterization

Morphology of ITO, ITO/SnO_2, and ITO/TiO_2 substrates

Figure 1 show the surface morphology of SnO_2 and TiO_2 electron transport materials (ETM) on the ITO substrates using SEM[50]. The SnO_2 and TiO_2 nanoparticles uniformly and fully cover on the ITO substrates, as shown in Figures 1a-c. Interesting, the SnO_2 forms more compact film on the ITO substrate compared with the TiO_2. The surface roughness of SnO_2 and TiO_2 is characterized by AFM, as shown in **Figure 2**. The SnO_2 film can achieve more flat surface with a surface roughness of 19.0 nm compared with that of TiO_2 sample (19.8 nm).

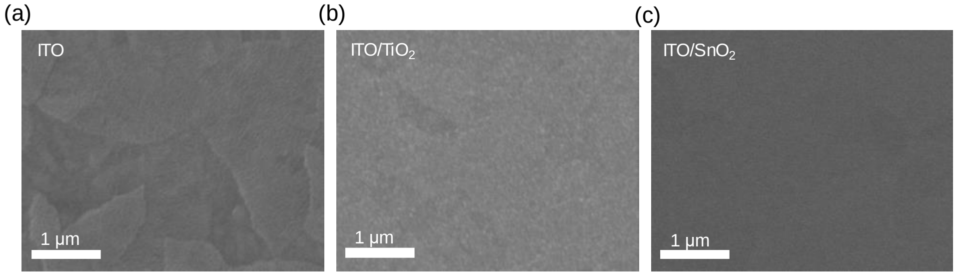

Figure 1. Surface morphology characterization of (a) ITO substrate, (b) ITO/ SnO_2, (c) ITO/TiO_2 using SEM, respectively. Reprinted with permission from ref. 50.

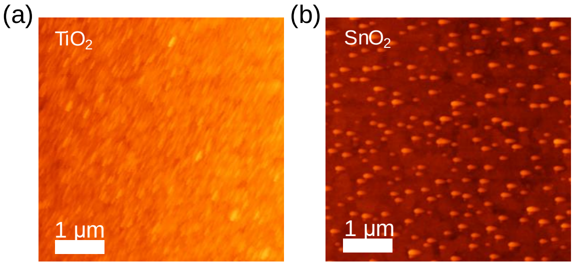

Figure 2. Surface roughness characterization of (a) ITO/TiO_2 and (b) ITO/ SnO_2 using AFM, respectively.

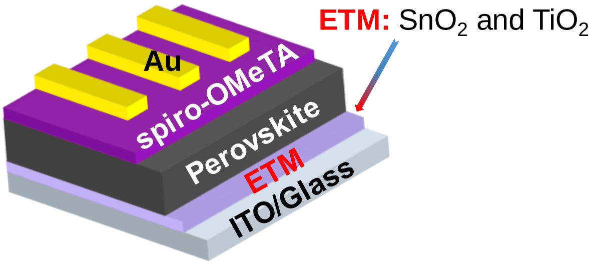

Figure 3. Planar architecture of PSCs using electron transport materials (ETM) of SnO_2 or TiO_2.

Schematic architecture of planar PSCs

Figure 3 shows the schematic architecture of planar PSCs. The PSCs consist of the glass/ITO substrate, ETM (SnO_2 and TiO_2), perovskite light harvester layer of $Cs_{0.05}(MA_{0.17}FA_{0.83})_{0.95}Pb(I_{0.83}Br_{0.17})_3$, HTL of spiro-OMeTAD and the Au electrode, respectively.

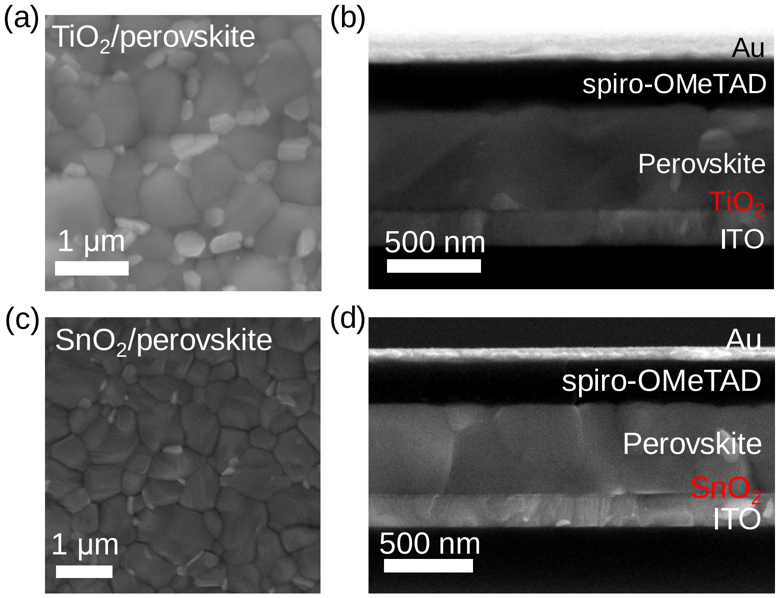

Figure 4. Surface and cross-sectional morphology characterization of perovskite and PSCs. (a, b) SEM images of TiO_2 based perovskite and PSCs. (c, d) SEM images of SnO_2 based perovskite and PSCs. The scale bar is 1 μm and 500 nm, respectively.

Morphology of perovskite on rigid substrates

Figure 4 shows the surface and cross-section morphology of perovskite light harvester

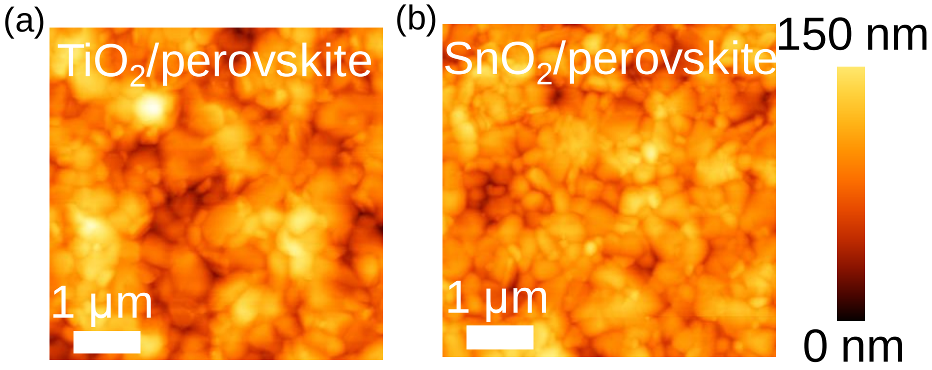

Figure 5. Surface roughness characterization of perovskite on the TiO_2 (a) and SnO_2 (b) ETM substrate. The scale bar is 1 μm.

layer and PSCs on TiO_2 and SnO_2 films surface, respectively. A dense and compact of perovskite light harvester layer fully covers on the TiO_2 and SnO_2 surface without any voids or cracks, as shown in Figures 4a and c. The perovskite light harvester crystals achieve an average grain size of ca. 700 nm and largest one exceeds 1 μm on SnO_2, which is substantially larger than those of TiO_2 based sample and previous reported values of Cs-perovskite[43,48,51]. Indicating that a high PV performance of PSCs will be achieved on the SnO_2 based devices with a high open-circuit voltage (V_{OC}) and hysteresis free, because the reduction of grain boundaries of large grain size of perovskite light harvester layer can decrease the trap-states and carrier recombination loss[18]. Figures 4b and d show the cross-sectional images of PSCs with various ETMs. A configuration of PSCs with various thickness of SnO_2, perovskite, HTL and Au is about 25, 500, 250 and 80 nm, respectively, and the thickness of TiO_2 is approximately 30 nm. The surface roughness of perovskite is evaluated using AFM and the results summarized in **Figure 5** and **Table 1**, respectively. The SnO_2 based perovskite light harvester sample shows a smaller surface roughness of about 62 nm comparing with that of 78 nm of perovskite on TiO_2.

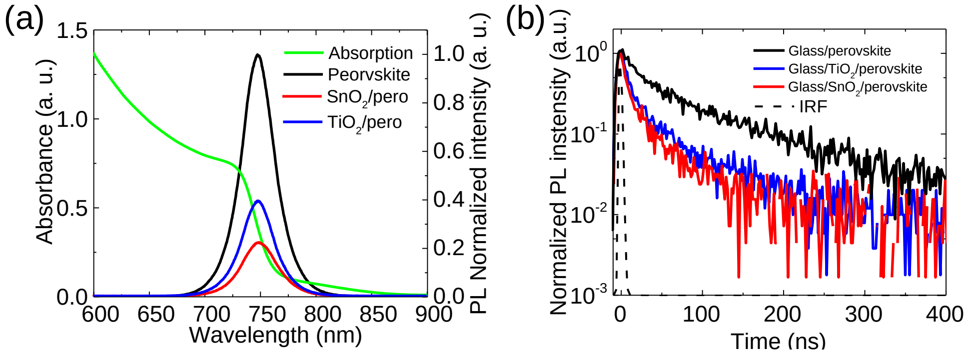

Figure 6. Optical properties of perovskite on glass, TiO_2 and SnO_2 substrates. (a) Absorption and PL spectra, (b) TRPL decay of perovskite on glass, TiO_2 and SnO_2 substrates. The instrumental response function (IRF) is also shown.

Table 2. Summary of TRPL decay of perovskite, TiO_2/perovskite and SnO_2/perovskite. Parameters a, τ_1, τ_2, τ_{PL} are amplitude ratio, decay constants of fast and slow components and the averaged PL decays.

Sample	a	τ_1 (ns)	τ_2 (ns)	τ_{PL} (ns)
Perovskite	0.49 ± 0.04	23.3 ± 2.2	103.3 ± 4.4	63.8 ± 0.3
SnO_2/perovskite	0.79 ± 0.01	6.9 ± 0.6	41.7 ± 4.4	13.7 ± 1.4
TiO_2/perovskite	0.79 ± 0.01	12.7 ± 0.4	60.7 ± 2.9	22.6 ± 0.5

Optical properties of perovskite light harvester layer

Figure 6 show the absorption, PL and time-resolved PL (TRPL) characterizations of perovskite light harvester layers on the glass, TiO_2 and SnO_2 surface, respectively. Figure 6a exhibits the absorption spectrum of perovskite light harvester layer on glass substrate with a 725 nm absorption peak, which causes about 10 nm blue-shifted compared with that of the previous obserations[43,48]. The PL spectra shows a peak at 750 nm, which also happen 10 nm blue-shifted compared with that of previous observations[43,48], indicating that a more higher V_{OC} of PSCs will be obtained due to the increased bandgap of blue-shifted absorption and PL spectra. Moreover, the PL intensities remarkably decrease after replacing the glass substrate by SnO_2 and TiO_2, indicating that the charge carrier of electron have been efficiently extracted by ETM. The dramatically decrease of PL intensities of SnO_2 compared with those of TiO_2, indicating that a much better electron extraction efficiency because of the deeper conduction band and higher carrier mobility of SnO_2[36,38]. The TRPL spectroscopy has been used to study the photoexcited carrier dynamics. TRPL decay profiles of perovskites, SnO_2/perovskite and TiO_2/perovskite, have been shown in Figure 6b. The SnO_2/perovskite exhibits the most shorter decay compared with that of two other samples. The TRPL profiles are re-drawn using the fitted curves of double-exponential functions as solid lines. The analyzed TRPL decay time has been summarized in **Table 2**. The lifetime of perovskite light harvester layer remarkably decreases from about 63.8 ns to 22.6 and 13.7 ns from glass to TiO_2 and SnO_2 substrates, respectively, which are well consistent with the results of PL intensity. The carrier extraction efficiency of SnO_2 is much higher than that of TiO_2, because of the shallower conduction band, lower carrier mobility of TiO_2 and interface trap states between the perovskite and TiO_2[38,52,53].

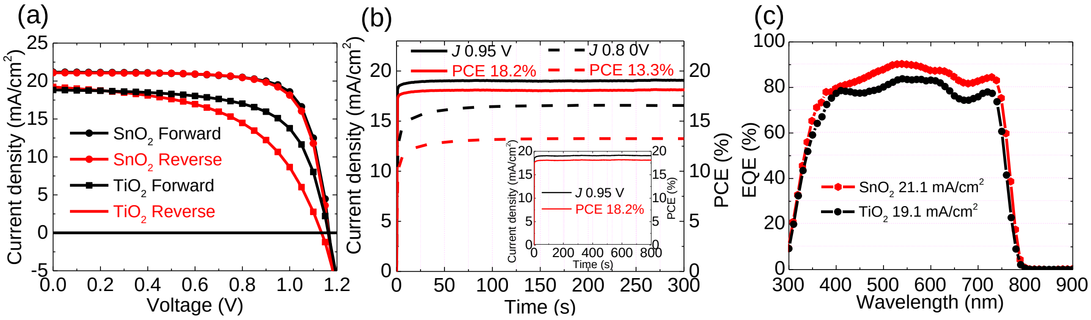

Figure 7. Photovoltaic performance of PSCs on TiO_2 and SnO_2 ETM. (a) *J*–*V* curves, (b) Time evolution of SPO under MPP extracted from forward scanning, (c) EQE and integrated current-density of TiO_2- and SnO_2-PSCs.

3.4.2 *J–V* characterization of perovskite solar cells on rigid substrates

Figure 7a shows the *J–V* curves of PSCs based on TiO_2 and SnO_2 ETM. The SnO_2-PSCs exhibit a high PCE of 18.6 (18.3)% with a high V_{OC} of 1.17 (1.17) V, a short-circuit current density (Jsc) of 21.2 (21.1) mA/cm^2, and a fill factor (FF) of 75.2 (74.4)%, which are much higher than those of TiO_2-PSCs with a PCE of 11.6 (14.4)%, a V_{OC} of 1.13 (1.16) V, a Jsc of 19.2 (18.8) mA/cm^2, and a FF of 53.1 (65.6)% measured at forward (reverse) voltage scanning. Noted that the hysteresis of *J–V* curves of SnO_2-PSCs is very small compared with that of the TiO_2-PSCs. The excellent photovoltaic performance of SnO_2-PSCs attributes to the high quality of perovskite light harvester layer, superior optical properties and high efficiency of carrier extraction compared with those of TiO_2-PSCs.

The stabilized power output (SPO) of PSCs has also been measured to evaluate the reliability of PCE extracted from *J–V* curves. Figure 7b shows the SPO of SnO_2-and TiO_2-PSCs under forward scanning maximum power point (MPP) with a bias voltage of 0.95 and 0.80 V, respectively. A 18.2% SPO of SnO_2-PSCs has achieved and much higher than that of the TiO_2-PSCs value of 13.3%. The achieved SPO of SnO_2- and TiO_2-PSCs are well consistent with the results from *J–V* curves and SnO_2-PSCs exhibits a very high stability without any reduction even after 800 s continuous measurements.

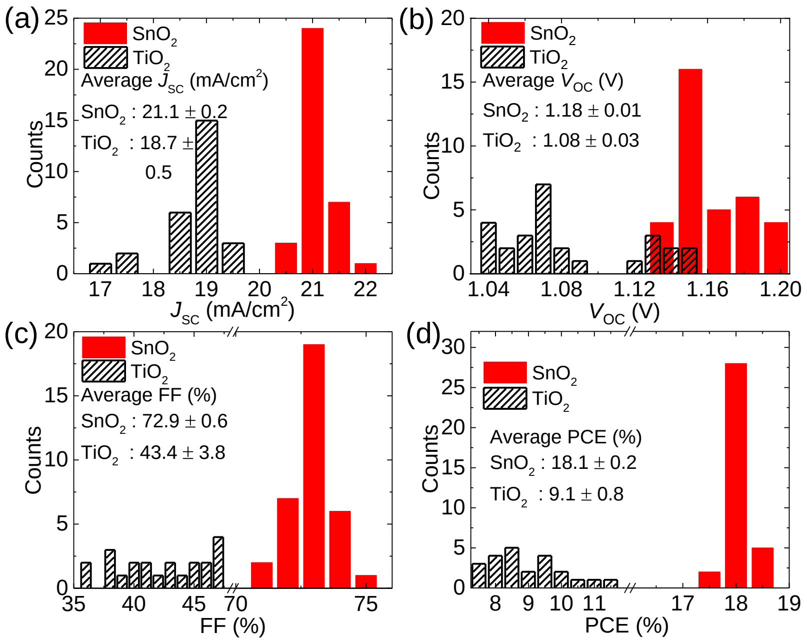

Figure 8. Repeatability properties of PSCs on TiO_2 and SnO_2 ETM. (a-d) Statistical calculation of repeatability of TiO_2- and SnO_2-PSCs, including J_{SC}, V_{OC}, FF and PCE. (red: 35 SnO_2-PSCs; black: 26 TiO_2-PSCs).

The external quantum efficiency (EQE) of PSCs has been determined by a typical incident-photon to current-efficiency (IPCE), as shown in Figure 7c. The SnO_2- and TiO_2-PSCs show a similar response range from 300 to 800 nm, however, the SnO_2-PSC exhibits a much higher maximum value of EQE of 90.5% compared with that of TiO_2-PSCs (84.2%). Moreover, the SnO_2-PSC obtains a higher integrated current-density of 21.1 mA/cm^2 compared with that of TiO_2-PSCs with 19.1 mA/cm^2, which are all well consistent with the results of *J–V* curves.

A large number of devices (35 SnO_2- and 26 TiO_2-PSCs) have been fabricated to evaluate the repeatability of devices' performance. **Figure 8** shows the statistical calculation of SnO_2- and TiO_2-PSCs, including the parameters of J_{SC}, V_{OC}, FF and PCE. The SnO_2-PSCs achieves an average value of ca. 18.1% PCE with a distribution from 17.5 to 18.6% on the forward scanning, which are much higher than those of TiO_2-PSCs with an average of approximately 9.1% PCE and a range from 7.4 to 11.6%, as shown in Figure 8a. All other parameters of J_{SC}, V_{OC}, FF of SnO_2-PSCs are exceeding over than those of TiO_2-PSCs, as shown in Figures 8b-d.

The excellent results of PCE, stability and repeatability of PV performance of SnO_2-

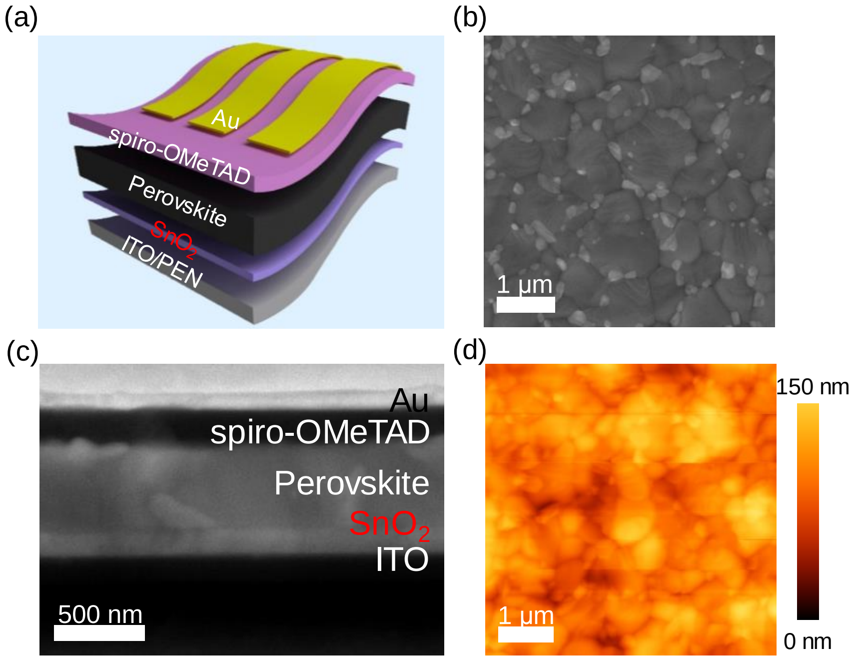

Figure 9. (a) Schematic of SnO_2-fPSCs. (b, c) Surface and cross-sectional SEM images of the perovskite layer on a flexible PEN/ITO substrate and SnO_2-fPSCs. (d) AFM image of the perovskite layer on flexible PEN/ITO/SnO_2 substrate. The scale bar is 1 μm and 500 nm, respectively.

PSCs and low temperature deposition indicate that the SnO_2 has a great potential application in flexible PSCs with high efficiency as an electron transport layer (ETL).

3.4.3 Perovskite light harvester layer characterization on flexible substrate

Surface morphology evaluation

Figure 9a shows the schematic configuration of flexible PSCs (fPSCs), consisting of PEN/ITO, SnO_2, perovskite, HTL and Au electrode. The SnO_2 nanoparticle has been directly deposited on the flexible ITO surface using same spin coating program and post-treated at 150 °C for 30 min in room condition. Figure 9b presents the surface morphology of perovskite light harvester layer on the flexible substrate using SEM. The perovskite exhibits a similar morphology of crystal size to that on the rigid substrate. Noted that some and obvious white plates appears on the perovskite surface because of the excessive PbI_2 in perovskite precursor composition, which is similar to that on the rigid substrate and previous study[37,48,49]. The cross-sectional characterization of flexible PSCs has been shown in Figure 9c. The thickness of each layer on the flexible substrate is similar to that on the rigid substrate. AFM has been conducted to record the surface roughness of perovskite light harvester layer on flexible substrate. An average roughness of 71 nm of perovskite layer on the flexible substrate is similar to those on the rigid substrate, as shown in Table 1.

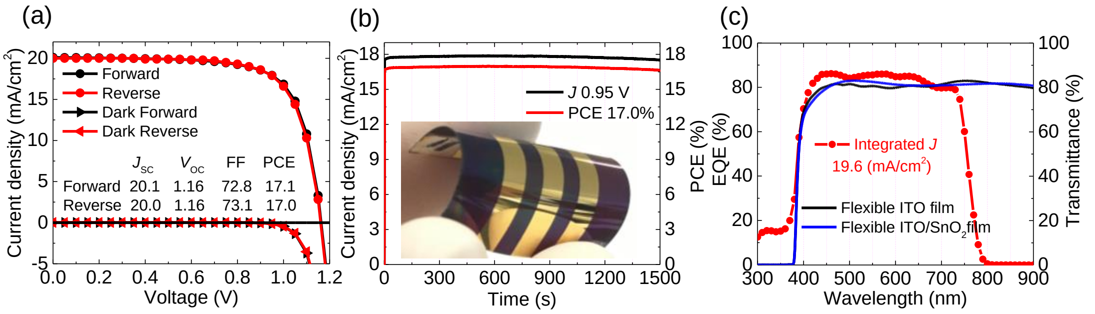

Figure 10. Photovoltaic performance of fPSCs on SnO_2 ETM. (a) *J–V* curves, (b) Time evolution of SPO under MPP extracted from forward scanning. The photograph of fPSCs is also shown. (c) EQE and integrated current-density of SnO_2-fPSCs.

3.4.4 *J–V* characterization of perovskite solar cells on flexible substrates

Figure 10 shows the *J–V* curves of best performance fPSCs using SnO_2 (SnO_2-fPSCs) as the ETL. The SnO_2-fPSCs achieved a high PCE of 17.0 (17.1)% with a V_{OC} of 1.16 (1.16) V, a *J*sc of 20.1 (20.0) mA/cm^2, and a FF of 72.8 (73.1)% measured at forward (reverse) voltage scanning with a negligible hysteresis, as shown in Figure 10a. The excellent PCE of 17.1% under reverse scanning condition of the SnO_2-fPSCs is higher than those of fPSCs in a normal structure[6,16,17,19,24,25,27–34] and some inverted architecture devices[7,18,54–56]. A high SPO of 17.0% has been obtained and maintained a superior stability even after 1500 s continuous light soaking characterization, as shown in Figure 10b. The high value of SPO is well agreement with the PCE result extracted from the *J*–*V* curves and significant higher than previous reported[6,7,16–19,24,25,27,28,29–34,43,52–54]. Figure 10c also shows the transmittance spectra of the flexible PEN/ITO and flexible PEN/ITO/SnO_2 films. The transmittance spectrum of the PEN/ITO/SnO_2 film shows almost same value of the flexible PEN/ITO film, indicating that the SnO_2 film has no affect the transmittance of substrate above 400 nm. The EQE of SnO_2-fPSCs has been analyzed from IPCE spectroscopy, as shown in the Figure 10d. The EQE spectrum shows a response range from 300 to 800 nm in SnO_2-fPSCs, which is well agreement with that on the rigid substrate results of SnO_2-PSCs. The SnO_2-fPSCs obtains a maximum EQE value of about 87.0% with an integrated current-density of 19.6 mA/cm^2, which is also well consistent with the *J*–*V* curves' value.

A large amount of SnO_2-fPSCs (28 devices) have been fabricated to confirm the

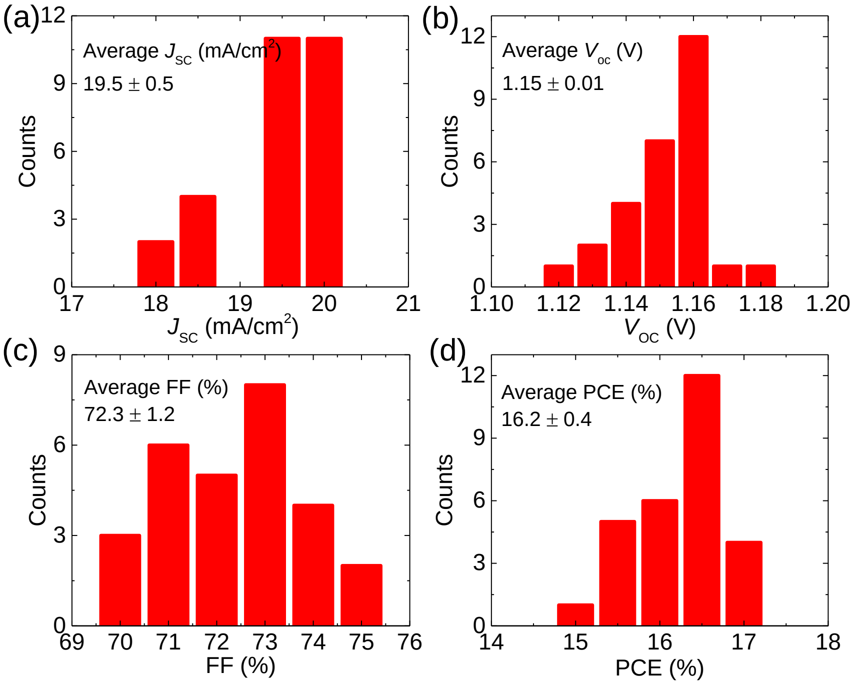

Figure 11. Repeatability property of fPSCs on SnO_2 ETM. (a-d) Statistical calculation of photovoltaic parameters of SnO_2-fPSCs, including J_{SC}, V_{OC}, FF and PCE. (28 SnO_2-fPSCs).

repeatability of flexible devices. **Figure 11** shows the all statistical calculation results of SnO_2-fPSCs with parameters of J_{SC}, V_{OC}, FF and PCE. The SnO_2-fPSCs shows a high average value of about 16.2% PCE with a narrow distribution from 15.0 to 17.0%, in Figure 11d. These high values of SnO_2-fPSCs are much higher than previous reported TiO_2, ZnO_2 and $ZnSnO_4$ based flexible PSCs with a normal architecture[6,24,29,32]. The J_{SC}, V_{OC} and FF of SnO_2-fPSCs also exhibit a narrow distribution.

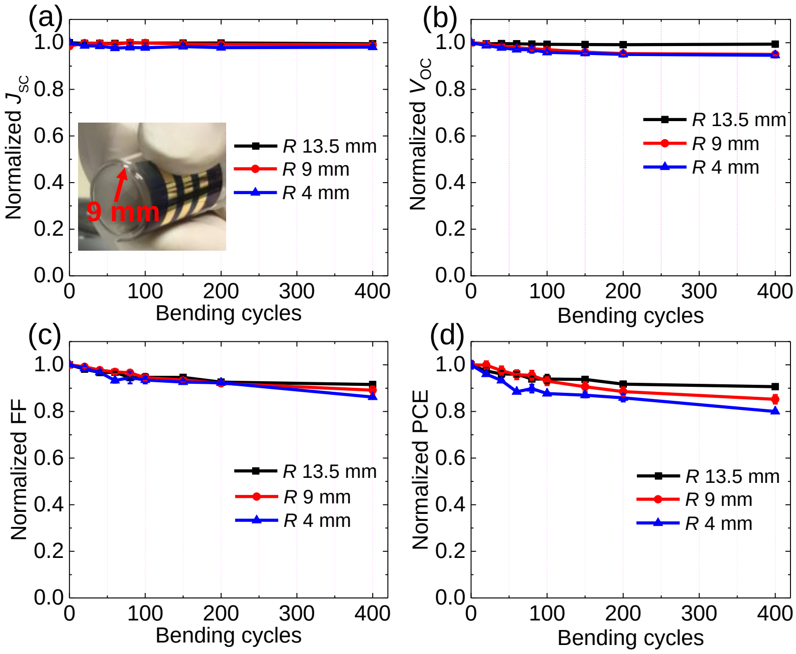

Figure 12. Bending durability testing of SnO_2-fPSCs at various bending radius of 13.5, 9 and 4 mm. (a-d) Normalized J_{SC}, V_{OC}, FF and PCE of SnO_2-fPSCs after 400 bending cycles testing. The photograph of SnO_2-fPSCs is also shown in (a).

3.4.5 Bending durability characterization of flexible perovskite solar cells

Mechanical bending resistance is one of the most critical evaluation index for specific utilizations of fPSCs such as a wearable and portable electronic equipment, therefore the bending stability is a main factor of performance in the fPSCs. **Figure 12** shows the analyzed results of bending durability characterization of the SnO_2-fPSCs. Various bending radii (R) of 13.5 mm ($R_{13.5}$), 9 mm ($R_{9.0}$) and 4 mm ($R_{4.0}$) has been used to evaluate the bending durability of SnO_2-fPSCs with normalized PCE, as shown in Figure 12a. As the extension of bending cycles, the PV performance of SnO_2-fPSCs decrease and the reduction degree of the PV performance increase as the bending radius becomes small. However, the SnO_2-fPSCs can sustain over 80.0% of its initial PCE value even after 400 bending cycles at the smallest bending radius of 4 mm. The other parameters of normalized J_{SC}, V_{OC} and FF keep a very high stability of 98.1, 94.6 and 86.2%, respectively, as shown in Figures 12b-d.

The harsh bending testing has been introduced into evaluate the bending durability at a small bending radii of $R_{9.0}$ and $R_{4.0}$, as shown in **Figure 13**. The SnO_2-fPSCs can maintain an excellent bending durability of ca. 80% normalized PCE and keep almost constant from 1000 to 2000 bending cycles at bending radii of $R_{9.0}$ and $R_{4.0}$ according to the Figure 13a. Figure 13 shows the SnO_2-fPSCs can sustain high values of normalized PV performance of ca. 76.5, ca. 97.8, ca. 94.1 and ca. 83.2% of the initial PCE, J_{SC}, V_{OC} and FF, especially in the bending radius of $R_{4.0}$. The superior bending durability of SnO_2-fPSCs can be compared with that of poly(bis(4-phenyl)(2,4,6-trimethylphenyl)amine) (PTAA) HTL based flexible devices[20], and much higher than those of normal structure PSCs using inorganic ETM and inverted architecture PSCs using graphene electrode[6,20,21,27－32,34,52,54], especially higher than SnO_2-fPSCs fabrication by other methods[27,44,45].

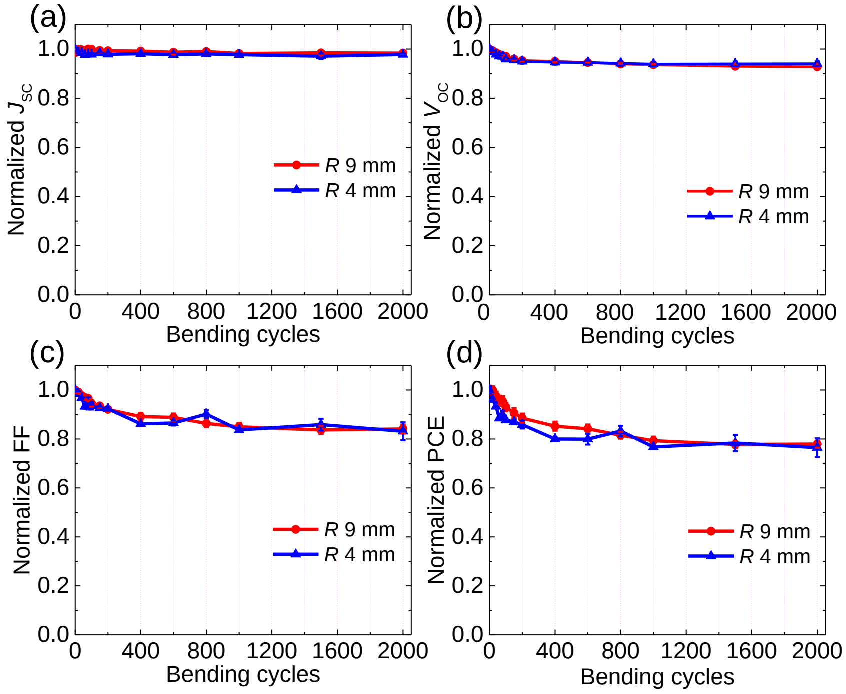

Figure 13. Bending durability testing of SnO_2-fPSCs at various bending radius of 9 and 4 mm. (a-d) Normalized J_{SC}, V_{OC}, FF and PCE of SnO_2-fPSCs after 2000 bending cycles testing.

The PV performance of SnO$_2$-fPSCs slowly reduces as the bending testing extends. Therefore, the *J–V* curves of SnO$_2$-fPSCs with bending testing of 2000 cycles at bending radius of $R_{9.0}$ has been summarized in **Figure 14a**. The seriously reductions of FF and V_{OC} are main reasons for the photovoltaic performance deterioration of SnO$_2$-fPSCs. The detailed parameters are summarized at **Table 3**.

The series resistance (R_s) has been summarized from *J–V* curves with bending cycles and plotted in Figure 14b. The R_s of SnO$_2$-fPSCs slowly increases as bending cycles and reaches to a relative stable value after 1000 bending cycles. The R_s value dose not increase obviously as bending cycles increase, which evidences the reason of the moderate reduction in the PV performance on high bending cycles until to 2000.

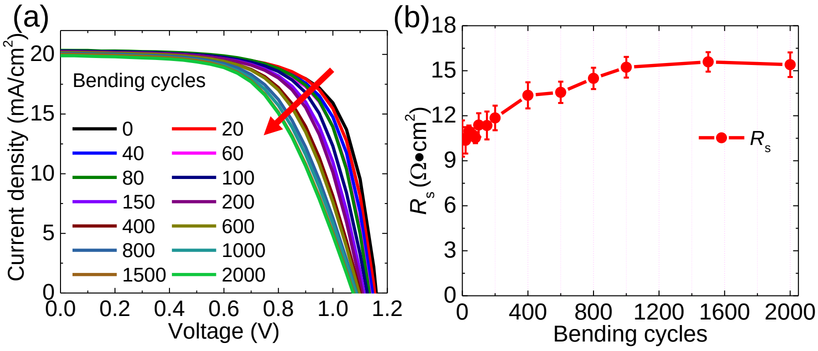

Figure 14. (a, b) *J–V* curves and R_s of SnO$_2$-fPSCs under various bending cycles at bending radius of 9 mm.

Table 3. Summary of the photovoltaic performance of SnO$_2$-fPSCs during 2000 bending cycles testing.

Bending cycles	J_{SC} (mA/cm^2)	V_{OC} (V)	FF (%)	PCE (%)	R_S (Ω*cm^2)
0	19.8 ± 0.1	1.15 ± 0.00	69.8 ± 0.7	15.9 ± 0.3	10.5 ± 1.2
20	20.0 ± 0.2	1.15 ± 0.01	69.2 ± 0.0	15.9 ± 0.3	10.4 ± 0.9
40	20.0 ± 0.1	1.14 ± 0.01	68.2 ± 0.5	15.5 ± 0.3	10.9 ± 0.4
60	19.9 ± 0.1	1.13 ± 0.01	67.7 ± 0. 6	15.2 ± 0.3	10.8 ± 0.4
80	20.1 ± 0.1	1.12 ± 0.01	67.4 ± 0.7	15.2 ± 0.3	10.5± 0.4
100	20.1 ± 0.1	1.12 ± 0.00	65.9 ± 1.0	14.8 ± 0.3	11.4 ± 0.8
150	20.0 ± 0.1	1.11 ± 0.01	65.2 ± 0.7	14.4 ± 0.3	11.4 ± 0.9
200	19.9 ± 0.2	1.10 ± 0.01	64.2 ± 0.7	14.1 ± 0.3	11.9 ± 0.8
400	19.9 ± 0.1	1.10 ± 0.00	62.2 ± 1.1	13.6 ± 0.3	13.4 ± 0.9
600	19.8± 0.2	1.09 ± 0.00	62.0 ± 1.1	13.4 ± 0.3	13.6 ± 0.7
800	19.9 ± 0.1	1.08 ± 0.00	60.2 ± 1.0	13.0 ± 0.2	14.5 ± 0.7
1000	19.7 ± 0.2	1.08 ± 0.01	59.3 ± 1.1	12.6 ± 0.3	15.2 ± 0.7
1500	19.8 ± 0.2	1.07 ± 0.00	58.4 ± 1.1	12.4 ± 0.2	15.6 ± 0.7
2000	19.7 ± 0.1	1.07 ± 0.00	58.7 ± 1.3	12.4 ± 0.2	15.4 ± 0.8

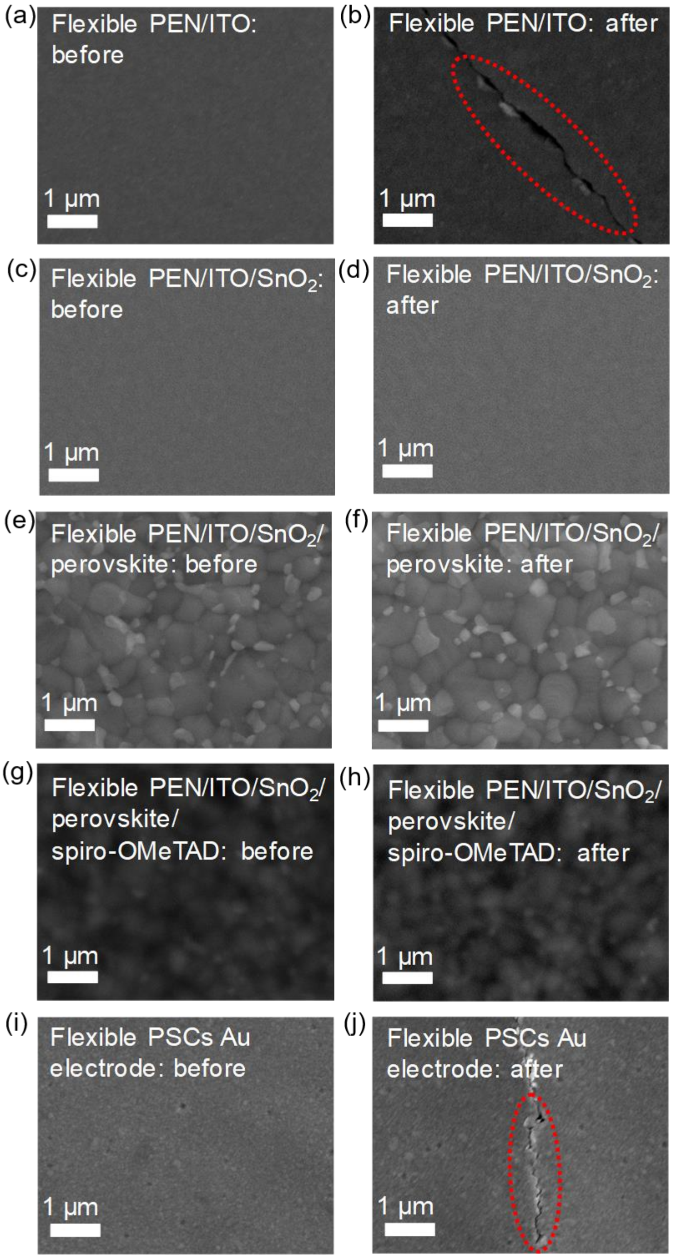

Figure 15. Surface morphology characterization of SnO_2-fPSCs before and after bending testing at 400 bending cycles. (a, c, e, g, i) and (b, d, f, h, j) SEM images of flexible PEN/ITO, flexible PEN/ITO/SnO_2, flexible PEN/ITO/SnO_2/perovskite, flexible PEN/ITO/SnO_2/perovskite/spiro-OMeTAD and flexible PEN/ITO/SnO_2/perovskite/spiro-OMeTAD/Au before and after bending testing, respectively. The scale bar is 1 μm.

3.4.6 Analysis of photovoltaic performance reduction of SnO_2 flexible perovskite

solar cells

The surface morphology of each component of SnO_2-fPSCs has been characterized to study the physical reason of degradation of PV performance as bending testing extension. **Figure 15** shows the surface morphology characterization of SnO_2-fPSCs using SEM at bending radius of $R_{9.0}$ after 400 bending cycles, including flexible PEN/ITO, flexible PEN/ITO/SnO_2, flexible PEN/ITO/SnO_2/perovskite, flexible PEN/ITO/SnO_2/perovskite/spiro-OMeTAD and flexible PEN/ITO/SnO_2/perovskite/spiro-OMeTAD/gold (Au). The component of SnO_2, perovskite and spiro-OMeTAD layer surface morphologies have no observable variations compared with their morphologies using SEM images before the bending testing. Interesting, the flexible PEN/ITO and Au electrode films surface appear some penetrating cracks compared with those of before bending testing, because of the brittles of ITO and Au, which are well consistent with the previously results[6,10,18,32].

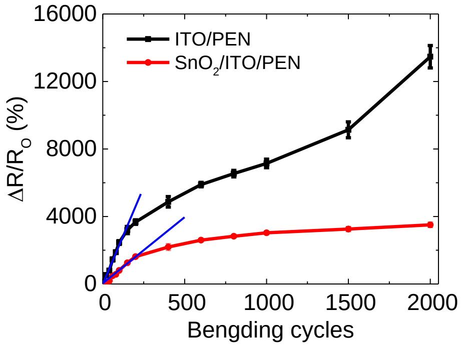

Figure 16. Relative resistance variation ($\Delta R/R_0$) of the ITO/PEN and ITO/PEN/SnO_2 films as the function of bending cycles at bending radius of 9.0 mm.

The augment of R_s comes from the deteriorated properties of the ITO and Au electrodes, which induces the PV performance reduction of SnO_2-fPSCs. Interesting, the surface morphology of SnO_2 film does not show any changes after harsh bending testing, in which the bending stress could be released between the nanoparticle grain boundaries because SnO_2 thin film consists with nanoparticles. These results indicate that the SnO_2 film can still sustain an excellent property of carrier extraction efficiency and transportation ability. The relative resistance of flexible ITO/PEN and SnO_2/ITO/PEN films has been measured using four points probe to confirm the resistance variations. **Figure 16** shows the relative resistance increment rate of flexible ITO/PEN and SnO_2/ITO/PEN films, indicating that the increase rate of flexible ITO/PEN film is much higher than that of SnO_2/ITO/PEN as the bending cycles extension, but that of the SnO_2/ITO/PEN shows slowly increase at low bending cycles (less 500) and reaches to relative stable value after 500 cycles until to 2000. That is why the SnO_2 can sustain high carrier transport ability.

3.4.7 Highest open-circuit voltage of SnO_2 flexible perovskite solar cells

An extremely high V_{OC} of 1.18 eV has been achieved on the SnO_2-fPSCs, as shown in **Figure 17**. It is the highest V_{OC} of flexible PSCs[6,7,16,17–21,24–32,34,43,44,52–54] and also can be compared with that of 1.20 V on the rigid substrates PSCs in Figure 8. The SnO_2-fPSCs with highest V_{OC} has obtained a high PCE and SPO of 15.9 and 15.7% according to the *J*–*V* curves and continuous light soaking measurements, respectively, as shown in Figure 17a and b.

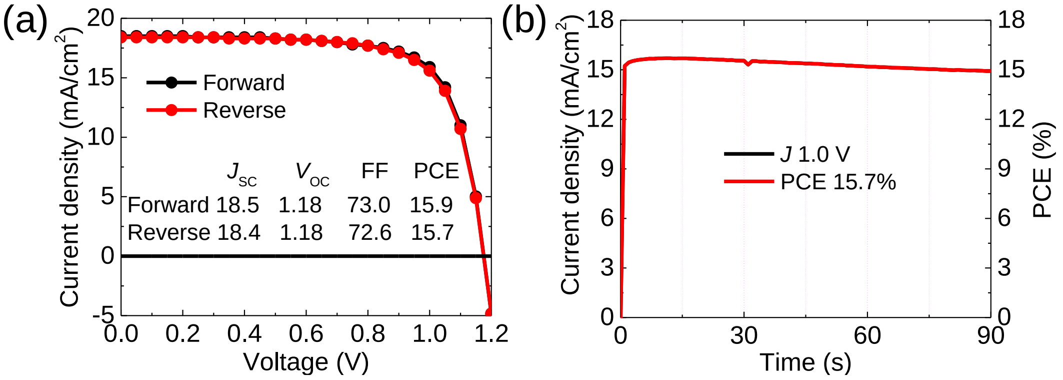

Figure 17. Photovoltaic performance of SnO_2-fPSCs with the highest V_{OC} at a small active area of 0.1 cm^2. (a) *J*–*V* curves, (b) SPO under MPP extracted from SnO_2-fPSCs under forward scanning.

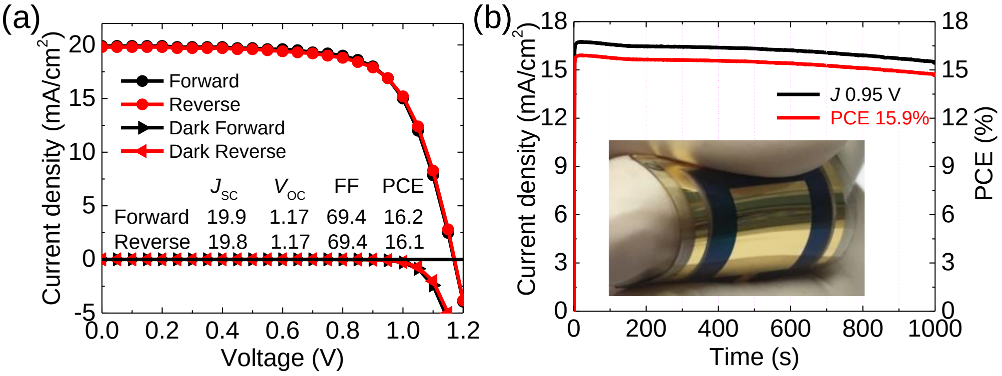

Figure 18. Photovoltaic performance of SnO_2-fPSCs with the highest V_{OC} at a large active area of 1 cm^2. (a) *J*–*V* curves, (b) SPO under MPP extracted from SnO_2-fPSCs under forward scanning. The photograph of is SnO_2-fPSCs with large active area of 1 cm^2 is also shown.

3.4.8 Large active area SnO_2 flexible perovskite solar cells

The enlargement of photoactive area and stability of fPSCs are also critical factors for the commercial application. Although the fPSCs has achieved a rapid progress on the PV performance, the active area of fPSCs is still very small and less than about 0.1 cm^2, which is far behind the application requirements. Interesting, the solution process is preferable for the large active area fPSCs due to the low fabrication temperature of SnO_2. Therefore, the large active area with 1 cm^2 of SnO_2-fPSCs has been fabricated and show *J–V* curves in **Figure 18**. According to the *J–V* curves, SnO_2-fPSCs achieve an excellent PCE of 16.2 (16.1)% with a V_{OC} of 1.17 (1.17) V, a J_{sc} of 19.9 (19.8) mA/cm^2, and a FF of 69.4 (69.4)% measured at forward (reverse) voltage scanning with a negligible hysteresis, which is the highest value on the large active area of fPSCs and much higher than that of previously reported result on 0.09 cm^2 photoactive area[18]. Figure 18b shows the SPO of 15.9% of SnO_2-fPSCs with a large active area of 1 cm^2 and keeps relative high stability even after 1000 s continuous light soaking evaluation, which is well agreement with the *J–V* curves results. The PCE values and SPO stability under continuous light soaking of large active area SnO_2-fPSCs are little worse than that of the small active area devices because of the more complicated interfaces and relative low quality. However, the successful certification of excellent PV performance of SnO_2-fPSCs with a large active area and high stability, indicating that the SnO_2 can be applied as the

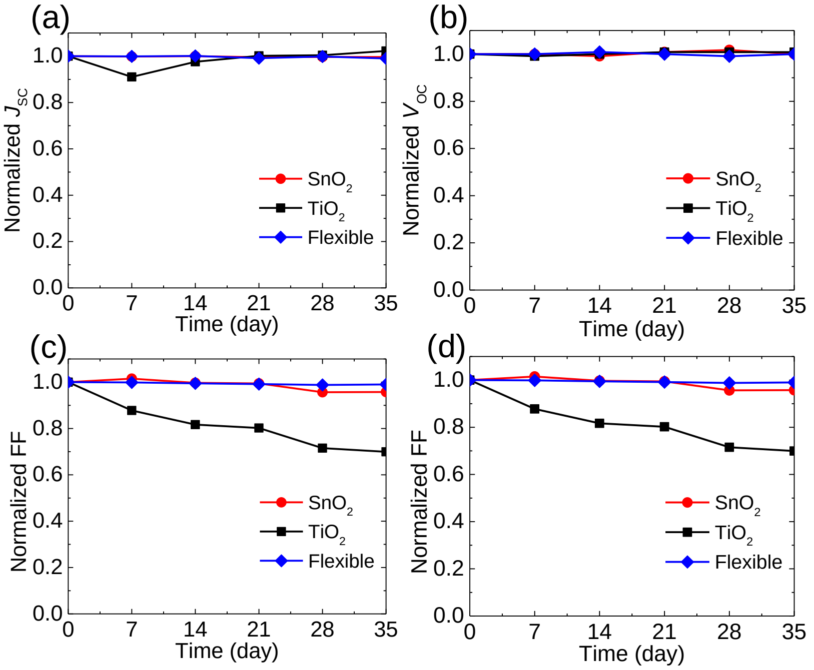

Figure 19. Dark storage stability of rigid substrate TiO_2- and SnO_2-PSCs and SnO_2-fPSCs at room temperature and a relative humidity of ca. 33.0%, respectively. (a-d) J_{SC}, V_{OC}, FF and PCE of TiO_2- and SnO_2-PSCs and SnO_2-fPSCs.

ETM in fPSCs due to the superior properties and could promote the competition of SnO_2-fPSCs for commercial applications.

3.4.9 Stability evaluation of perovskite solar cells

The storage stability of TiO_2-PSCs, SnO_2-PSCs and SnO_2-fPSCs has been evaluated at ambient condition with ca. 30% humidity, as shown in **Figure 19**. The SnO_2-fPSCs sustains an almost same stability as the SnO_2-PSCs and show much better stability compared with that of TiO_2-PSCs. The SnO_2-PSCs and SnO_2-fPSCs can sustain an excellent value about over 95% compared with that of 75% of TiO_2-PSCs. The serious decrease of FF of TiO_2-PSCs is main reason for reduction of PV performance, as shown in Figure 19c, which should come from the weak stability of TiO_2 and low quality of interface between perovskite light harvester layer and TiO_2. The continuous light soaking stability of TiO_2-PSCs and SnO_2-PSCs have been characterized at room temperature with a high humidity of ca. 60% under one sun condition.

Figure 20 shows the analysis results of continuous light soaking of TiO_2-PSCs and SnO_2-PSCs. Both of TiO_2-PSCs and SnO_2-PSCs quickly reduce as soaking time extension but the SnO_2-PSCs can sustain more long decay compared with that of TiO_2-PSCs because of the UV un-stability of TiO_2[57] and interfaces deterioration. The quickly decrease of two devices should come from the drastic vibration of interface as the functions of humidity and light soaking. Therefore, the better stability of PSCs has been

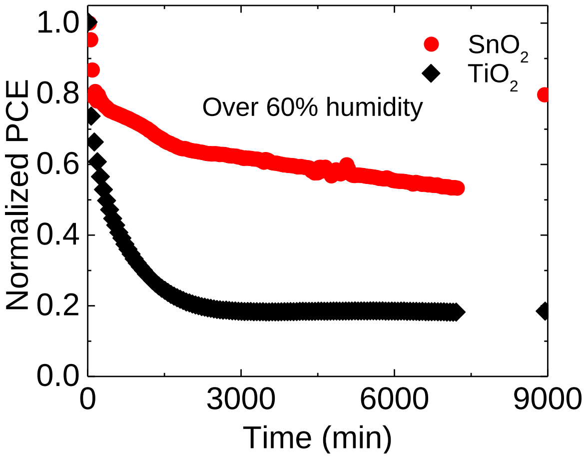

Figure 20. Normalized PCE of SnO_2- and TiO_2- PSCs evaluated under continuous 1-Sun light soaking condition with high humidity of over 60.0% and temperature of ca. 25.0 °C in ambient conditions. Both PSCs were not encapsulated. The recovery efficiencies were measured after the soaking measurement and storing at dark condition for 24 hours with a humidity of ca. 33.0%.

achieved using SnO_2 as the ETM, and this outstanding stability can be compared with those of highest reported value via calculating the degradation rate, as shown in **Table 4**.

Table 4. Summary of degradation rate of fPSCs in the storage condition.

	Structure	Storage stability (%)	Humidity (%)	Time (h)	Degradation rate(%/h)	Ref.
n-i-p	PEN/ITO/SnO_2/Perovskite/spiro-OMeTAD/Au	97.9	~ 33	840	0.003	This work
	PEN/ITO/ZnO(TiO_2)/$MAPbI_3$/PTAA/Au	~ 80 (90)	~ 40	360	~ 0.06	32
	PEN/ITO/ED-TiO_x/BK-TiO_2+Perovskite/spiro-OMeTAD/Au	64	dry	1000	0.036	29
	ITO/CPTA/$MAPbI_3$/spiro-OMeTAD/Au	96	N_2 glovebox	2400	0.002	35
p-i-n	PET/ITO/NiO_x(PEDOT:PSS)/$MAPbI_3$/C_{60} /Ag	85 (0)	air	100	0.15	53
	PEN/ITO/PEDOT:PSS/PEI.HI/$MAPbI_{3-x}Cl_3$-$MAPbI_3$/PCBM/LiF/Ag	<80	air	120	> 0.17	55
	PEN/ITO/CNT/ $MAPbI_3$/ SnO@CSCNT	80	80	600	0.03	26
	PET/ITO/Ag-mesh/PH1000/PEDOT:PSS/$MAPbI_3$/Al	90.5	N_2 glovebox	600	0.016	17

3.5 Chapter summary

The SnO_2 has been successfully applied in PSCs and achieved a high PCE of 18.6% with a negligible hysteresis compared with those of TiO_2 based devices (11.6%) with severe hysteresis. The SnO_2-PSCs can sustain much better storage stability and continuous light stability compared with those of TiO_2 based device.

The low temperature fabrication of SnO_2 ETM has also been successfully used in the fPSCs and achieved high PV performance and bending durability. The SnO_2-fPSCs obtains a high PCE of 17.1% with negligible hysteresis and SPO of 17.0% in 0.1 cm^2 active area, which can sustain a high bending durability of ca. 76.5% compared with initial efficiency even after 2000 bending cycles testing at bending radius of 4 mm. The SnO_2-fPSCs also achieve a high PCE of 16.2% with an ignorable hysteresis and SPO of 15.9% on large active area of 1 cm^2. The excellent the PV performance of SnO_2-fPSCs can enhance the competition of flexible PSCs for future industrial application using facile fabrication technique, such as roll-to-roll, doctor blade and printing, etc. The outstanding finding of SnO_2 nanoparticle film as the ETM for flexible PSCs with superior mechanical resistance properties and large photoactive area establishes a milestone for the commercial application in the future.

The stability of PSCs using SnO_2 ETM has been significantly enhanced, however, the quality of perovskite still limits the PCE because of the short lifetime of perovskite film and existed PbI_2. And, the severely cracks on the flexible substrate and noble Au electrode seriously affect the bending durability of fPSCs. Therefore, it is necessary to further enhancing the perovskite quality, utilizing new materials and new structure for photovoltaic performance and bending durability promotion.

Reference

1. Kojima, A. *et al.* Organometal halide perovskites as visible-light sensitizers for photovoltaic cells. *J. Am. Chem. Soc.* **131**, 6050–6051 (2009).
2. Yang, F. *et al.* Roles of polymer layer in enhanced photovoltaic performance of perovskite solar cells via interface engineering. *Adv. Mater. Interfaces* **5**, 1701256 (2018).
3. Yang, W. S. *et al.* Iodide management in formamidinium-lead-halide-based perovskite layers for efficient solar cells. *Science* **356**, 1376–1379 (2017).
4. Jiang, Q. *et al.* Surface passivation of perovskite film for efficient solar cells. *Nat. Photon.* **10**, 1038 (2019).
5. Best Research-Cell Efficiencies Chart. National Renewable Energy Laboratory (NREL), https://www.nrel.gov/pv/assets/pdfs/best-research-cell-efficiencies-190416 (2019).
6. Kim, B. J. *et al.* Highly efficient and bending durable perovskite solar cells: toward a wearable power source. *Energy Environ. Sci.* **8**, 916–921 (2015).
7. Kaltenbrunner, M. *et al.* Flexible high power-per-weight perovskite solar cells with chromium oxide-metal contacts for improved stability in air. *Nat. Mater.* **14**, 1032–1039 (2015).
8. Kim, Y. Y. *et al.* Gravure-printed flexible perovskite solar cells: toward roll-to-roll manufacturing. *Adv. Sci.* **6**, 1802094 (2019).
9. Najafi, M. *et al.* Highly efficient and stable flexible perovskite solar cells with metal oxides nanoparticle charge extraction layers. *Small* **14**, 1702775 (2018).
10. Jo, J. W. *et al.* Improving performance and stability of flexible planar-heterojunction perovskite solar cells using polymeric hole-transport material. *Adv. Funct. Mater.* **26**, 4464–4471 (2016).
11. Bu, T. *et al.* Low-temperature presynthesized crystalline tin oxide for efficient flexible perovskite solar cells and modules. *ACS Appl. Mater. Interfaces* **10**, 14922–14929 (2018).
12. Cong, S. *et al.* Fabrication of nickel oxide nanopillar arrays on flexible electrodes for highly efficient perovskite solar cells. *Nano Lett.* (2019).

13. Haque, S. *et al.* Photonic-structured TiO_2 for high-efficiency, flexible and stable Perovskite solar cells. *Nano Energy* **59**, 91–101 (2019).
14. Liu, C. *et al.* Hydrothermally treated SnO_2 as the electron transport layer in high-efficiency flexible perovskite solar cells with a certificated efficiency of 17.3%. *Adv. Funct. Mater.* 1807604 (2019).
15. Li, M. *et al.* Perovskite grains embraced in a soft fullerene network make highly efficient flexible solar cells with superior mechanical stability. *Adv. Mater.* 1901519 (2019).
16. Yang, D. *et al.* High efficiency flexible perovskite solar cells using superior low temperature TiO_2. *Energy Environ. Sci.* **8**, 3208–3214 (2015).
17. Li, Y. *et al.* High-efficiency robust perovskite solar cells on ultrathin flexible substrates. *Nat. Commun.* **7**, 10214 (2016).
18. Yoon, J. *et al.* Superflexible, high-efficiency perovskite solar cells utilizing graphene electrodes: towards future foldable power sources. *Energy Environ. Sci.* **10**, 337–345 (2017).
19. Yang, D. *et al.* Hysteresis-suppressed high-efficiency flexible perovskite solar cells using solid-state ionic-liquids for effective electron transport. *Adv. Mater.* **28**, 5206–5213 (2016).
20. Bi, C. *et al.* Efficient flexible solar cell based on composition-tailored hybrid perovskite. *Adv. Mater.* **29**, 1605900 (2017).
21. Heo, J. H. *et al.* Highly flexible, high-performance perovskite solar cells with adhesion promoted AuCl3-doped graphene electrodes. *J. Mater. Chem. A* **5**, 21146–21152 (2017).
22. Luo, Q. *et al.* All-carbon-electrode-based endurable flexible perovskite solar cells. *Adv. Funct. Mater.* **28**, 1706777 (2018).
23. Feng, J. *et al.* Record efficiency stable flexible perovskite solar cell using effective additive assistant strategy. *Adv. Mater.* **30**, 1801418 (2018).
24. Shin, S. S. *et al.* Tailoring of electron-collecting oxide nanoparticulate layer for flexible perovskite solar cells. *J. Phys. Chem. Lett.* **7**, 1845–1851 (2016).
25. Shin, S. S. *et al.* High-performance flexible perovskite solar cells exploiting Zn_2SnO_4 prepared in solution below 100 °C. *Nat. Commun.* **6**, 7410 (2015).
26. Luo, Q. *et al.* Carbon nanotube based Inverted flexible perovskite solar cells with all-inorganic charge contacts. *Adv. Funct. Mater.* **27**, 1703068 (2017).
27. Wang, C. *et al.* Water vapor treatment of low-temperature deposited SnO_2 electron selective layers for efficient flexible perovskite solar cells. *ACS Energy Lett.* **2**, 2118–2124 (2017).

28. Jeong, I. *et al.* A tailored TiO_2 electron selective layer for high-performance flexible perovskite solar cells via low temperature UV process. *Nano Energy* **28**, 380–389 (2016).

29. Lin, S. Y. *et al.* Efficient plastic perovskite solar cell with a low-temperature processable electrodeposited TiO_2 compact layer and a brookite TiO_2 scaffold. *Adv. Energy Mater.* **7**, 1700169 (2017).

30. Liu, D. & Kelly, T. L. Perovskite solar cells with a planar heterojunction structure prepared using room-temperature solution processing techniques. *Nat. Photon.* **8**, 133–138 (2014).

31. Tavakoli, M. M. *et al.* Highly efficient flexible perovskite solar cells with antireflection and self-cleaning nanostructures. *ACS Nano* **9**, 10287–10295 (2015).

32. Heo, J. H. *et al.* Highly efficient low temperature solution processable planar type $CH_3NH_3PbI_3$ perovskite flexible solar cells. *J. Mater. Chem. A* **4**, 1572–1578 (2016).

33. Zhou, H. *et al.* Low-temperature processed and carbon-based $ZnO/CH_3NH_3PbI_3/C$ planar heterojunction perovskite solar cells. *J. Phys. Chem. C* **119**, 4600–4605 (2015).

34. Ryu, S. *et al.* Fabrication of metal-oxide-free $CH_3NH_3PbI_3$ perovskite solar cells processed at low temperature. *J. Mater. Chem. A* **3**, 3271–3275 (2015).

35. Wang, Y.-C. *et al.* Efficient and hysteresis-free perovskite solar cells based on a solution processable polar fullerene electron transport layer. *Adv. Energy Mater.* **7**, 1701144 (2017).

36. Snaith, H. J. & Ducati, C. SnO_2-Based dye-sensitized hybrid solar cells exhibiting near unity absorbed photon-to-electron conversion efficiency. *Nano Lett.* **10**, 1259–1265 (2010).

37. Bob, B. *et al.* Nanoscale dispersions of gelled SnO_2: Material properties and device applications. *Chem. Mater.* **25**, 4725–4730 (2013).

38. Jiang, Q. *et al.* Enhanced electron extraction using SnO_2 for high-efficiency planar-structure $HC(NH_2)_2PbI_3$-based perovskite solar cells. *Nat. Energy* **2**, 16177 (2016).

39. Ke, W. *et al.* Low-temperature solution-processed tin oxide as an alternative electron transporting layer for efficient perovskite solar cells. *J. Am. Chem. Soc.* **137**, 6730–6733 (2015).

40. Correa Baena, J. P. *et al.* Highly efficient planar perovskite solar cells through band alignment engineering. *Energy Environ. Sci.* **8**, 2928–2934 (2015).

41. Anaraki, E. H. *et al.* Highly efficient and stable planar perovskite solar cells by solution-processed tin oxide. *Energy Environ. Sci.* **9**, 3128–3134 (2016).

42. Jiang, Q. *et al.* Planar-structure perovskite solar cells with efficiency beyond 21%. *Adv. Mater.* **29**, 1703852 (2017).
43. Jung, K.-H. *et al.* Solution-processed SnO_2 thin film for hysteresis-less 19.2% planar perovskite solar cell. *J. Mater. Chem. A* **5**, 24790–24803 (2017).
44. Wang, C. *et al.* Low-temperature plasma-enhanced atomic layer deposition of tin oxide electron selective layers for highly efficient planar perovskite solar cells. *J. Mater. Chem. A* **4**, 12080–12087 (2016).
45. Wang, C. *et al.* Compositional and morphological engineering of mixed cation perovskite films for highly efficient planar and flexible solar cells with reduced hysteresis. *Nano Energy* **35**, 223–232 (2017).
46. Dou, B. *et al.* High-performance flexible perovskite solar cells on ultrathin glass: Implications of the TCO. *J. Phys. Chem. Lett.* **8**, 4960–4966 (2017).
47. Zhou, H. *et al.* Interface engineering of highly efficient perovskite solar cells. *Science* **345**, 542–546 (2014).
48. Saliba, M. *et al.* Cesium-containing triple cation perovskite solar cells: improved stability, reproducibility and high efficiency. *Energy Environ. Sci.* **9**, 1989–1997 (2016).
49. Bi, D. *et al.* Efficient luminescent solar cells based on tailored mixed-cation perovskites. *Sci. Adv.* **2**, e1501170 (2016).
50. Yang, F. *et al.* High bending durability of efficient flexible perovskite solar cells using metal oxide electron transport layer. *J. Phys. Chem. C* **122**, 17088–17095 (2018).
51. Singh, T. & Miyasaka, T. Stabilizing the efficiency beyond 20% with a mixed cation perovskite solar cell fabricated in ambient air under controlled humidity. *Adv. Energy Mater.* **8**, 1700677 (2017).
52. Wojciechowski, K. *et al.* Heterojunction modification for highly efficient organic-inorganic perovskite solar cells. *ACS Nano* **8**, 12701–12709 (2014).
53. Li, Y. *et al.* Multifunctional fullerene derivative for interface engineering in perovskite solar cells. *J. Am. Chem. Soc.* **137**, 15540–15547 (2015).
54. Zhang, H. *et al.* Pinhole-free and surface-nanostructured niox film by room-Temperature solution process for high-performance flexible perovskite solar cells with good stability and reproducibility. *ACS Nano* **10**, 1503–1511 (2016).
55. Yin, X. *et al.* Highly efficient flexible perovskite solar cells using solution-derived NiOx hole contacts. *ACS Nano* **10**, 3630–3636 (2016).
56. Yao, K. *et al.* A general fabrication procedure for efficient and stable planar perovskite solar cells: morphological and interfacial control by in-situ-generated

layered perovskite. *Nano Energy* **18**, 165–175 (2015).

57. Leijtens, T. *et al.* Overcoming ultraviolet light instability of sensitized TiO_2 with meso-superstructured organometal tri-halide perovskite solar cells. *Nat. Commun.* **4**, 2885 (2013).

Chapter 4. Second solution growth process of perovskite solar cells

4.1 Abstract

Hybrid organic/inorganic metal perovskite solar cells (PSCs) have treated as a promising new-generation solar-electric conversion devices attribute to the explosive development on power conversion efficiency (PCE) and conceivable replacement of mainstream photovoltaics of silicon. The continuous increasing PCE of PSCs come from the quality of perovskite light harvester layer. Here, a high quality of perovskite with highly crystallinity and large crystal size has been obtained using excessive PbI_2 and second solution growth process (SSGP) approach, which evidenced a high photovoltaic performance of planar PSCs in normal structure. The PSCs has achieved a highest fill factor (FF) of 83.4% as our knowledge without at expensive of the short-circuit current-density and open-circuit voltage. Moreover, a high PCE of 21.6% with a FF 81.2% and negligible hysteresis in reverse scanning has been obtained. The PSCs can sustain a high robust stability, maintaining ca. 70% under continuous light soaking with high humidity and ca. 75% under thermal treatment at high temperature of 80 °C in nitrogen condition of their initial efficiencies, respectively. And, the PSCs obtain a high PCE of 20.1% with an ignorable hysteresis at a large active area of 1 cm^2. The enhancement mechanisms of PSCs have been analyzed using optical properties, carrier extraction efficiency and recombination loss of perovskite light harvester.

Keywords: perovskite solar cells, excessive PbI_2, second solution growth process, photovoltaic performance, stability

4.2 Introduction

Unprecedented development of hybrid organic/inorganic perovskite solar cells (PSCs) has grasped numerous interesting due to the enhancement of power conversion efficiency (PCE) to 24.2% within a decade with endeavors of community[1–9]. Rapidly progressing of photovoltaic (PV) performance of PSCs attributes to the incomparable properties of organic/inorganic perovskite light harvester layer, for instance, large absorption coefficient in visible regions and long carrier diffusion length[10,11], high carrier mobility[12], low exciton binding energy[10], and tunable bandgap[13–15]. A high PV performance of PSCs is mainly determined by the quality of perovskite light harvester layer and its interfaces, because the carrier generation and transport processes happen on the perovskite and its interfaces[16]. Therefore, countless of endeavors have been invested into improving the quality of perovskite light harvester layer, for example, changing the composition of the perovskite precursor[13,15,17], vacuum-assisted solution deposition technique[18,19] and solution process secondary growth[5,20].

Among above methods, the application of excessive lead iodide (PbI_2)[21–28] could promote the quality of perovskite light harvester layer, including crystallinity[22] and perovskite crystals' size[22]. A proper remained PbI_2 has been demonstrated the passivation of the grain boundaries of perovskite and its interfaces[24–26,28], enhancement of electron blocking function, reduction of carrier recombination and improvement of hole injection[3,21,23,25,29]. However, the uncertainly amount of remained PbI_2 comes from over post-treatment or non-stoichiometry of perovskite light harvester layer[21,22,25,26], which could seriously deteriorate the perovskite quality and induce intrinsic stability under continuous light illumination[26,28]. The PV performance of PSCs using excessive PbI_2 fabrication approached still locates at a dissatisfied and inefficient because the PCE is still about 21.0%, even if the short-circuit current density (J_{SC}) has been improved at the cost of the reduction of open-circuit voltage (V_{OC}) or fill factor (FF)[3,24,25]. Therefore, an effective approach for achieving a high PCE and stability is necessary using excessive PbI_2 for perovskite preparation. The obtaining a FF exceeding over 80.0% becomes a critical challenge because the FF is always improved at sacrifice of V_{OC} or J_{SC}[30,31].

In this chapter, an effective approach for achieving high PV performance on planar n-i-p structure PSCs using the combination of excessive PbI_2 and second-solution-growth-process (SSGP) of perovskite light harvester layer. The X-ray diffraction (XRD), scanning electron microscopy (SEM), atomic force microscopy (AFM), photoluminescence (PL) mapping/spectroscopy and photoelectron yield spectroscopy have been systematically studied the properties of perovskite light harvester layer. The removal of excessive PbI_2 can remarkably improve perovskite layer quality and reduce the trap states. A high PCE of 21.6% with a negligible hysteresis, a stabilized power output (SPO) of 21.3% and a FF of 80.0% have been achieved on the small active area of 0.1 cm^2. The PSCs can maintain a high stability of ca. 70.0% after 250 hours continuous light soaking at humidity of ca. 50.0% and ca. 75.0% after 270 hours at high temperature treatment (80 °C) in nitrogen condition. The PSCs also achieved a highest FF of 83.4% in the planar structure devices up to date. Moreover, a high PCE of 20.1% with a negligible hysteresis and SPO of 19.3% of PSCs has been realized on large active area of 1.0 cm^2. The high PV performance and stability of PSCs using excessive PbI_2 and SSGP process has paved a new way for commercial application.

4.3 Experimental section

Materials: All chemicals were used as received, without further purification. Tin oxide substrate (ITO, 10 Ω) and flexible PEN/ITO (10 Ω) were obtained from GEOMATEC and Oike & Co., Ltd. SnO_2 nanoparticles (15 wt%) with a particle size of 10–15 nm in H_2O colloidal dispersion were acquired from Alfa Aesar. Lead (II) iodide (PbI_2, 99.99%), lead (II) bromide ($PbBr_2$, 99%), methylammonium bromide (MABr, > 98.0%) formamidinium iodide (FAI, > 98.0%), cesium iodide (CsI, 99.9%) and titanium diisopropoxide bis(acetylacetonate) (TiAcac) were purchased from Tokyo Chemical Industry Co., Ltd. Benzyl alcohol (99.8%) and $TiCl_4$ (99.0%) were acquired from Sigma-Aldrich Co., Ltd. The solvent chemicals *N*,*N*-dimethylformamide (DMF), dimethyl sulfoxide (DMSO), and chlorobenzene were dried before use. 2,2′,7,7′-Tetrakis(*N*,*N*-di-*p*-methoxyphenylamino)-9,9′-spirobifluorene (spiro-OMeTAD) was purchased from Merck Co., Ltd. Lithium bis(trifluoromethanesulfonyl)imide (Li-TFSI) salt powder, dehydrated ethanol, acetone, 2-propanol, other solvents were purchased from Wako Chemical Co., Ltd. and used as received without no special treatment unless otherwise noted.

ITO substrate preparation: The ITO substrate is prepared using zinc powder and 6 M HCl solution to etch some part of ITO. The etched ITO is cleaned as following procedures: ca. 1 wt% aqueous detergent solution washing, sonication of about 10 min in each step of acetone, IPA and distilled water, respectively. The cleaned ITO substrates are cut into 25×25 mm^2 size after drying using an air gun, and stored at a dry box for following experiments.

SnO_2* *ETM deposition: The ITO substrates are deposited SnO_2 nanoparticles with concentration of 5 wt% as ETM using following program: spin coating at 3000 rpm for 30 s and annealed at 150 °C for 30 min at room condition. The SnO_2 ETM substrates are kept in a dry condition after post-treatment.

PSCs fabrication: The perovskite precursor solution with excessive PbI_2 is prepared by mixing the FAI (1 M), PbI_2 (1.1 M), MABr (0.2 M), $PbBr_2$ (0.2 M) and a 1.5 M CsI-DMSO solution in anhydrous DMF:DMSO 4:1 (*v*:*v*) solvent. The perovskite precursor is dissolving at 40 °C until fully dissolving of all chemicals.

The perovskite precursor deposits as two-step spin coating process for perovskite light harvester layer: 1000 and 6000 rpm for 10 and 20 s, respectively. The anti-solvent of toluene with 400 μL is quickly splashed on ITO substrate within 2 s at 8 s before finishing the coating program. Interesting, the color of substrate quickly changes from transparency to light brown after dropping toluene. The sample is directly transferred onto hotplate for post-treatment at 150 °C and 10 min to achieve large crystal size and compact perovskite film.

As for the standard PSCs, the hole transport layer (HTL) solution with 0.06 mmol spiro-OMeTAD, 0.009 mmol Co(4-*tert*-butylpyridyl-2-1*H*-pyrazole)3·3TFSI, 0.03 mmol Li-TFSI and 0.1 mmol tBP in 1 mL chlorobenzene is prepared and spin coated on perovskite light harvester layer surface at program of 4000 rpm and 30 s. The ~80 nm of Au electrode film is deposited on HTL surface after annealing the HTL film at 70 °C for 30 min.

As for the SSGP PSCs, a spiro-OMeTAD chlorobenzene solution with extremely low concentrations (0, 2 and 5 mg/mL) is loaded on perovskite layer surface to passivate the surface and eliminate the trap states before the SSGP, because the thick film of spiro-OMeTAD will block the electron transport after formation of the second layer of perovskite and deteriorate the PV performance of PSCs. The thin film of spiro-OMeTAD is deposited at 4000 rpm for 30 s after fully dissolving the spiro-OMeTAD in chlorobenzene without any additives at 70 °C. After drying the spiro-OMeTAD thin film at 70 °C, the second layer of perovskite film is fabricated by dynamically depositing a halide of FABr, FAI and MACl isopropanol (IPA) solution at program of 5000 rpm for 35 s with various concentrations (3, 5 and 8 mg/mL), in which the FABr, FAI and MACl are dissolving in IPA solvent. The IPA solution must be quickly and continuously splashed on the sample's surface, because the polar property of IPA can dissolve the as-prepared perovskite film and deteriorate the PV performance of PSCs. The as-prepared perovskite film surface shows shine before post-treatment and changes to dark brown after post-treatment at 100 °C for 15 min. The HTL and Au films are deposited using same approach as the standard PSCs.

Characterizations: All the characterizations of perovskite layer and PSCs are finished at air condition. A ca. 500 nm thickness of perovskite layer is prepared for photoluminescence (PL) and absorption measurements at an excitation wavelength of 532 nm (a power of 75 μW) and UV/Vis spectrophotometer (Shimadzu, UV-1800) apparatuses. The time-resolved PL decay was determined using a single-photon counting technique with a 520-nm semiconductor laser and an incident power of 20 nW. The top of valance band of perovskite layer is recorded using a photoelectron yield spectrophotometer (AC-3E, Riken Keiki Co.) with an excitation power of 10 nW in ambient condition. XRD pattern is recorded using X-ray diffractometer (RINT 2500, Rigaku Co.). Atomic force microscopy (AFM) (SII, Nanocute) and SEM (JEOL, JEM-6500F) are applied to characterize the surface roughness, surface and cross-sectional morphology of perovskite photoactive layer and PSCs, respectively. Energy dispersive X-ray spectroscopy (EDX) measurement is conducted by S4800 (Hitachi High-Technologies Co.) instrument.

Photovoltaic performance of PSCs was conducted at a solar simulator (San-Ei Electric, XES-40S1) under AM 1.5 conditions (100 mW/cm^2) with a calibration cells (Bunkoukeiki, BS-500BK). The current density–voltage (*J*–*V*) curves were measured using a source meter (Keithley, 2400) and a 0.1 cm^2 metal mask at ambient condition. *J*–*V* curves of PSCs were recorded from forward (−0.1 to 1.2 V) and reverse (1.2 to −0.1 V) scanning directions without any preconditioning (light soaking or the application of a forward bias voltage for a prolonged period before starting the measurement) at a 50 mV/s voltage sweep rate. The stabilized power output (SPO) was evaluated under maximum power point (MPP) tracking with a bias voltage from the *J*–*V* scanning. The external quantum efficiency (EQE) was analyzed at a monochromatic Xe arc light system (Bunkoukeiki, SMO-250III) by measuring incident-to-power conversion efficiency. An electrochemical analyzer (ALS/HCH, 660 EAW) was used to record the impedance spectroscopy of PSCs with a 5 mV AC amplitude and frequency ranging from 100 kHz to 0.1 Hz. The continuous light soaking stability of PSCs was conducted at the heat and weather resistibility test system (Bunkoukeihi, BIR-50P1).

4.4 Results and discussion

4.4.1 Perovskite films characterizations

Structure description of planar PSCs

Fabrication procedures and detailed architecture of PSC has been shown in **Figure 1**. A schematic of normal-structure (n-i-p) planar SSGP PSCs, consisting of ITO/SnO_2/first perovskite layer/spiro-OMeTAD (2,2,7,7-tetrakiss(N,N-di-p-methoxyphenylamine)-9,9-spirobifluorene) treatment/second growth perovskite layer/spiro-OMeTAD/Au[32], is exhibited in the center of Figure 1. The first layer of perovskite light harvester of $Cs_{0.05}(MA_{0.17}FA_{0.83})_{0.95}Pb(I_{0.83}Br_{0.17})_3$ is quickly annealed at 150 °C for 10 min after dropping the toluene as anti-solvent. The excessive PbI_2 composition of perovskite precursor solution is used to obtain a large crystal size and high crystallinity[15,24]. The excessive perovskite nuclei formation can be prevented by using the quickly and high-temperature post-treatment. Subsequently, the as-prepared perovskite light harvester layer is passivated using low concentration of spiro-OMeTAD without any additives and protected from the damage of second layer perovskite fabrication. The SSGP process has been realized through dynamically splashing the halide solution (including formamidinium bromide (FABr), formamidinium iodide (FAI) and methylammonium

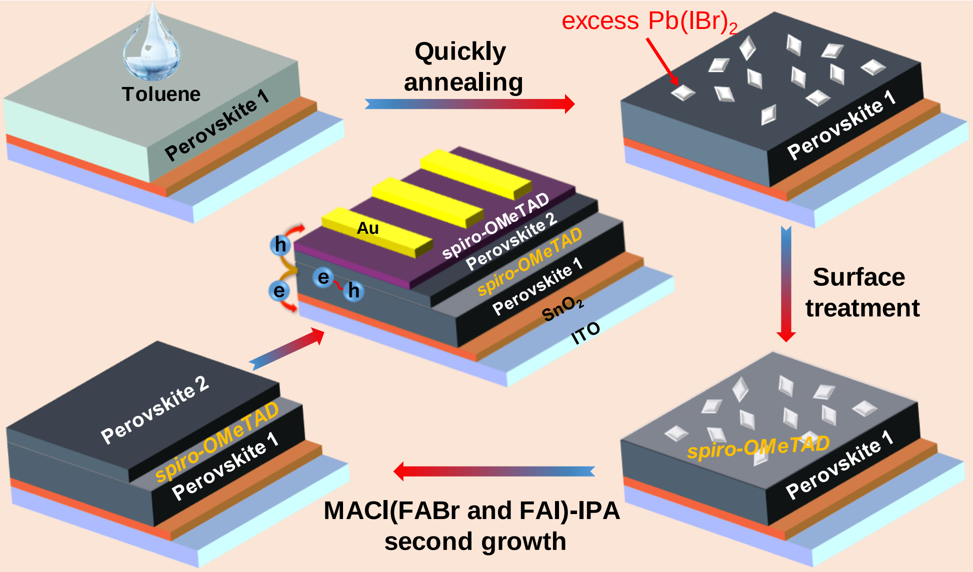

Figure 1. Illustration of the fabrication process of two-steps growth of perovskite using high temperature post-treatment, surface passivation and second solution growth process (SSGP) via halide isopropanol solution splashing on $Cs_{0.05}(MA_{0.17}FA_{0.83})_{0.95}Pb$ $(I_{0.83}Br_{0.17})_3$. The architecture of SSGP PSCs, ITO/SnO_2/$Cs_{0.05}(MA_{0.17}FA_{0.83})_{0.95}Pb(I_{0.83}Br_{0.17})_3$/spiro-OMeTAD treatment/SSGP perovskite/Au is shown in the center. Reprinted with permission from ref. 32.

chloride (MACl)) using isopropanol (IPA) solvent, which are employed to fabricate second layer perovskite to eliminate the excessive PbI_2 and trap states induced by excessive PbI_2. The detailed of fabrication processes can be described in the Experimental Section.

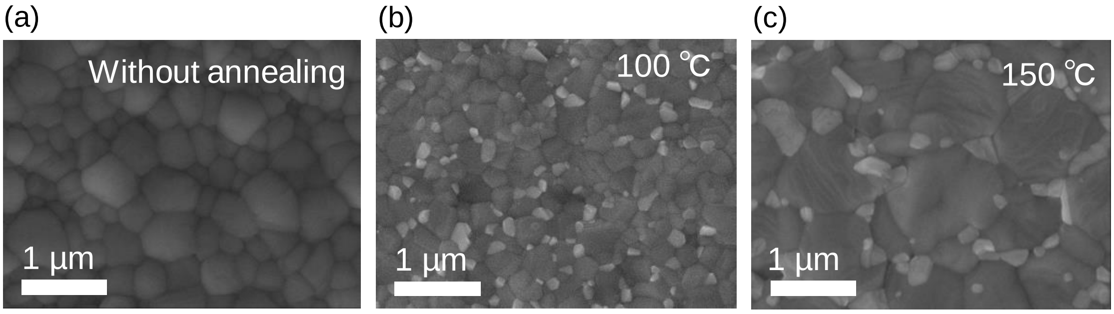

Figure 2. (a-c) Surface morphology characterization of the $Cs_{0.05}(MA_{0.17}FA_{0.83})_{0.95}Pb(I_{0.83}Br_{0.17})_3$-perovskite without post-treatment, 100 °C and 150 °C annealing. The scale bar is 1 µm.

SEM images of perovskite film without and with SSGP

Figure 2 shows the SEM images of the perovskite surface morphology without post-treatment, which is defined as "as-prepared perovskite" and that after 100 and 150 °C post-treatment, respectively. Figure 2a shows the un-uniformly formation of the nucleus and small grain size (<400 nm) of perovskite light harvester layer because of the quickly growth of crystals without annealing treatment. According to previously reported results[33], the growth process of a large grain size is usually at the expensive of small particles for the uniform nucleation process. The grains size of perovskite crystals are quickly increased at 150 °C annealing, and most of them are larger than 1 µm, while the small white plates of $Pb(I_{1-x}Br_x)_2$ evidenced by XRD appear on the perovskite surface with a

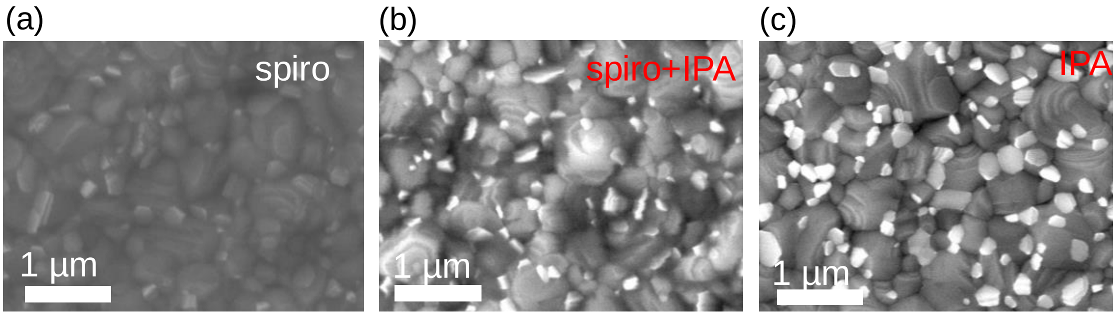

Figure 3. (a-c) Surface morphology characterization of the $Cs_{0.05}(MA_{0.17}FA_{0.83})_{0.95}Pb(I_{0.83}Br_{0.17})_3$-perovskite with treatment of spiro-OMeTAD, spiro-OMeTAD+IPA and IPA, respectively. The scale bar is 1 µm.

density of ca. 5/µm^2 according to SEM image in Figure 2b. The white plates of Pb($I_{1-x}Br_x$)$_2$ are randomly distributed on the perovskite surface and grain boundary, which is similar to the previously observations[24]. The average grain size of perovskite crystals is remarkable higher than that of the sample with a post-treatment at 100 °C even after 40 min (as shown in Figure 2c) and previously reported values[15,34], indicating that the grains size of perovskite do not enlarge and form the new nuclei during 100 °C post-treatment. In contrast, the concentration of existed white plates of Pb($I_{1-x}Br_x$)$_2$ perovskite sample at 100 °C annealing is almost same as those of the 150 °C sample, indicating that the white plates of Pb($I_{1-x}Br_x$)$_2$ are not coming from the perovskite degradation process. The grain boundaries and lattice distortion can be reduced by increasing the grain size. Hence, it is necessary to balance the growth' rate and nucleation processes of perovskite crystals.

An extremely low concentration (2 mg/mL) of spiro-OMeTAD solution is used to enhance quality and passivate the perovskite layer, as shown in **Figure 3a**. The thin film of spiro-OMeTAD can protect the underneath of perovskite from dissolving by IPA, as shown in Figures 3b and c. The white plates of Pb($I_{1-x}Br_x$)$_2$ changes position from some grain boundaries after dropping the IPA, but the Pb($I_{1-x}Br_x$)$_2$ particles still remain on the initial position with an inserting layer of thin film spiro-OMeTAD, which indicates a protection of the as-prepared perovskite film from IPA.

After inserting thin film of spiro-OMeTAD, the second perovskite layer has been fabricated using a halide IPA solution. **Figure 4** shows the surface morphologies of perovskite light harvester layers after second growth, including FABr, FAI and MACl solution, respectively. According to the SEM images of Figures 4a-c, the amount of excessive Pb($I_{1-x}Br_x$)$_2$ remarkably decreases and almost disappears after the splashing of

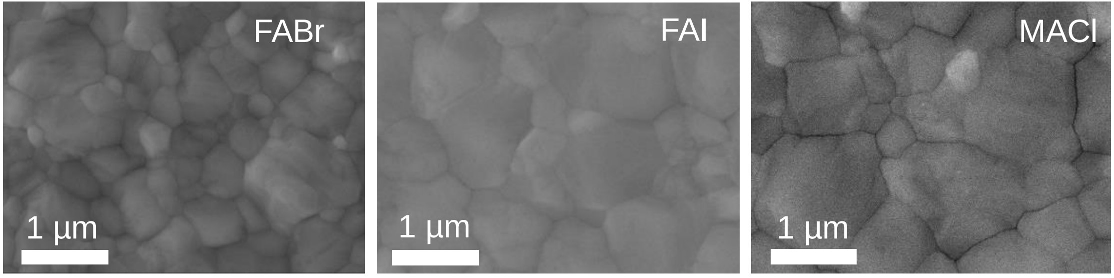

Figure 4. (a-c) Surface morphology characterization of the $Cs_{0.05}(MA_{0.17}FA_{0.83})_{0.95}Pb(I_{0.83}Br_{0.17})_3$-perovskite after SSGP using FABr-, FAI- and MACl-IPA solution, respectively. The scale bar is 1 µm.

the halide (MACl-, FABr- and FAI-) IPA solution. But the average grain size of perovskite crystals is still large and the largest one is larger than 1 μm, indicating that the SSGP process does not affect the grain size of perovskite and can sustain low carrier recombination centers of grain boundaries.

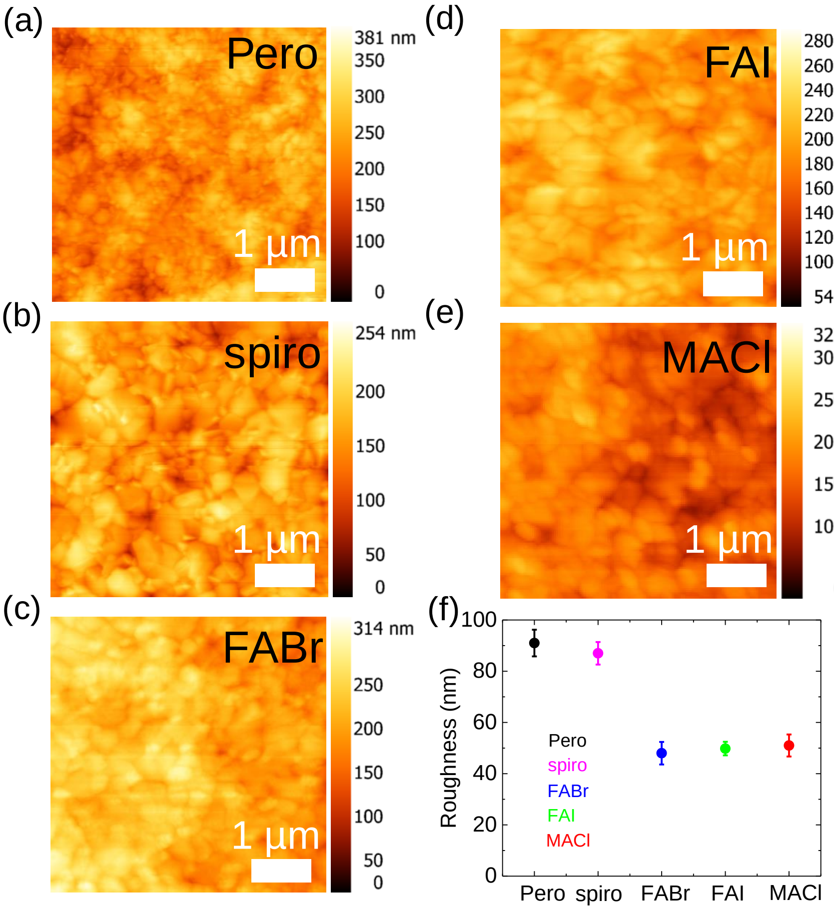

Figure 5. (a-e) Surface roughness characterization of the Cs$_{0.05}$(MA$_{0.17}$FA$_{0.83}$)$_{0.95}$Pb (I$_{0.83}$Br$_{0.17}$)$_3$-perovskite before and after spiro-OMeTAD treatment and SSGP using MACl-, FABr- and FAI-IPA solution, respectively. The scale bar is 1 μm. (f) Summarization of perovskite roughness before and after treatment.

Surface roughness characterization of perovskite light harvester layer

The surface roughness of perovskite light harvester layers will seriously affect the average transport length of carrier and carrier recombination process. Therefore, the surface roughness of perovskite layers has been characterized under various conditions, including as-prepared, spiro-OMeTAD passivation, SSGP using FABr, FAI and MACl, respectively, as shown in **Figure 5**. According to the AFM measurement of Figures 5a and b, the surface images are almost same before and after sipro-OMeTAD treatments, indicating that the thin film of spiro-OMeTAD has not obviously impact on the surface roughness of perovskite light harvester layer. Moreover, the surface roughness values decrease as the SSGP application, and FABr based sample reaches to the minimum value of about 42 nm, as shown in Figure 5f. The reduction of surface roughness of perovskite light harvester layers should come from the excessive PbI_2 eliminating.

Crystal structure characterization of perovskite light harvester layer

Figure 6 shows the crystals' variation without and with SSGP perovskites using FABr, FAI, and MACl, which are defined as FABr-, FAI-, and MACl-SSGP, respectively. The asterisks symbol represents $Pb(I_{1-x}Br_x)_2$ crystals in the X-ray diffraction peaks, and other peaks mean the diffraction signal of $Cs_{0.05}(MA_{0.17}FA_{0.83})_{0.95}Pb(I_{0.83}Br_{0.17})_3$ perovskite. The diffraction intensity of XRD peaks remarkable reduces on FAI-SSGP, and almost vanishes on FABr- and MACl-SSGP perovskites, as shown in Figure 6a. The composition of $Pb(I_{1-x}Br_x)_2$ is calculated as $Pb(I_{0.8}Br_{0.2})_2$ by the Vegard's law through the diffraction angle position of typical diffraction peaks of PbI_2 (12.7°) and $PbBr_2$ (14.4°)[13,35], respectively. The normalized relative intensity of $Pb(I_{0.8}Br_{0.2})_2$ and full-width of half maximum (FWHM) for the as-prepared and SSGP perovskites are summarized in Figure 6b. The average particle size of $Pb(I_{0.8}Br_{0.2})_2$ is 180 nm and well agreement with the SEM observation, which is calculated using Scherrer's formula according to the FWHM values. The XRD peaks have been expanded to confirm the crystal structure variation after SSGP and shown in Figure 6c. The main diffraction peaks of

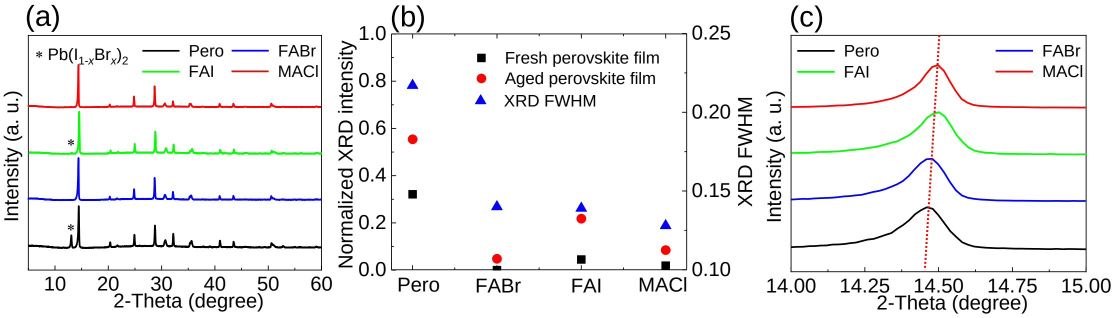

Figure 6. Crystal characterization of the $Cs_{0.05}(MA_{0.17}FA_{0.83})_{0.95}Pb$ $(I_{0.83}Br_{0.17})_3$-perovskite after SSGP. (a) XRD pattern for as-prepared and SGGP perovskites using FABr, FAI and MACl. (b) Normalized XRD intensity of $Pb(I_{0.8}Br_{0.2})_2$ at 13.0° for the as-prepared and SSGP perovskite films, before and after 10 d of aging. The FWHM of the diffraction peak at 14.49° is also shown. (c) Expanded main XRD peaks of perovskite before and after SSGP.

$Cs_{0.05}(MA_{0.17}FA_{0.83})_{0.95}Pb(I_{0.83}Br_{0.17})_3$–perovskite appears at 14.49°, however, the main diffraction peak position causes some higher angle shifts after using SSGP by FABr, FAI and MACl, indicating that perovskite crystals structure changes because of composition variation after SSGP, such as $Cs_{0.05}(MA_{0.17}FA_{0.83})_{0.95}Pb(I_{0.83}Br_{0.17})_3$-$MAPb(I_xBr_yCl_z)_3$ of MACl-SSGP perovskite. These results strongly indicate that the various composition of perovskite has been formed on as-prepared perovskite surface using SSGP.

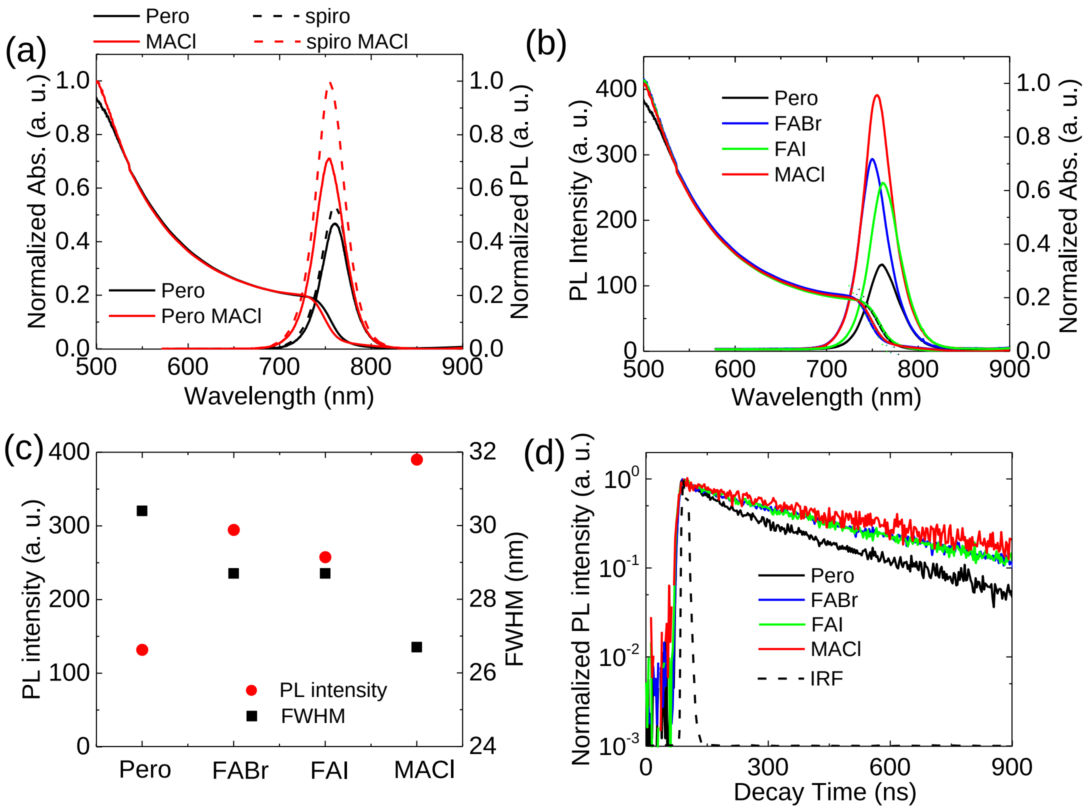

Figure 7. Optical properties of perovskites without and with treatment. (a) Optical absorption and PL spectra of the as-prepared and MACl-SSGP perovskites. The concentration of spiro-OMeTAD treatment is 2 mg/mL. (b) PL spectra of perovskites before and after SSGP. (c) Integrated PL mapping intensity and FWHM of the perovskites before and after SSGP. (d) TRPL decay profiles of the perovskites without and with SSGP.

Optical properties evaluations of perovskite light harvester layer

The optical spectroscopy and microscopy have been employed to evaluate the optical properties of the as-prepared and SSGP perovskite layers. **Figure 7a** shows the absorption and photoluminescence (PL) spectra of the as-prepared, spiro-OMeTADA passivated and

MACl-SSGP perovskites. The absorption shoulder position and PL peak of perovskites causes some blue-shifts after SSGP, and PL intensities become much higher when spiro-OMeTAD inserts between the as-prepared and second layer of perovskites, indicating that the spiro-OMeTAD can also improve perovskite surface quality and realize the function of passivation. Figure 7b exhibits the absorption and PL spectra of perovskites layer fabricated by FABr- and FAI-SSGP. Interesting, the absorption and PL also happen some blue-shifts on FABr-SSGP except for the FAI-SSGP, indicating that the bandgap (E_g) of FABr-and MACl-SSGP perovskites become larger after second-growth except for FAI-SSGP[3,15,20]. Therefore, the E_g of the as-prepared, FABr-, FAI- and MACl-perovskites has been calculated according to the absorption spectral tails as following: 1.60, 1.62, 1.60 and 1.61 eV, respectively. The PL intensity and FWHM of PL spectra have been summarized in Figure 7c. It is obviously founded that the PL intensity reaches maximum and the FWHM reduces to minimum at MACl-SSGP, indicating that the quality of perovskite layer becomes best at MACl-SSGP. The enhancement of PL intensity should come from the excessive PbI_2 elimination after SSGP, in which large E_g of PbI_2 hinder photon absorption[21].

Table 1. Summary of TRPL decay of the as-prepared perovskite, and SSGP-perovskites using FABr-, FAI- and MACl-IPA solution. Parameters a, τ_1, τ_2, τ_{PL} are amplitude ratio, decay constants of fast and slow components and the averaged PL decays.

Concentration	a	τ_1 (ns)	τ_2 (ns)	τ_{PL} (ns)
Pero	0.62 ± 0.02	38.7 ± 2.4	312.0 ± 9.3	143.4 ± 5.1
FABr	0.35 ± 0.00	48.3 ± 2.4	392.0 ± 2.0	271.7 ± 1.8
FAI	0.38 ± 0.00	47.7 ± 1.5	389.0 ± 2.7	259.3 ± 2.5
MACl	0.33 ± 0.01	54.4 ± 1.7	409.2 ± 2.5	290.7 ± 2.4

Figure 7d shows the time-resolved PL (TRPL) of the as-prepared and SSGP perovskite light harvester layers using FABr, FAI and MACl. The TRPL decay of SSGP perovskites becomes much longer compared with that of the as-prepared perovskite, indicating that the optical lifetime of perovskites become significant longer after SSGP. The TRPL decay of perovskites consists with two components of fast and slow, coming from surface recombination and bulk radiative recombination of electron-hole pairs[36], respectively. The lifetime parameters of perovskites have been calculated using double exponential formula and summarized in **Table1**. The amplitude ratio and decay time of the fast-component remarkably reduces and increases, respectively, meaning that the surface recombination loss has been substantially decreased due to the promotion of perovskites' surface quality. Moreover, the slow-component lifetime significantly increases from ca. 310 to ca. 410 ns of the as-prepared and MACl-SSGP perovskites, and the amplitude of slow-component enlarges at same time. The longer lifetime of the fast- and slow-component indicates that the SSGP not only reduces the trap states of perovskite's surface on the as-prepared perovskite, but also promote the quality of bulk part in the perovskite. The improvement of optical properties of SSGP-perovskite suggests the promotion of charge-carrier diffusion length[10] and superior PV performance of SSGP-PSCs[22,33,37].

Figure 8 shows the integrated PL intensity mapping of the as-prepared and SSGP perovskites using FABr, FAI and MACl. The PL mapping of the as-prepared perovskite exhibits a spatially homogeneous intensity distribution compared with that of SSGP perovskites with a relative larger fluctuation, as shown Figures 8a-d. However, the average PL intensities of SSGP perovskites are remarkable enhanced compared with those of the as-prepared perovskite, which are well agreement with those in PL spectra in Figure 7.

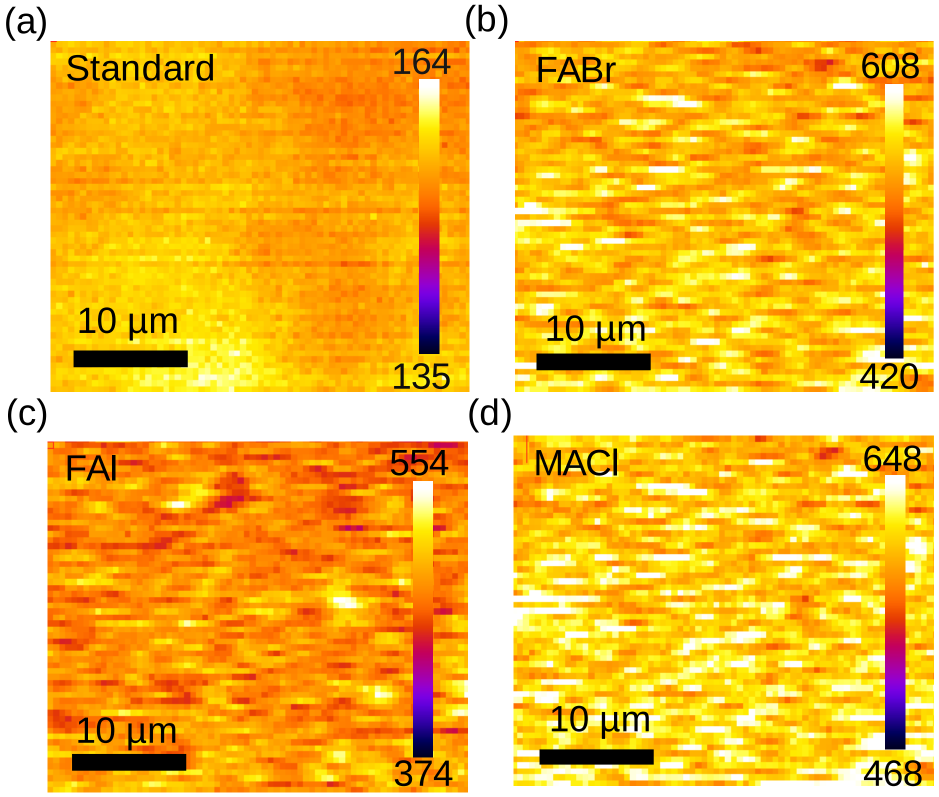

Figure 8. Optical properties of perovskites before and after treatment. (a-e) Integrated PL mapping of the as-prepared perovskite and SSGP perovskites using FABr-, FAI- and MACl-IPA solution. The scale bar is 1 µm.

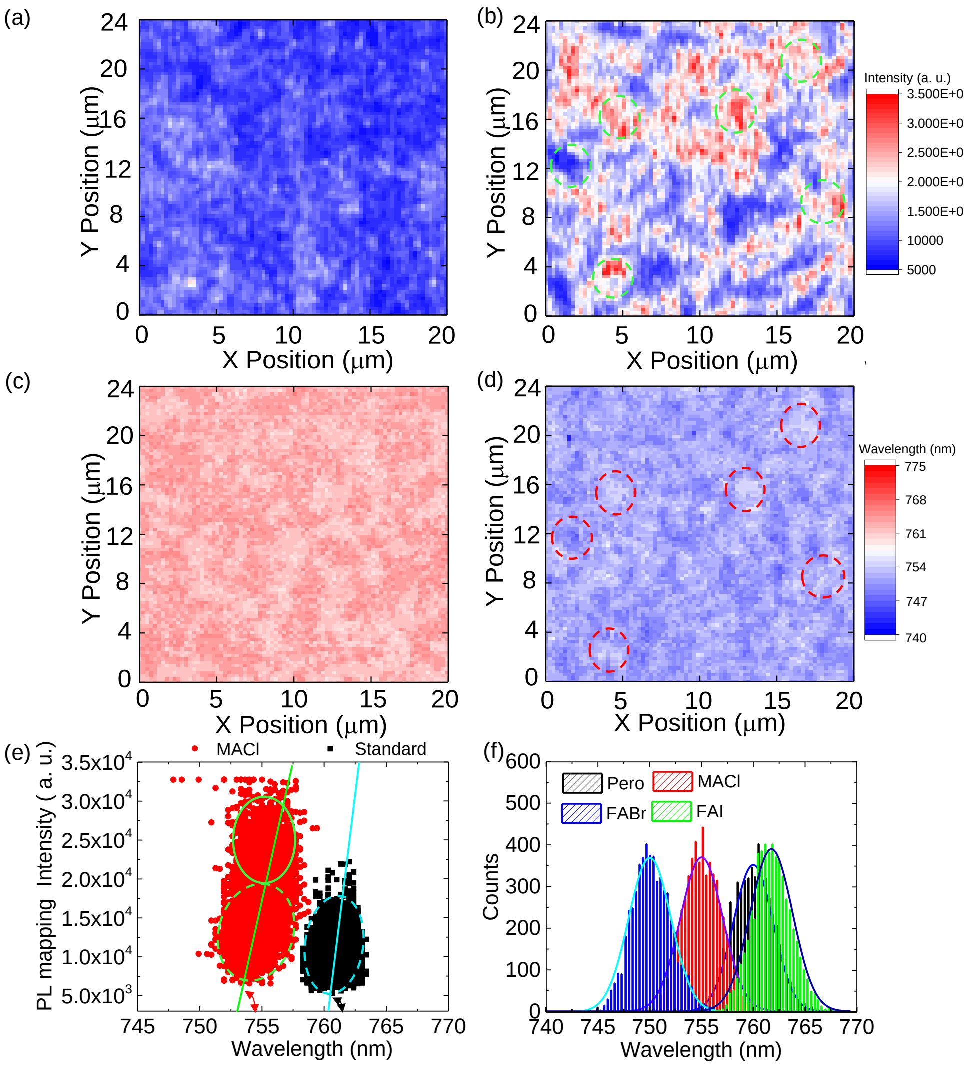

Figure 9. Optical properties of perovskites before and after SSGP treatment. (a, b) and (c, d) Intensity and wavelength position of the integrated PL mapping calculation of the as-prepared perovskite and SSGP perovskite using MACl-IPA solution, respectively. (e) Distribution of PL intensity as a functions of wavelength in the as-prepared and SSGP-MACl perovskite. (f) Distributions of full width at half maximum (FWHM) of PL spectra in as-prepared and SSGP perovskites using FABr, FAI and MACl, respectively.

The average PL intensities of MACl-SSGP perovskite reaches to maximum, therefore, this has been selected for more details analysis. A large amount of PL spectra (5476) have been collected to calculate the distribution of PL intensity as a function of the peak wavelength of the as-prepared and MACl-SSGP perovskites, as shown in **Figure 9a-**e. The PL intensity of MACl-SSGP perovskite shows a broad distribution compared with that of the as-prepared perovskite, and its distributed component consists of two parts, as marked using solid and dotted circles, where the distribution of the lower PL intensity component is similar to that of the as-prepared perovskite. The lower PL intensity of the as-prepared perovskite comes from the excessive $Pb(I_{0.8}Br_{0.2})_2$ with a large E_g of 2.3 eV[21], resulting in the reduction of photon absorption of perovskite light harvester layer and a higher non-radiative recombination loss. The improvement of the PL average intensity of MACl-SSGP perovskite results from the increment of PL intensity component attributing to the decrease of $Pb(I_{0.8}Br_{0.2})_2$ using SSGP, which is characterized using the experimental results of SEM and XRD in the Figures 2 and 6. The FABr- and FAI-SSGP perovskites achieve similar results on PL mapping and PL wavelength distribution is summarized in Figure 9f. The SSGP perovskite light harvester layers show a relative broader spectra position distribution compared with that of the as-prepared perovskite due to the reduction of the concentration of $Pb(I_{0.8}Br_{0.2})_2$.

Energy band alignment analysis of perovskite light harvester layer

The photoelectron yield spectroscopy has been applied to analyze the top of valance band (VB) of perovskite light harvester layers, including as-prepared and SSGP-perovskites (FABr, FAI and MACl). **Figure 10a** shows the photoelectron spectroscopy profile of the perovskite light harvester layers, the signals shift to the higher side in the order of of -5.46, -5.42, -5.41 and -5.39 eV of the as-prepared, FABr-, FAI- and MACl-SSGP perovskites, respectively. Figure 10b shows the energy of the VB top of the as-prepared, FABr-, FAI- and MACl-SSGP perovskites, respectively, compared with the

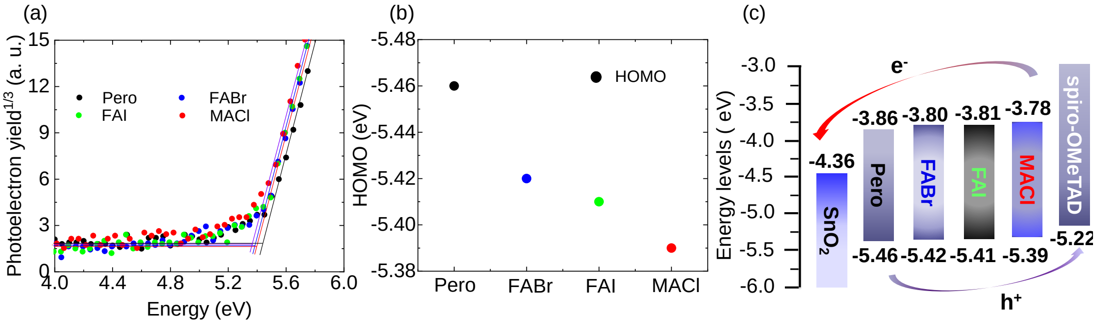

Figure 10. Energy alignment of the as-prepared perovskite and SSGP perovskite using FABr-, FAI- and MACl-IPA solution. (a) Photoelectron spectra of as-prepared and SSGP perovskite, as the photoelectron intensity is plotted by its third-root. The solid lines correspond to the guides for the energy positions of top of valence band. (b) Energy calculation of as-prepared perovskite and SSGP perovskite using FABr-, FAI- and MACl-IPA. (c) Band alignment of the PSCs of the as-prepared perovskite and SSGP perovskite using FABr-, FAI- and MACl-IPA, respectively.

vacuum level. The energy alignment has been calculated by combination with the E_g, bottom of conduction band (CB) and top of VB of the as-prepared, FABr-, FAI- and MACl-SSGP perovskites, respectively, as shown in Figure 10c. Interesting, the VB top and CB bottom of SSGP perovskites (in the order of FABr-, FAI- and MACl-SSGP perovskites) become relative shallower and shift to higher energy side compared with those of the as-prepared perovskite. The shallow VB will be optimized regarding the energy alignment between the perovskite and HTL, and accelerate the carrier transport. Moreover, the shallowed CB bottom of SSGP perovskites indicate that the efficiency of electron blocking function of perovskite layer will be enhanced, enrich the hole transfer in the interfaces between perovskite and HTL, and reduce the recombination possibilities of electron-hole. The carrier recombination possibilities of PSCs has been confirmed using impedance spectroscopy, which will be discussed later.

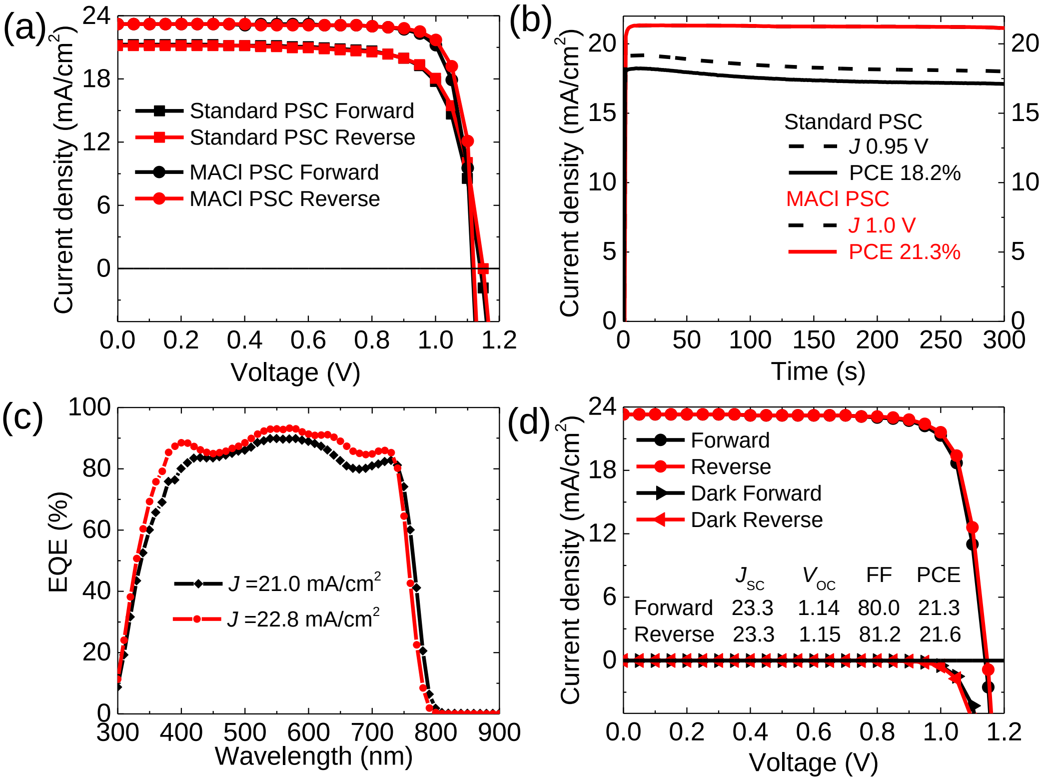

	J_{SC}	V_{OC}	FF	PCE
Forward	23.3	1.14	80.0	21.3
Reverse	23.3	1.15	81.2	21.6

Figure 11. Photovoltaic performance of standard and MACl-SSGP PSCs. (a) *J–V* curves, (b) SPO under MPP extracted from forward scanning condition, (c) EQE and integrated current-density of standard and MACl-SSGP PSCs, and (d) Best *J–V* curves performance of MACl-SSGP PSCs.

4.4.2 *J–V* characterization of perovskite solar cells

Photovoltaic performance on the small active area of 0.1 cm^2

The PSCs has been fabricated with referring above systematic analysis and achieved a high PV performance. **Figure 11** shows the PV performance of PSCs using the as-prepared perovskite (standard-PSCs) and SSGP PSCs using MACl treated perovskite (MACl-SSGP PSCs). The current density–voltage (*J–V*) curves of PSCs are recorded with two scanning directions with a scanning rate of 50 mV/s as following: the forward scanning from J_{SC} to V_{OC}, and the reverse scanning from V_{OC} to J_{SC}.

Table 2. Summary of photovoltaic parameters of the standard and MACl-SSGP PSCs, as shown in Figure 11a.

Sample	Scan direction	J_{SC} (mA/cm^2)	V_{OC} (V)	FF (%)	PCE (%)
Standard PSCs	Forward	21.3	1.14	75.4	18.3
	Reverse	21.2	1.15	75.3	18.4
Second growth PSCs	Forward	23.1	1.12	82.0	21.2
	Reverse	23.1	1.12	83.4	21.5

Table 3. Summary of the superior PV performances for heterojunction PSCs with a similar FF value in recent studies. The normal planar heterojunction PSCs based on the SSGP in our study exhibit an optimized interface with the highest FF—even higher than some inverted architectures—along with a high power conversion efficiency. “I” represents the inverted architecture (p-i-n), and “N” represents the normal architecture (n-i-p).

J_{SC} (mA/cm^2)	V_{OC} (V)	FF (%)	PCE (%)	Reference
23.1	1.12	83.4	21.5	This work
23.7	1.14	78.0	21.6	[37] (N)
20.6	0.99	84.0	17.1	[31] (I)
20.6	1.03	85.0	18.0	[39] (I)
18.1	0.86	86.7	13.5	[30] (I)
20.6	1.08	81.9	18.1	[40] (I)
20.5	0.97	84.0	16.8	[41] (I)
22.5	1.21	79.0	21.5	[5] (I)
20.2	0.97	82.0	16.0	[42] (I)
25.0	1.11	81.7	22.6	[2] (N)
23.7	1.13	80.6	21.5	[3] (N)
23.5	1.03	83.0	20.1	[43] (I)

The PV performance of PSCs has been remarkable promoted after using SSGP with a negligible hysteresis, as shown in Figure 11a and **Table 2**. The all parameters of the standard and SSGP PSCs are summarized and shown in Table 2, including forward and reverse scanning. The J_{SC} and FF of PSCs significantly promote from 21.2 to 23.1 mA/cm^2 and from 75.3 to 83.4%, respectively, after applying the SSGP technique under reverse scanning condition. The achieved FF value in the SSGP-PSCs is the highest result in the normal architecture with a high V_{OC}[38,39] and comparable with those in some inverted structure devices[40–44] according to the summary of **Table 3**, which is very close to the Shockley-Queisser limit (~90%) at room temperature[2,3,45]. The PCE also substantially increases from 18.4 to the 21.5% from standard- to MACl-SSGP PSCs. The relative unsatisfied PV performance of standard-PSCs should attribute to the excessive PbI_2 with high bandgap of 2.3 eV[21,28,35,46,47], because the as-prepared perovskite contains large concentration of $Pb(I_{0.8}Br_{0.2})_2$, which will decrease the light absorption and cause serious carrier recombination loss at $Pb(I_{0.8}Br_{0.2})_2$.

Table 4. Summary of the PV performances for planar heterojunction SSGP-PSCs with various MACl-IPA solution concentrations. Five samples were tested.

Concentration (mg/mL)	Scanning direction	J_{SC} (mA/cm^2)	V_{OC} (V)	FF (%)	PCE (%)
3	Forward	23.1 ± 0.1	1.14 ± 0.01	76.3 ± 0.0	20.0 ± 0.2
	Reverse	23.1 ± 0.1	1.14 ± 0.00	77.5 ± 0.0	20.4 ± 0.2
5	Forward	23.1 ± 0.0	1.14 ± 0.01	78.1 ± 0.0	20.6 ± 0.2
	Reverse	23.2 ± 0.1	1.14 ± 0.01	79.8 ± 0.0	20.9 ± 0.2
8	Forward	22.8 ± 0.2	1.15 ± 0.01	75.9 ± 0.0	19.9 ± 0.3
	Reverse	22.9 ± 0.1	1.15 ± 0.01	77.5 ± 0.0	20.0 ± 0.4

Table 5. Summary of the PV performances for planar heterojunction SSGP-PSCs fabricated at various annealing temperature. Five MACl SSGP PSCs samples were tested.

Annealing time (min)	Scanning direction	J_{SC} (mA/cm^2)	V_{OC} (V)	FF (%)	PCE (%)
10	Forward	22.9 ± 0.1	1.13 ± 0.01	77.6 ± 0.0	20.1 ± 0.3
	Reverse	23.0 ± 0.1	1.12 ± 0.01	78.5 ± 0.0	20.2 ± 0.3
15	Forward	23.1 ± 0.0	1.14 ± 0.01	78.1 ± 0.0	20.6 ± 0.2
	Reverse	23.2 ± 0.1	1.14 ± 0.01	79.8 ± 0.0	20.9 ± 0.2
20	Forward	22.9 ± 0.1	1.14 ± 0.01	76.3 ± 0.0	19.8 ± 0.2
	Reverse	22.9 ± 0.1	1.14 ± 0.01	77.8 ± 0.0	20.4 ± 0.3

The stabilized power output (SPO) is characterized using a bias voltage extracting from the *J–V* curves under the maximum-power-point (MPP), as shown in Figure 11b. The SPO significantly enhances from 18.2% of the standard-PSCs to 21.3% of the MACl-SSGP PSCs and exhibits a better stability.

The incident-photon-to-current-efficiency spectroscopy (IPCE) has been applied to record the external quantum efficiency (EQE) of the standard and MACl-SSGP PSCs. Figure 11c shows the EQE spectra of standard and MACl-SSGP PSCs. The EQE of MACl-SSGP PSCs achieves a high average value of 88.4% at a range from 400 to 730 nm and a 22.8 mA/cm^2 of integrated current-density, which is remarkable higher than that of 84.9% of EQE values of the standard PSCs with an integrated current density of 21.0 mA/cm^2. The MACl-SSGP PSCs obtain a higher value of EQE at ca. 400 nm compared with that of the standard PSCs because of the elimination of $Pb(I_{0.8}Br_{0.2})_2$, and the signal decrease at a relative shorter wavelength at ca. 800 nm because of the E_g increment of perovskite layer after SSGP[20].

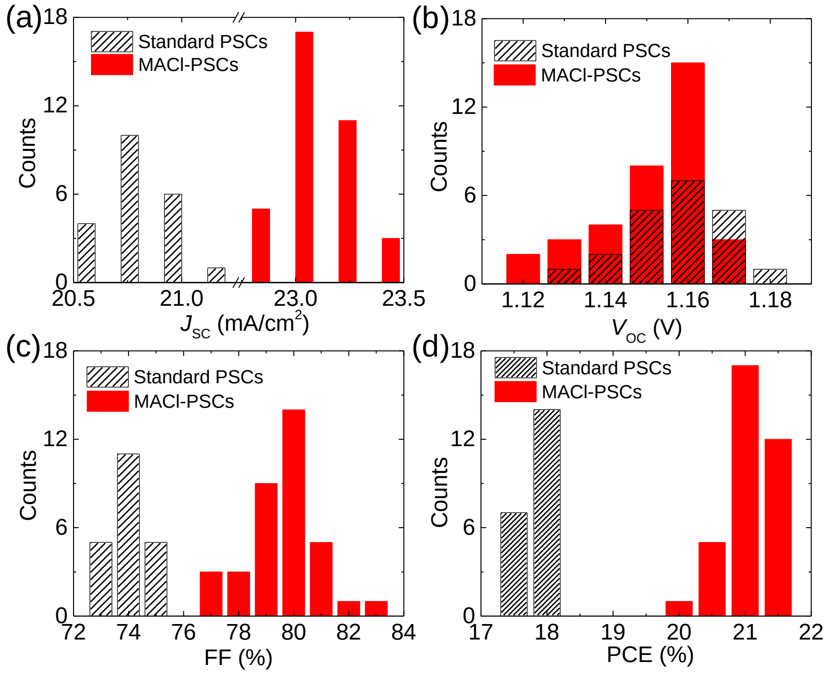

Figure 12. Reproducibility property of the standard and MACl-SSGP PSCs. (a-d) Statistical calculation of the standard and MACl-SSGP PSCs, including J_{SC}, V_{OC}, FF and PCE. (Black: 20 standard PSCs; red: 35 MACl-SSGP PSCs).

The highest PV performance of the MACl-SSGP PSCs has been shown in the Figure

11d. The MACl-SSGP PSCs achieves a high PCE of 21.3 (21.6)% with a V_{OC} of 1.14 (1.15) V, a Jsc of 23.3 (23.3) mA/cm^2, and a FF of 80.0 (81.2)% measured at forward (reverse) voltage scanning with a negligible hysteresis. The PCE of MACl-SSGP PSCs is substantially higher than those of inverted structures devices with a high FF (>80.0%) and comparable to those of normal structure photovoltaics with a high FF according to the summarization of Table 3.

A large amount of the standard and MACl-SSGP PSCs (20 and 36 devices, respectively) have been fabricated to evaluate the repeatability of PV performance, as shown in **Figure 12**. The MACl-SSGP PSCs achieves a substantially higher PCE compared with that of the standard PSCs with a narrower distribution according to Figure 12a. All parameters

Table 6. Summary of the PV performances for planar heterojunction PSCs treated with various concentrations of spiro-OMeTAD chlorobenzene. 5 samples were tested.

Concentration (mg/mL)	Scanning direction	J_{SC} (mA/cm^2)	V_{OC} (V)	FF (%)	PCE (%)
0	Forward	23.1 ± 0.0	1.14 ± 0.01	78.1 ± 0.0	20.6 ± 0.2
	Reverse	23.2 ± 0.1	1.14 ± 0.01	79.8 ± 0.0	20.9 ± 0.2
2	Forward	23.1 ± 0.1	1.14 ± 0.01	79.4 ± 0.0	21.0 ± 0.2
	Reverse	23.2 ± 0.1	1.14 ± 0.02	80.3 ± 0.0	21.3 ± 0.1
5	Forward	22.9 ± 0.1	1.15 ± 0.01	75.5 ± 0.0	19.8 ± 0.3
	Reverse	22.9 ± 0.1	1.15 ± 0.01	78.4 ± 0.0	20.7 ± 0.3

Table 7. Summary of the PV performances for planar heterojunction SSGP-PSCs prepared with various SSGP solution of FABr-, FAI-, MACl- and FACl-IPA. The standard PSCs contain 20 samples, FABr-, FAI- and FACl-SSGP PSCs contain 10 samples, and the MACl-SSGP PSCs comprise 36 samples.

Sample name	Scanning direction	J_{SC} (mA/cm^2)	V_{OC} (V)	FF (%)	PCE (%)
Standard PSCs	Forward	20.9 ± 0.2	1.16 ± 0.01	72.3 ± 0.0	17.4 ± 0.3
	Reverse	21.0 ± 0.2	1.16 ± 0.01	73.4 ± 0.0	18.0 ± 0.2
FABr-PSCs	Forward	23.1 ± 0.1	1.16 ± 0.00	75.4 ± 0.0	20.2 ± 0.3
	Reverse	23.1 ± 0.1	1.16 ± 0.01	76.7 ± 0.0	20.5 ± 0.3
FAI-PSCs	Forward	23.1 ± 0.2	1.12 ± 0.02	77.0 ± 0.0	19.9 ± 0.4
	Reverse	23.2 ± 0.2	1.12 ± 0.02	77.8 ± 0.0	20.1 ± 0.4
MACl-PSCs	Forward	23.1 ± 0.1	1.14 ± 0.02	79.2 ± 0.0	20.9 ± 0.4
	Reverse	23.1 ± 0.1	1.14 ± 0.02	80.1 ± 0.0	21.2 ± 0.3

of MACl-SSGP PSCs are higher than those of the standard PSCs except for the V_{OC}, as shown in Figure 12c.

In order to explore the optimized condition for the MACl-SSGP PSCs, the various conditions have been studied during the SSGP fabrication, including the various concentrations of MACl in IPA solution of **Table 4**, diverse post-treated time after dropping the MACl-IPA solution of **Table 5** and various concentrations of spiro-OMeTAD surface treatment of **Table 6**. The MACl-SSGP PSCs achieves a highest PV performance at condition of 5 mg/mL of MACl-IPA solution, 15 min of the post-treatment and 2 mg/mL of spiro-OMeTAD.

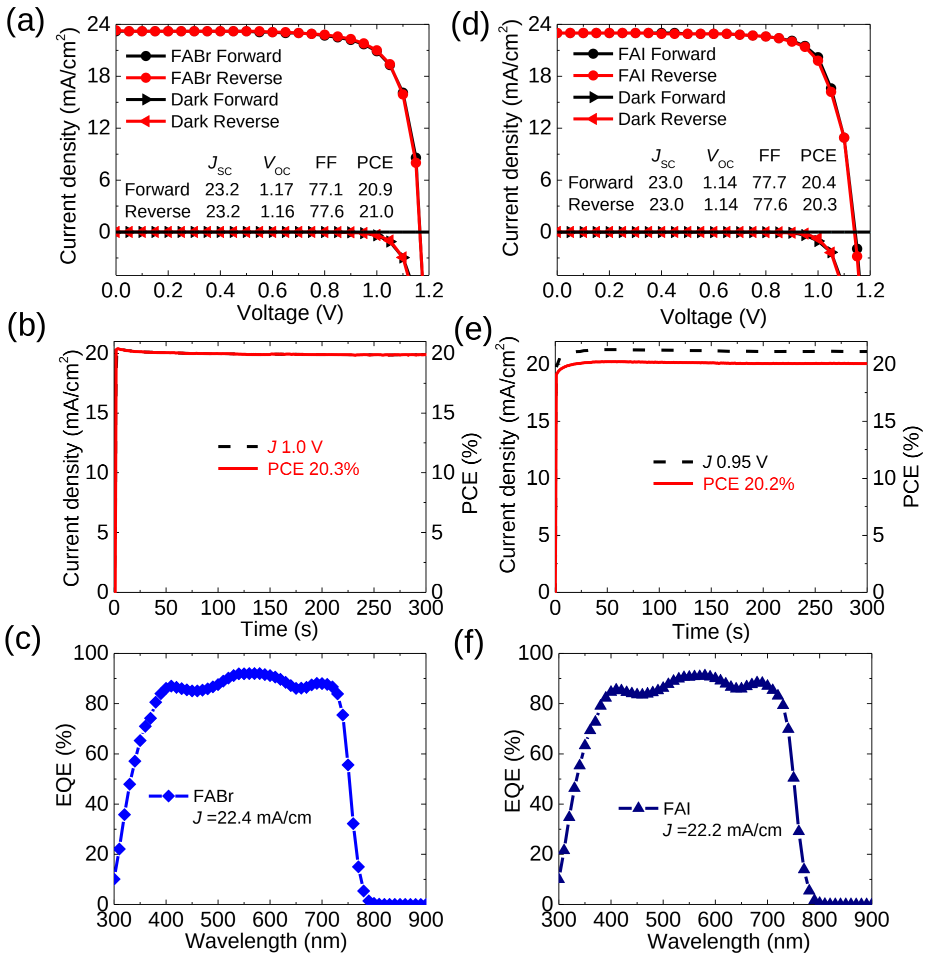

Figure 13. PV performance of the FABr- and FAI-SSGP PSCs. (a, d) *J–V* curves, (b, e) SPO under MPP extracted from forward scanning condition, (c, f) EQE and integrated current-density of the FABr- and FAI-SSGP PSCs, respectively.

The optimized condition of MACl-SSGP PSCs fabrication parameters have been introduced into the FABr- and FAI-SSGP PSCs preparation, as shown in **Figure 13**. The FABr- and FAI-SSGP PSCs achieves a high PV performance, including a high PCE of 20.9 (21.0)% with a V_{OC} of 1.17 (1.16) V, a *J*sc of 23.2 (23.2) mA/cm^2, and a FF of 77.1 (77.6)% for FABr based devices; and a high PCE of 20.4 (20.3)% with a V_{OC} of 1.14 (1.14) V, a *J*sc of 23.0 (23.0) mA/cm^2, and a FF of 77.7 (77.6)% for FAI based device. However, these values are relative lower compared with those of the PV performance of MACl-SSGP PSCs, which are well consistent with analyzed results of surface morphologies, optical properties, and energy alignment. The repeatability of FABr- and FAI-SSGP PSCs are summarized in the **Table 7**. Notably, FABr-SSGP PSCs obtains a higher V_{OC} of 1.17 V compared with that of the FAI-SSGP PSCs (1.14 V) according to the Figure 13.

The "passivation layer" of spiro-OMeTAD affects the PV performance, which has been shown in **Figure 14**. The spiro-OMeTAD passivated PSCs have achieved a high PCE of 19.1 (19.3)% with a V_{OC} of 1.16 (1.16) V, a *J*sc of 21.9 (21.7) mA/cm^2, and a FF of 75.6 (75.9)% with a very small hysteresis, as shown in Figure 14a. A high SPO of 18.6% has been obtained with a relative stable value according to Figure 14b.

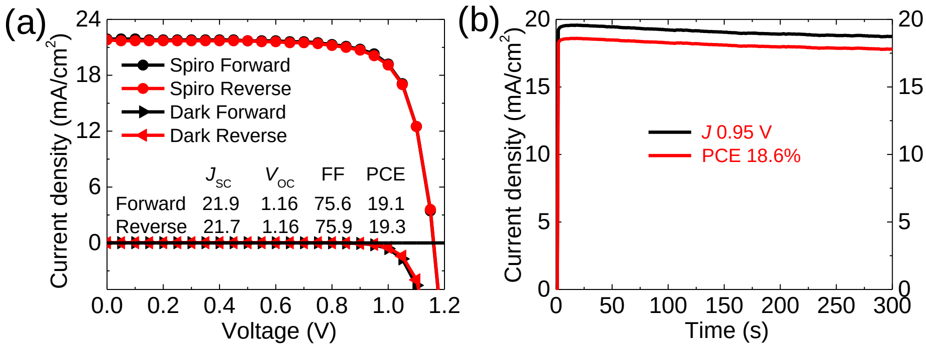

	J_{SC}	V_{OC}	FF	PCE
Forward	21.9	1.16	75.6	19.1
Reverse	21.7	1.16	75.9	19.3

Figure 14. PV performance of PSCs after spiro-OMeTAD treatment with concentration of 2 mg/mL. (a) *J–V* curves, (b) Time evolution of SPO under MPP extracted from forward scanning condition of PSCs.

The FF promotion is usually accompanied by the V_{OC} decrease according to previously literatures' observations[31,39,48–50], however, a high PV performance of SSGP PSCs has obtained without sacrificing the V_{OC} and increasing the FF in my study. Interesting that the thickness of spiro-OMeTAD passivated layer also seriously affects the PV performance of PSCs, because the performance and the hysteresis of SSGP PSCs become obviously worse and larger after the concentration of spiro-OMeTAD exceeding over 2 mg/mL.

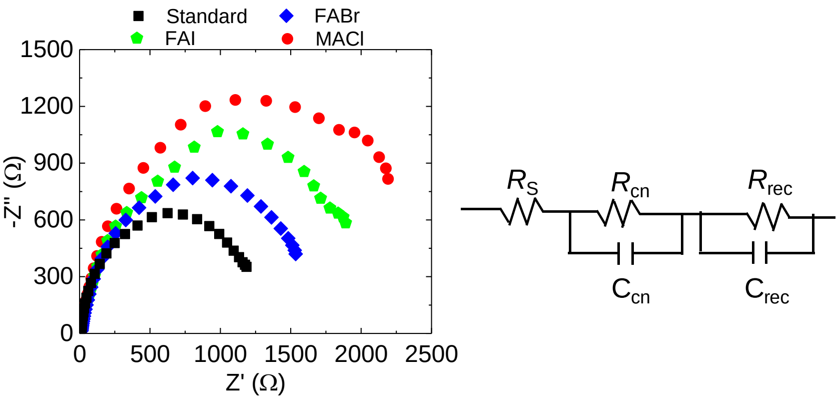

Figure 15. Nyquist plots for the standard and SSGP PSCs using FABr, FAI and MACl under illumination at bias voltage of 0.1 V. The right figure shows the equivalent circuit diagram of the PSCs.

Carrier recombination loss property of perovskite solar cells

Figure 15 shows the impedance spectra of the standard and SSGP PSCs using FABr, FAI and MACl. The Nyquist plots consist of two-semicircles, including two regions of the high and low frequency. The low frequency region signal is contributed by the recombination resistance (R_{rec})[51] and capacitance of the simulated equivalent circuit model. The larger arcs in the low frequency regions indicates a higher R_{rec} of SSGP PSCs compared with that of the standard PSCs, meaning a lower carrier recombination possibility in the order of FABr, FAI, and MACl. The lower carrier recombination loss in SSGP PSCs is well agreement with the analysis of higher carrier extraction efficiency

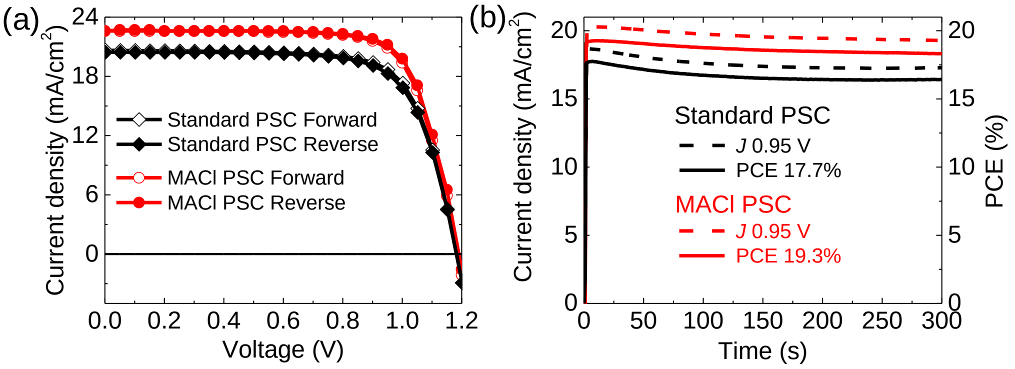

Figure 16. PV performance of the standard and MACl-SSGP PSCs on a large active area of 1 cm^2. (a) *J*–*V* curves, (b) Time evolution of SPO under MPP extracted from forward scanning condition of PSCs.

from band alignment in Figure 10.

Table 8. Summary of the PV performances for planar heterojunction standard and MACl-SSGP PSCs with large active area of 1.0 cm^2 under forward and reverse scanning.

Concentration (mg/mL)	Scanning direction	J_{SC} (mA/cm^2)	V_{OC} (V)	FF (%)	PCE (%)
Standard PSCs	Forward	20.6	1.18	72.9	17.8
	Reverse	20.5	1.18	72.0	17.4
Second growth PSCs	Forward	22.6	1.19	74.0	19.9
	Reverse	22.6	1.19	74.5	20.1

Photovoltaic performance on the large active area of 1 cm^2

The active area enlargement of PSCs has already become a one of main study trend because of promoting the commercial applications. A large active area of 1.0 cm^2 of standard and MACl-SSGP PSCs have been fabricated using the optimized condition. **Figure 16a** shows the *J*–*V* curves of the standard and MACl-SSGP PSCs. The MACl-SSGP PSCs achieves a high PCE of 20.1% with a V_{OC} of 1.19 V, a *J*sc of 22.6 mA/cm^2, and a FF of 74.5% under reverse scanning with a negligible hysteresis; these parameters are much higher than those of standard PSCs with a high PCE of 17.4% with a V_{OC} of 1.18 V, a *J*sc of 20.6 mA/cm^2, and a FF of 72.0% under reverse scanning. The parameters of forward scanning of large active area are summarized in **Table 8**. The high value of FF in MACl-SSGP PSCs can be compared with the record value in the previously literatures on the large active area[18,52–54]. The SPO of 19.3% of MACl-SSGP PSCs is also higher than that of standard PSCs (17.7%) under a bias voltage of 0.95 V extracted from the MPP of *J*–*V* curves under forward scan, as shown in Figure 18b. The repeatability of large

Table 9. Summary of the PV performances for planar heterojunction standard and MACl-SSGP PSCs with a large active area of 1.0 cm^2. For each case, 9 samples were tested.

Sample name	Scanning direction	J_{SC} (mA/cm^2)	V_{OC} (V)	FF (%)	PCE (%)
Standard PSCs	Forward	20.8 ± 0.3	1.19 ± 0.01	69.7 ± 0.0	17.3 ± 0.3
	Reverse	20.7 ± 0.3	1.18 ± 0.01	68.2 ± 0.0	16.6 ± 0.5
MACl-PSCs	Forward	22.8 ± 0.2	1.18 ± 0.01	72.0 ± 0.0	19.2 ± 0.4
	Reverse	22.8 ± 0.2	1.18 ± 0.01	73.7 ± 0.0	19.7 ± 0.3

active area PSCs has been fabricated and summarized in the **Table 9**, indicating a superior performance of the MACl-SSGP PSCs even increasing the active area up to 1.0 cm^2.

4.4.3 Stability evaluation of perovskite solar cells

Stability evaluation of PV devices

Even though PSCs have obtained an unprecedented progress on PCE, the stability development is still far behind and limits the commercial application. Therefore, the continuously light soaking and high temperature stabilities of the standard and MACl-SSGP PSCs have been characterized under the harsh conditions with a high humidity of ca. 50% and a high treatment temperature of 80 °C without any encapsulations.

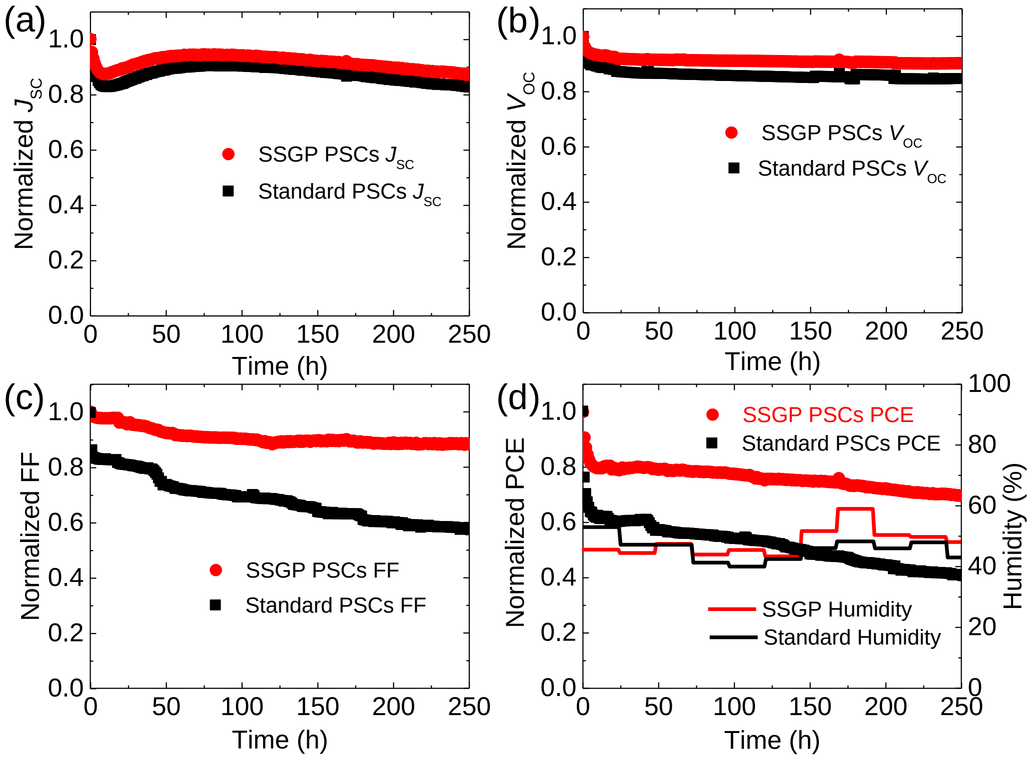

Figure 17. Continuous light soaking stability of the standard and MACl-SSGP PSCs. (a-d) Summary of PV parameters of the standard and MACl-SSGP PSCs under continuous light soaking. The humidity of measurements is also shown.

Figure 17 shows the characterized results of the continuously light soaking stability of the standard and MACl-SSGP PSCs. The PCE quickly decreases to ca. 80% at short time and can sustain about 70.0% of compared with the initial value of MACl-SSGP PSCs even after 250 hours continuous light soaking, which is much higher than of the standard PSCs with about 40.3%, as shown in Figure 17a. The quickly reduction of PCE of PSCs results from the remarkable decrease of J_{SC}, which should attribute to the serious variation of interface conditions of components in PSCs. The parameters of V_{OC} and J_{SC} can sustain relative high values even finishing the final measurement in both PSCs. The main reduction of PCE of PSCs should attribute to the decrease of the FF, however, the MACl-SSGP PSCs can maintain a value of ca. 88.1% of FF and higher than the standard PSCs (ca. 57.3%), as shown in Figure 17d.

Figure 18 shows the evaluated results of the high temperature treatment of the standard and MACl-SSGP PSCs. The MACl-SSGP PSCs can maintain a higher thermal stability of ca. 75.0% compared with the initial PCE even after 270 hours treatment in the nitrogen condition, which is much higher than that of the standard PSCs. The parameters of V_{OC} and J_{SC} of MACl-SSGP PSCs can keep much better stability than the standard PSCs according to the Figures 18b and c. The main reduction of both devices should attribute to the FF deterioration, as shown in Figure 18d, because the interfaces between the perovskite and HTL become worse and increase the series resistance of PSCs. This

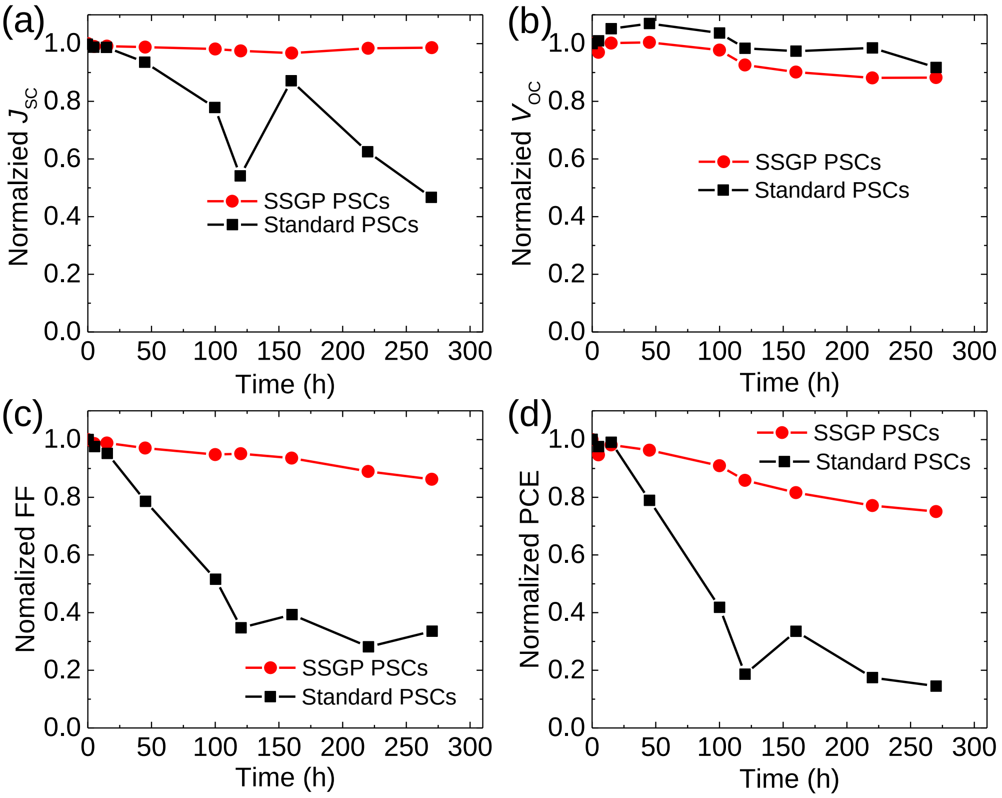

Figure 18. Thermal stability characterization of the standard and MACl-SSGP PSCs. (a-d) Summarization of PV parameters of the standard and MACl-SSGP PSCs under 80 °C in nitrogen condition.

hypothesis has been confirmed by using the cross-sectional morphology of PSCs using the SEM. **Figure 19** shows the cross-sectional morphology variation of the standard and MACl-SSGP PSCs after 270 hours thermal treatment. The cross-sectional morphology of standard PSCs exhibits a much high density of voids between the perovskite and HTL compared with those of the MACl-SSGP PSCs, demonstrating the reason that the MACl-SSGP PSCs can sustain much better thermal stability. Therefore, the MACl-SSGP PSCs can keep a higher stability under continuously light soaking and thermal treatment compared with the standard PSCs because of the promotion of the quality of perovskite light harvester layer, and interfaces between perovskite and HTL using SSGP.

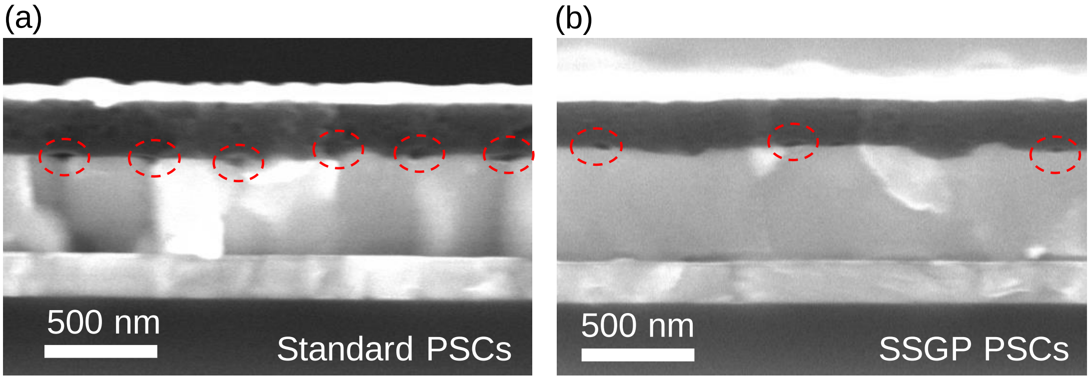

Figure 19. Cross-sectional morphology characterization of the standard and MACl-SSGP PSCs after thermal stability measurement after 270 h. (a, b) Cross-sectional SEM images of the standard and MACl-SSGP PSCs. The scale bar is 500 nm.

Stability evaluation of perovskite light harvester layer

The enhancement of stability should come from the improvement of perovskite light harvester layer, especially the thermal stability, because the organic nature of spiro-OMeTAD cannot sustain such high temperature of 80 °C. The XRD and PL spectroscopy have been applied to monitor the degradation of the as-prepared and SSGP-perovskite light harvester layers after 10 days storage at room condition.

Figure 20 shows the XRD characterization of the as-prepared and SSGP-perovskite light harvester layers after 10 days aging. The diffraction signal of $Pb(I_{0.8}Br_{0.2})_2$ of XRD patterns become obvious and the intensity increases, as show in Figure 20a, where the humidity values of each days have been recorded and shown in **Table 10**. The increase scale of the $Pb(I_{0.8}Br_{0.2})_2$ diffraction intensity of SSGP perovskites is smaller than that of the as-prepared perovskite in Figure 20b, indicating that the anti-humidity ability of perovskite light harvester layer has been enhanced after using SSGP.

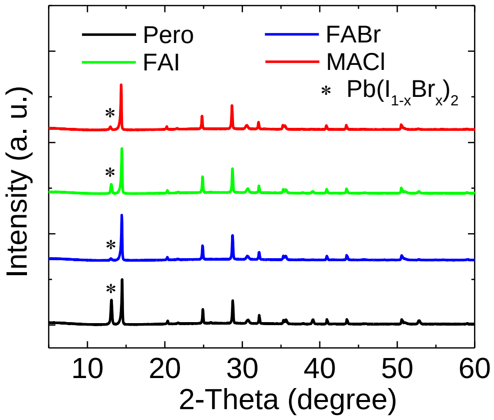

Figure 20. XRD patterns of the as-prepared perovskite and FABr-, FAI-, and MACl-SSGP perovskite films after 10 days of aging with a high humidity at room temperature (ca. 25 °C).

Table 10. Humidity-recorded values of the as-prepared perovskite and FABr-, FAI-, and MACl-SSGP perovskite films for 10 days at room temperature (ca. 25 °C).

Concentration	Day 1	Day 2	Day 3	Day 4	Day 5	Day 6	Day 7	Day 8	Day 9	Day 10
Humidity (%)	68	70	68	67	71	62	65	68	77	82

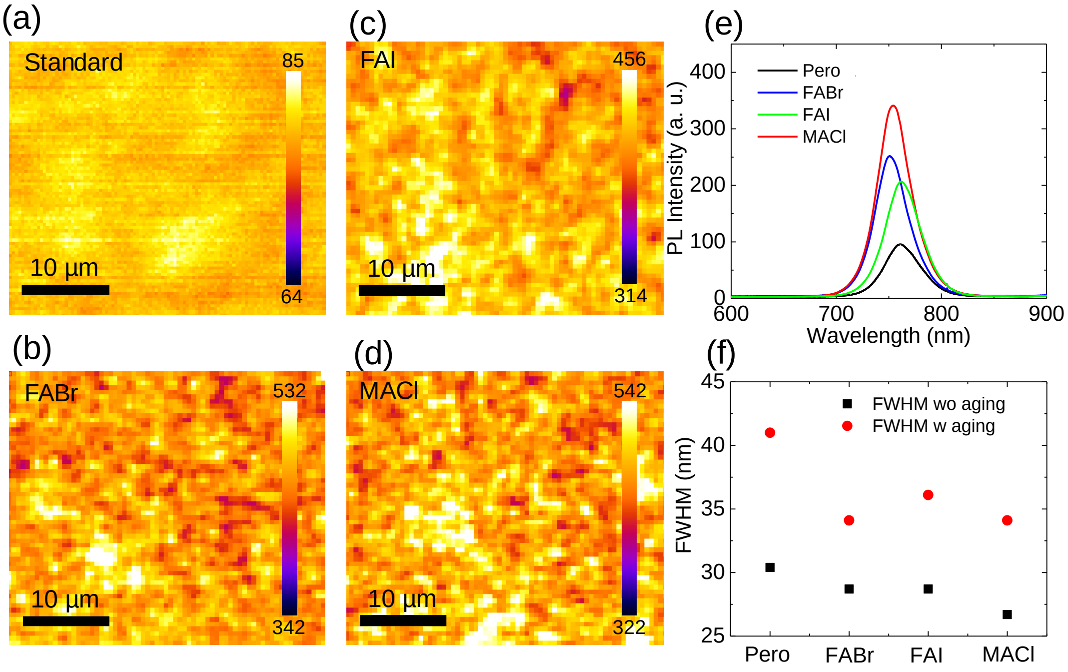

Figure 21. (a–d) Integrated PL intensity mapping of the as-prepared and FABr, FAI and MACl-SSGP perovskite films, respectively, after 10 days aging. (e, f) PL spectra and FWHM of the as-prepared and SSGP perovskite films after 10 days aging.

Figure 21 shows the PL spectra of the as-prepared and SSGP-perovskite light harvester layers after 10 days aging. The PL mapping and spectral intensity become lower after 10 days aging, however, the reduction scale of intensity of the SSGP-perovskites is much smaller than that in the as-prepared perovskite, as shown in Figures 21a-e. The FWHM of the PL spectra are summarized in Figure 21f, indicating that the FWHM become larger after 10 days aging, but the increment scale of as-prepared perovskite is much higher than that in the SSGP-perovskites. Therefore, the quality of perovskite light harvester layers has been dramatically promoted using SSGP compared with that of the as-prepared perovskite, which has been confirmed by evolutions of PV performance described above.

4.5 Chapter summary

A superior PV performance of PSCs has been achieved using the technique of excessive PbI_2 and the SSGP. The crystallinity and crystal grain size of perovskite light harvester layer have been promoted using excessive PbI_2 during the fabrication of first layer. The quality of perovskite layers is further improving using the SSGP by reacting the excessive $Pb(I_{0.8}Br_{0.2})_2$. The SSGP could sustain the large crystal size of perovskite layer, accompanying by the surface trap states elimination. Therefore, the MACl-SSGP PSCs achieves a high PV performance with a highest FF of 83.4% of planar normal architecture devices without sacrificing the J_{SC} and V_{OC}. The MACl-SSGP PSCs also obtains a highest PCE of 21.6% with a negligible hysteresis under reverse scanning in this study. The MACl-SSGP PSCs can sustain an excellent continuous light soaking stability of ca. 70% of initial PCE value even after 250 hours working and a thermal stability of ca. 75% of initial PCE value even after 270 hours treatment at 80 °C in nitrogen condition. A high PCE of 20.1% of MACl-SSGP PSCs has obtained at a large active area of 1.0 cm^2, which is much higher than that of 17.8% in the standard PSCs. The SSGP technique not only enhances the crystallinity of perovskite, but also remarkably improves the carrier extraction from perovskite to HTL, and decreases the carrier recombination loss at the interface between the perovskite and HTL, resulting a high PV performance and stability of PSCs. The proposed SSGP technique could be paid as a milestone of fabrication of PSCs toward commercial applications.

Reference

1. Wang, S. *et al.* Accelerated degradation of methylammonium lead iodide perovskites induced by exposure to iodine vapour. *Nat. Energy* **2**, 16195 (2017).

2. Yang, W. S. *et al.* Iodide management in formamidinium-lead-halide-based perovskite layers for efficient solar cells. *Science* **356**, 1376–1379 (2017).
3. Jiang, Q. *et al.* Planar-structure perovskite solar cells with efficiency beyond 21%. *Adv. Mater.* **29**, 1703852 (2017).
4. Peng, J. *et al.* A universal double-side passivation for high open-circuit voltage in perovskite solar cells : role of carbonyl groups in poly (methyl methacrylate). *Adv. Energy Mater.* **8**, 1801208 (2018).
5. Luo, D. *et al.* Enhanced photovoltage for inverted planar heterojunction perovskite solar cells. *Science* **1446**, 1442–1446 (2018).
6. Yang, F. *et al.* Roles of polymer layer in enhanced photovoltaic performance of perovskite solar cells via interface engineering. *Adv. Mater. Interfaces* **5**, 1701256 (2018).
7. Yang, Y. *et al.* Enormously improved $CH_3NH_3PbI_3$ film surface for environmentally stable planar perovskite solar cells with PCE exceeding 19.9%. *Nano Energy* **48**, 10–19 (2018).
8. Cai, F. *et al.* Molecular engineering of conjugated polymers for efficient hole transport and defect passivation in perovskite solar cells. *Nano Energy* **45**, 28–36 (2018).
9. Best Research-Cell Efficiencies Chart. National Renewable Energy Laboratory (NREL), https://www.nrel.gov/pv/assets/pdfs/best-research-cell-efficiencies-190416 (2019).
10. Stranks, S. D. *et al.* Electron-hole diffusion lengths exceeding 1 micrometer in an organometal trihalide perovskite absorber. *Science* **342**, 341–344 (2013).
11. Dong, Q. *et al.* Electron-hole diffusion lengths >175 μm in solution-grown $CH_3NH_3PbI_3$ single crystals. *Science* **347**, 967–970 (2015).
12. Herz, L. M. Charge-carrier mobilities in metal halide perovskites: fundamental mechanisms and limits. *ACS Energy Lett.* **2**, 1539–1548 (2017).
13. Jeon, N. J. *et al.* Compositional engineering of perovskite materials for high-performance solar cells. *Nature* **517**, 476–480 (2015).
14. Eperon, G. E. *et al.* Perovskite-perovskite tandem photovoltaics with optimized band gaps. *Science* **354**, 861–865 (2016).
15. Saliba, M. *et al.* Cesium-containing triple cation perovskite solar cells: improved stability, reproducibility and high efficiency. *Energy Environ. Sci.* **9**, 1989–1997 (2016).
16. Heo, J. H. *et al.* Efficient inorganic-organic hybrid heterojunction solar cells containing perovskite compound and polymeric hole conductors. *Nat. Photon.* **7**,

486–491 (2013).

17. Wang, Z. *et al.* Efficient ambient-air-stable solar cells with 2D–3D heterostructured butylammonium-caesium-formamidinium lead halide perovskites. *Nat. Energy* **2**, 17135 (2017).
18. Li, X. *et al.* A vacuum flash-assisted solution process for high-efficiency large-area perovskite solar cells. *Science* **353**, 58–62 (2016).
19. Momblona, C. *et al.* Efficient vacuum deposited p-i-n and n-i-p perovskite solar cells employing doped charge transport layers. *Energy Environ. Sci.* **9**, 3456–3463 (2016).
20. Cho, K. T. *et al.* Highly efficient perovskite solar cells with a compositionally engineered perovskite/hole transporting material interface. *Energy Environ. Sci.* **10**, 621–627 (2017).
21. Chen, Q. *et al.* Controllable self-induced passivation of hybrid lead iodide perovskites toward high performance solar cells. *Nano Lett.* **14**, 4158–4163 (2014).
22. Roldán-Carmona, C. *et al.* High efficiency methylammonium lead triiodide perovskite solar cells: The relevance of non-stoichiometric precursors. *Energy Environ. Sci.* **8**, 3550–3556 (2015).
23. Jacobsson, T. J. *et al.* Unreacted PbI_2 as a double-edged sword for enhancing the performance of perovskite solar cells. *J. Am. Chem. Soc.* **138**, 10331–10343 (2016).
24. Abate, A. *et al.* Efficient luminescent solar cells based on tailored mixed-cation perovskites. *Sci. Adv.* **2**, e1501170 (2016).
25. Jiang, Q. *et al.* Enhanced electron extraction using SnO_2 for high-efficiency planar-structure $HC(NH_2)_2PbI_3$-based perovskite solar cells. *Nat. Energy* **2**, 16177 (2016).
26. Kim, Y. C. *et al.* Beneficial effects of PbI_2 incorporated in organo-lead halide perovskite solar cells. *Adv. Energy Mater.* **6**, 1502104 (2016).
27. Liu, F. *et al.* Is excess PbI_2 beneficial for perovskite solar cell performance? *Adv. Energy Mater.* **6**, 1502206 (2016).
28. Gujar, T. P. *et al.* The role of PbI_2 on $CH_3NH_3PbI_3$ perovskite stability, solar cell parameters and device degradation. *Phys. Chem. Chem. Phys.* **85**, 605–614 (2017).
29. Wang, L. *et al.* Femtosecond time-resolved transient absorption spectroscopy of CH3NH3PbI3 perovskite films: evidence for passivation effect of PbI_2. *J. Am. Chem. Soc.* **136**, 12205–12208 (2014).
30. Wang, K. *et al.* Bulk heterojunction perovskite hybrid solar cells with large fill factor. *Energy Environ. Sci.* **8**, 1245–1255 (2015).
31. Stolterfoht, M. *et al.* Approaching the fill factor Shockley-Queisser limit in stable, dopant-free triple cation perovskite solar cells. *Energy Environ. Sci.* **10**, 1530–

1539 (2017).

32. Yang, F. *et al.* Planar perovskite solar cells with high efficiency and fill factor obtained using two-step growth process. *ACS Appl. Mater. Interfaces* **11**, 15680–15687 (2019).
33. Liang, P. W. *et al.* Additive enhanced crystallization of solution-processed perovskite for highly efficient planar-heterojunction solar cells. *Adv. Mater.* **26**, 3748–3754 (2014).
34. Singh, T. & Miyasaka, T. Stabilizing the efficiency beyond 20% with a mixed cation perovskite solar cell fabricated in ambient air under controlled humidity. *Adv. Energy Mater.* **8**, 1700677 (2017).
35. Yun, J. S. *et al.* Critical role of grain boundaries for ion migration in formamidinium and methylammonium lead halide perovskite solar cells. *Adv. Energy Mater.* **6**, 1600330 (2016).
36. Shi, D. *et al.* Low trap-state density and long carrier diffusion in organolead trihalide perovskite single crystals. *Science* **347**, 519–522 (2015).
37. Yang, Y. *et al.* Low-temperature solution-processed perovskite solar cells with high efficiency and flexibility. *ACS Nano* **8**, 1674–1680 (2014).
38. Bi, D. *et al.* Polymer-templated nucleation and crystal growth of perovskite films for solar cells with efficiency greater than 21%. *Nat. Energy* **1**, 16142 (2016).
39. Zhao, X. *et al.* Efficient planar perovskite solar cells with improved fill factor via interface engineering with graphene. *Nano Lett.* **18**, 2442–2449 (2018).
40. Wu, C. G. *et al.* High efficiency stable inverted perovskite solar cells without current hysteresis. *Energy Environ. Sci.* **8**, 2725–2733 (2015).
41. Hu, L. *et al.* Inverted planar perovskite solar cells with a high fill factor and negligible hysteresis by the dual effect of NaCl-doped PEDOT:PSS. *ACS Appl. Mater. Interfaces* **9**, 43902–43909 (2017).
42. Jahandar, M. *et al.* High-performance $CH_3NH_3PbI_3$-inverted planar perovskite solar cells with fill factor over 83% via excess organic/inorganic halide. *ACS Appl. Mater. Interfaces* **9**, 35871–35879 (2017).
43. Chiang, C. H. & Wu, C. G. Bulk heterojunction perovskite-PCBM solar cells with high fill factor. *Nat. Photon.* **10**, 196–200 (2016).
44. Chiang, C. H. *et al.* The synergistic effect of H_2O and DMF towards stable and 20% efficiency inverted perovskite solar cells. *Energy Environ. Sci.* **10**, 808–817 (2017).
45. Shockley, W. & Queisser, H. J. Detailed balance limit of efficiency of p-n junction solar cells. *J. Appl. Phys.* **32**, 510–519 (1961).

46. Jacobsson, T. J. *et al.* Unreacted PbI2 as a double-edged sword for enhancing the performance of perovskite solar cells. *J. Am. Chem. Soc.* **138**, 10331–10343 (2016).
47. Grancini, G. *et al.* The impact of the crystallization processes on the structural and optical properties of hybrid perovskite films for photovoltaics. *J. Phys. Chem. Lett.* **5**, 3836–3842 (2014).
48. Yu, H. *et al.* Superfast room-temperature activation of SnO_2 thin films via atmospheric plasma oxidation and their spplication in planar perovskite photovoltaics. *Adv. Mater.* **30**, 1704825 (2018).
49. Wang, Y. C. *et al.* Electron-transport-layer-assisted crystallization of perovskite films for high-efficiency planar heterojunction solar cells. *Adv. Funct. Mater.* **28**, 1706317 (2018).
50. Kim, G. W. *et al.* Donor–acceptor type dopant-free, polymeric hole transport material for planar perovskite solar cells (19.8%). *Adv. Energy Mater.* **8**, 1701935 (2018).
51. Ke, W. *et al.* Low-temperature solution-processed tin oxide as an alternative electron transporting layer for efficient perovskite solar cells. *J. Am. Chem. Soc.* **137**, 6730–6733 (2015).
52. Pan, J. *et al.* Room-temperature, gydrochloride-assisted, one-step deposition for highly efficient and air-stable perovskite solar cells. *Adv. Mater.* **28**, 8309–8314 (2016).
53. Tan, H. *et al.* Efficient and stable solution-processed planar perovskite solar cells via contact passivation. *Science* **355**, 722–726 (2017).
54. Stolterfoht, M. *et al.* Visualization and suppression of interfacial recombination for high-efficiency large-area pin perovskite solar cells. *Nat. Energy* **3**, 847–854 (2018).

Chapter 5. Recycled utilization of nanoporous Au film in perovskite solar cells

5.1 Abstract

Hybrid organic/inorganic metal perovskite is a kind of the most promising optoelectronic material for next generation photovoltaic devices, because of the unprecedented development of the efficiency on photovoltaics, low fabrication cost and temperature. However, the complicated and rigorous thermal deposition of metal electrode film is a still challenge issue for industrial application, and single time utilization of the metal contact electrode seriously causes issue of resource waste and environmental pollution during the PSCs preparation. Here, the nanoporous Au film is directly transferred and applied in PSCs as the electrode to replace the evaporated Au film by simplifying the deposition process, which the PSCs obtain a high conversion efficiency (PCE) of 19.0% under reverse scanning with a negligible hysteresis, and realize more than 12 times recycling using of nanoporous Au film in PSCs devices. The decrease of the active area of nanoporous Au film and residual element in nanoporous Au deteriorates the conductivity and photovoltaic performance of PSCs. The nanoporous Au film can also be introduced into flexible PSCs and achieve a high PCE of 17.3% with a negligible hysteresis. Moreover, this flexible PSCs can maintain an excellent bending mechanical resistance of ca. 98.5% compared with the initial value and much better than that of the evaporated Au flexible PSCs (ca. 91.0%) even after 1000 bending cycles at bending radius of 5 mm. The non-penetrating cracks and nano pores structure of nanoporous Au film provide a much better bending durability of flexible PSCs.

Keywords: perovskite solar cells, photovoltaic performance, nanoporous Au film, recycled utilization, bending durability

5.2 Introduction

Hybrid organic/inorganic metal perovskites have attracted numerous attention and treated as the most promising materials of optoelectronic devices due to the unprecedented development on power conversion efficiency (PCE) from 3.8 to 24.2% within few years[1–6]. The rapid progress the PCE of perovskite solar cells (PSCs) come from the superior properties of perovskite light harvester layers, such as high light absorption coefficient in visible range[7], long distance diffusion of carrier[8], low exciton binding energy[8], high carrier mobility (electrons and holes)[9], variable bandgap[10–12] and low temperature fabrication process[13]. The high efficient PSCs are usually composed of glass based electrode/carrier transport layer/perovskite light harvester layer/carrier transport layer/contact electrode for n-i-p and p-i-n structures. The metallic materials are usually used as the contact electrode, for example, Au[14–17], Cu[18,19], Ag[20–24] and Al[25–28], which will increase the fabrication cost of PSCs and severely impact the industrial applications because of the limited resource of noble metals and rigorous deposition of electrode films, including high vacuum and long-term thermal evaporation. The energy payback time of PSCs also still every long even though high efficiency has been achieved using noble metallic electrode, because of the regrettable stability of perovskite photovoltaics[29,30]. Only single time employment of the metallic electrode usually causes severely resource wasting and ecological environment pollution.

Carbon based materials seem to be a more preferable choice to replace the typical metallic electrode in PSCs, because they are inexhaustible resource, low cost, excellent conductivity and stability[31–33]. A various types carbon materials have been employed in PSCs as contact electrode with a relatively high PCE by sundry approaches, including doctor blade[34,35], direct transfer[36,37], inked printing[32,38–40] and embedment route[41]. However, the photovoltaic (PV) performance of carbon based electrode PSCs still lower than the metallic electrode based photovoltaics because of the poor contact interfaces between the hole transport layer (HTL) and carbon electrode. Moreover, the mismatch energy alignment of HTL and carbon electrode still limit the progress of carbon based PSCs compared with that of Au electrode photovoltaics[38,42]. In order to promote the PCE of carbon based electrode PSCs, some of additional treatment has been employed to enhance PCE of PSCs, such as p-type semiconductor materials (such as NiO_x, CuPc) [43,44], $AuCl_3$ doping[45], molybdenum trioxide[46] and solvent-exchange process[37]. State-of-the-art of carbon based electrode PSCs have been realized using the adhesive macroporous carbon, and achieved a high PCE of 19.2% with relative high stability[37]. The carbon materials are also employed as a bottom electrode to replace the indium tin oxide (ITO) in PSCs, especially the flexible photovoltaics[45–47]. The graphene electrode flexible PSCs (fPSCs) have obtained a high PCE of 16.8% on a small active area and sustained a 85% of mechanical resistance at a bending radius of 2 mm by inserting a thin film of molybdenum trioxide (MoO_3) to reduce the series resistance of graphene[46]. Although the PV performance of carbon based electrode PSCs has significantly enhanced, the PCE of PSCs is still far behind them of metallic electrode based PSCs. Moreover, all the carbon based electrode are used only one time in PSCs after perovskite degradation and fabrication process of perovskite-photovoltaics still little complicated for getting high PV performance.

In order to realize the reuse of contact electrode in PSCs, a type of monolithic structure of PSCs has been proposed, such as mesoporous nickel and nanoporous Au contact electrode[48,49] in structure. However, they still cannot refrain from complicated fabrication process, for instance, high fabrication temperature[48] and vacuum thermal evaporation[49]. Moreover, the PCE of their PSCs are severely far behind the typical evaporated Au based PSCs at the same contemporary, and the performance of PSCs become much worse after reusing the electrode because of the low quality of perovskite films. The perovskite cannot form a flatness film with low trap-states in monolithic template, resulting in variations of carrier's diffusion length and severe recombination loss. Therefore, it is a still pursuing and necessary to explore a simple deposition of contact electrode materials with potential recycled utilization.

In this chapter, a new and facile deposition method of electrode has been firstly and successfully explored for drying transfer nanoporous Au films as contact electrode in PSCs. The high specific surface energy of nanoporous Au films can tightly stack on HTL surface of 2,2,7,7-tetrakis(N,N-di-p-methoxyphenylamine)-9,9-spirobifluorene (spiro-OMeTAD) and realize a high PCE of 19.0% with an ignorable hysteresis. The superior properties of nanoporous Au films can also obtain tightly contact after recycled utilization in PSCs and realize more than 12 times recycled application. The nanoporous Au film based fPSCs achieve a high PCE of 17.3% and excellent bending durability of ca. 98.5% compared with that of the evaporated Au film flexible perovskite-photovoltaics (ca. 91.0%) even after 1000 bending cycles at bending radius of 5 mm, which comes from the excellent bending mechanical resistance of nanoporous Au film and non-penetrating cracks after bending testing. The fundamental properties and PV performance of nanoporous Au film and PSCs will be systematically analyzed.

5.3 Experimental section

Materials: All chemicals and solvents were directly used as achieved without further refinement. The ITO substrate (10 Ω) was purchased from GEOMATEC Co., Ltd. SnO_2 nanoparticle (15 wt%) in H_2O colloidal dispersion with a particle size of 10–15 nm was ordered from Alfa Aesar. Lead (II) iodide (PbI_2, 99.99%), lead (II) bromide ($PbBr_2$, 99%), methylammonium bromide (MABr, >98.0%) formamidinium iodide (FAI, >98.0%), cesium iodide (CsI, 99.9%) were purchased from Tokyo Chemical Industry Co., Ltd. Poly(methyl methacrylate) (PMMA) (M_w≈15 000, powder), 4-tert-butylpyridine (TBP), Co(4-tertbutylpyridyl-2-1H-pyrazole)3·3TFSI (TFSI=bis(trifluoromethanesulfonyl) imide) were purchased from Sigma-Aldrich Co., Ltd. The solvents of *N*,*N*-dimethylformamide (DMF), dimethyl sulfoxide (DMSO), chlorobenzene, toluene, ethanol and isopropanol (IPA) were dried before use. 2,2′,7,7′-Tetrakis(*N*,*N*-di-*p*-methoxyphenylamino)-9,9′-spirobifluorene (spiro-OMeTAD) was ordered from Merck Co., Ltd. Lithium bis(trifluoromethanesulfonyl)imide (Li-TFSI) salt powder, acetone, other solvents were purchased from Wako Chemical Co., Ltd. and used as received without no special treatment unless otherwise noted. The membrane films were ordered from Merck Millipore Ltd.

ITO substrate preparation: The glass/ITO and PEN/ITO substrate are etched using zinc powder and 6 M HCl solution. The etched ITO glass substrates are washed in concentration of about 1 wt% aqueous detergent solution, acetone, IPA and distilled water under sonication for 10 min in each step, respectively. The cleaned FTO glass substrates are dried by an air gun and cut into 25×25 mm^2 size. The PEN/ITO substrates are washed by distilled water after etching and dried by bibulous papers to remove the residual water on the surface. The all substrates are stored in a dry box for following experiment.

SnO_2 ETM deposition: The SnO_2 nanoparticles with concentration of 5 wt% as ETM are deposited on the substrate using following program: spin coating at 3000 rpm for 30 s and annealed at 150 °C for 30 min at room condition. The SnO_2 ETM substrates are kept in a dry condition after post-treatment.

Nanoporous Au film preparation: The commercial $Au_{35}Ag_{65}$ (at.%, atomic percentage) is chose to fabricate nanoporous Au films using the dealloying approach in HNO_3 solution with a concentration of 69 wt.% for 6 hours in ambient condition, leaving a thickness of less than 100 nm[50,51].The residual chemical substances within pore channels are rinsed with deionized water for three times. The obtained nanoporous Au films are transferred to the membrane surface, dried in the ambient condition and stored in cleaning box of followed transferring process onto perovskite solar cells.

PSCs fabrication: The perovskite precursor solution with excessive PbI_2 is prepared by mixing the FAI (1 M), PbI_2 (1.1 M), MABr (0.2 M), $PbBr_2$ (0.2 M) and a 1.5 M CsI-DMSO solution in anhydrous DMF:DMSO 4:1 (*v*:*v*) solvent. The perovskite precursor is dissolving at 40 °C until fully dissolving of all chemicals.

The perovskite precursor is deposited as two-step spin coating process for perovskite light harvester layer: 1000 and 6000 rpm for 10 and 20 s, respectively. The anti-solvent of toluene with 400 μL is quickly splashed on ITO substrate within 2 s at 8 s before finishing of coating program. Interesting, the color of substrate quickly changes from transparence to light brown after dropping anti-solvent. The sample is directly transferred onto hotplate for post-treatment at 150 °C and 10 mins to achieve large crystal size and compact perovskite film. The as-prepared perovskite is passivated by PMMA using optimized concentration of 10 mg/mL after dissolving PMMA in chlorobenzene solvent at 50 ℃ for 30 mins. As for the PMMA&spiro-OMeTAD mixed passivation, the spiro-OMeTAD and PMMA are dissolved in chlorobenzene solvent separately. The spiro-OMeTAD dissolved at 70 ℃ for 30 min, and PMMA&spiro-OMeTAD solution with various concentration ratio (10:(0, 0.5, 1.0, 1.5, 2.0, 3.0 and 5.0) mg/mL) are prepared, which is into the PMMA and spiro-OMeTAD solution. The PMMA and PMMA&spiro-OMeTAD solution is deposited using spin coating program of 4000 rpm for 30 s, and then post-treated at 70 ℃ for 30 mins.

The HTL solution is prepared with 0.06 mmol spiro-OMeTAD, 0.009 mmol Co(4-*tert*-butylpyridyl-2-1*H*-pyrazole)3·3TFSI, 0.03 mmol Li-TFSI and 0.1 mmol tBP in 1 mL chlorobenzene. The fully dissolved HTL solution is spin coated at 4000 rpm for 30 s and post-treated at 70 °C for 30 min. Finally, the ca. 80 nm of Au electrode film is thermal deposited on vacuum condition.

Nanoporous Au film transfer: All the transfer process is conducted at ambient condition. The nanoporous Au on the membrane film is slowly pasted on the HTL surface and dropped 200 μL dried ethanol on back side of membrane film to wet the nanoporous Au film and HTL. The dried ethanol is thrown away by spin coating at 5000 rpm for 60 s. The membrane film is slowly separated using a plastic tape to prevent the damage of nanoporous Au film. Then, PSCs are kept in vacuum condition to enhance the contact between nanoporous Au film and HTL, and remove the remained ethanol. As for the recycling of nanoporous Au film, the HTL and perovskite are dissolved by acetone and transferred the nanoporous Au film to the fresh membrane film surface. The transferred nanoporous Au film is washed by acetone for five times to reduce the chemicals remained. Then, the recollected nanoporous Au film was dried at ambient condition and stored at dry box.

Characterizations: All evaluations of perovskite photoactive layer and PSCs are conducted at ambient condition. The perovskite photoactive layer with about 500 nm thickness are used for the photoluminescence (PL) and absorption measurements at an excitation wavelength of 532 nm (a power of 110 nW) and by UV/Vis spectrophotometer (UV-1800) apparatuses. The time-resolved PL decay is characterized using a single-photon counting technique with a 520-nm semiconductor laser and an incident power of 11.4 nW. Energy dispersive X-ray spectroscopy (EDX) measurement is conducted by SEM (Hitachi High-Technologies Co., S4800). Atomic force microscopy (AFM) (SII, Nanocute) and SEM (JEOL, JEM-6500F) are applied to characterize the surface roughness, surface and cross-sectional morphology of perovskite photoactive layer and PSCs, respectively. Specific surface area was measured using nitrogen adsorption–desorption isotherm on Quantachrome Autosorb-iQ.

The photovoltaic performance of PSCs is evaluated by a solar simulator (San-Ei Electric, XES-40S1) under AM 1.5 conditions (100 mW/cm^2) with a calibration cells (Bunkoukeiki, BS-500BK). The current density–voltage (*J*–*V*) curves are measured using a source meter (Keithley, 2400) and a 0.1 cm^2 metal mask at ambient condition. The *J*–*V* curves of PSCs are recorded from forward (−0.1 to 1.2 V) and reverse (1.2 to −0.1 V) scanning directions without any preconditioning (light soaking or the application of a forward bias voltage for a prolonged period before starting the measurement) at a 50 mV/s voltage sweep rate. The stabilized power output (SPO) is evaluated under maximum power point (MPP) tracking with a bias voltage from the *J*–*V* scanning. The external quantum efficiency (EQE) is analyzed at a monochromatic Xe arc light system (Bunkoukeiki, SMO-250III) by measuring incident-to-power-conversion efficiency. The impedance spectroscopy is conducted at one sun condition with various bias voltages using a platform of electrochemical analyzer (ALS/HCH, 660 EAW).

5.4 Results and discussion

5.4.1 Perovskite and Au films characterization

Perovskite films characterizations

To realize the main purposes of simplified deposition process and recycled utilization of metallic contact electrode in PSCs, the nanoporous Au film has been adopted as electrode in this study. **Figure 1** shows the transfer flow diagram of nanoporous Au film and recycled utilization in PSCs. The photograph of nanoporous Au film on the membrane film was directly pasted on the hole transport layer (HTL) surface. Then, the membrane film was slowly teared off and separated from nanoporous Au film surface using plastic tape to prevent the damages for first time application. The PSCs device was put on the glass substrate with fresh membrane film in acetone solvent into the culture dish for dissolving perovskite and HTL. The nanoporous Au film was transferred to membrane film surface using tweezers. The collected nanoporous Au film was washed about 5 times using acetone for the next time utilization. The detailed transfer process of nanoporous Au film on HTL surface has been described in Experimental section. The detailed configuration of PSCs, $ITO/SnO_2/Cs_{0.05}(MA_{0.17}FA_{0.83})_{0.95}Pb(I_{0.83}Br_{0.17})_3$ perovskite/poly(methyl methacrylate) (PMMA) &spiro-OMeTAD/doped spiro-OMeTAD/Au electrode (evaporated Au and nanoporous Au), has also been shown in Figure 1. To realize the high PV performance of PSCs using nanoporous Au films as electrode, the surface passivation technique should be introduced to enhance the quality of perovskite film surface because of the severe recombination loss by excessive PbI_2.

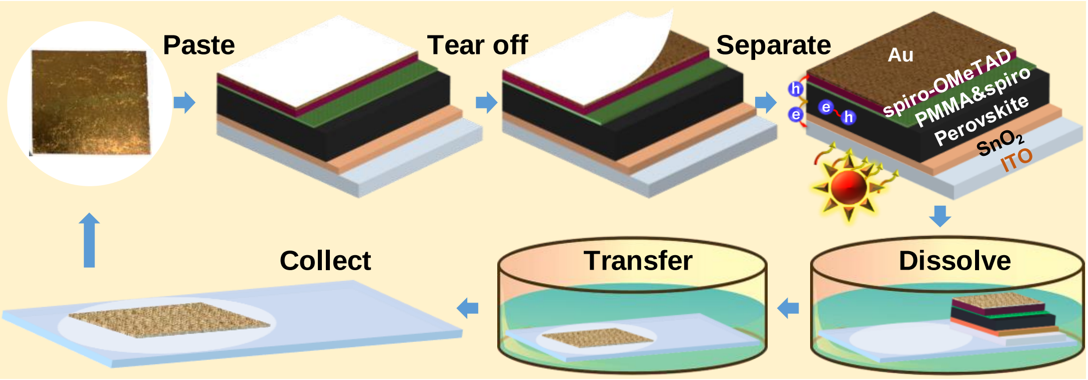

Figure 1. Illustration the dry transfer and recollection process of nanoporous Au film in PSCs device and acetone solvent, respectively. The photograph of nanoporous Au is also shown at the beginning of fabrication flow. And, the architecture of PSCs, $ITO/SnO_2/Cs_{0.05}(MA_{0.17}FA_{0.83})_{0.95}Pb(I_{0.83}Br_{0.17})_3$/PMMA&spiro-OMeTAD treatment/SSGP perovskite/Au (evaporated and nanoporous Au), has also shown.

Table 1. Summary of PV performance of PSCs with the standard and various concentration of PMMA&spiro-OMeTAD surface passivation.

Concentration ratio	Scanning direction	J_{SC} (mA/cm^2)	V_{OC} (V)	FF (%)	PCE (%)
Standard PSCs	Forward	21.6	1.15	72.5	18.0
	Reverse	21.6	1.16	74.1	18.6
10:0.0 PSCs	Forward	21.9	1.16	73.2	18.5
	Reverse	22.0	1.16	77.3	19.7
10:0.5 PSCs	Forward	22.3	1.17	72.3	18.8
	Reverse	22.3	1.16	75.0	19.4
10:1.0 PSCs	Forward	22.4	1.17	74.5	19.5
	Reverse	22.4	1.17	75.9	19.8
10:1.5 PSCs	Forward	22.3	1.16	79.0	20.4
	Reverse	22.3	1.16	78.9	20.4
10:2.0 PSCs	Forward	21.5	1.16	72.2	17.9
	Reverse	21.5	1.15	74.6	18.6

In order to improve the quality of perovskite light harvester layer, the PMMA has been employed to passivate the perovskite surface using similar approach as our previous chapter[4]. The PV performance of PMMA passivated PSCs (PMMA-PSCs) has become much better compared with that of the standard PSCs without PMMA passivation, as shown in **Table 1**. However, the hysteresis of PMMA-PSCs become a little larger than that of standard PSCs, which is a similar phenomenon to our previous results[4], because the insulating properties of PMMA accumulate the carriers during PV conversion process. Therefore, mixing some semiconducting materials to eliminate the carrier accumulation at the interface of PMMA seems a preferable way for the hysteresis elimination, such as

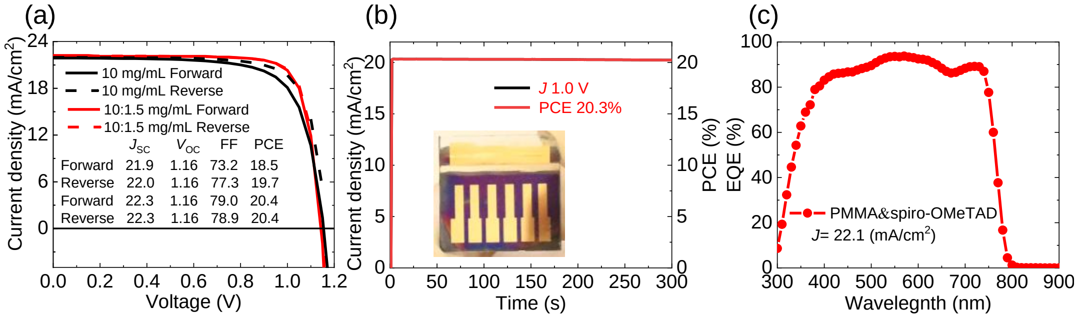

	J_{SC}	V_{OC}	FF	PCE
Forward	21.9	1.16	73.2	18.5
Reverse	22.0	1.16	77.3	19.7
Forward	22.3	1.16	79.0	20.4
Reverse	22.3	1.16	78.9	20.4

Figure 2. PV performance of the PMMA and PMMA&spiro-OMeTAD passivated PSCs. (a) *J*–*V* curves of the PMMA and PMMA&spiro-OMeTAD passivated PSCs, (b, c) SPO under MPP extracted from *J*–*V* curves, EQE and integrated current-density of the PMMA&spiro-OMeTAD passivated PSCs.

spiro-OMeTAD, at reverse scan from open-circuit voltage (V_{OC}) to short-circuit current density (J_{SC})[4].

Current density–voltage (*J*–*V*) evaluation of perovskite solar cells after passivation

Figure 2 shows the current density–voltage (*J*–*V*) curves of the standard and PMMA&spiro-OMeTAD passivated PSCs. The standard PSCs mean that the perovskite surface is only passivated by PMMA. The PMMA&spiro-OMeTAD passivated PSCs exhibits a best PV performance and an ignorable hysteresis when the concentration ratio is 10:1.5 mg/mL of PMMA and spiro-OMeTAD according to the Table 1. The PMMA&spiro-OMeTAD passivated PSCs achieve a PCE of 20.4 (20.4)% with a V_{OC} of 1.16 (1.16) V, a *J*sc of 22.3 (22.3) mA/cm^2, and a fill factor (FF) of 79.0 (78.9)%, measured at forward (reverse) scanning. These PV performances of PMMA&spiro-OMeTAD passivated PSCs are much higher than those of standard PSCs with a PCE of 18.5 (19.7)%, a V_{OC} of 1.16 (1.16) V, a *J*sc of 21.9 (22.0) mA/cm^2, and a FF of 73.2 (77.3)%, measured at forward (reverse) scanning. The PMMA&spiro-OMeTAD passivated PSCs also obtains a relative high value of stabilized power output (SPO) of 20.3% with a bias voltage extracted from under maximum-power-point (MPP) of *J*–*V* curves, as shown in Figure 2b. External quantum efficiency (EQE) of the PMMA&spiro-

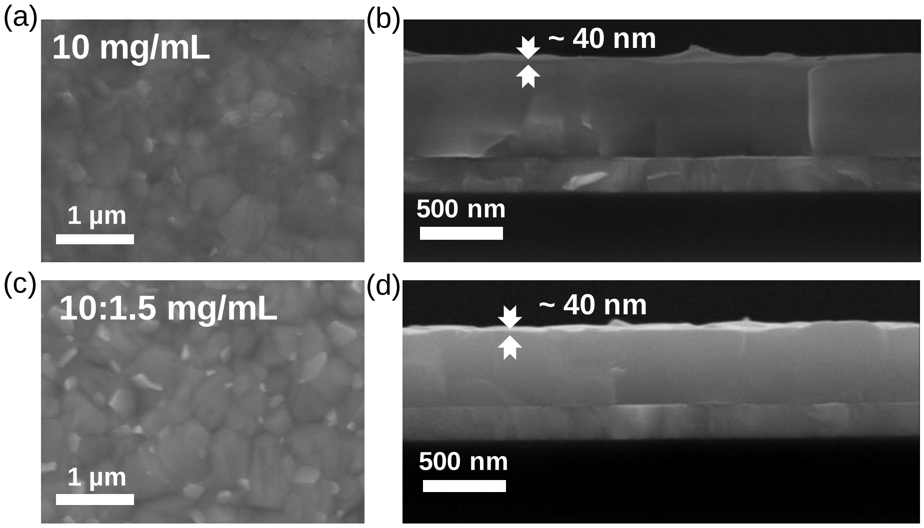

Figure 3. Surface and cross-sectional morphology characterization of perovskite passivated using PMMA and PMMA&spiro-OMeTAD using SEM. (a, c) and (b, d) SEM images of surface and cross-sectional morphologies of perovskite passivated by PMMA and PMMA&spiro-OMeTAD, respectively. The scale bars are 1 μm and 500 nm of surface and cross-sectional SEM images, respectively.

OMeTAD passivated PSCs is evaluated using incident-photon-to-current-efficiency spectroscopy (IPCE), as shown in Figure 2c. The PMMA&spiro-OMeTAD passivated PSCs exhibits an average value of 89.3% in the range from 400 to 740 nm of EQE with an integrated current-density of 22.1 mA/cm^2.

Surface characterization of passivated perovskite surface

The PV performance and hysteresis become higher and smaller as the concentration increase of spiro-OMeTAD until concentration of 1.5 mg/mL, however, the PV performance and hysteresis become worse when the concentration of spiro-OMeTAD exceeds than 1.5 mg/mL according to the results of Table 1. The deteriorated PV performance of the PMMA&spiro-OMeTAD passivated PSCs should attribute to the quality of PMMA&spiro-OMeTAD passivated perovskite surface. **Figure 3** shows the surface and cross-sectional morphology of perovskite film passivated using PMMA and PMMA&spiro-OMeTAD. The perovskite films surface exhibits a similar morphology after PMMA and PMMA&spiro-OMeTAD passivation according to Figures 3a and c, however, the cross-sectional image of PMMA thickness of PMMA&spiro-OMeTAD perovskite film become dim compared with that of the PMMA sample, as shown in Figures 3b and d.

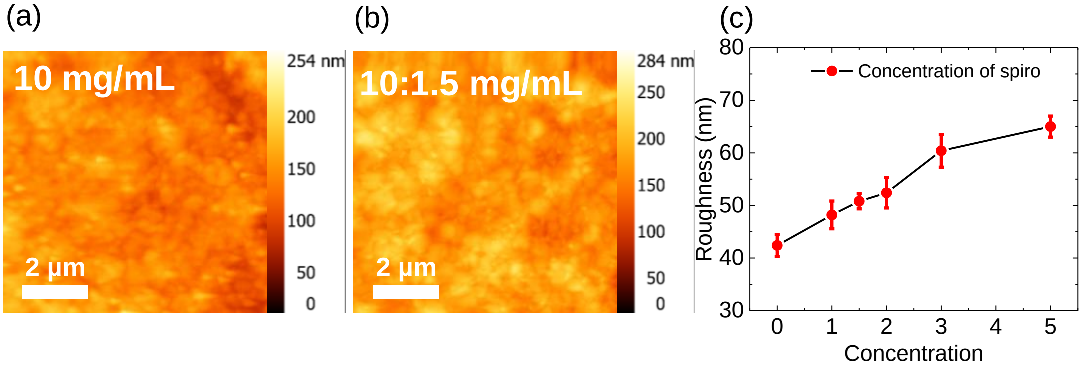

Figure 4. Surface roughness characterization of the perovskites passivated using PMMA and PMMA&spiro-OMeTAD with 10 and 10:1.5 mg/mL. (a, b) AFM images of the perovskites passivated using PMMA and PMMA&spiro-OMeTAD with 10 and 10:1.5 mg/mL, respectively. The scale bar is 2 µm. (c) Surface roughness values function as concentration of spiro-OMeTAD.

The atomic force microscopy (AFM) has been employed to characterize the surface roughness of perovskite light harvester layers. **Figures 4a** and b show the AFM images of perovskite passivated using PMMA and PMMA&spiro-OMeTAD with a concentration of 10 and 10:1.5 mg/mL, respectively. The summarized values of surface roughness of perovskites have been shown in Figure 4c. The surface roughness values augment as the increase of concentration ratio of spiro-OMeTAD, and dramatically increase when the concentration exceeds than 1.5 mg/mL. The reduction of surface roughness of perovskite film contributes to the enhancement of PV performance of PSCs. Thus, the optimized concentration ratio of 10:1.5 mg/mL PMMA and spiro-OMeTAD has been selected for nanoporous Au application.

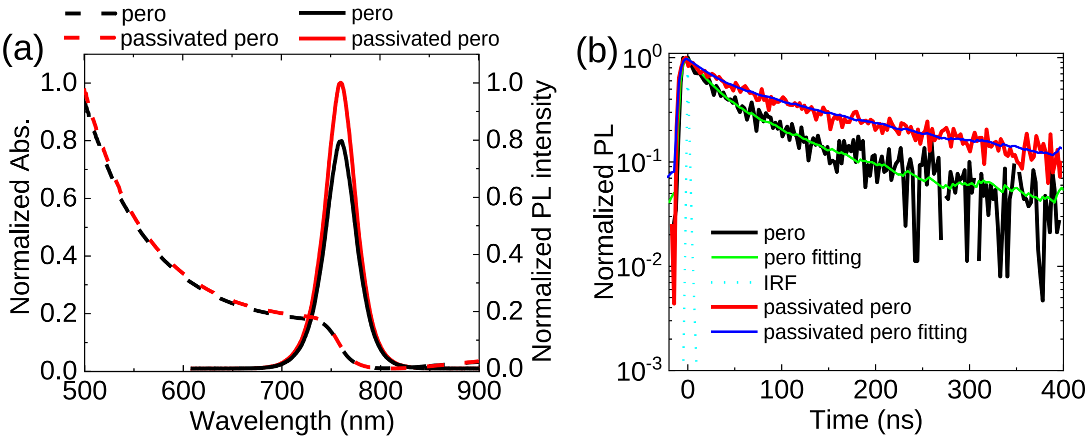

Figure 5. Optical properties of the perovskites without and with PMMA&spiro-OMeTAD passivation. (a) Absorption and PL spectra, (b) TRPL decay of perovskites on glass substrate. The instrumental response function (IRF) is also shown.

Table 2. Summary of the TRPL decay of the perovskite films without and with PMMA&spiro-OMeTAD passivation. The parameters a, τ_1, τ_2, and τ_{PL} represent the amplitude ratio, the lifetime constants of the fast and slow components, and the averaged PL decays, respectively.

Sample	a_1	τ_1 (ns)	τ_2 (ns)	τ_{PL} (ns)
Standard pero	0.52 ± 0.01	25.7 ± 1.6	162.3 ± 6.9	92.2 ± 3.0
Passivated pero	0.46 ± 0.01	44.4 ± 2.4	177.7 ± 1.7	115.9 ± 2.7

Optical properties characterization of perovskite films

The optical spectroscopy has been employed to explore the enhancement mechanism of PMMA and PMMA&spiro-OMeTAD passivation, as shown in **Figure 5**. Figure 5a shows the absorption and photoluminescence (PL) spectra of perovskite passivated without and with PMMA&spiro-OMeTAD layer. The perovskite films exhibit similar absorption spectra and shoulder without and with PMMA&spiro-OMeTAD passivation, however, the PL intensity has significantly enhanced after passivation. Figure 5b shows the time-resolved PL (TRPL) decay of perovskite films without and with PMMA&spiro-OMeTAD passivation. The TRPL decay tail becomes much longer with PMMA&spiro-OMeTAD passivation compared with that of perovskite without passivation. The TRPL decay profiles are consist with two components of a fast decay from surface recombination and a slow decay from bulk radiative recombination of electron-hole pairs[52]. The TRPL decays has been well reproduced using two-exponential functions and the obtained amplitude and lifetime are summarized in **Table 2**. The amplitude ratio and lifetime of the fast component significantly become smaller and longer, respectively, which means that the surface recombination loss of perovskite has been dramatically reduced because of the improvement of surface quality higher with PMMA&spiro-OMeTAD passivation. Moreover, the lifetime of slow component slightly augments from ca. 160 ns of the standard perovskite to ca. 180 ns of PMMA&spiro-OMeTAD passivated perovskite, which is similar to our previous observations[4]. Therefore, the enhancement of PSCs should be owing to the improved quality of perovskite films with PMMA&spiro-OMeTAD passivation.

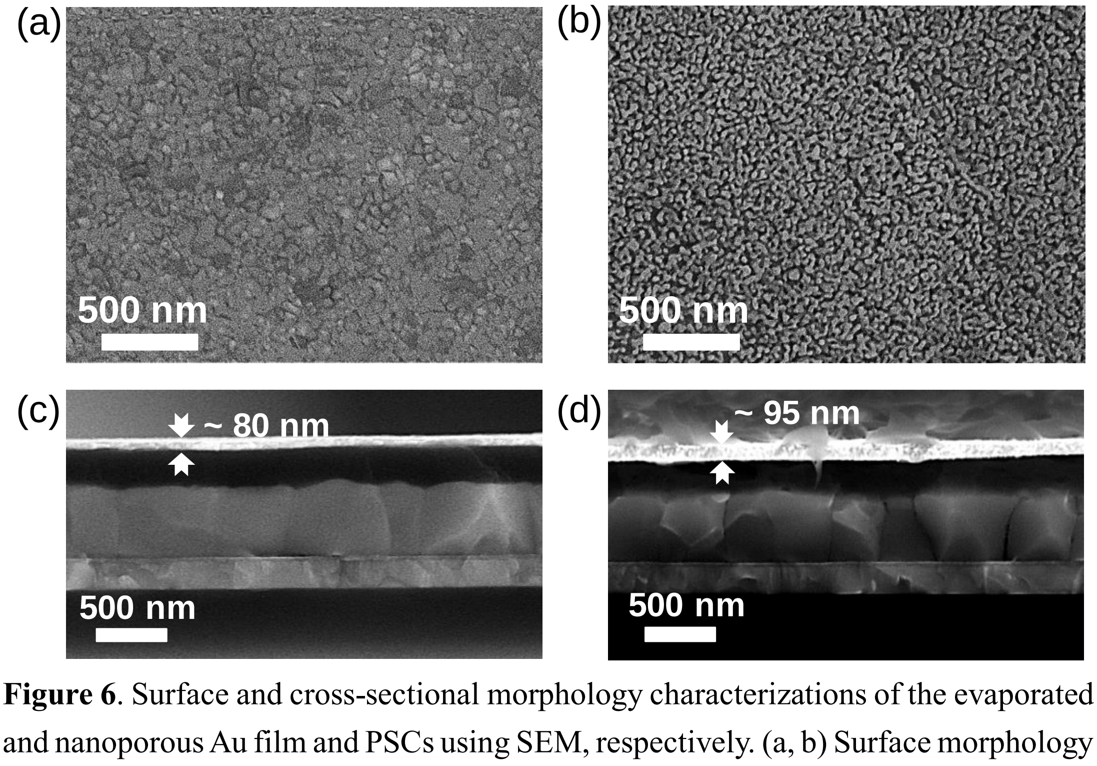

Figure 6. Surface and cross-sectional morphology characterizations of the evaporated and nanoporous Au film and PSCs using SEM, respectively. (a, b) Surface morphology of the evaporated and nanoporous Au films. (c, d) Cross-sectional morphology of PSCs using evaporated and nanoporous Au films as electrodes. The scale bar is 500 nm.

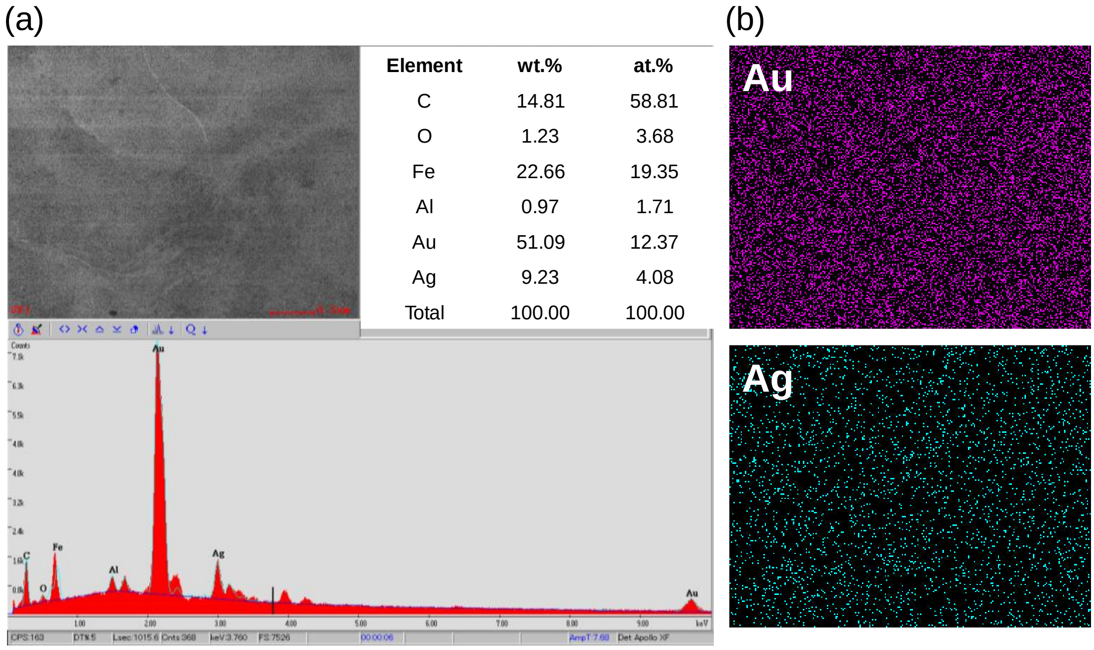

Element	wt.%	at.%
C	14.81	58.81
O	1.23	3.68
Fe	22.66	19.35
Al	0.97	1.71
Au	51.09	12.37
Ag	9.23	4.08
Total	100.00	100.00

Figure 7. Energy dispersive X-ray spectroscopy (EDX) spectra and mapping of nanoporous Au film. (a) Characterized atomic percentage of the main elements (C, O, Fe, Au and Ag) in the nanoporous Au film are summarized in inset table. The atomic ratio of Au and Ag is 3.3:1. (b) EDX mapping spectra of Au and Ag elements shows the uniform distribution of Au and Ag elements. The main element of film is Au. The scale bar is 500 nm.

Surface characterization of Au films

The surface morphology of evaporated and nanoprous Au films has been characterized using SEM. **Figures 6a** and b show surface SEM images of evaporated and nanoprous Au film. The nanoporous Au film consists of nano-scale pores structure. The pore structure of nanoporous Au film seems have a larger specific surface energy than that of the evaporated Au film. The contact properties of Au film and HTL have been evaluated using cross-sectional SEM images, as shown in Figures 6c and d. The nanoporous Au film enables to realize tightly contact on HTL surface without using high vacuum thermal evaporation process. The thickness of nanoporous Au film is approximate 95 nm comparable with that of the evaporated Au film (ca. 80 nm).

The composition of nanoporous Au film has been evaluated using energy dispersive X-ray (EDX) spectroscopy, as shown in **Figure 7**. Figure 7a shows the EDX spectra and element ratio of nanoporous Au film, indicating that the main component of nanoporous film is Au and Ag, and the atomic ratio is 3.3:1. The Au is homogeneously distributed on the nanoporous Au sample according to the EDX mapping of Figures 7c and d, which will severely impact on the conductivity of nanoporous Au film.

The surface roughness of evaporated and nanoporous Au films have be characterized using AFM. **Figure 8** shows the AFM images of evaporated and nanoporous Au films. The nanoporous Au film has a surface roughness of 18.5 ± 1.0 nm, which is slightly larger than that of 8.8 ± 0.9 nm in the evaporated Au film. The low surface roughness of nanoporous Au film causes significantly improvement of the interface contact between the spiro-OMeTAD and Au electrode film, as shown in cross-sectional SEM images of PSCs device.

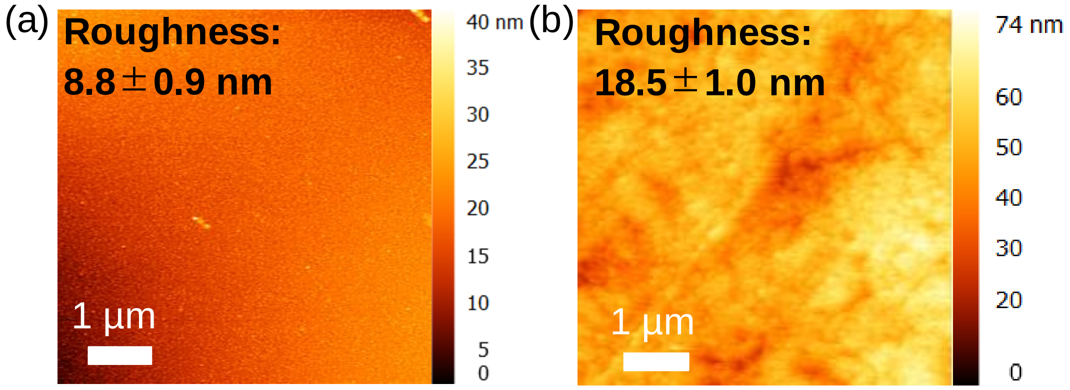

Figure 8. (a, b) Surface roughness characterization of the evaporated and nanoporous Au films, respectively. The scale bar is 1 µm.

The conductivity and specific surface area of both films have been characterized and summarized in **Table 3**. The sheet resistances of Au films have been evaluated using four-point-probe system. The sheet resistance of the nanoporous Au film is 11.3 ± 0.5 Ω, which is slightly larger than that of the evaporated Au film (5.3 ± 0.5 Ω). These results should be owing to the nanoporous structure according to EDX characterizations. The nanoporous Au film based PSCs can achieve a high value of J_{SC} without using the high vacuum thermal evaporation process. The specific surface area of nanoporous Au film (133.0 m^2/g) is much higher than that of the evaporated Au film (1.7 m^2/g), which is a

Table3. Summarization of the sheet resistance and specific surface area of the evaporated and nanoporous Au film.

Sample	Sheet resistance (Ω)	Specific surface area (m^2/g)
Evaporated Au film	5.3±0.5	1.7
Nanoporous Au film	11.3±0.5	133.0

critical evidence to demonstrate the tightly contact properties of nanoporous Au on HTL surface. Therefore, the superior properties of nanoporous Au film can achieve a high PV performance in PSCs.

5.4.2 *J–V* characterization of perovskite solar cells using nanoporous Au films

PV performance of nanoporous Au film based electrode PSCs

The nanoporous Au films have been introduced into PSCs as contact electrode without using high vacuum thermal evaporation. The dried ethanol has been used to wet the nanoporous Au film and improve separation from membrane film. The dried ethanol solvent cannot dissolve the PMMA and spiro-OMeTAD even after keeping one hour, indicating that the thin film of PMMA and HTL of spiro-OMeTAD can protect the perovskite light harvester layer from dissolving by ethanol during the nanoporous Au film transfer, as shown in **Figure 9**.

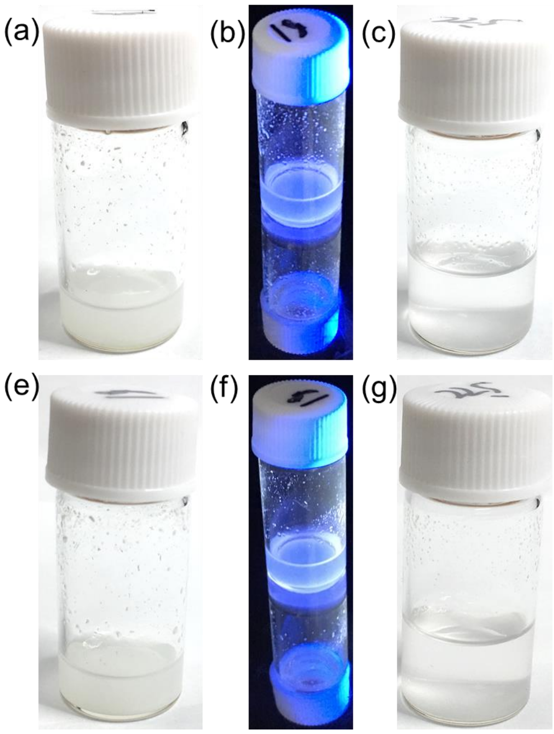

Figure 9. Photographs of PMMA and spiro-OMeTAD ethanol solution. (a–c) Fresh chemicals of PMMA and spiro-OMeTAD in ethanol solution with concentrations of 20 and 10 mg/mL, respectively. (e–g) One hour later of PMMA and spiro-OMeTAD in ethanol solution. (b) and (f) spiro-OMeTAD ethanol solutions were soaked at UV light with 245 nm wavelength.

Figure 10a shows the current density–voltage (*J–V*) curves and a photograph of the nanoporous Au film based PSCs (nano-Au-PSCs) with best PV performance. The nano-Au-PSCs achieve a high PCE of 18.7 (19.0)% with a high V_{OC} of 1.17 (1.16) V, a Jsc of 21.5 (21.5) mA/cm^2, and a FF of 74.3 (76.0)%, when measured at forward (reverse) voltage scanning. These results can be compared with the highest PCE of carbon based PSCs using complicated preparation process and only one-time utilization[37]. The stabilized power output (SPO) of nano-Au-PSCs has been evaluated using a bias voltage

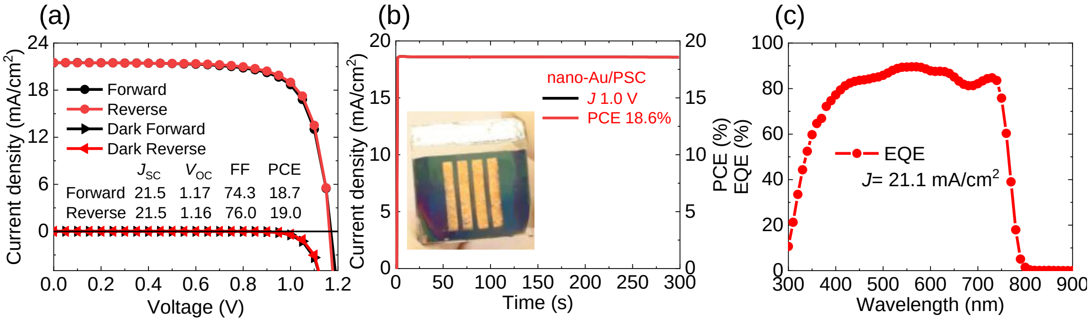

Figure 10. PV performance of PSCs using evaporated and nanoporous Au film as electrode. (a) *J–V* curves, (b) Time evolution of SPO under MPP extracted from forward scanning, (c) EQE and integrated current-density of PSCs using evaporated and nanoporous Au film as electrode.

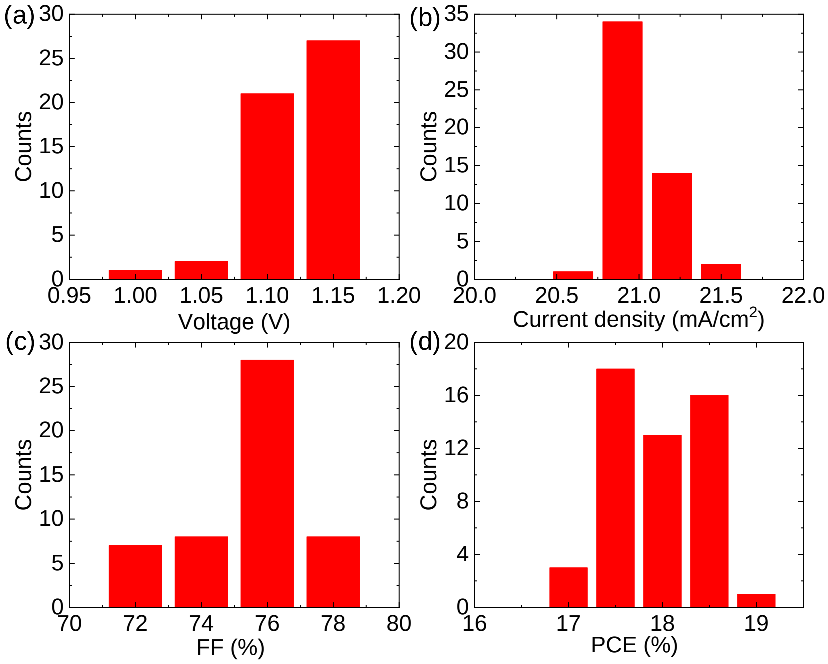

Figure 11. Reproducibility property of the PSCs using nanoporous Au film as electrode. (a-d) Statistical calculation of nano-Au PSCs includes J_{SC}, V_{OC}, FF and PCE (50 PSCs devices).

of 1.0 V extracted from maximum-power-point (MPP) of *J–V* curves, as shown in Figure 10b. The nano-Au-PSCs achieve a high SPO of 18.6% and maintain a relative stable value during measurement, is a slightly higher than those in self-adhesive macroporous carbon electrode PSCs[37] and much higher than those in the monolithic nanoporous Ni and Au electrode PSCs using complicated fabrication procedure[48,49]. The EQE of nano-Au-PSCs is characterized using IPCE in the dark condition. Figure 10c shows the EQE spectrum of nano-Au-PSCs. The nano-Au-PSCs can obtain a high average value of 85.1% of EQE from 400 to 740 nm region with an integrated current-density of 21.1 mA/cm^2.

To confirm the reproducibility of performance, a large amount of devices has been fabricated and shown the statistically results in **Figure 11**. The nano-Au-PSCs exhibit a high average value of 17.8 ± 0.5% PCE and a narrow distribution from 17.0 to 19.0%, which is much narrower than that of monolithic nanoporous Au PSCs[49], without using high vacuum and long-term thermal Au deposition process, as shown in Figure 11a. The other parameters of J_{SC}, V_{OC} and FF also exhibit a narrow distribution, as shown in Figures 11b-c. Therefore, nano-Au-PSCs achieved a comparable PV performance with those of the evaporated Au films based PSCs.

Electrochemical properties of perovskite solar cells

Impedance spectroscopy has been employed to characterize the carrier dynamics of PSCs with evaporated and nanoporous Au films as electrodes. **Figure 12a** shows the Nyquist plots of impedance and its simulated equivalent circuit of evaporated Au film based PSCs (evap-Au-PSCs) and nano-Au-PSCs. The Nyquist plots show a similar shape

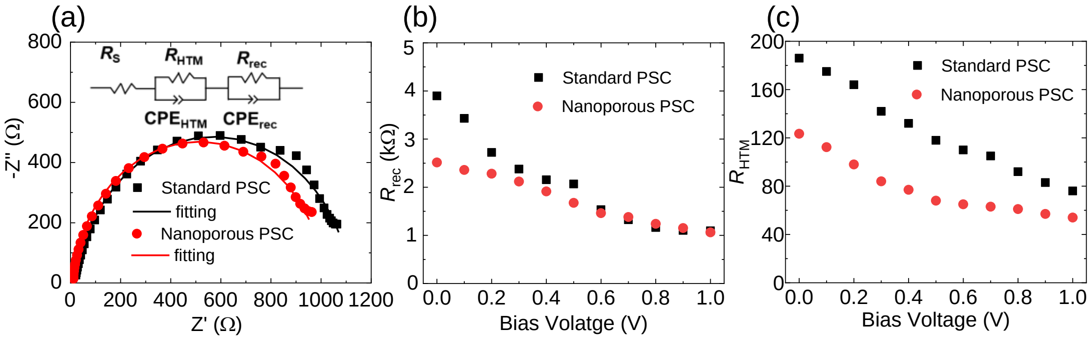

Figure 12. Impedance-capacitance properties of PSCs. (a) Nyquist plots of the impedance measurement of PSCs using evaporated and nanoporous Au films as electrode. The devices were measured at a bias voltage of 1.0 Vand one sun illumination conditions. The simulated equivalent circuit is shown in the inset. (b, c) R_{rec} and R_{HTM} values of evap-Au-PSC and nano-Au-PSCs, respectively.

of evap-Au- and nano-Au-PSCs with various radius. The plots consist of two components of high and low frequency range from the two contributions of carriers transport from perovskite to HTL and recombination process of carreris[4,53–55], respectively. The simulated curves of Nyquist plots with parameters of hole transport resistance (R_{HTM}) and recombination resistance (R_{rec})[55] have well reproduced the experimental results.

Figures 12b and c show the obtained values of R_{rec} and R_{HTM} under various bias voltage with one sun light illuminations. The R_{rec} and R_{HTM} of evap-Au- and nano-Au-PSCs are continuously decreased as the bias voltage increment, which are similar to the previous observations[4,56,57]. However, the reduce rate of evap-Au-PSCs is slightly larger than that of nano-Au-PSCs because of larger initial values. The lower initial values of R_{rec} and R_{HTM} of nano-Au-PSCs should attribute to a relative weak contact between the HTL and nanoporous Au film compared with those of evap-Au-PSCs. Hence, the carrier recombination loss and PV performance of nano-Au-PSCs is slightly higher and lower than those of evap-Au-PSCs, and the hysteresis becomes also increased using in

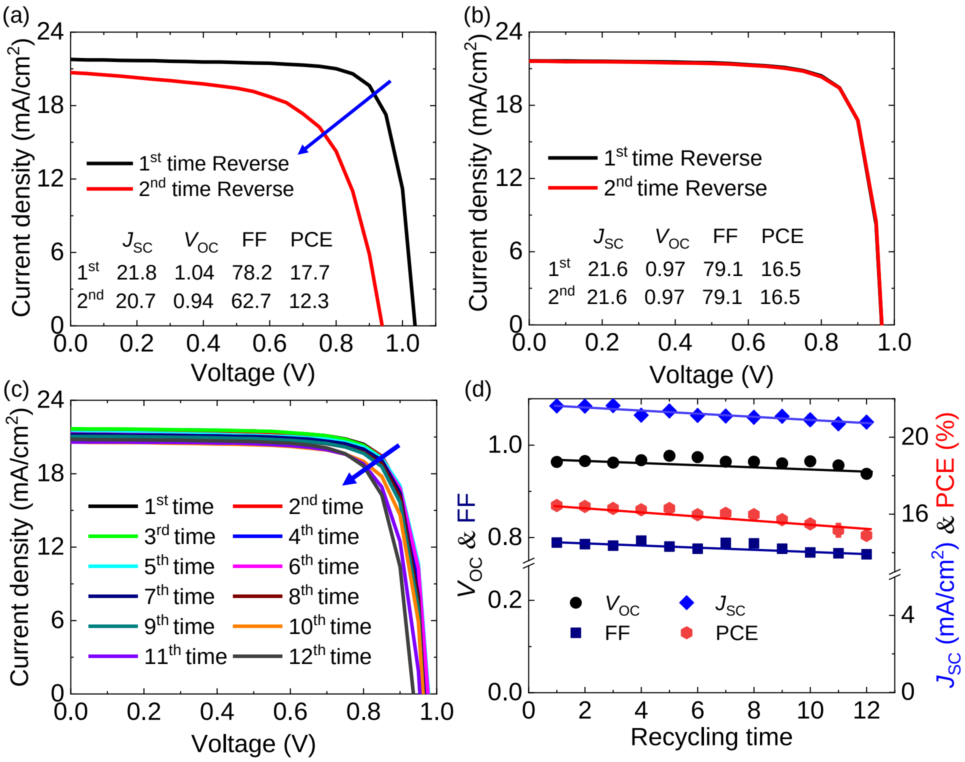

Figure 13. PV performance of PSCs reusing evaporated and nanoporous Au film as electrode. (a, b) *J–V* curves of PSCs with one time reused evaporated and nanoporous Au film as electrode. (c) *J–V* curves of the PSCs with 12 times recycled utilization of nanoporous Au film electrode. (d) Summary of PV parameters of the PSCs with 12 times recycled utilization of nanoporous Au film electrode.

nanoporous Au contact electrode, as shown in Figures 2 and 10.

5.4.3 Recycled nanoporous Au film in perovskite solar cells

The environmental stability of PSCs against moisture and oxygen is not enough satisfied toward the industrial application, which is the one of critical and ongoing issue in the studies of PSCs. The Au electrode is usually used as only single-time, and frequently discarded after the degradation of perovskite photoactive layer in the PSCs. The nanoporous Au film can be applicable to the recycling in the PSCs in addition to the advantages of simple and facile fabrication by dry transfer. We tried to realize the recycling of nanoporous Au electrode in the PSCs to reduce the noble metal resource waste and environmental pollution.

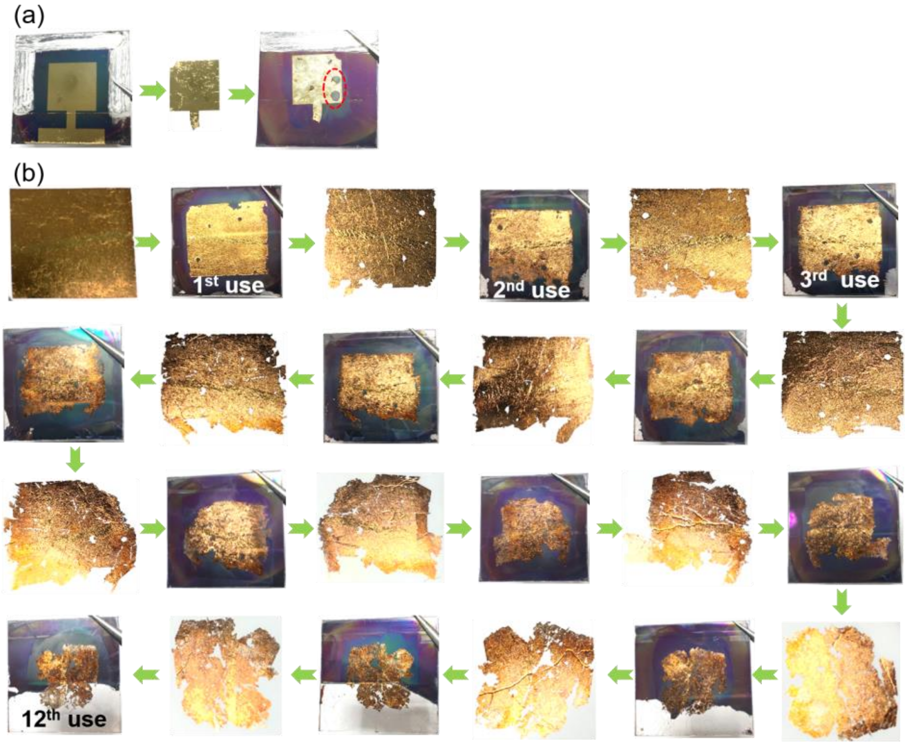

Figure 14. Physical images of Au film and PSCs. (a) Recycled utilization of evaporated Au film in PSCs. (b) Recycled application of nanoporous Au film in PSCs. The scale size of PSCs is 25×25 mm^2.

Figures 13a and b show the *J–V* curves of PSCs with reusing of evaporated and nanoporous Au films collected after dissolving the perovskite and HTL of spiro-OMeTAD, and transferring to the fresh film of membrane. The nano-Au-PSCs exhibit a much higher photovoltaic performance after reusing the Au electrode film compared with that of reusing evaporated Au film in PSCs, especially the substantial reduction of FF and V_{OC} in evaporated Au device. This is the first time to realize the recycled utilization of Au electrode in PSCs as our knowledge. The serious decrease of the photovoltaic performance of PSCs on the reusing evaporated Au film should come from the stacking properties of Au film to HTL after the transfer. The collected evaporated Au film surface exists some folded textures after dissolving the perovskite and HTL, which seriously reduce the stacking quality, and contact area between HTL and Au electrode film, as shown in **Figure 14a**. In contract, the nanoporous Au film shows the clear interface without any folded textures on surface and cracks, as shown in Figure 14b.

Continuously recycled utilization of nanoporous Au film in PSCs has been conducted by dissolving perovskite and HTL using acetone, washing 5 times to remove residual chemicals and repeating the transferring process. The detailed procedures are described in Experimental Section. Figures 13c and d show the J–V curves under reverse scanning and summarized photovoltaic parameters of PSCs with reusing of nanoporous Au film. This is the first time to successfully realize recycled utilization of electrode film for more than 10 times with superior performance. The physical reason of reduction of the photovoltaic performance of PSCs using the reused nanoporous Au films results from the severe deterioration of FF and J_{SC}, and slight decrease of V_{OC}, as shown in Figure 13d. As shown in Figure 14b, the main decrease of the PSCs' performance should come from the reduction of active area of the nanoporous Au film during the recycling. Interesting, the cost of PSCs has been significantly reduced after using nanoporous Au film as electrode, and the fabrication cost further reduce after 6 and 12 times recycled utilization, as shown in Figure 15a. And, the cost of nanoporous Au film almost zero compared with

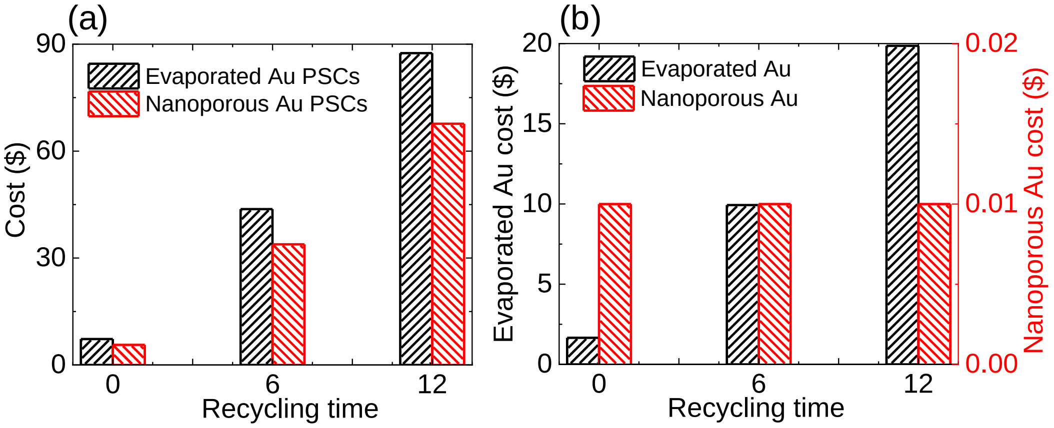

Figure 15. (a) Cost of each PSCs fabrication, 6 and 12 times recycled utilization of nanoporous Au film. (b) Cost of each piece of evaporated and nanoporous Au film, 6 and 12 times recycled utilization.

the evaporated Au film, and the cost of evaporated Au film further increase as the recycled times increment, indicating that the nanoporous Au film can reduce the Au metal consuming and environmental pollution, as shown in Figure 15b.

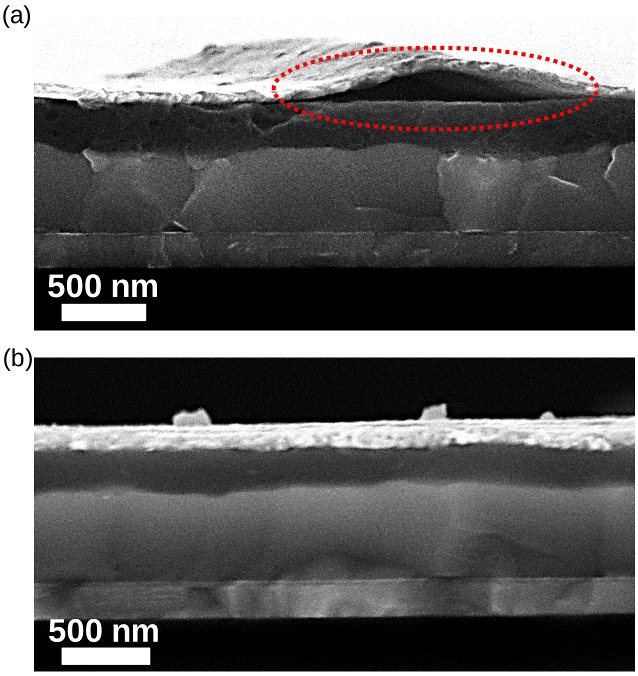

Figure 16. (a, b) Cross-sectional morphology characterization of PSCs with one time reusing the evaporated and nanoporous Au film via SEM, respectively. The scale bar is 500 nm.

Physical reason of decreasing performance of PSCS with reused Au film

The SEM has been used to characterize the stacking properties of Au films on the HTL surface, affecting the photovoltaic performance of PSCs. **Figure 16** shows the cross-sectional morphology of reused evaporated and nanoporous Au films in PSCs. The cross-sectional image of evaporated Au film PSCs shows the large voids between the Au film and HTL of spiro-OMeTAD because of the folded textures of collected evaporated Au film, resulting in a serious reduction of the PSCs, as shown in Figure 16a. In contrast, the nanoporous Au film can tightly stack on the HTL surface, which is similar to the first time utilization, as shown in Figure 16b. Therefore, the nanoporous Au film can realize high performance in PSCs even reusing this Au film.

The composition of nanoporous Au film has been characterized using SEM-EDX after 12 times recycled utilization, as shown in **Figure 17**. Figure 17a shows the measurement area and EDX spectrum of reused nanoporous Au. The main elements of reused nanoporous Au film are Au and Ag, and the atomic ratio is 3.9:1, which is similar to the fresh nanoporous Au film. Notably, the reused nanoporous Au film surface also appears some I element, and the atomic ratio of Au, Ag and I is 44.4:11.3:1. The elements of Au, Ag and residual I homogeneously distribute on the reused nanoporous Au film as shown in Figure 17b, in which the residual I element is another reason of performance reduction for nano-Au-PSCs because of the conductivity decrease of nanoporous Au and J_{SC} after several times reusing.

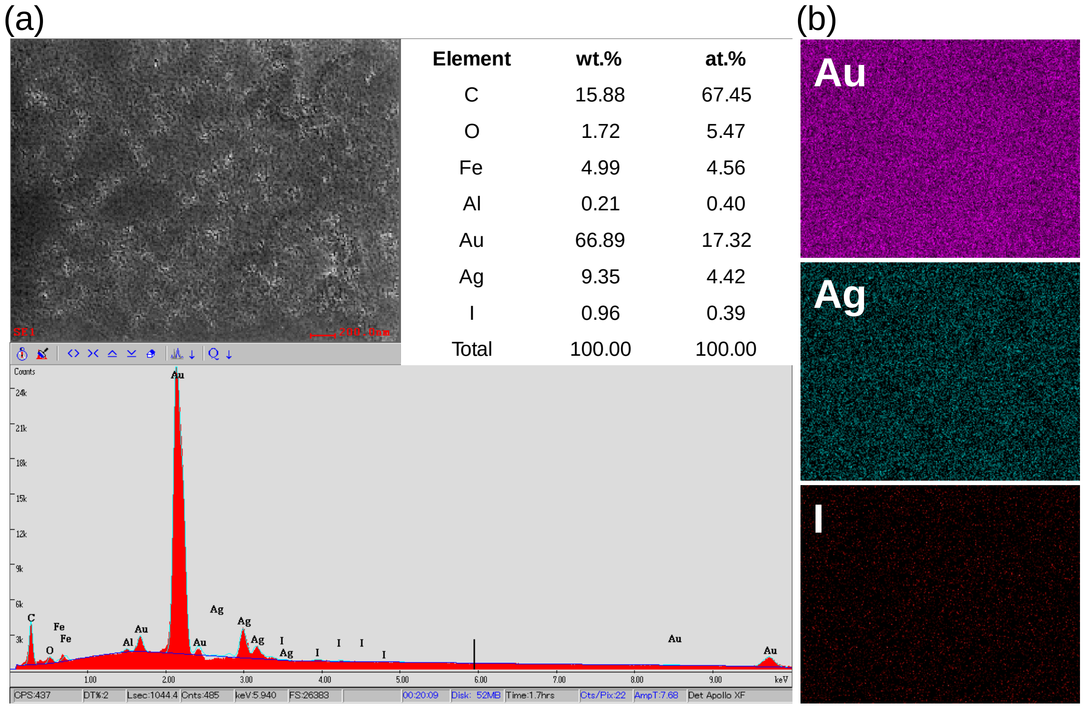

Element	wt.%	at.%
C	15.88	67.45
O	1.72	5.47
Fe	4.99	4.56
Al	0.21	0.40
Au	66.89	17.32
Ag	9.35	4.42
I	0.96	0.39
Total	100.00	100.00

Figure 17. Energy dispersive X-ray spectroscopy (EDX) spectra and mapping of 12 times used nanoporous Au film. (a) characterized atomic percentage of the main elements (C, O, Fe, Au and Ag) in the nanoporous Au film are summarized in table. The atomic ratio of Au, Ag and I is 44.4:11.3:1. (b) EDX mapping spectra of Au, Ag and I elements shows the uniform distribution of Au, Ag and I elements. The remained element of I is one reason of PSCs performance reduction.

5.4.4 *J–V* characterization of flexible perovskite solar cells

The nanoporous Au film has been also employed in the flexible PSCs (nano-Au-fPSCs) to confirm the enhancement of bending durability, because the penetrating cracks of Au electrode film is another reason for fPSCs performance reduction according to the previous observation[46,58]. **Figures 18a** and b show the *J–V* curves of the best photovoltaic performance of evaporated Au film based fPSCs (evap-Au-fPSCs) and nano-Au-fPSCs in this study. The nano-Au-fPSCs achieve a high PCE of 17.2 (17.3)% with a V_{OC} of 1.15 (1.14) V, a Jsc of 19.3 (19.4) mA/cm^2, and a FF of 77.3 (78.0)%, comparable with the evap-Au-fPSCs with a high PCE of 18.2 (18.3)% with a V_{OC} of 1.14 (1.14) V, a Jsc of 21.1 (21.1) mA/cm^2, and a FF of 75.9 (76.5)%, measured at forward (reverse) voltage

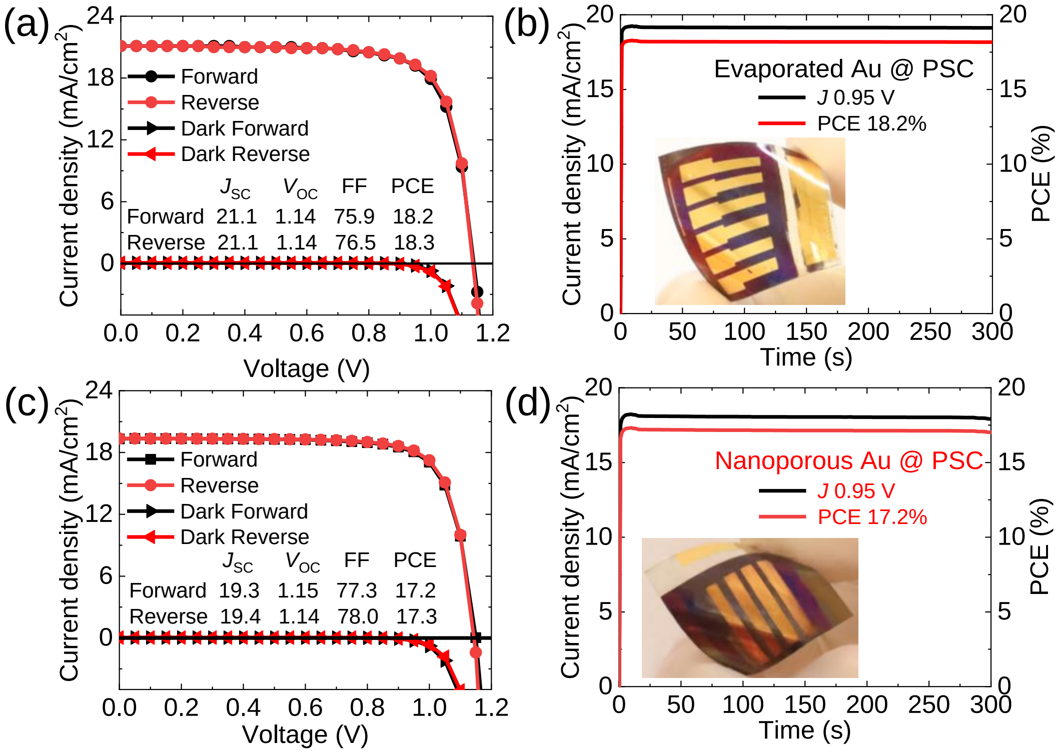

Figure 18. Photovoltaic performance of fPSCs using evaporated and nanoporous Au film as electrode. (a, c) and (c, d) J–V curves and SPO of fPSCs using the evaporated and nanoporous Au film as electrode.

Table 4. Summary of the photovoltaic performance of fPSCs using the evaporated and nanoporous Au film as electrode. (Evaporated Au fPSCs: 10 devices, Nanoporous Au fPSCs: 20 devices)

Sample	Scan direction	J_{SC} (mA/cm^2)	V_{OC} (V)	FF (%)	PCE (%)
Evaporated Au PSCs	Forward	20.6 ± 0.5	1.13 ± 0.01	75.7 ± 0.0	17.6 ± 0.5
	Reverse	20.7 ± 0.5	1.12 ± 0.01	76.6 ± 0.0	17.7 ± 0.5
Nanoporous Au PSCs	Forward	19.5 ± 0.2	1.12 ± 0.01	75.5 ± 0.0	16.5 ± 0.4
	Reverse	19.5 ± 0.2	1.12 ± 0.01	76.2 ± 0.0	16.7 ± 0.4

scanning. The evap-Au-fPSCs and nano-Au-fPSCs exhibit an ignorable hysteresis on *J–V* curves, and a high SPO of 17.2 and 18.2% under the MPP extracted from *J–V* curves under continuously light soaking with relative stable value during the measurement, as shown in Figures 18c and d.

A large number of evap-Au-fPSCs and nano-Au-fPSCs have been fabricated to evaluate the reproducibility and the statistical calculation results are summarized in **Table 4**. The two type devices exhibit a high average value of 17.7 ± 0.5% of evap-Au-fPSCs and 16.7 ± 0.4% of nano-Au-fPSCs, respectively, indicating that a comparable

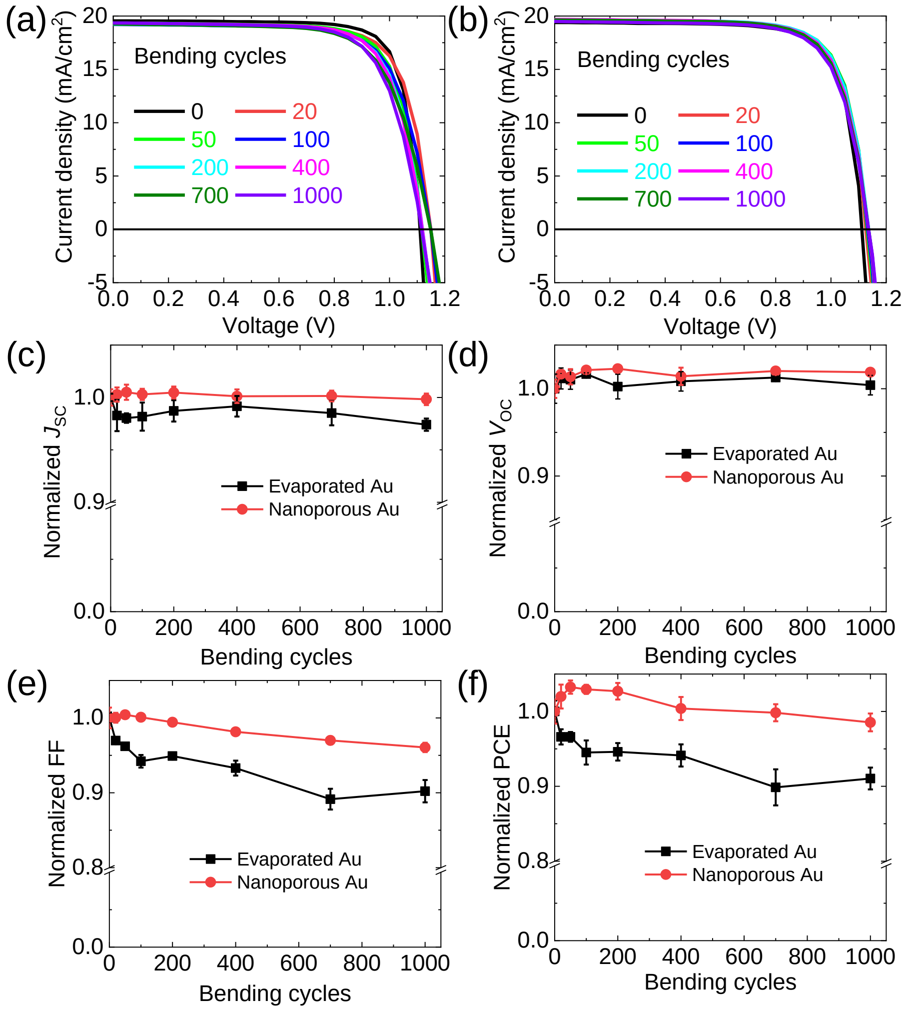

Figure 19. PV performance of fPSCs using evaporated and nanoporous Au film as electrode after bending testing. (a, b) *J–V* curves, (c-f) Statistical calculation of bending durability of fPSCs using evaporated and nanoporous Au film as electrode after 1000 cycles bending testing at a bending radius of 5 mm.

performance of nano-Au-fPSCs compared with evap-Au-fPSCs.

5.4.5 Bending durability of flexible perovskite solar cells

A harsh bending testing has been introduced into fPSCs to evaluate the bending durability of evap-Au-fPSCs and nano-Au-fPSCs at a bending radius of 5 mm. **Figures 19a** and b show the *J–V* curves of evap-Au-fPSCs and nano-Au-fPSCs at various bending cycles, indicating that the reduction of two-types devices is FF decrease and V_{OC}, especially the FF, which is similar to our previous observations[58]. However, the nano-Au-fPSCs can sustain much better bending durability compared with evap-Au-fPSCs. Figures 19c-f show the statistical calculation of bending durability of 4 devices of evap-Au-fPSCs and nano-Au-fPSCs. The nano-Au-fPSCs can maintain a high mechanical resistance of ca. 98.5% compared with the initial PCE, which is much better than that of the evap-Au-fPSCs with ca. 91.0% of initial value even after 1000 bending cycles testing at a bending radius of 5 mm. The other parameters including J_{SC}, V_{OC} and FF of the nano-Au-fPSCs exhibit much better values compared with those of the evap-Au-fPSCs, as shown in Figures 19c-f.

Interesting, the bending durability of the nano-Au-fPSCs slightly increases as bending testing during the bending less than 50 cycles, which should be attributed the enhancement of stacking contact between the HTL and nanoporous Au film during the low bending testing cycles because the structure of nanoporous Au film can release the bending stress to adjacent nano pores. As the bending testing extension, the deterioration of evap-Au-fPSCs and nano-Au-fPSCs should come from the cracks of the ITO substrate and Au electrode films, as similar to our previous observations[58].

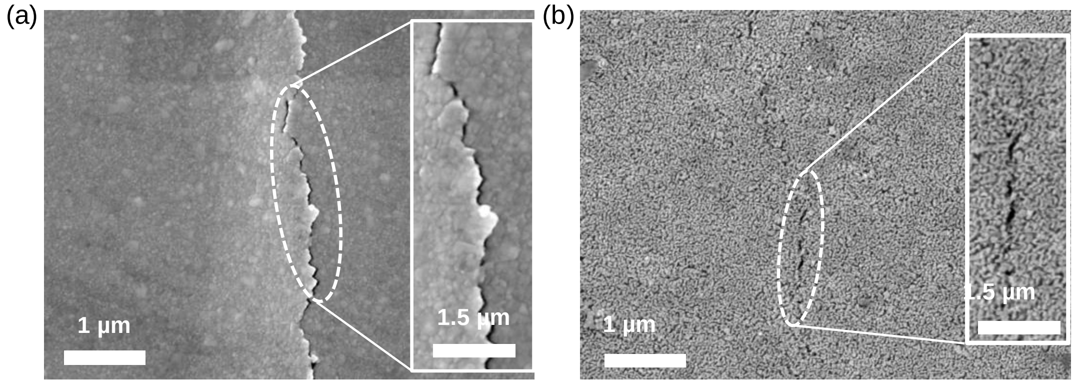

Figure 20. (a, b) Surface morphology characterization of fPSCs using the evaporated and nanoporous Au film as electrode via SEM after 400 bending cycles testing at bending radius of 5 mm, respectively. The scale bar is 1 and 1.5 μm, respectively.

However, the nanoporous Au film can maintain much better bending durability compared with that of the evaporated Au film according to SEM characterizations, as shown in **Figure 20**. Figure 20a show the surface morphology of the evaporated and nanoporous Au films after 400 bending cycles testing at the bending radius of 5 mm. The evaporated Au film surface causes severe cracks with penetrating textures, however, the nanoprous Au film only appears some non-penetrating cracks textures, which is the main reason that the nanoporous Au film sustains better carrier transport ability and much higher values of J_{SC}, FF and PCE in nano-Au-fPSCs.

5.5 Chapter summary

The nanoporous Au film has been successfully introduced into the rigid and flexible planar PSCs as contact electrode and achieved a high PV performance without using typical complicated high vacuum thermal evaporation process. As results, a high PCE of 19.0% with an ignorable hysteresis has been obtained on rigid nano-Au-PSCs and realized more than 12 times recycled utilization of the nanoporous Au in PSCs with a small reduction of PV performance. The main decrease reasons of the PV performance on reusing nanoporous Au film based PSCs should attribute to the active area reduction and the residual elements on nanoporous Au film. A high PCE of 17.3% with a negligible hysteresis has been achieved on nano-Au-fPSCs and maintained a high bending durability of ca. 98.5% even after 1000 bending cycles at bending radius of 5 mm. The excellent bending durability of the nano-Au-fPSCs should come from the perovskite quality enhancement and the superior bending durability of the nanoporous Au film. Findings on a facile, feasible and effective approach to deposit the nanoporous Au film as the contact electrode with high PV performance in PSCs by replacing the typical complicated high vacuum thermal evaporation deposition could simplify the fabrication process of PSCs and accelerate the commercial application. Recycled utilization of the nanoporous Au film in PSCs as contact electrode can substantially reduce the fabrication cost, resource waste and ecological environmental pollution.

Reference

1. Wang, S. *et al.* Accelerated degradation of methylammonium lead iodide perovskites induced by exposure to iodine vapour. *Nat. Energy* **2**, 16195 (2017).
2. Yang, W. S. *et al.* Iodide management in formamidinium-lead-halide-based perovskite layers for efficient solar cells. *Science* **356**, 1376–1379 (2017).

3. Peng, J. *et al.* A universal double-side passivation for high open-circuit voltage in perovskite solar cells : role of carbonyl groups in poly (methyl methacrylate). *Adv. Energy Mater.* **8**, 1801208 (2018).
4. Yang, F. *et al.* Roles of polymer layer in enhanced photovoltaic performance of perovskite solar cells via interface engineering. *Adv. Mater. Interfaces* **5**, 1701256 (2018).
5. Yang, F. *et al.* Planar perovskite solar cells with high efficiency and fill factor obtained using two-step growth process. *ACS Appl. Mater. Interfaces* **11**, 15680–15687 (2019).
6. Best Research-Cell Efficiencies Chart. National Renewable Energy Laboratory (NREL), https://www.nrel.gov/pv/assets/pdfs/best-research-cell-efficiencies-190416 (2019).
7. Burschka, J. *et al.* Sequential deposition as a route to high-performance perovskite-sensitized solar cells. *Nature* **499**, 316–319 (2013).
8. Stranks, S. D. *et al.* Electron-hole diffusion lengths exceeding 1 micrometer in an organometal trihalide perovskite absorber. *Science* **342**, 341–344 (2013).
9. Herz, L. M. Charge-carrier mobilities in metal halide perovskites: fundamental mechanisms and limits. *ACS Energy Lett.* **2**, 1539–1548 (2017).
10. Jeon, N. J. *et al.* Compositional engineering of perovskite materials for high-performance solar cells. *Nature* **517**, 476–480 (2015).
11. Eperon, G. E. *et al.* Perovskite-perovskite tandem photovoltaics with optimized band gaps. *Science* **354**, 861–865 (2016).
12. Saliba, M. *et al.* Cesium-containing triple cation perovskite solar cells: improved stability, reproducibility and high efficiency. *Energy Environ. Sci.* **9**, 1989–1997 (2016).
13. Ball, J. M. *et al.* Low-temperature processed meso-superstructured to thin-film perovskite solar cells. *Energy Environ. Sci.* **6**, 1739–1743 (2013).
14. Hao, F. *et al.* Lead-free solid-state organic-inorganic halide perovskite solar cells. *Nat. Photon.* **8**, 489–494 (2014).
15. Heo, J. H. *et al.* Efficient inorganic-organic hybrid heterojunction solar cells containing perovskite compound and polymeric hole conductors. *Nat. Photon.* **7**, 486–491 (2013).
16. Malinkiewicz, O. *et al.* Perovskite solar cells employing organic charge-transport layers. *Nat. Photon.* **8**, 128–132 (2014).
17. Wang, Z. *et al.* Efficient ambient-air-stable solar cells with 2D–3D heterostructured butylammonium-caesium-formamidinium lead halide perovskites.

Nat. Energy **2**, 17135 (2017).

18. Deng, Y. *et al.* Air-stable, efficient mixed-cation perovskite solar cells with Cu electrode by scalable fabrication of active layer. *Adv. Energy Mater.* **6**, 1600372 (2016).
19. Zheng, X. *et al.* Defect passivation in hybrid perovskite solar cells using quaternary ammonium halide anions and cations. *Nat. Energy* **2**, 17102 (2017).
20. Liu, D. & Kelly, T. L. Perovskite solar cells with a planar heterojunction structure prepared using room-temperature solution processing techniques. *Nat. Photon.* **8**, 133–138 (2014).
21. Lee, M. M. *et al.* Efficient hybrid solar cells based on meso-superstructured organometal halide perovskites. *Science* **338**, 643–647 (2012).
22. McMeekin, D. P. *et al.* A mixed-cation lead mixed-halide perovskite absorber for tandem solar cells. *Science* **351**, 151–155 (2016).
23. Liu, J. *et al.* Crystal growth lead-free solar cells based on tin halide perovskite films with high coverage and improved aggregation angewandte. *Angew. Chemie - Int. Ed.* **57**, 13221–13225 (2018).
24. Yang, M. *et al.* Facile fabrication of large-grain $CH_3NH_3PbI_{3-x}Br_x$ films for high-efficiency solar cells via CH_3NH_3Br-selective Ostwald ripening. *Nat. Commun.* **7**, 12305 (2016).
25. You, J. *et al.* Improved air stability of perovskite solar cells via solution-processed metal oxide transport layers. *Nat. Nanotechnol.* **11**, 75–81 (2016).
26. Kuang, C. *et al.* Highly efficient electron transport obtained by doping PCBM with graphdiyne in planar-heterojunction perovskite solar cells. *Nano Lett.* **15**, 2756–2762 (2015).
27. Nie, W. *et al.* High-efficiency solution-processed perovskite solar cells with millimeter-scale grains. *Science* **347**, 522–525 (2015).
28. Li, Y. *et al.* High-efficiency robust perovskite solar cells on ultrathin flexible substrates. *Nat. Commun.* **7**, 10214 (2016).
29. Grancini, G. *et al.* One-year stable perovskite solar cells by 2D/3D interface engineering. *Nat. Commun.* **8**, 15864 (2017).
30. Arora, N. *et al.* Perovskite solar cells with CuSCN hole extraction layers yield stabilized efficiencies greater than 20%. *Science* **358**, 768–771 (2017).
31. Wang, J. T. *et al.* Low-temperature processed electron collection layers of graphene/TiO_2 nanocomposites in thin film perovskite solar cells. *Nano Lett.* **14**, 724–730 (2014).
32. Mei, A. *et al.* A hole-conductor-free, fully printable mesoscopic perovskite solar

cell with high stability. *Science* **345**, 295–298 (2014).

33. Xiao, J. *et al.* Efficient $CH_3NH_3PbI_3$ perovskite solar cells based on graphdiyne (GD)-modified P3HT hole-transporting material. *Adv. Energy Mater.* **5**, 1401943 (2015).
34. Liu, Z. *et al.* Using a low-temperature carbon electrode for preparing hole-conductor-free perovskite heterojunction solar cells under high relative humidity. *Nanoscale* **8**, 7017–7023 (2016).
35. Liang, J. *et al.* $CsPb_{0.9}Sn_{0.1}IBr_2$ based all-inorganic perovskite solar cells with exceptional efficiency and stability. *J. Am. Chem. Soc.* **139**, 14009–14012 (2017).
36. Luo, Q. *et al.* All-carbon-electrode-based endurable flexible perovskite solar cells. *Adv. Funct. Mater.* **28**, 1706777 (2018).
37. Zhang, H. *et al.* Self-adhesive macroporous carbon electrodes for efficient and stable perovskite solar cells. *Adv. Funct. Mater.* **28**, 1802985 (2018).
38. Chen, H. *et al.* Solvent engineering boosts the efficiency of paintable carbon-based perovskite solar cells to beyond 14%. *Adv. Energy Mater.* **6**, 1502087 (2016).
39. Zhu, W. *et al.* Intermolecular exchange boosts efficiency of air-stable, carbon-based all-inorganic planar $CsPbIBr_2$ perovskite solar cells to over 9%. *Adv. Energy Mater.* **8**, 1802080 (2018).
40. Duan, M. *et al.* Efficient hole-conductor-free, fully printable mesoscopic perovskite solar cells with carbon electrode based on ultrathin graphite. *Carbon* **120**, 71–76 (2017).
41. Wei, Z. *et al.* Cost-efficient clamping solar cells using candle soot for hole extraction from ambipolar. *Energy Environ. Sci.* **7**, 3326–3333 (2014).
42. Zhou, H. *et al.* Interface engineering of highly efficient perovskite solar cells. *Science* **345**, 542–546 (2014).
43. Liu, S. *et al.* 17% efficient printable mesoscopic PIN metal oxide framework perovskite solar cells using cesium-containing triple cation perovskite. *J. Mater. Chem. A* **5**, 22952–22958 (2017).
44. Zhang, F. *et al.* Boosting the efficiency and the stability of low cost perovskite solar cells by using CuPc nanorods as hole transport material and carbon as counter electrode. *Nano Energy* **20**, 108–116 (2016).
45. Heo, J. H. *et al.* Highly flexible, high-performance perovskite solar cells with adhesion promoted $AuCl_3$-doped graphene electrodes. *J. Mater. Chem. A* **5**, 21146–21152 (2017).
46. Yoon, J. *et al.* Superflexible, high-efficiency perovskite solar cells utilizing graphene electrodes: Towards future foldable power sources. *Energy Environ. Sci.*

10, 337–345 (2017).

47. Jeon, I. *et al.* Single-walled carbon nanotube film as electrode in indium-free planar heterojunction perovskite solar cells: investigation of electron-blocking layers and dopants. *Nano Lett.* **15**, 6665–6671 (2015).
48. Ku, Z. *et al.* A mesoporous nickel counter electrode for printable and reusable perovskite solar cells. *Nanoscale* **7**, 13363–13368 (2015).
49. Li, M. H. *et al.* Robust and recyclable substrate template with an ultrathin nanoporous counter electrode for organic-hole-conductor-free monolithic perovskite solar cells. *ACS Appl. Mater. Interfaces* **9**, 41845–41854 (2017).
50. Liquid, R. *et al.* Evolution of nanoporosity in dealloying. *Nature* **410**, 5–8 (2001).
51. Chen, L. Y. *et al.* Toward the theoretical capacitance of RuO_2 reinforced by highly conductive nanoporous gold. *Adv. Energy. Mater.* **3**, 851–856 (2013).
52. Shi, D. *et al.* Low trap-state density and long carrier diffusion in organolead trihalide perovskite single crystals. *Science* **347**, 519–522 (2015).
53. Cells, D. S. *et al.* Temperature dependence of transport properties of spiro-MeOTAD as a hole transport material in solid-state. *ACS Nano* **7**, 2292–2301 (2013).
54. Rutile, S. *et al.* High efficiency solid-state sensitized solar cell-based on submicrometer rutile TiO_2 nanorod and $CH_3NH_3PbI_3$ perovskite sensitizer. *Nano Lett.* **13**, 2412–2417 (2013).
55. Ke, W. *et al.* Low temperature solution-processed tin oxide as an alternative electron transporting layer for efficient perovskite solar cells. *J. Am. Chem. Soc.* **137**, 6730–6733 (2015).
56. Li, Z. *et al.* Laminated carbon nanotube networks for metal electrode-free efficient perovskite solar cells. *ACS Nano* **8**, 6797–6804 (2014).
57. Juarez-perez, E. J. *et al.* Role of the selective contacts in the performance of lead halide perovskite solar cells. *J. Phys. Chem. Lett.* **5**, 680–685 (2014).
58. Yang, F. *et al.* High bending durability of efficient flexible perovskite solar cells using metal oxide electron transport layer. *J. Phys. Chem. C* **122**, 17088–17095 (2018).

Chapter 6. Conclusions

I have successfully realized the significant enhancement of the photovoltaic performance of perovskite solar cells (PSCs) using architecture design, including the perovskite light harvester layer passivation, compositional change of perovskite, replacement of carrier transport materials, new perovskite crystal growth approach and application of new metal electrode. Moreover, the recycling of noble metal electrode proposed in this study will pave new pathway for low cost, shorten energy payback period, resource waste elimination and eco-friendly fabrication of PSCs. The architecture designing have potentially acceleration for the industrial application of PSCs.

The quality of $MAPbI_3$-peovkiste has been dramatically enhanced using polymer passivation of PMMA. The power conversion efficiency (PCE) of $MAPbI_3$-PSCs has been promoted up to 20.5%, meanwhile, and the stability also has been enhanced under stabilized power output (SPO) measurement at continuous light soaking. However, the insulating properties of polymers deteriorated the hysteresis of PSCs because of the carrier accumulation on the interface between perovskite and polymer materials.

The fragile humidity resistance of $MAPbI_3$-peovkiste and sensitivity to ultraviolet stability of TiO_2 have been replaced by Cs mixed-cations based perovskite and SnO_2 as electron transport material (ETM) in the PSCs. The photovoltaic performance and stability of PSCs have been significantly promoted. Moreover, a high PCE of 17.1% of SnO_2 based fPSCs has been realized with taking the advantage of low-temperature fabrication of perovskite and superior ETM of SnO_2, in which the fPSCs can sustain an excellent bending durability of ca. 76.5% compared with that of the initial PCE even after 2000 bending cycles at bending radius of 4 mm. The SnO_2 electro transport layer composed of SnO_2 nanoparticles enable the high bending durability by releasing the bending stress.

The excessive PbI_2 as a Cs-perovskite precursor induces serious the carrier recombination loss, even though the large crystal perovskite film can be obtained. To improve the photovoltaic performance of PSCs, the second solution growth process (SSGP) technique has been introduced into perovskite crystals growth to eliminate the excessive PbI_2. The SSGP-PSCs has promoted the PCE up to 21.6%. Moreover, the stability of PSCs has also been substantially enhanced under the continuous light soaking at humidity of ca. 50% and thermal stability at 80 °C in nitrogen condition, respectively.

The excellent photovoltaic performance of PSCs has been usually realized on noble metal electrode using high vacuum thermal deposition process, however the PCSs has been discarded after the degradation of perovskite and increase the fabrication cost of perovskite-photovotaics. Thus, the nanoporous Au film has been introduced into PSCs to replace the conventional deposition technology of metal electrode. The nanoporous Au film based PSCs realized a high PCE of 19.0%, and more than 12 times recycled utilization of metal electrode. The nanoporous Au film enables an excellent bending durability of ca. 98.5% of fPSCs even after 1000 bending cycles testing at a bending radius of 5 mm, in which the nanoporous structure of Au film can prevent from penetrating cracks generated in the bending tests.

Improving the photovoltaic performance of PSCs by an approach of architecture design by varying the stacking configuration, passivation, and material innovation paves a potential way toward its commercial application.

List of publications

1. **Fengjiu Yang**, Jinzhe Liu, Zheng Lu, Pengfei Dai, Tomoya Nakamura, Keisuke Shinokita, Yuhei Miyauchi, Shenghao Wang, Luyang Chen, Atsushi Wakamiya, and Kazunari Matsuda, Facile Fabrication and Recycling of Nanoporous Au Electrode for Reducing Cost of Perovskite Solar Cells. (***Submitted***)
2. **Fengjiu Yang**, Jiewei Liu, Xiaofan Wang, Kenya Tanaka, Keisuke Shinokita, Yuhei Miyauchi, Atsushi Wakamiya, and Kazunari Matsuda, Highly efficient planar perovskite solar cells with high fill factor obtained using two-steps growth process. ***ACS Applied Materials & Interfaces***, 2019, 11, 15680–15687.
3. **Fengjiu Yang**, Jiewei Liu, Hong En Lim, Yasuhisa Ishikura, Keisuke Shinokita, Yuhei Miyauchi, Atsushi Wakamiya, Yasujiro Murata, and Kazunari Matsuda, High bending durability of efficient flexible perovskite solar cells using metal oxide electron transport layer. ***The Journal of Physical Chemistry C***, 2018, 122, 17088–17095.
4. **Fengjiu Yang**, Hong En Lim, Feijiu Wang, Masashi Ozaki, Ai Shimazaki, Jiewei Liu, Nur Baizura Mohamed, Keisuke Shinokita, Yuhei Miyauchi, Atsushi Wakamiya, Yasujiro Murata, and Kazunari Matsuda, Roles of polymer layer in enhanced photovoltaic performance of perovskite solar cells via interface engineering. ***Advanced Materials Interfaces***, 2018, 5, 1701256.
5. Feijiu Wang, Ai Shimazaki, **Fengjiu Yang**, Kaito Kanahashi, Keiichiro Matsuki, Yuhei Miyauchi, Taishi Takenobu, Atsushi Wakamiya, Yasujiro Murata, and Kazunari Matsuda, Highly efficient and stable perovskite solar cells by interfacial engineering using solution-processed polymer layer. ***The Journal of Physical Chemistry C***, 2017, 122, 1562-1568.

Conferences

International presentations

1. **Fengjiu Yang**, Jiewei Liu, Yuhei Miyauchi, Atsushi Wakamiya, and Kazunari Matsuda, Superior bending durability of flexible perovskite solar cells using metal oxide electron transport layer. The International Conference on Perovskite and Organic Photovoltaics and Optoelectronics (IPEROP19), January 2019, Kyoto, Japan, **poster presentation**.
2. **Fengjiu Yang**, Jiewei Liu, Yuhei Miyauchi, Atsushi Wakamiya, and Kazunari Matsuda, Superior bending durability of flexible perovskite solar cells using metal oxide electron transport layer. The Ajou-Kyoto-Zhejiang Joint Symposium on Energy Science, the annual symposium of energy scientists in Ajou, Kyoto, and Zhejiang Universities. January 2019, Ajou University, Korea, **oral presentation**.
3. **Fengjiu Yang**, Jiewei Liu, Yuhei Miyauchi, Atsushi Wakamiya, and Kazunari Matsuda, A facile solution processed SnO_2 for high efficient flexible perovskite solar cells. The 4th International Conference on Perovskite Solar Cells and Optoelectronics (PSCO-2018), September 2018, École polytechnique fédérale de Lausanne, Lausanne, Switzerland, **poster presentation**.
4. **Fengjiu Yang**, Hong En Lim, Masashi Ozaki, Ai Shimazaki, Yuhei Miyauchi, Atsushi Wakamiya, Yasujiro Murata, and Kazunari Matsuda, Highly enhanced photovoltaic performance of perovskite solar cells via polymer interface engineering and mechanism investigation. The 2nd Asia-Pacific Hybrid and Organic Photovoltaics (AP-HOPV18), January 2018, Kitakyushu, Japan, **oral presentation**.
5. **Fengjiu Yang**, Hong En Lim, Feijiu Wang, Mina Jung, Yuhei Miyauchi, Atsushi Wakamiya, Yasujiro Murata, and Kazunari Matsuda, Highly enhanced photovoltaic performance via polymer interface engineering of perovskite solar cells, The 3rd International Conference on Perovskite Solar Cells and Optoelectronics (PSCO-2017), September 2017, Oxford University, Oxford, United Kingdom, **poster presentation**.

Domestic presentations

1. **Fengjiu Yang**, Keisuke Shinokita, Yuhei Miyauchi, Atsushi Wakamiya, Luyang Chen, and Kazunari Matsuda, Application of nanoporous Au film as electrodes for high efficient perovskite solar cells. The 66th Japan Society of Applied Physics (JSAP) Spring Meeting, March 2018, Tokyo Institute of Tchenology, Tokyo, Japan, **oral presentation**.
2. **Fengjiu Yang**, Jiewei Liu, Yuhei Miyauchi, Atsushi Wakamiya, and Kazunari Matsuda, Highly efficient perovskite solar cells via two-steps growth approach of perovskite film. The 79th Japan Society of Applied Physics (JSAP) Autumn Meeting, Autumn 2018, Nagoya University, Nagoya, Japan, **oral presentation**.
3. **Fengjiu Yang,** Hong En Lim, Jiewei Liu, Yasuhisa Ishikura, Keisuke Shinokita, Yuhei Miyauchi, Atsushi Wakamiya, Yasujiro Murata, and Kazunari Matsuda, Flexible perovskite solar cells with high photovoltaic performance using solution processed tin oxide nanoparticle, The 65th Japan Society of Applied Physics (JSAP) Spring Meeting, March 2018, Waseda University, Tokyo, Japan, **highlight oral presentation**.
4. **Fengjiu Yang,** Hong En Lim, Mina Jung, Yuhei Miyauchi, Atsushi Wakamiya, Yasujiro Murata, and Kazunari Matsuda, Roles of polymer layer in enhanced photovoltaic performance of perovskite solar cells via interface engineering, The 53th Fullerenes-Nanotubes-Graphene (FNTG) Autumn Meeting, September 2017, Kyoto University, Kyoto, Japan, **poster presentation**.

Acknowledgement

The study described in this thesis was elaborately instructed by my supervisor of Professor Kazunari Matsuda and self-less supported by collaborated Professor Atsushi Wakamiya from October 2016 to September 2019.

First of all, I would like sincerely express my appreciation to my supervisor of Professor Kazunari Matsuda for instructing and supporting my Ph.D course academic study. Your gradually and mildly encouragements and instructions promoted my abilities, including broaden horizons and tamp foundational knowledge according to regular study, enhance technologies from summarization, reduce mistakes from self-examination and innovate ideas from self-exploration. It is difficult to finish my study and thesis without your continuous instruction and help.

Meanwhile, I would like sincerely express gratitude to my collaborated Professor Atsushi Wakamiya for full and unselfish supporting for the almost all needs of my experiment, giving me critical suggestions and helping me on vital moments. With your persistent supporting, I had preciously chances to attempt and explore the new possibilities. I also deeply impressed of you open minds and candid personality from the cooperation and discussion.

I also want to sincerely appreciate Associate Professor Yuhei Miyauchi for elaborating help. Your solid knowledge of physics and unremitting exploration of two dimensional materials are still me pursuing mark.

And, I want to sincerely thanks to the following people for their kindness help and assistance in my Ph.D study:

Professor Yasujiro Murata (Kyoto Univeristy) who helped me about the manuscript revision, allowed me to do experiment even condition changed of collaboration and gave me some precious suggestions.

Professor Luyang Chen (East China University of Science and Technology) who selfless supported the precious thin film sample of nanoporous Au for realizing the amazing designing for reusing Au electrode film in perovskite solar cells.

Professor Shenghao Wang (Shanghai University) who measured the specific surface area of Au film, supported evaporated Au film for characterization, and solar cells theoretical discussion.

Dr. Jiewei Liu (Kyoto University) who introduced the latest knowledge and research direction of perovskite solar cells when I just started my study. And, you always gave me some important helps of precious suggestions, data analysis and equipment operations.

Assistance Professor of Tomoya Nakamura (Kyoto University) who help me to use the new measurement of photoelectron microscopy and SEM-EDX, explained the analysis and gave me some convenient helping of experiments.

Dr. Masashi Ozaki who taught me the basic fabrication processes of perovskite solar cells and all related equipment operations.

Assistance Professor Hong En Lim (Tokyo Metropolitan University) who helped me to measure the optical properties of perovskite light harvester, analysis and JSPS application.

Mr. Yasuhisa Ishikura (Kyoto University) who taught me how to prepare the flexible perovskite solar cells substrates and supported me flexible PEN/ITO substrates.

Ms. Ai Shimazaki (Kyoto University) who helped me to prepare the fresh solvents and taught me sample preparations.

Ms. Mina June who taught me the thin film fabrication, thermal deposition equipment operation and composition discussion of perovskite.

Professor Fengjiu Wang (Henan University) who taught me the thin film polymer fabrication, discussion and explanation.

Assistance Professor Keisuke Shinokita (Kyoto University) who deeply inspired me of your strong physics knowledge and sharply comments.

I also want to sincere appreciation to Assistance Professor Richard Murdey, Ms. Yasuko Iwasaki, Mr. Masanaga Tanabe of Professor Wakamiya group; Mr. Xiaofan Wang, Mr. Wenjin Zhang, Dr. Dezhi Tan, Miss Yan Zhang, Dr. Takashi Someya, Dr. Taishi Nishihara, Dr. Akira Takakura, Mr. Masafumi Shimasaki, Mr. Kenya Tanaka, Mr. Shotaro Yano, Ms. Shiori Fujiwara and other previous members of Professor Matsuda group; Ms. Tomoko Aharen sincerely help, supports and encouragement.

Finally, I want to sincerely appreciate my family member: Mr. Lianjian Yang, Ms. Guihua Chen, Ms. Yang Meng, Ms. Xiulin Yang, Ms. Xiuxia Yang, Mr. Fengkai Yang, and other relatives selfless and sincerely support, encouragement and help.